

Oil & Natural Gas Technology

DOE Award No.: DE- FC26-08NT0005641

Final Research Performance Report

Producing Light Oil from a Frozen Reservoir: Reservoir and Fluid Characterization of Umiat Field, National Petroleum Reserve, Alaska

Project Period: October 1, 2008 to December 31, 2012

Submitted by:
Catherine L. Hanks

Signature

Geophysical Institute
University of Alaska Fairbanks
DUNS #: 615245164
Fairbanks, Alaska 99775
e-mail: chanks@gi.alaska.edu
Phone number: (907) 474-5562

Prepared for:
United States Department of Energy
National Energy Technology Laboratory

February 2013



Office of Fossil Energy

Disclaimer

This report was prepared as an account of work sponsored by an agency of the United States Government. Neither the United States Government nor any agency thereof, nor any of their employees, makes any warranty, express or implied, or assumes any legal liability or responsibility for the accuracy, completeness, or usefulness of any information, apparatus, product, or process disclosed, or represents that its use would not infringe privately owned rights. Reference herein to any specific commercial product, process, or service by trade name, trademark, manufacturer, or otherwise does not necessarily constitute or imply its endorsement, recommendation, or favoring by the United States Government or any agency thereof. The views and opinions of authors expressed herein do not necessarily state or reflect those of the United States Government or any agency thereof.

EXECUTIVE SUMMARY

Umiat oil field is a light oil in a shallow, frozen reservoir in the Brooks Range foothills of northern Alaska with estimated oil-in-place of over 1 billion barrels. Umiat field was discovered in the 1940's but was never considered viable because it is shallow, in the permafrost, and far from any transportation infrastructure. The advent of modern drilling and production techniques has made Umiat and similar fields in northern Alaska attractive exploration and production targets. Since 2008 UAF has been working with Renaissance Alaska Inc. and, more recently, Linc Energy, to develop a more robust reservoir model that can be combined with rock and fluid property data to simulate potential production techniques. This work will be used to by Linc Energy as they prepare to drill up to 5 horizontal wells during the 2012-2013 drilling season.

This new work identified three potential reservoir horizons within the Cretaceous Nanushuk Formation: the Upper and Lower Grandstand sands, and the overlying Ninuluk sand, with the Lower Grandstand considered the primary target. Seals are provided by thick interlayered shales. Reserve estimates for the Lower Grandstand alone range from 739 million barrels to 2437 million barrels, with an average of 1527 million bbls. Reservoir simulations predict that cold gas injection from a wagon-wheel pattern of multilateral injectors and producers located on 5 drill sites on the crest of the structure will yield 12-15% recovery, with actual recovery depending upon the injection pressure used, the actual Kv/Kh encountered, and other geologic factors.

Key to understanding the flow behavior of the Umiat reservoir is determining the permeability structure of the sands. Sandstones of the Cretaceous Nanushuk Formation consist of mixed shoreface and deltaic sandstones and mudstones. A core-based study of the sedimentary facies of these sands combined with outcrop observations identified six distinct facies associations with distinctive permeability trends. The Lower Grandstand sand consists of two coarsening-upward shoreface sands sequences while the Upper Grandstand consists of a single coarsening-upward shoreface sand. Each of the shoreface sands shows a distinctive permeability profile with high horizontal permeability at the top getting progressively poorer towards the base of the sand. In contrast, deltaic sandstones in the overlying Ninuluk are more permeable at the base of the sands, with decreasing permeability towards the sand top. These trends impart a strong permeability anisotropy to the reservoir and are being incorporated into the reservoir model. These observations also suggest that horizontal wells should target the upper part of the major sands.

Natural fractures may superimpose another permeability pattern on the Umiat reservoir that need to be accounted for in both the simulation and in drilling. Examination of legacy core from Umiat field indicate that fractures are present in the subsurface, but don't provide information on their orientation and density. Nearby surface exposures of folds in similar stratigraphy indicate there are at least three possible fracture sets: an early, N/S striking set that may predate folding and two sets possibly related to folding: an EW striking set of extension fractures that are parallel to the fold axes and a set of conjugate shear fractures oriented NE and NW. Analysis of fracture spacing suggests that these natural fractures are fairly widely spaced (25-59 cm depending upon the fracture set), but could provide improved reservoir permeability in horizontal legs drilled perpendicular to the open fracture set.

The phase behavior of the Umiat fluid needed to be well understood in order for the reservoir simulation to be accurate. However, only a small amount of Umiat oil was available; this oil was collected in the 1940's and was severely weathered. The composition of this 'dead' Umiat fluid was characterized by gas chromatography. This analysis was then compared to theoretical Umiat composition derived using the Pedersen method with original Umiat fluid properties published in the original reports. This comparison allowed estimation of the 'lost' light hydrocarbon fractions. An Umiat 'dead' oil sample then could be physically created by adding the lost light ends to the weatherized Umiat dead oil sample. This recreated sample was recombined with solution gas to create a 'pseudo-live' Umiat oil sample which was then used for experimental PVT and phase behavior studies to determine fluid properties over the range of reservoir pressures and temperatures. The phase behavior of the 'pseudo-live' oil was also simulated using the Peng-Robinson equations of state (EOS). The EOS model was tuned with measured experimental data to accurately simulate the differential liberation tests in order to obtain the necessary data for reservoir simulation studies, including bubble point pressure and oil viscosity. The bubble point pressure of the reconstructed Umiat oil is 345 psi, suggesting that maintenance of reservoir pressures above that pressure will be important for the any proposed production technique.

A major part of predicting how the Umiat reservoir will perform is determining the relative permeability of oil in the presence of ice. Early in the project, UAF work on samples of the Umiat reservoir indicated that there is a significant reduction in the relative permeability of oil in the presence of ice. However, it was not clear as to why this reduction occurred or where the ice resided. To explore this further, additional experimental and theoretical work was conducted. Core flood experiments were performed on two clean Berea sandstone cores under permafrost conditions to determine the relative permeability to oil (k_{ro}) over a temperature range of 23°C to -10°C and for a range of connate water salinities. Both cores showed maximum reduction in relative permeability to oil when saturated with deionized water and less reduction when saturated with saline water.

This reduction in relative permeability can be explained by formation of ice crystals in the center of pores. Theoretically, the radius of ice formed in the center of the pore can be determined using the Kozeny–Carman Equation by assuming the pores and pore throats as a cube with 'N' identical parallel pipes embedded in it. Using the values of k_{ro} obtained from the experimental work as input to the Kozeny–Carman Equation at -10°C, the radius of ice crystals dropped from 0.145 μm to 0.069 μm when flooding-water salinity is increased to 6467 ppm. This explains the reduction of relative permeability with decreasing salinity but does not take into consideration other effects such as variations in pore throat structure.

In addition, fluids like deionized water, saline water, and antifreeze (a mixture of 60% ethylene or propylene glycol with 40% water) were tested to find the best flooding agent for frozen reservoirs. At 0°C, 9% greater recovery was observed with antifreeze was used as a flooding agent as compared to using saline water. Antifreeze showed 48% recovery even at -10°C, at which temperature the rest of the fluids failed to increase production.

Preliminary evaluation of drilling fluids indicate that the brine-based muds caused significantly less swelling in the Umiat reservoir sands when compared to fresh-water based muds. However

since freezing filtrate is another cause of formation damage, a simple water-based-mud may not be a viable option. It is recommended that new fluids be tested, including different salts, brines, polymers and oil-based fluids. These fluids should be tested at low temperatures in order to determine the potential for formation damage, the fluid properties under these conditions and to ensure that the freezing point is below that of the reservoir.

In order to reduce the surface footprint while accessing the maximum amount of the Lower Grandstand interval, simulations used development from 5 surface locations with a wagon-wheel pattern of multilateral injectors and producers. There is no active aquifer support due to small piezometric head in the area and no existing gas cap, so an alternative method of pressure support is needed. Cold gas injection was used in the simulations as it is considered the most viable means of providing pressure maintenance while maintaining wellbore stability and reducing impact on the permafrost. Saline water injection may be a viable alternative, though this may have a detrimental effect on permafrost.

In the short term, the results of this work are being incorporated into Linc Energy's drilling and development plan. This project has also provided valuable information on the rock and fluid properties of low temperature reservoirs as well as the efficacy of potential production techniques for Umiat or similar shallow frozen reservoirs in the circum-Arctic.

TABLE OF CONTENTS

Introduction and geologic setting	1
Sedimentology, stratigraphy, and reservoir properties of an unconventional reservoir in the Cretaceous Nanushuk Formation at Umiat field, North Slope, Alaska	5
Fracture distribution and character in exposed and subsurface Cretaceous rocks in the Umiat area	41
Measurement of gas-oil relative permeability for frozen rock systems	54
Effect of below 0°C reservoir temperature on relative permeability to oil: a theoretical and experimental approach	68
Efficacy of saline water and antifreeze as flooding fluids in a frozen reservoir	81
Fluid Characterization and Phase Behavior Studies of Oil from Frozen Reservoir of Umiat Oil Field, Alaska	85
Effect of Drilling Fluid characteristics on Rock Properties of Umiat Field formations	107
Geological Modeling and Reservoir Simulation of Umiat	112
Project summary and conclusions	151
Acknowledgments	175
References	176
Bibliography	187

Introduction and Geologic Setting

The Umiat field of the National Petroleum Reserve of Alaska (NPRRA) was discovered during the initial exploration of northern Alaska in the 1940's and 50's (Collins, 1958). Initial estimates of recoverable reserves in the Umiat field ranged from 30 to over 100 million bbl, with an average of about 70 million bbl (Baptist, 1960). The reservoir is at very shallow depths (275-1055 ft), with most of the reservoir in permafrost. Moreover, the reservoir pressures are very low, with small quantities of solution gas. These factors along with the lack of a drilling technology to economically extract such shallow and frozen oil have precluded Umiat development.

However, the oil at Umiat is high gravity (37°API) and not biodegraded, despite being at very shallow depths. This makes it an attractive target, if production issues can be overcome.

Recent advances in the understanding of Northern Alaska geology and in drilling technology have led to a renewed industry interest in Umiat. Current industry estimates indicate that the oil in place at Umiat may be as high as 1 BBl. Horizontal drilling techniques have opened the possibility of economically developing such a shallow reservoir. However, the unusual reservoir conditions that exist at Umiat continue to pose a significant challenge for any commercial development. While the original analysis of the Umiat oil suggested it should flow under normal reservoir conditions, the reservoir is shallow with low reservoir pressures. Low reservoir temperatures and the presence of ice is a complicating factor—there is no published information on how ice would be distributed in the pore spaces of a frozen reservoir or the relative permeability of oil and gas in the presence of ice. In addition, there are few remaining samples of the reservoir fluid and those that are available are significantly degraded. This lack of physical data on Umiat oils or its behavior under the Umiat reservoir conditions or of the rock properties precludes conducting simulation studies that could help determine which production method would be the most effective.

The goal of this project is to collect and analyze the data necessary to determine how to most effectively produce this shallow, frozen reservoir. In order to achieve this goal, the project will:

- develop a robust geologic model that includes both the sedimentologic and structural character of the reservoir;
- upscale the geologic model into a reservoir model
- collect the necessary fluid and reservoir properties data for the simulation
- test possible production methods via desktop simulation

The project's original industry partner was Renaissance Alaska Inc. Linc Energy bought Renaissance Alaska's interest in Umiat in July 2011 and plans to drill three to five new vertical wells during the 2012-2013 drilling season to reevaluate the field and to evaluate possible drilling and production approaches.

Scope of this report

This report summarizes the final results of the project. Each section summarizes a different aspect of the study and include:

- Sedimentology, stratigraphy, and reservoir properties of an unconventional reservoir in the Cretaceous Nanushuk Formation at Umiat field, North Slope, Alaska by G. Shimer (Ph.D. candidate), P. McCarthy, C. Hanks and J. Davis (M.S. student)
- Fracture distribution and character in exposed and subsurface Cretaceous rocks in the Umiat area by R. Wentz (M.S. student) and C. Hanks
- Relative permeability of oil in the presence of ice: an experimental approach by V. Godabrelidze (M.S. student) and A.Dandekar
- Influence of salinity and temperature on the relative permeability of oil in the presence of ice: an experimental and theoretical approach by K. Venepalli (M.S. student) and J. Mongrain
- Efficacy of saline water and antifreeze as flooding fluids in a frozen reservoir by K. Venepalli (M.S. student) and J. Mongrain
- Fluid properties of the Umiat fluids and implications for fluid behavior during production by C. Shukla (M.S. student) and A. Dandekar
- Effect of drilling fluid characteristics on rock properties of Umiat field formations by A. Kamel and J. Demallie (B.S. student)
- Geological Modeling and Reservoir Simulation by I. Oraki Kohshour (M.S. student), M. Ahmadi and C. Hanks

Geology of Umiat field

Umiat is a thrust-related anticline at the leading edge of the Brooks Range fold-and-thrust belt (Figures 1 and 2). The Brooks Range is the northern continuation of the Rocky Mountain orogen and, in Alaska, formed as a result of the collision of an intraoceanic island arc with a south-facing Paleozoic and early Mesozoic passive continental margin (Moore et al., 1994). Collapse of the passive continental margin and subsequent loading of the lithosphere resulted in the formation of an asymmetric foreland basin, the Colville basin. While most of the shortening occurred during Late Jurassic-Early Cretaceous time, contraction has continued episodically during the Cretaceous and Early Tertiary, resulting in progradation of the fold-and-thrust belt into the Colville basin. The Umiat structure is a fault-related anticline in this younger portion of the Brooks Range fold-and-thrust belt.

The reservoir at Umiat consists of multiple shallow marine sands of the Cretaceous Nanushuk Formation (Figure 3). The main reservoir interval at Umiat lies within the Albian-Cenomanian

Nanushuk Formation, a unit that is widespread in the subsurface of the North Slope and in outcrop along the Brooks Range fold-and-thrust belt. Regionally, the Nanushuk consists of topset deltaic facies associated with deep marine mudstones of the Torok Fm. (Houseknecht and Schenk, 2005). Though the Nanushuk Formation has been considered largely deltaic, the formation varies considerably from west to east, reflecting changing source areas as the Colville basin filled from west to east.

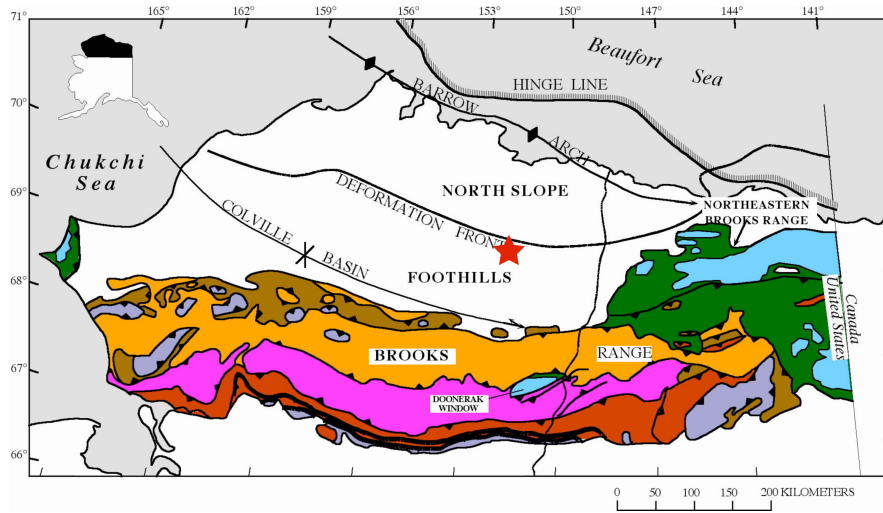


Figure 1. Geologic map of northern Alaska. Umiat field is located at the leading edge of the Brooks Range fold-and-thrust belt. Map modified from Moore and others, 1994.

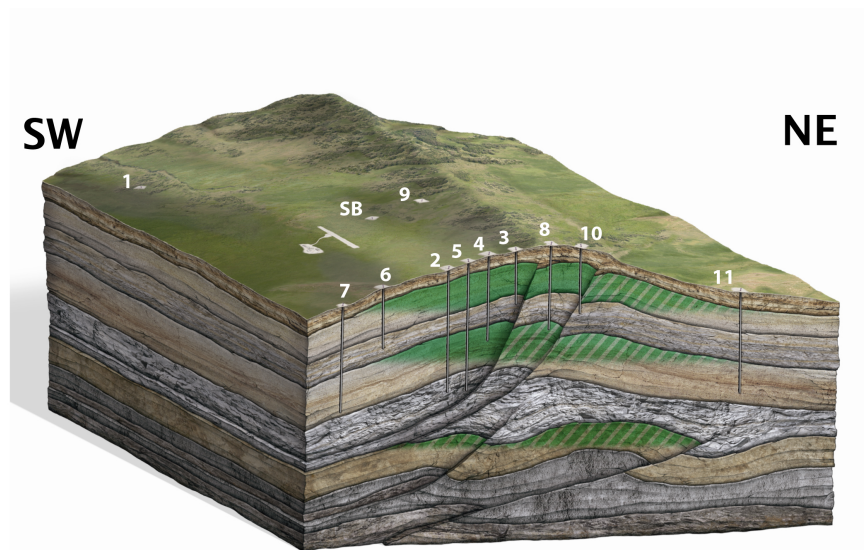


Figure 2. Block diagram of Umiat field showing the structural geometry of the field and location of existing wells. Wells 2-8 and 10-11 are projected onto the line of section. Structural interpretation courtesy of Renaissance Alaska LLC.

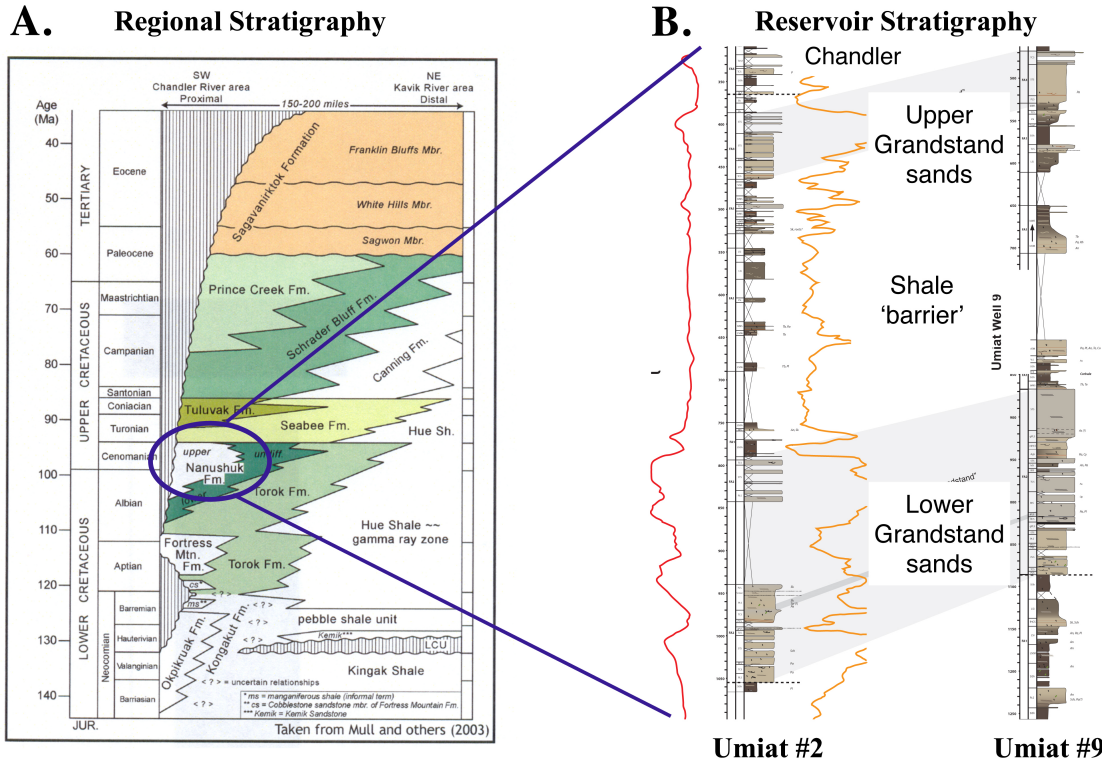


Figure 3. A. Regional stratigraphy of northern Alaska, showing the stratigraphic position of the Umiat reservoir in the Early Cretaceous Nanushuk Formation. Modified from Mull and others, 2003; B. Reservoir stratigraphic nomenclature used at Umiat field.

In the subsurface at Umiat field, the Nanushuk has been divided into 4 informal units: the Chandler sand (aka Killik), Upper Grandstand sand, Shale barrier and the Lower Grandstand sands (Figure 3; Collins, 1958). These units, while informal, will be used throughout this report.

Sedimentology, stratigraphy, and reservoir properties of an unconventional reservoir in the Cretaceous Nanushuk Formation at Umiat field, North Slope, Alaska.¹

ABSTRACT

There are numerous oil and gas accumulations in the Brooks Range foothills of the National Petroleum Reserve–Alaska (NPRA). We use cores and well logs from twelve legacy wells at Umiat oil field to characterize the sedimentology and stratigraphy of an unconventional frozen reservoir at the southeastern boundary of the NPRA. Previous studies of Umiat field delineated a shallow, permafrost-affected reservoir in sandstones of the Cretaceous (Albian-Cenomanian) Nanushuk Formation. We identify five facies associations: offshore and prodelta, lower shoreface, upper shoreface, delta front, and delta plain.

There are three stratigraphically distinct, regionally extensive depositional systems within the Nanushuk Formation at Umiat. These systems contain several potential petroleum reservoirs. The lower Nanushuk Formation, including a reservoir unit known informally as the Lower Grandstand, primarily consists of marine mudstone and shoreface sandstones. The middle Nanushuk Formation is dominantly deltaic, and contains a second major reservoir unit in the informal Upper Grandstand sand. Both the Upper and Lower Grandstand are regressive. The upper Nanushuk Formation is transgressive, and contains an additional potential reservoir unit in shoreface sandstones of the informal Ninuluk unit. The primary reservoir units at Umiat field are upper shoreface and delta front sandstones in the Lower and Upper Grandstand, where increased sorting and decreased bioturbation in high-energy depositional environments affect overall permeability and permeability anisotropy.

INTRODUCTION

Umiat field is an undeveloped petroleum accumulation in the Brooks Range foothills of the National Petroleum Reserve–Alaska (NPRA: Fig. 1). The field consists of clastic deposits of the Albian-Cenomanian Nanushuk Formation deformed in a thrust-faulted anticline (Fig. 2a: Collins, 1958; Molenaar, 1982). There are two known shallow reservoirs with oil-water contacts at 450 ft (173 m) and 640 ft (195 m) below sea level, and the field lies almost entirely within deep permafrost found from 770-1055 ft (235-322 m) below ground surface (Molenaar, 1982). The field remains undeveloped due to low reservoir pressures and the permeability-reducing effects of pore ice. The site also lies at a distant location from existing pipeline infrastructure, approximately 100 miles southwest of Prudhoe Bay and 80 miles west of the Trans-Alaska Pipeline System (TAPS). Though early estimates of recoverable oil were in the range of 70 million

¹ Modified from manuscript submitted to *AAPG Bulletin*, December 2012.

barrels (Molenaar, 1982), there may be up to 1.4 billion barrels of oil in place (Levi-Johnson, 2010).

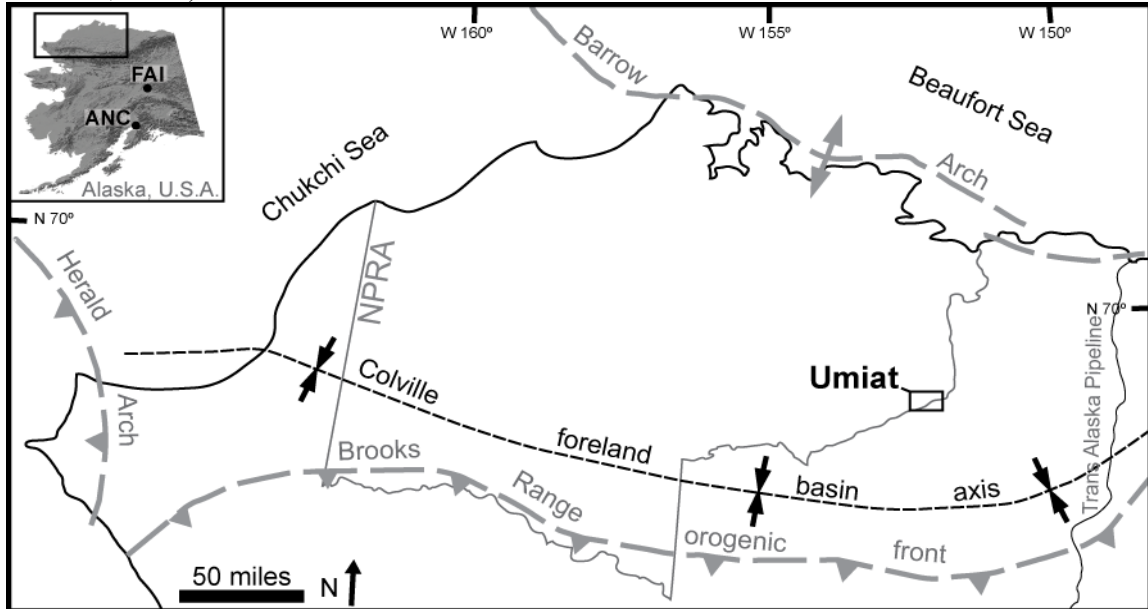


Figure 1. A map of northern Alaska shows the location of Umiat field (black rectangle) in relation to the axis of the Colville Basin, the thrust front of the Brooks Range, and the Herald and Barrow arches (modified from Decker, 2007). The Colville River forms the eastern boundary of the National Petroleum Reserve – Alaska (NPRA) in the Umiat area. Inset (upper left): digital elevation model of Alaska with the study area outlined in black and locations of Fairbanks (FAI) and Anchorage (ANC) for reference.

Despite known engineering challenges, advances in horizontal drilling technology and high oil prices created renewed interest in Umiat field and justified a reassessment of the field.

Several previous generations of research focused on the Nanushuk Fm. at Umiat field. The field was discovered during federal investigations of Naval Petroleum Reserve No. 4 (NPR-4) between 1944-1953, when eleven wells were drilled at the site (Fig. 2b: Collins, 1958). Core samples from these legacy wells are stored at the Alaska Geologic Materials Center (GMC) in Eagle River, Alaska, and at the United States Geological Survey (USGS) Core Research Center in Lakewood, Colorado. The original report on drilling operations (Collins, 1958) includes core and cuttings descriptions, microfaunal analyses, well logs (resistivity and spontaneous potential), and a summary of reservoir characteristics. Seven of the eleven Umiat wells produced oil from the upper Nanushuk Fm., while there was no recovery from an additional well (Umiat No. 2) because of interactions between the rock, permafrost, and freshwater drilling fluids (Collins, 1958). Though approximately 40,000 barrels of oil were recovered before 1953, the recovery factor estimates for this time ranged from 8-32.5% in the permafrost-affected reservoir (Molenaar, 1982). All eleven Umiat wells have not been studied publicly in detail since the original drilling reports (Collins, 1958), and they represent a valuable resource for the evaluation of the Nanushuk Fm. in the subsurface.

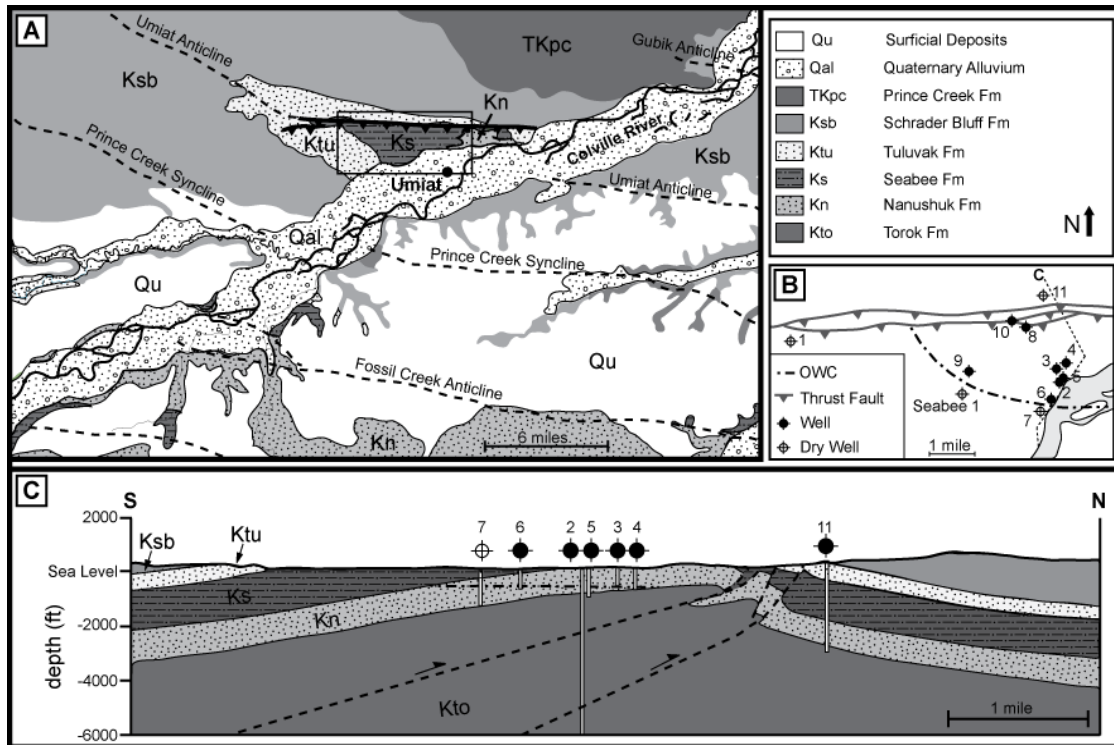


Figure 2. (A) Geologic map of the Umiat area (modified from Mull et al., 2004). There is limited exposure of the Nanushuk Fm. at the surface along the Umiat anticline. Note the orientation of major anticlines and synclines, indicative of the fold-and-thrust origin of the Brooks Range foothills. Black rectangle shows the location of Figure 2b. **(B) Map showing locations of the eleven Umiat wells and the Seabee No. 1 well.** Dash-dot line indicates oil-water contact on the south side of the Umiat anticline, while dashed line marks the trace of the cross section in Figure 2c. **(C) North-south cross section of Umiat anticline with basic stratigraphy, major thrust faults, and well locations (modified from Molenaar 1982).** Dash-dot line within the Nanushuk Fm. (Kn) show the oil-water contact.

A federal reinvestigation of the petroleum resources of the NPR-4 began in 1974, and in 1977 the National Petroleum Reserves Production Act transferred the NPR-4 from the U.S. Navy to the Department of the Interior, when it became the NPRA (Schindler, 1988). New reservoir quality assessments of the Nanushuk Fm. during this time included core description, biostratigraphy, petrographic analyses, and 2-D seismic interpretations (Ahlbrandt, 1979; Fox et al., 1979). In 1978 the Seabee No. 1 well was also drilled at Umiat to sample deep strata below the Nanushuk Fm.. Seabee No. 1 lies outside of the oil-water contact at Umiat and lacks any core samples from the Nanushuk Fm. (Fig. 2b). The well does have a modern suite of geophysical well logs through that interval (Legg and Brockway, 1983), and these are valuable for subsurface interpretations.

The second generation of summary reports and reviews of Umiat and the Nanushuk Fm. ended in the 1980's (Molenaar, 1982; Huffman, 1985; Gryc, 1988). Following years of inactivity, recent studies of the Nanushuk Fm. at various locations on the North Slope utilized modern facies analysis (LePain and Kirkham, 2001; Houseknecht and Schenk, 2005; LePain et al., 2009) and sequence stratigraphic interpretations (Decker, 2007; Houseknecht and Schenk, 2005) to establish the Nanushuk Fm. as a spatially and

chronstratigraphically variable mix of wave-, river-, and tide-influenced facies deposited in a largely deltaic setting (LePain et al., 2009).

The purpose of this study is to assess facies variability within the Nanushuk Fm. at Umiat field, characterize the reservoir-scale stratigraphic architecture, and investigate how facies variability affects reservoir distribution. We interpret cores and well logs from all eleven Umiat wells and the nearby Seabee No. 1 well (Fig. 2b), and define five facies associations within three distinct depositional systems. Four broadly distributed major reservoir units correspond to informal units of the Nanushuk Fm.. Different sedimentary processes are responsible for each reservoir unit, but three of the units have similar characteristic permeability profiles and degrees of heterogeneity. The fourth unit is distinct in character, but poorly represented in the subsurface. The results of this evaluation of the sedimentology and stratigraphy of the Nanushuk Fm. at Umiat field are important for evolving production models, and have implications for broader interpretations of Nanushuk Fm. depositional environments on the east-central North Slope.

GEOLOGIC SETTING

Umiat field, Alaska (N 69° 22'12", W 152° 8'10") is located in the northern Brooks Range foothills along the southeastern boundary of the NPRA (Fig. 1). Most of the infrastructure at Umiat, including some of the original well sites, sits on Quaternary sediments of the Colville River floodplain on the southern limb of an asymmetric, northward-vergent, thrust-faulted anticline (Fig. 2a-c). The anticline deforms Lower Cretaceous to Tertiary sediments derived from the ancestral Brooks Range to the south (Mull et al., 2004). These "Brookian" strata are part of a thick package of clastic sediments that filled the Colville foreland basin starting in the Early Cretaceous (Fig. 3: Mull et al., 2003). The four relevant Brookian formations at Umiat are the Albian-Cenomanian Torok and Nanushuk formations and the overlying Cenomanian-Turonian Seabee and Tuluvak formations. These formation pairs make up two distinct depositional megasequences (Mull, 1985; Hubbard et al., 1987; Decker, 2007). Cenomanian-Turonian strata, including the upper portion of the Nanushuk Fm., are exposed on the eastern limb of the Umiat anticline in bluffs at Umiat Mountain (Houseknecht and Schenk, 2005), but the underlying Nanushuk Fm. reservoir units are not exposed at the surface.

The Nanushuk Fm. prograded from west-to-east along the axis of the Colville Basin, with an additional south-to-north component in the area that now makes up the east-central Brooks Range foothills (Houseknecht and Schenk, 2005; Decker, 2007; Houseknecht et al., 2009; LePain et al., 2009). The formation has been described as fluvial, deltaic, and shallow marine, with major deltaic depocenters in the west and central North Slope (Ahlbrandt et al., 1979; Mull, 1985), but there is considerable west-to-east variation in Nanushuk Fm. depositional environments across the North Slope. In the Umiat area the Nanushuk Fm. is slightly younger and more sand-rich than in the west, possibly due to sources from multiple, shorter rivers draining the northern flank of the ancestral Brooks

Range and/or due to greater wave-influence and reworking (Molenaar, 1985; LePain and Kirkham, 2001; Houseknecht and Schenk, 2005; LePain et al., 2009).

Originally defined as the Nanushuk Group (Detterman, 1956), with numerous shallow marine and non-marine formations the Nanushuk was lowered to formation status to comply with international Collins, guidelines (Mull et al., 2003). Though now informal units, the formations of the former Nanushuk Group remain in common use in the subsurface (Fig. 3b). At Umiat field these units include the marine Tuktuk, shallow marine to deltaic Grandstand, marginal marine to non-marine Killik tongue of the Chandler, and the shallow marine Ninuluk "formations". We use Killik instead of Chandler to emphasize the local character of the former formation. Furthermore, in the subsurface at Umiat the Grandstand consists of two distinct sand-rich intervals (Upper and Lower Grandstand) separated by a tongue of marine mudstone of the Tuktuk, commonly referred to as the Shale Barrier.

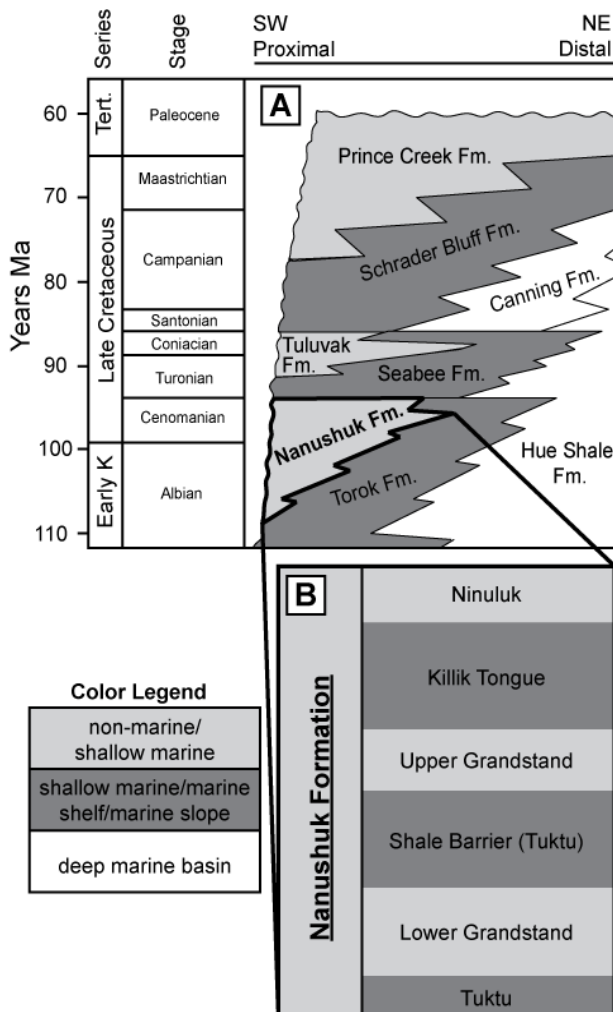


Figure 3. (A) Brookian stratigraphic units of the Colville Basin relevant to this study. Nanushuk Fm. outlined in bold (modified from Mull et al., 2003). A color legend refers to the generalized depositional environments for each formation. (B) Informal subsurface stratigraphy of the Nanushuk Fm. in common usage at Umiat field.

Umiat reservoir tests during the 1944-1953 drilling period produced oil primarily from the Upper Grandstand, with minor production from the Ninuluk and oil shows in the

other "formations" (Molenaar, 1982). In Umiat No. 11 the Grandstand and Killik have higher average porosity and permeability than the Ninuluk, probably due to changes in depositional environment and possible changes in provenance (Fox et al., 1979). This relationship has been assumed to be consistent in the subsurface throughout the reservoir, but it is important to note that Umiat No. 11 was a dry well that lies in the footwall of the thrust structure and outside the limits of the known petroleum trap.

Regional Context

The Colville basin formed in flexural response to tectonic loading along the ancestral Brooks Range and Herald Arch (Fig. 1: Nunn et al., 1987; Coakley and Watts, 1991; Moore et al., 1994). The earliest sedimentary evidence for initiation of the Brookian orogeny is Hauterivian in age (Bird and Molenaar, 1992), but the Albian-Cenomanian (112-93.5 Ma; Walker and Geissman, 2009) Torok and Nanushuk formations were deposited during a period of extension and exhumation on the south side of the Brooks Range that started ~113 Ma (Blythe et al., 1996; O'Sullivan et al., 1997). Cooling and exhumation slowed by ~95 Ma (O'Sullivan et al., 1997) and by the late Albian, the high volume of sediment represented by the Torok and Nanushuk formations filled much of the Colville Basin and overtopped the Barrow Arch (Molenaar, 1985; LePain et al., 2009).

METHODS

We photographed, described, and logged all available cores from each of the eleven Umiat wells at the Alaska Geologic Materials Center (GMC) and cross-referenced the results with the original core and cuttings descriptions (Collins, 1958). Where resistivity and spontaneous potential (SP) well logs are available, we use the data to interpret gaps between cored intervals and to correlate between the Umiat wells. The Seabee No. 1 well also has a gamma ray log, used for further correlation.

We collected air-permeability data using a New England Research Tiny Perm II mini-permeameter. Horizontal permeability was recorded at 1-ft intervals from slabbed sandstone cores. The rough surfaces of unslabbed cores prevented the formation of an adequate seal for permeameter readings. Vertical permeability measurements were made on relatively flat, unlaminate surfaces at more irregular intervals. For ease of interpretation, individual permeability values (K_h and K_v) underwent log transformation:

$$\text{Eq. 1: } \log(K) = \log_{\text{permeability}}$$

Log transformed values range from 0 (log1 md) to 3 (log1000 md). We calculated permeability anisotropy (K_v/K_h), and present this data as averages for reservoir units. Any ratio over 2.0 was considered an outlier caused by instrumental or operator error, and was not included in the average values.

We also quantified the thickness of sandstone and mudstone units in all of the Umiat wells using core description and published cuttings data (Collins, 1958), and calculated a sand:mud ratio for the mudstone-dominated units in the subsurface.

A total of 31 rock samples were collected (11 from Umiat well 1, 5 from Umiat well 3, 5 from Umiat well 9, and 10 from Umiat well 11) and include representative sandstones of the potential reservoir interval of the Nanushuk Formation. Thin sections were manufactured for all samples at the University of Iowa petrographic laboratory, Iowa City, Iowa. Each sample was vacuum-impregnated with blue epoxy resin prior to thin section preparation. All thin sections were etched with hydrofluoric acid and stained with Amaranth Red and Sodium Cobaltinitrate for identification of plagioclase and potassium feldspar, respectively. After staining, point counts were conducted by a single operator. A minimum of 300 framework grains per thin section were counted. Matrix and cements were not counted. Separate classifications and tabulations of the framework grains were made using the Gazzi-Dickinson method (Gazzi 1966; Dickinson 1970). The data were then normalized and plotted on a QFL diagram. Data for Umiat # 1 compiled from Geological Survey Professional Paper 305-B by Paul D. Krynine (Collins, 1958) was included in the ternary diagrams for comparison across the Umiat anticline.

Sorting and roundness were measured visually using a Wentworth sand classification card from Precision Core Analysis, Inc. Packing was qualitatively measured on the basis of the amount of blue dye epoxy present and grain-to-grain contacts. Sandstones were considered tight where there were more than 5 grain-to-grain contacts and little blue dye epoxy. Moderate packing was designated where there was intergranular space shown by the blue dye and on average less than 5 grain-to-grain contacts, but no floating grains. Sandstones were considered to have loose packing when there were floating grains present. Cement compositions were determined using plane polarized and cross polarized optical microscopy. Criteria include color in plane polarized light and birefringence in cross-polarized light. Mineral replacement was analyzed using optical microscopy based on grain dissolution, ghost structures, clay rims, and abrupt changes in birefringence within the grain boundary. Degree of compaction was determined based on the tightness of packing and traditional sedimentary grain fabrics such as, point contacts, concavo-convex contacts, sutured contacts, and intergranular porosity (Figure). Porosity was estimated based on intergranular space shown by blue dye epoxy and secondary porosity created by framework grain dissolution.

FACIES AND FACIES ASSOCIATIONS

We distinguish facies on the basis of grain size, sedimentary structures, and biological features (Table 1; Fig. 4). Individual facies are grouped into facies associations (Table 2) on the basis of bedding relationships observed in core, and upward coarsening or fining trends from lithologic logs and well logs. We define five facies associations (Fig. 6-8), with additional subdivision of facies associations to differentiate distinct elements (i.e.: distal and proximal lower shoreface).

Facies Association 1 (FA-1)

FA-1 (Figs. 6, 7; Table 2) comprises successions of silty shale (F-1), massive mudstone (F-2), and wavy or lenticular bedded mudstone (F-3). Highly bioturbated (BI 4-6) mudstones contain abundant *Phycosiphon* and *Schaubcylindrichnus freyi* (Fig. 5). *Paleophycus* and *Planolites* are associated with increasing sand content and the transition to FA-2a. Lenticular or wavy-bedded mudstones (F-3) have lower bioturbation intensities (BI 0-3). Both F-2 and F-3 mudstones contain arenaceous and calcareous foraminifera of the Albian *Verneuilinoides borealis* faunal zone (Bergquist, 1958), and have the highest percentage of dinoflagellates in the Nanushuk Fm. (May and Shane, 1985).

Table 1. Facies Described in Core at Umiat Field

Facies	Diagnostic Features	Process Interpretation
F-1: Silty Shale	Laminated silty mudstone with color dependent on both grain size and organic matter content. Laminations are parallel/subparallel. Grades up into F-3 in some settings. BI of 3 or less.	Suspension settling in low energy settings. Well-preserved laminations may indicate low oxygen (dysoxic) conditions that inhibit biogenic activity.
F-2: Mudstone	a. Dark grey to black shale to sandy silt, with color dependent on both grain size and organic matter content. Some red-orange staining is present. Either massive, or with a BI of 4 or greater: individual traces are discernable, but bedding features are indistinct. Includes a wide range of trace fossils. Bivalve and gastropod shells present. b. carbonaceous mudstone, with common plant fossils and bivalve fossils.	Suspension settling in an environment that supports significant biogenic activity. Red-orange staining may indicate exposure to the atmosphere or diagenetic alteration. Accumulation of organic matter and mud in water-saturated and poorly oxygenated lake or bay environments.
F-3: Lenticular-Wavy Bedded Mudstone	Dark grey lenticular to wavy bedded mudstone. Very fine to fine grained sand or silty laminations (1-5 cm thick) have internal ripple cross laminations.	Suspension settling interrupted by rare unidirectional currents.
F-4: Apparently Massive Sandstone	Light grey, well-sorted, very fine- to fine-grained sandstone with rare beds of medium sandstone. No visible structures, but rare carbonaceous partings.	Lack of visible structure due to rapid deposition, high degree of sorting, dewatering, or cryptobioturbation.
F-5: Low Angle Cross-Laminated Sandstone	Light grey, well-sorted very fine- to fine-grained sandstone. Low angle laminations dip <15° and show changes in thickness. Beds 0.5-2 m thick. Associated features include mudstone rip-up clasts and shell lags.	Hummocky to swaley cross stratification deposited by oscillatory currents. (Dott and Bourgeois, 1982)
F-6: Ripple Cross-Laminated Sandstone	a. Light grey very fine- to fine-grained asymmetrical ripple cross-laminated sandstone. Mudstone laminations are common. b. Light grey very fine- to fine-grained symmetrical ripple cross-laminated sandstone. Mudstone laminations are common.	Ripple migration under unidirectional currents as part of larger, subaqueous bar-forming processes. Ripple formation under oscillatory currents.
F-7: Mud Draped Ripple Cross-Laminated Sandstone	Light grey to tan, fine- to medium-grained ripple cross-laminated sandstones with cm-thick, oxidized mud drapes.	Mixed energy conditions, with suspension settling during low energy slack water conditions.
F-8: Parallel Laminated Sandstone	Light grey, well-sorted very fine- to medium-grained plane parallel laminated sandstone. Larger laminations show normal grading. Lamination surfaces are often associated with carbonaceous partings.	Upper flow regime plane bed conditions, or swash zone conditions (Paola et al., 1989)
F-9: Trough Cross-Laminated Sandstone	Grey to tan very fine- to medium-grained sandstone with high angle (>15°) laminations.	Subaqueous dunes formed by unidirectional currents in the distributary system or by cross-shore and longshore currents along the coast.
F-10: Poorly Sorted Sandstone and Gravelly Sandstone	Grey to tan poorly sorted very fine- to coarse-grained sand. Sand is always the dominant grain size, with pebble-sized clasts that include mudstone rip-ups, coal fragments, and rare lithics. Pebbles occur as lag deposits or mixed into a poorly sorted matrix.	Channel lag and bar formed by unidirectional currents. Coal fragments point to terrestrial origin.
F-11: Coal	Black coal deposits from 5 cm-10 cm thick, Often found in association with F12.	Accumulation of organic matter in low-lying, water-saturated, and poorly-oxygenated terrestrial environments.
F-12: Bentonite	Yellow and light grey beds of clay (montmorillonite; Anderson and Reynolds, 1966), some biotite-rich. Occasionally with root traces. Commonly found with F11.	Altered volcanic air fall deposits preserved in low energy terrestrial settings.
F-13 Lag Deposits	Layers of mudstone rip-up or disarticulated bivalve shells. Typical layer only as thick as a single clast.	Coarse-grained deposits associated with high-energy deposition of storm beds.

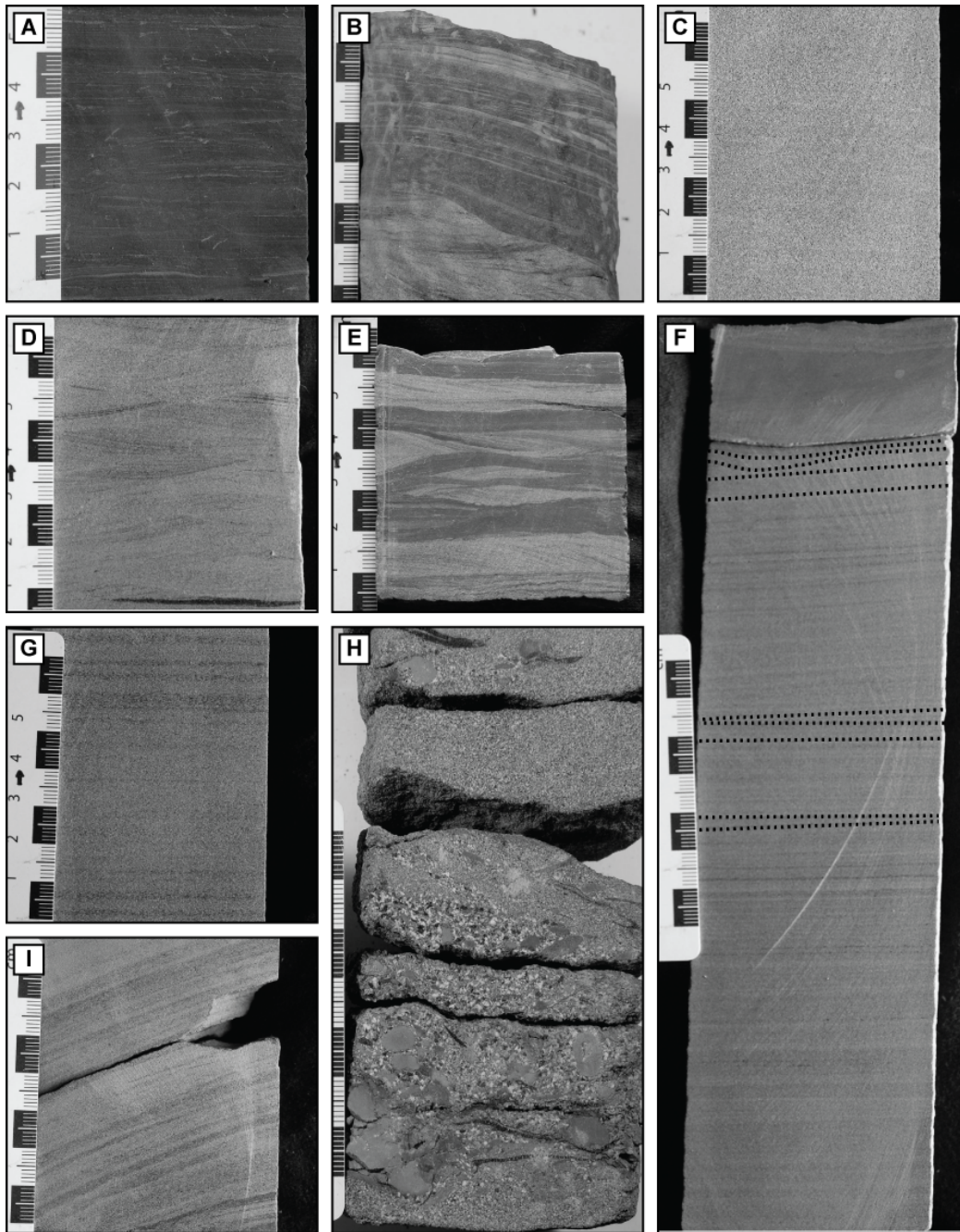


Figure 4. Core photographs from the Nanushuk Fm. at Umiat field showing selected sedimentary facies described in the text. (A) F-1, laminated mudstone, Umiat No. 9 Core 20 (B) F-3, wavy/lenticular bedded mudstone, Umiat No. 11 Core 44 (C) F-4, apparently massive sandstone, with possible faint parallel bedding, Umiat 9 Core 10 (D) F-6, ripple cross-laminated sandstone, Umiat No. 9 Core 24 (E) F-7, mud-draped ripple cross-laminated sandstone, Umiat No. 9 Core 19 (F) F-5, low-angle cross-laminated sandstone, with dotted lines to highlight lamination surfaces. Umiat No. 9 Core 46 (G) F-8, parallel laminated sandstone, Umiat No. 9 Core 44 (H) F-10, poorly sorted sand and gravel, Umiat No. 11 Core 38 (I) F-9, trough cross-bedded sandstone with foreset dips $>15^\circ$, Umiat No. 11 Core 39. Not pictured: F-2 mudstone; F-11 coal; F-12 bentonite; F-13 lag deposits.

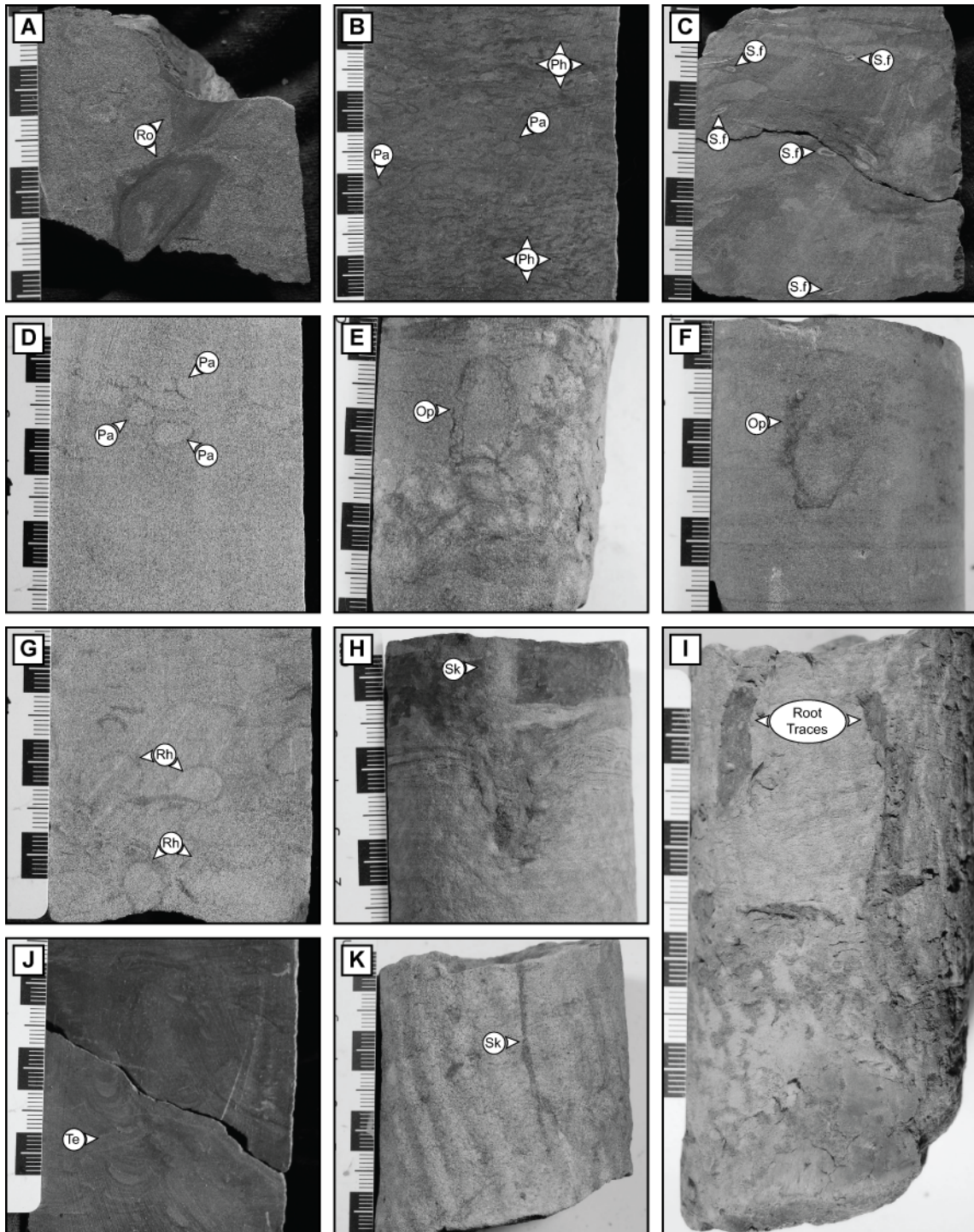


Figure 5. Trace fossils observed in core. (A) *Rosselia*, Umiat No. 9 Core 21 (B) *Phycosiphon* and *Paleophycus*, Umiat No. 9 Core 48 (C) *Schaubcylindrichnus freyi*, Umiat No. 9 Core 63 (D) *Paleophycus*, Umiat No. 9 Core 52 (E) *Ophiomorpha*, Umiat 9 Core 53 (F) *Ophiomorpha*, Umiat No. 9 Core 61 (G) *Rhizocorallium*, Umiat 9 Core 54 (H) *Skolithos* Umiat No. 9 Core 67 (I) Root traces, Umiat No. 9 Core 38 (J) faint *Teichichnus*, Umiat No. 9 Core 48 (K) *Skolithos* Umiat No. 11 Core 46.

Interpretation: Offshore

Published faunal and palynological analyses establish the marine character of FA-1 mudstones. The *Verneuilioides borealis* faunal zone consists of shallow marine fauna (Bergquist, 1958), while the palynological assemblage of dinoflagellates, acritarchs, and spores is typical of a near shore, shallow marine setting (May and Shane, 1985). Furthermore, the trace fossil assemblage closely resembles the *Cruziana* ichnofacies, which is associated with both offshore marine and prodelta settings (MacEachern et al., 2005).

We follow the convention of LePain et al. (2009), and group prodelta and non-deltaic shelf mudstones of the Nanushuk Fm. into a single offshore facies association deposited below storm wave base (*sensu* VanWagoner et al., 1990; Hampson and Storms, 2003). Thin sandy laminations or wavy and lenticular bedding found in FA-1 may be the distal expression of storm-wave, surge, or river flood-derived turbidity flows that bring sand onto the inner shelf (Nelson, 1982; Myrow and Southard, 1996; Myrow et al., 2002; Pattinson, 2005; Lamb et al., 2008). These features link FA-1 with overlying shallow marine and deltaic facies associations in progradational systems (Figs. 6-7).

Facies Association 2 (FA-2a)

FA-2a is a heterolithic facies association composed of bioturbated mudstone (F-2) interbedded with thin beds (1-10 ft) of low-angle, cross-laminated very-fine sand (F-5) or ripple cross-laminated very-fine sand (F-6). Sandy beds typically coarsen upward, and increase in number, thickness, and degree of amalgamation up core. Beds of mudstone may contain laminations or lenticular bedding disturbed by bioturbation (BI 1-4). Mud drapes and thin (<1 ft) beds of mudstone that occur between the sandy beds are heavily bioturbated (BI \geq 4). Some thin sandstone beds are heavily bioturbated (BI \geq 4), resulting in sand-rich mudstones associated with *Phycosiphon*, but most sandstone beds are not (BI < 3). The trace fossil assemblage in sand-rich mudstones and sandstones also includes *Schaubcylindrichnus freyi*, *Planolites* and, rarely, *Conichnus*, *Diplocraterion*, and *Ophiomorpha* (Fig. 5).

Interpretation: Distal Lower Shoreface

Beds of very-fine sandstone with low-angle cross-lamination (F-5) and ripple cross-lamination (F-6) interbedded with laminated or massive mudstone (F-2) beds are interpreted to represent hummocky cross-stratification formed by the oscillatory energy of storm waves in the distal lower shoreface (Dott and Bourgeois, 1982; Dumas and Arnott, 2006). The storm wave-derived hummocky cross-strata in the distal lower shoreface represent discontinuities that punctuate periods of deposition dominated by suspension settling (*sensu* Hampson, 2000). These beds coarsen upward (Fig. 6), suggesting a regressive character of the shoreface environment and a gradual transition to the proximal lower shoreface (FA-2b). Similar wave-derived facies successions have been described in shoreface settings from the Cretaceous Western Interior Seaway (Pattinson, 1995; Hampson and Storms, 2003) and in modern and ancient asymmetric wave-dominated

deltas, where wave energy concentrates sand on the up-drift side of a river (Bhattacharya and Giosan, 2003; Li et al., 2011). The trace fossil assemblage includes *Phycosiphon*, *Planolites*, and *Schaubcylindrichnus freyi*, components of the *Cruziana* ichnofacies found in both distal shoreface and wave-influenced deltaic environments (Buatois et al., 2008; Dafoe et al., 2010, Gingras et al., 2011).

Table 2: Summary of Facies Associations at Umiat Field

Facies Association		Diagnostic Features	Environmental Interpretation	Depositional Processes
FA-1	F-1, F-2	Laminated shale or bioturbated mudstone (<i>Cruziana</i> ichnofacies)	Offshore/Prodelta	Suspension settling in the prodelta or the marine shelf near storm wave base
FA-2	F-2, F-3, F-5, F-13	Interbedded bioturbated mudstone (<i>Cruziana</i> ichnofacies) and upward coarsening hummocky and swaley cross-stratified sand (<i>Skolithos</i> ichnofacies). Some sand beds obliterated by bioturbation (BI 5-6).	a. Distal Lower Shoreface	Mixed-energy shelf, above storm wave base. Deposition by suspension settling and storm-wave redistribution of sand and silt originally delivered to the coast by deltaic systems.
	F-4, F-5	Amalgamated sand beds with hummocky and swaley cross-laminated very-fine sandstone, with highly bioturbated beds (<i>Skolithos</i> ichnofacies)	b. Proximal Lower Shoreface	Storm wave deposition and redistribution of sand between fair-weather and storm wave base.
FA-3	F-4, F-5, F-9, F-13	Low-angle and trough cross-stratified, and plane-laminated fine-grained sandstone. Rare bioturbation (<i>Skolithos</i> ichnofacies)	Upper Shoreface/Foreshore	Subaqueous bar migration above fair-weather wave base, with some swash zone deposits.
FA-4	F-3, F-6a, F-7, F-8, F-9, F-10, F-13	Wavy and lenticular bedding with occasional soft sediment deformation coarsens up into ripple cross-laminated and massive sand. Bioturbation intensity and diversity low	Delta Front	Progradation of distributary mouth bars into muddy prodelta. Rapid deposition associated with massive sand, soft sediment deformation, low BI.
FA-5	F-1, F-2, F-3, F-6a, F-6b, F-7, F-11, F-12	Carbonaceous mudstone with brackish water bivalve assemblage (<i>Corbula</i>), volcanic ash deposits, and plant fossils. Closely associated with the top FA-3 and FA-4. Thin ripple cross-laminated sandstone beds <10 ft thick, heavily oxidized.	a. Delta Plain	Suspension settling in protected interdistributary bays or lagoons, with some tidal influence (F-7), organic matter accumulation in marshes or swamps.
	F-3; F-6a, F-7, F-8 (rare), F-13	Wavy bedding coarsens up into flaser bedding and ripple cross-laminated sandstone. Beds are 5-10 ft thick. Mud-drapes are common in some sandstone beds, and are often sideritized, especially in Umiat No. 11. Rare mudstone rip-up clasts.	b. Crevasse Sands	Crevasse channel and splay deposits that form during flood or avulsion into interdistributary bays or the delta plain. Some tidal influence indicated by mud drapes.

Facies Association 2-b (FA-2b)

FA-2b consists of amalgamated beds of very fine- to fine-grained sandstone. Sedimentary structures include low angle (F-5), parallel (F-8), and ripple cross-laminated sandstones (F-6), which are occasionally lined with plant debris. Well-sorted, apparently massive sandstone (F-4) intervals increase in frequency up-well from more clearly laminated or bioturbated sandstones with higher concentrations of organic matter. The trend of upward coarsening, increasingly amalgamated sandstone beds continues up-well into FA-3. Isolated siderite rip-up clasts also increase in frequency up-well. Bioturbation is common,

and trace fossils are more visible where organic matter is abundant. Traces include *Paleophycus*, *Ophiomorpha*, *Diplocraterion*, *Rosselia*, and *Schaubcylindrichnus freyi* (Fig. 5).

Interpretation: Proximal Lower Shoreface

The distinction between the distal lower shoreface (FA-2a) and proximal lower shoreface (FA-2b) is largely based on amalgamation of sandstone beds (Fig. 6: *sensu* Van Wagoner et al., 1990; Hampson, 2000; Hampson and Storms, 2003). Outside of wells No. 9 and No. 2, core samples are sparse or of poor quality and the boundary between distal and proximal lower shoreface is indistinct. Bioturbation intensity decreases in this facies association, but beds that appear well-sorted and massive may contain extensive cryptobioturbation as in other storm- or wave-influenced environments (MacEachern et al., 2005).

Facies Association 3 (FA-3)

Trough-cross laminated (F-9), massive (F-4), and parallel-laminated fine-grained sandstones (F-8), are the most common facies in FA-3. The vertical distribution of these facies is not systematic. Sets of amalgamated beds are 50 to 60 ft thick. Bioturbation intensity and trace diversity are both low (Fig. 6). Rare trace fossils includes *Skolithos* trace fossils.

Interpretation: Upper Shoreface

Amalgamated sandstones in FA-3 (Fig. 6) are interpreted to reflect deposition at or above fair-weather wave base where wave energy is constant (*sensu* Hampson, 2000). Higher energy corresponds with an increase in grain size from very fine-sandstone of the lower shoreface to fine-grained sandstone in the upper shoreface (Fig. 6). In the upper shoreface, trough cross-lamination is interpreted as the result of sub-aqueous longshore dune migration (Flint, 1988; Hampson and Storms, 2003; Clifton, 2006). High-energy conditions in shoreface and foreshore settings prohibit bioturbation or inhibit preservation (Li et al., 2011), and are responsible for low bioturbation intensity and trace diversity.

Facies Association 4 (FA-4)

Significant lenticular to wavy bedding (F-3) transitions up-well to ripple cross-laminated (F-6a), parallel laminated (F-8), and trough cross-laminated (F-9) sandstone. Sets of amalgamated beds are 60 to 70 ft thick. Occasional beds of mud-draped ripple cross-laminated sandstones are also present (Fig. 4). Gravel lag deposits (F-13) consisting of single pebble layers comprised of mudstone rip-up clasts are rare. Bioturbation intensity is low (BI 0-3) in sandstones and lenticular or wavy-bedded mudstones (F-3), but soft sediment deformation occurs in muddy facies and may obscure traces.

Interpretation: Delta Front

A delta front generally encompasses shoreline and seaward dipping subaqueous topset and foreset beds of coarse sediment (Bhattacharya, 2006). Major depositional environments in a river-dominated delta front are derived from terminal distributary channels, and include subaqueous levees, distributary mouth bars, and distributary channels themselves (Coleman and Gagliano, 1965). In the Umiat wells, parallel-laminated, ripple cross-laminated, and trough cross-laminated sandstones are attributed to distributary mouth bars or distributary channel bars that rapidly prograded out over distal delta front mudstones, as indicated by soft sediment deformation (Fig. 7). Sparse bioturbation is also typical of delta front deposits, where high water turbidity, high sedimentation rate, and salinity fluctuations can inhibit burrowing organisms (MacEachern et al., 2005). We interpret gravel lag deposits as evidence for channelization. The lack of additional evidence for channels is not surprising, given the limited amount of core available, as well as the propensity for delta distributary channels to be actively filled by distributary mouth bars (Olariu and Bhattacharya, 2006). The rare occurrence of mud-draped ripples is interpreted as minimal evidence for tidal influence in the distributary system. Though commonly associated with fluctuations in energy in tidal systems (Bhattacharya, 2006), mud drapes are not always tidal in origin (Clifton, 2006).

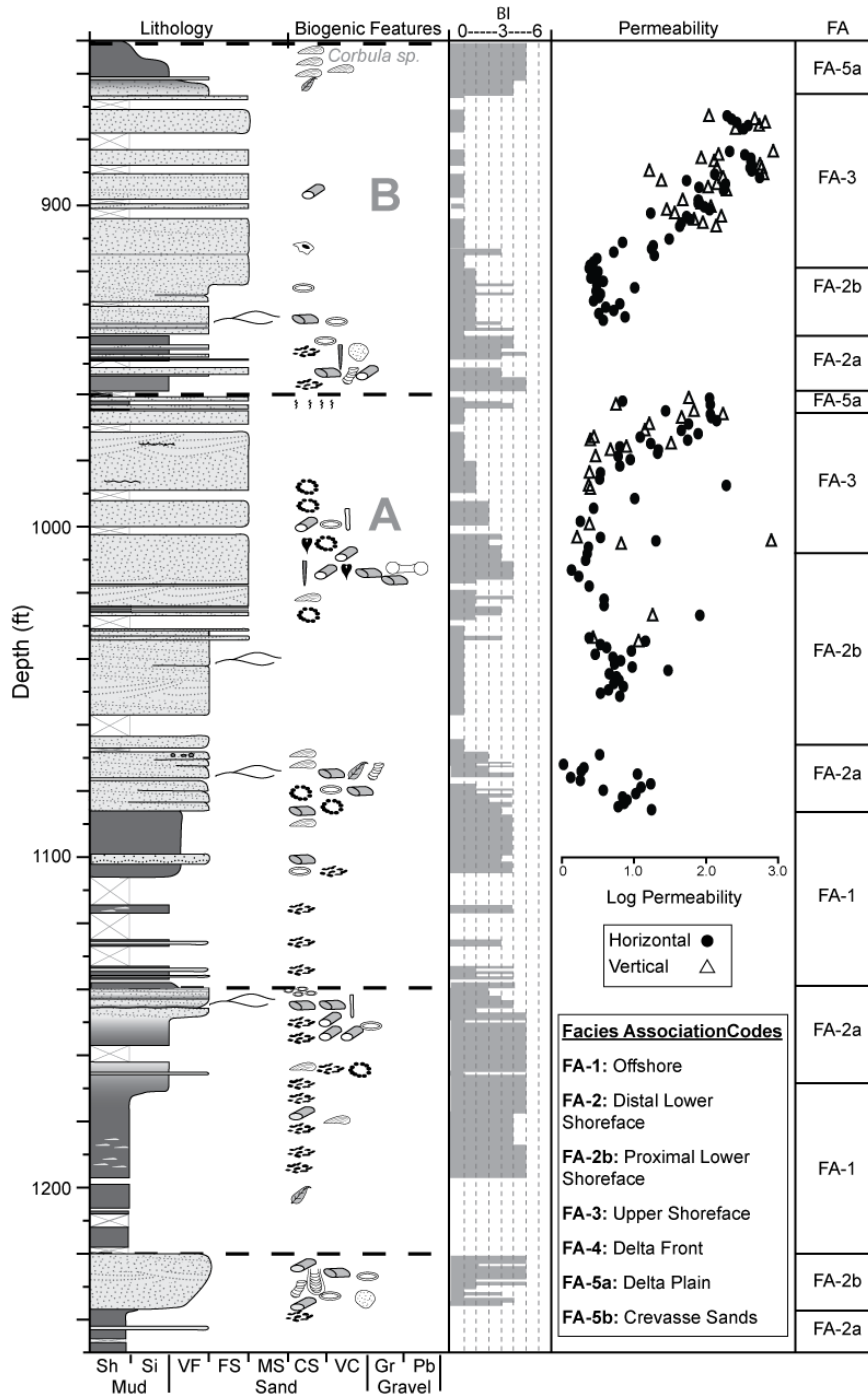


Figure 6. Four upward-coarsening successions (bound by dashed lines) consist of offshore (FA-1), distal lower shoreface (FA-2a), proximal lower shoreface (FA-2b), and upper shoreface (FA-3) deposits in Umiat No. 9. This multi-storey shoreface succession is typical of the Lower Grandstand in the Umiat wells. Thin delta plain (FA-5a) mudstones occur at the top of the two uppermost shoreface sandstones. Bioturbation intensity is highest in muddy or heterolithic deposits, and decreases as sand beds become amalgamated from 1020-970 ft and 920-870 ft. Permeability, in contrast, increases towards the top of shoreface successions (990-970 ft and 930-870 ft). A and B refer to reservoir units. Lighter shaded areas with dashed lines are interpretations based on original cuttings data (Collins, 1958). See Figure 7 for complete symbol legend.

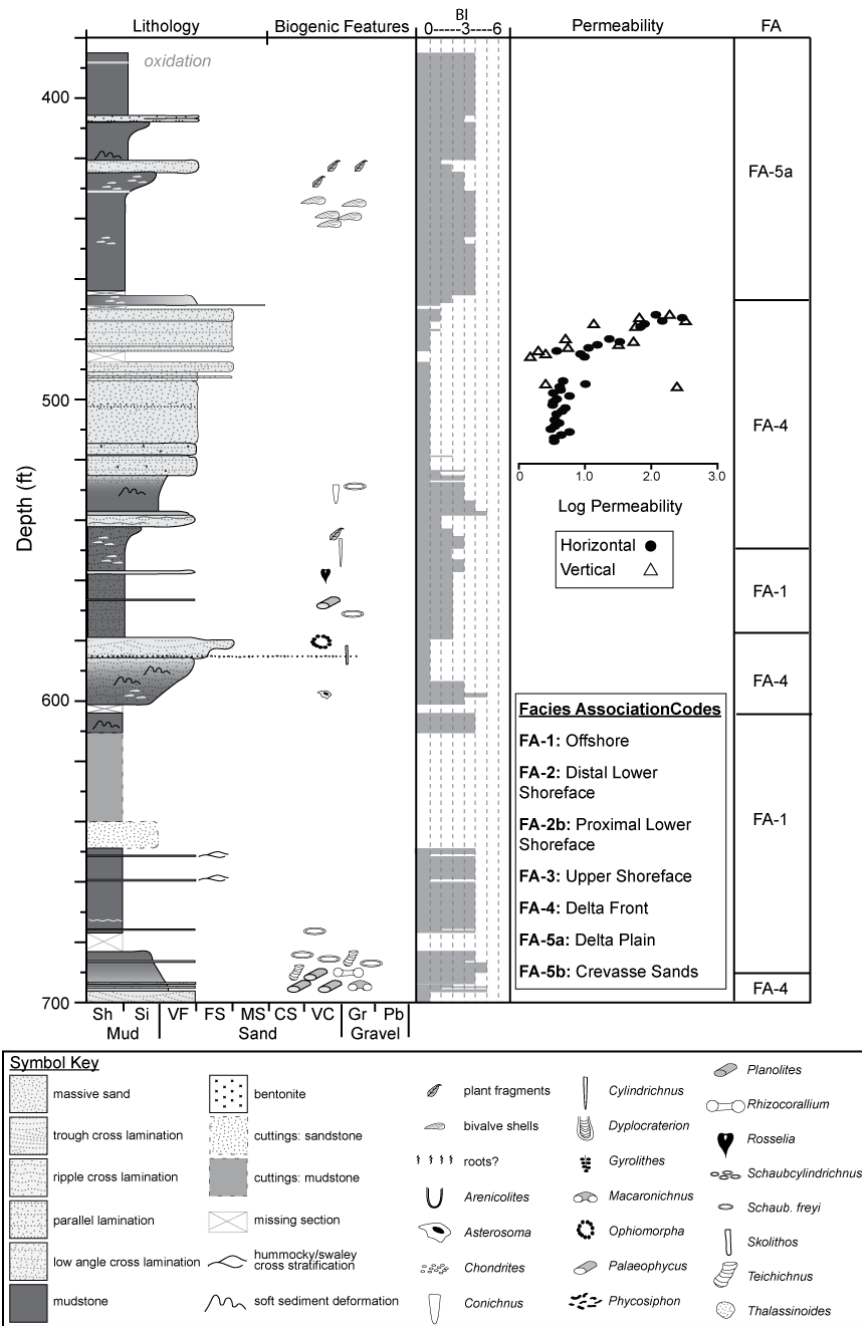


Figure 7. An upward-coarsening delta-front succession from 580-470 ft in Umiat No. 9 consists of prodelta (FA-1), delta front (FA-4), and delta plain (FA-5) deposits. The single-storey delta front succession is typical of the Upper Grandstand in the Umiat wells. Bioturbation intensity is low, even in prodelta or distal delta front deposits (580-530 ft). Permeability increases towards the top of the delta front sands (490-470 ft). Lighter shaded areas with dashed lines are interpretations based on original cuttings data (Collins, 1958).

Facies Association 5a (FA-5a)

FA-5a includes dark grey to black mudstones, typically carbonaceous, both laminated (F-1) and massive (F-2), with lenticular or wavy bedded mudstones (F-3) that have rare syneresis cracks. Other characteristic features are layers of oxidized siltstone or claystone, *Corbiculid* bivalves, plant fossils, root traces, coal (F-11), and bentonites (F-12). Coal deposits are thin (<1 ft). *Teichichnus* and *Skolithos* trace fossils are found in interbedded mudstone and sandstone intervals. *Teichichnus* in particular is more common in FA-5a than in other facies associations. In Umiat wells 1 and 11 there is a mix of dinoflagellates and acritarchs, spores, and gymnosperm pollen (May and Shane, 1985) in associated intervals.

Interpretation: Delta Plain

The mudstones of FA-5a are interpreted as marginal marine to non-marine lagoon, interdistributary bay, and lake deposits based on several factors. *Corbiculid* bivalve beds, abundant plant fragments, spores, gymnosperm pollen, and thin beds of coal distinguish FA-5 from marine mudstones of FA-1. *Corbiculid* bivalves are found in brackish or hypoxic water conditions (May and Shane, 1985; Holmes and Miller, 2006), and the palynological assemblage of dinoflagellates, acritarchs, spores, and gymnosperm pollen suggest brackish conditions as well (May and Shane, 1985). Syneresis cracks also occur in settings with mixed salinity, such as brackish water bays (Pratt, 1998). The trace fossil assemblage also supports a brackish delta plain interpretation. Though not exclusive to brackish conditions, *Teichichnus* is typically one of the dominant trace fossils in brackish interdistributary bays and is frequently found in association with syneresis cracks (Buatois et al., 2008). A similar set of facies occurs in brackish to non-marine shallow water deposits of the Dunvegan Formation in northwestern Alberta (Bhattacharya and Walker, 1991). These facies are typical of delta comprised of numerous mud-dominated sub-environments, including swamps, marshes, tidal flats, lagoons, and interdistributary bays, which can be difficult to distinguish in ancient settings (Bhattacharya, 2006). Bay or lagoon environments are also important down-drift components of asymmetric wave-dominated deltas (Bhattacharya and Giosan, 2003) and in wave-dominated shoreface successions (Flint, 1988). We prefer a delta plain or coastal plain interpretation based on the stratigraphic position of FA-5 on top of upper shoreface (FA-3) or delta front (FA-4) deposits (Figs. 6-7).

Facies Association 5b (FA-5b)

Wavy bedded mudstones (F-3) grade up into thin (5-10 ft) flaser bedded and asymmetrical ripple cross-laminated sandstone (F-6a) and mud-draped, ripple cross-laminated sandstone (F-7). Mud drapes are frequently sideritized, especially in Umiat No. 11. In isolated instances a gravel lag of mudstone rip-up clasts, a thin sandstone, and a subsequent upward fining succession interrupt upward coarsening flaser bedding (F-7). Underlying interbedded mudstone intervals (FA-5a) commonly exhibit soft sediment deformation (probably convolute bedding or ball and pillow structures, but core samples are too small

to definitively determine the origin of soft sediment deformation features). *Skolithos* and *Teichichnus* are common, and the palynological assemblage is the same as FA-5a. Plant fragments are preserved on lamination surfaces in ripple cross-laminated sandstones.

Interpretation: Crevasse Sands

FA-5b represents sandstones and mudstone rip-up lag deposits found in association with mudstones and coals of FA-5a (Fig. 8). We interpret these deposits as overbank sandstones and mudstones or avulsion-derived influxes of sand into interdistributary bays and lagoons on the delta plain. Specific process interpretations vary based on grain size trends observed in core or inferred from well logs, and follow deltaic facies interpretations (Elliot, 1974; Bhattacharya and Walker, 1991). Where beds coarsen upward, a crevasse-splay or crevasse delta interpretation is preferred. Rarer upward fining successions with mudstone rip-up lags are interpreted as passively filled crevasse channels.

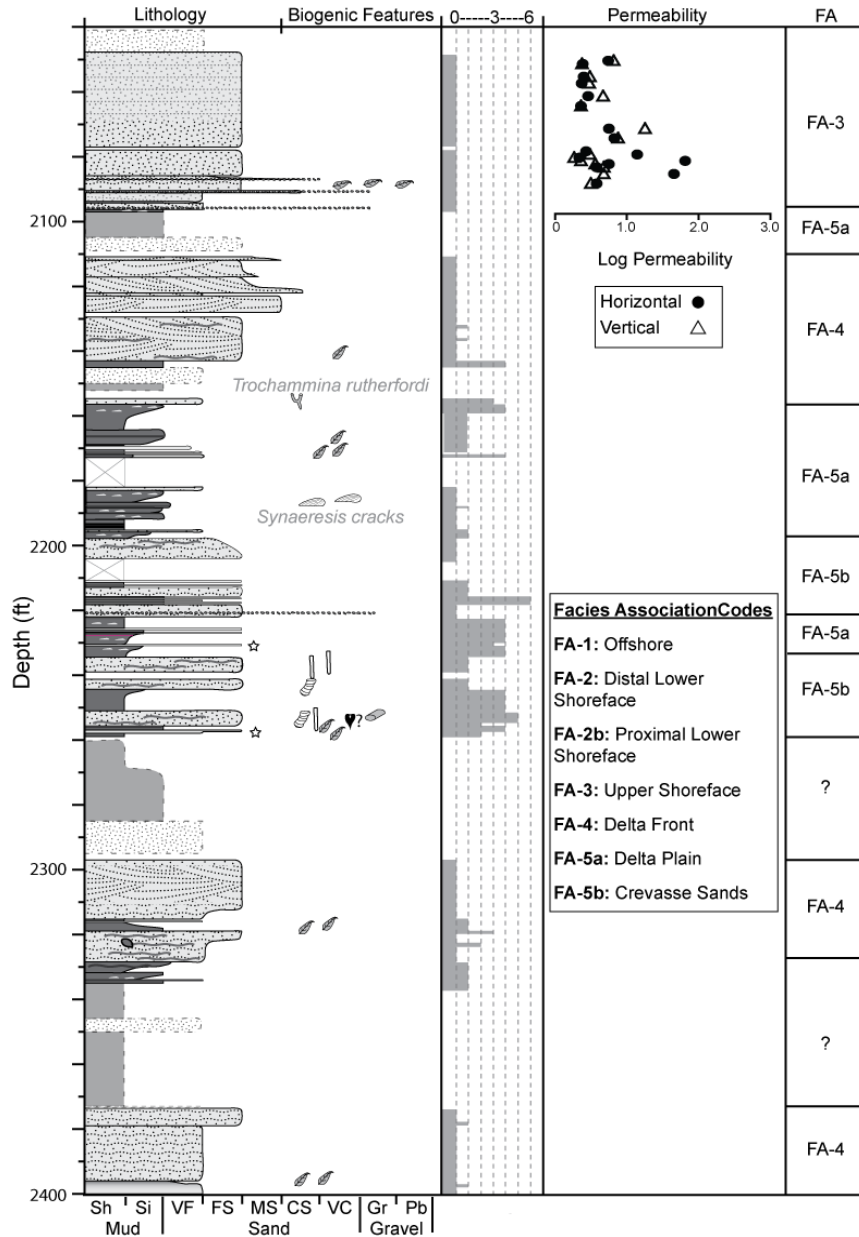


Figure 8. Umiat No. 11 is the only well with a complete succession of delta plain deposits in core, including interdistributary bay-fills (FA-5a) and crevasse splay sandstones (FA-5b). *Corbula sp.* bivalves and an increase in gymnosperm and angiosperm pollen (May and Shane, 1985) provide evidence for the marginal marine character of the delta plain. A thick sandstones at the top of the delta plain succession (2095-2040 ft) is transgressive in origin and shows a reverse trend in permeability compared to lower sandstones (Figs. 6 and 7).). Lighter shaded areas with dashed lines are interpretations based on original cuttings data (Collins, 1958). See Figure 7 for complete symbol legend.

PETROGRAPHY

The results of point counting determined that the Nanushuk Formation sandstones are largely lithic arenites sourced from a recycled orogen, based on a simple Quartz-Feldspar-Lithic (QFL) diagram (Fig. 9). The lithic fragments are primarily of sedimentary and metamorphic in origin (Fig. 10).

There are several types of diagenetic minerals present in the samples imaged using the SEM. Common diagenetic minerals or features include multiple illite and kaolinite clay, pyrite, and quartz and feldspar overgrowths (Figs. 11-12).

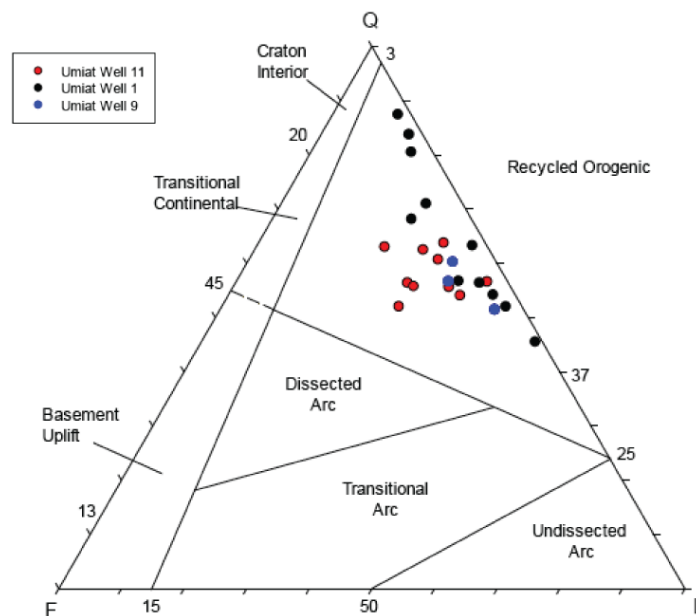


Figure 9. QFL diagram for the Nanushuk Formation in Umiat wells No. 11, 1, and 9. The Nanushuk Formation consists of lithic arenites from recycled orogenic sources (the Brooks Range).

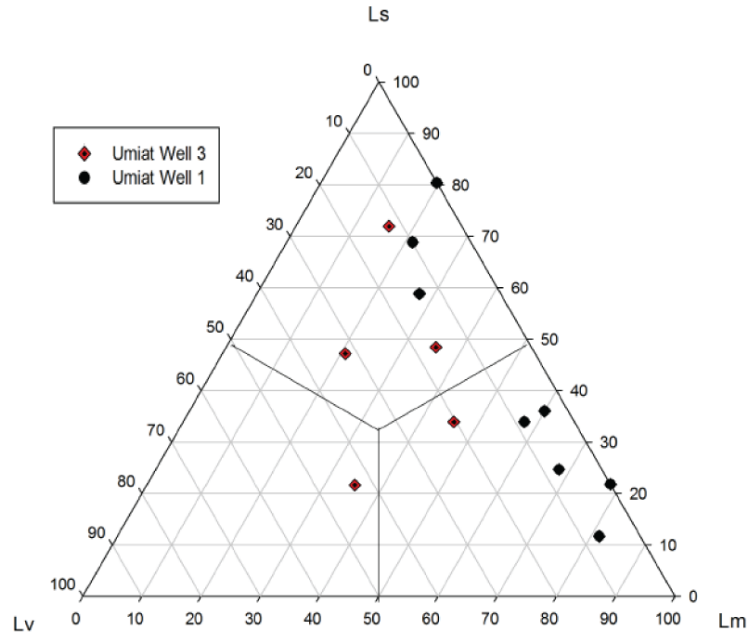


Figure 10. The lithic fragments in the Nanushuk Formation sandstones are primarily from sedimentary and metamorphic sources.

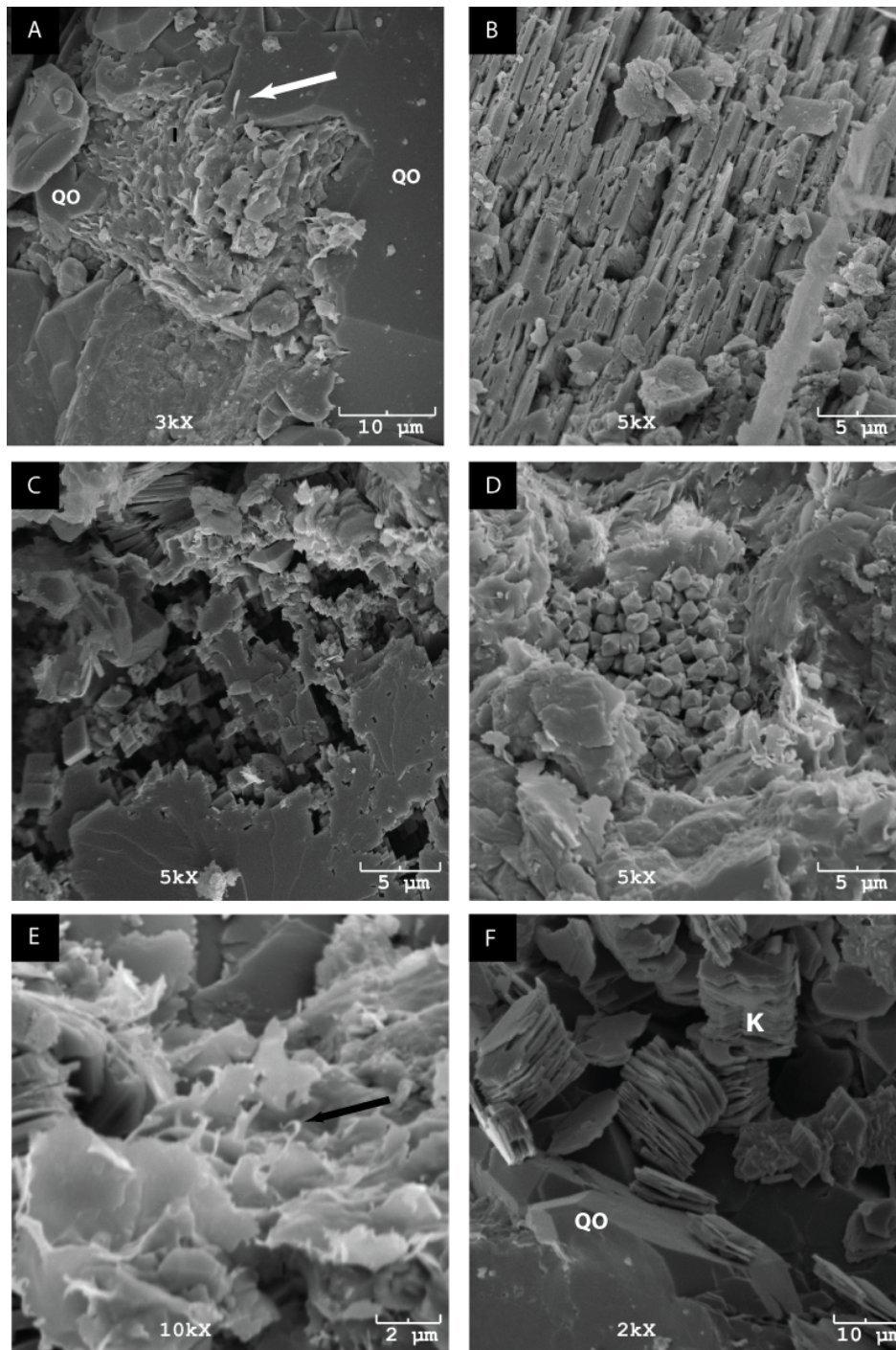


Figure 11. SEM photomicrographs of diagenetic mineral phases. (A) Large euhedral quartz overgrowths and their relationship to grain coating illitic clays (I). Note the overgrowth engulfing the flake of illite (arrow). Umiat 3 350'. (B) Corroded feldspar overgrowth exhibiting a serrated texture. Umiat 9 906' (C) Euhedral rhombic feldspar overgrowth coalescing into smooth faced overgrowth. Umiat 9 996'. (D) Cluster of pore filling octahedral pyrite. Umiat 11 Core 59. (E) High magnification of ribbon-like projections of illite (arrow). Umiat 11 Core 59. (F) Books of pseudo-hexagonal kaolinite (K) and quartz overgrowths (QO). Umiat 11 Core 53.

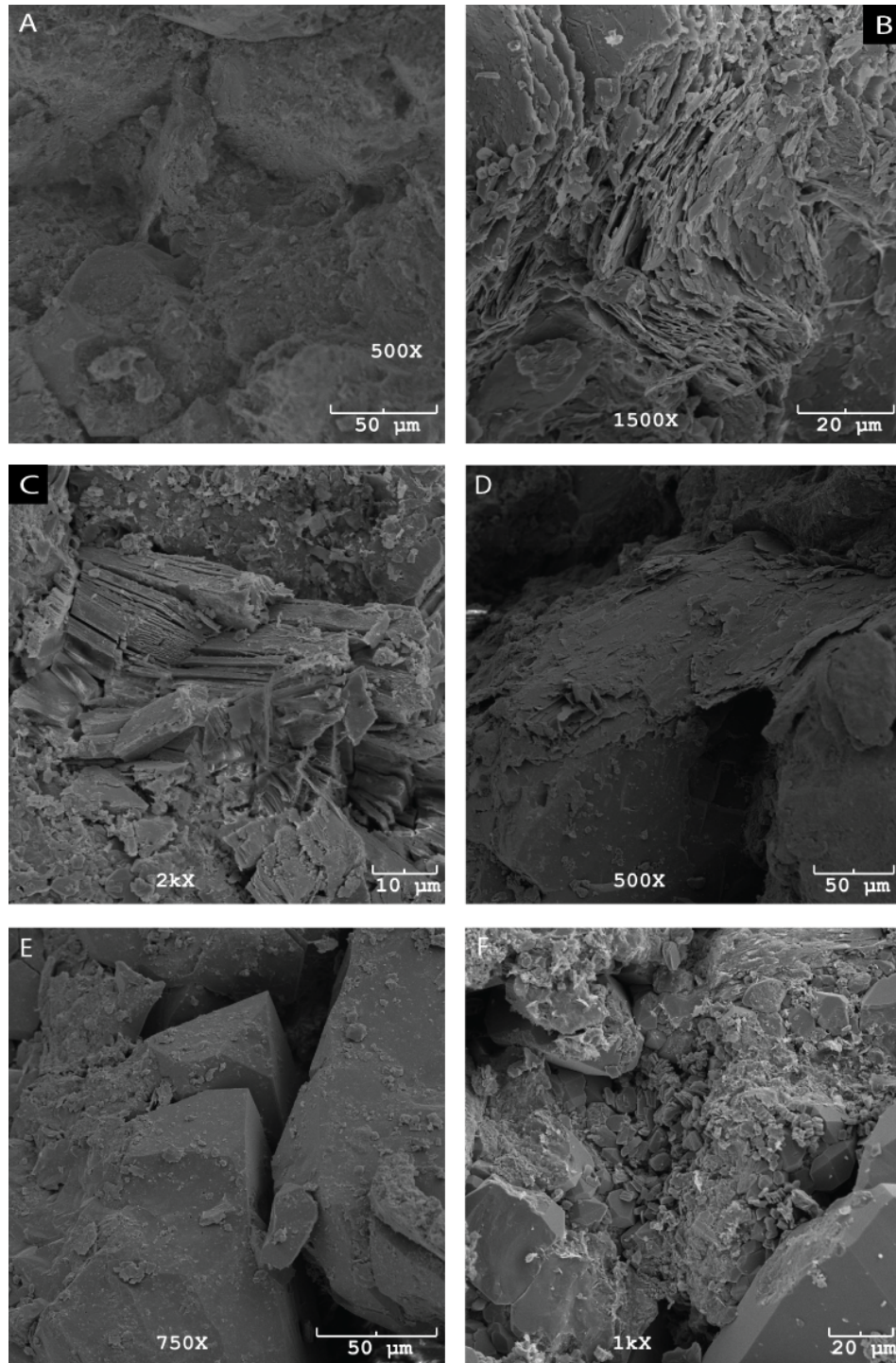


Figure 12. Permeability-affecting diagenetic features. (A) Depressions on detrital grains created by compaction resulting in pressure solution. Porosity reducing clay bridge spanning pore throat (arrow). (B) Phylitic fragment which has been ductilely deformed through compaction. This is an example of pseudomatrix. (C) Brittle grain fracturing indicative of mechanical compaction. (D) Clay bridge closing a pore through, reducing permeability. (E) Euhedral overgrowths protruding into pore space. (F) Multiple authigenic minerals forming cements and filling pore space, reducing porosity and permeability.

PERMEABILITY-FACIES DISTRIBUTION

Permeability profiles for different facies associations illustrate the relationship between permeability and depositional processes in the Nanushuk Fm. at Umiat (Fig. 6-8). Though sandstones reservoir units reach up to 120 ft in total thickness, only a small percentage of each sandstone unit has air permeability values greater than 10 md ($\log_{\text{permeability}} > 1$). Permeable zones are restricted to sandstones from upper shoreface (FA-3) and delta front (FA-4) facies associations (Figs. 6-7). Both K_h and K_v are associated with the coarsest and most well-sorted portions of upper shoreface and deltaic deposits. In most cases these deposits coarsen upward (Figs. 6-7), except near the top of the Nanushuk Fm. (Fig. 8).

Permeability anisotropy varies depending on facies and facies association (Table 3). The lowest anisotropy (values near 1.0) occurs in upper shoreface deposits. This presumably occurs due to increased sorting, and is associated with apparently massive sand (F-4) and a decrease in visible trace fossils ($BI < 2$) related to high energy, increased water turbidity, and substrate instability (MacEachern et al., 2005; Li et al., 2011). Anisotropy is higher in delta front (FA-4) sandstones, which are comprised of ripple cross laminated (F6), trough cross laminated (F-9), and massive sand (F-4), and contain more frequent laminations defined by thin mudstone layers or carbonaceous debris. Bioturbation intensity is low ($BI < 2$) and mud deposition rates are high, in contrast to shoreface environments where wave energy transports suspended sediment offshore (MacEachern et al., 2005). Well-preserved mud drapes and carbonaceous laminations reduce vertical permeability and are the likely cause of higher anisotropy.

Table 3. Permeability Anisotropy

Well	Depth (ft)	Facies Association	Anisotropy (K_v/K_h)	Reservoir Unit ¹
Umiat No. 10	420-490	FA-4: Delta Front/ FA-3 Shoreface	0.09	Ninuluk
Umiat No. 10	1066-1085	FA-4: Delta Front	0.05	Upper Grandstand
Umiat No. 9	873-907	FA-3: Upper Shoreface	0.73	Lower Grandstand B
Umiat No. 9	960-1003	FA-3: Upper Shoreface	0.59	Lower Grandstand A

¹See further discussion below, and figures 6-10

RESERVOIR-SCALE STRATIGRAPHIC ARCHITECTURE

The commonly used informal subsurface units of the Nanushuk Fm. (Fig. 3b) are effective for describing the stratigraphic architecture of shallow marine and deltaic sandstones at Umiat field. Each of these informal units (Tuktu, Lower Grandstand, Shale Barrier, Upper Grandstand, Killik, Ninuluk) generally corresponds to unique depositional environments that determine reservoir distribution and quality.

Tuktu

The Tuktu consists of marine mudstone (FA-1) that underlies and intertongues with shallow marine (FA-2, FA-3) and deltaic (FA-4) sandstones of the Lower Grandstand and Upper Grandstand. Tongues of the Tuktu are present beneath the Lower Grandstand, particularly in the west at Umiat No. 1 (Figs. 11 and 12). Elsewhere on the North Slope and below the depths studied in the Umiat wells, Tuktu mudstones at the base of the

Nanushuk Fm. transition downward into the Torok Fm., which consists of mudstones and turbidites deposited in marine slope and basin-floor settings (Mull et al., 2003). Another thick tongue of the Tuktu separates the Lower Grandstand from the Upper Grandstand (Fig. 13). This tongue is known informally as the Shale Barrier at Umiat field, and is best discussed with the Upper Grandstand (see below).

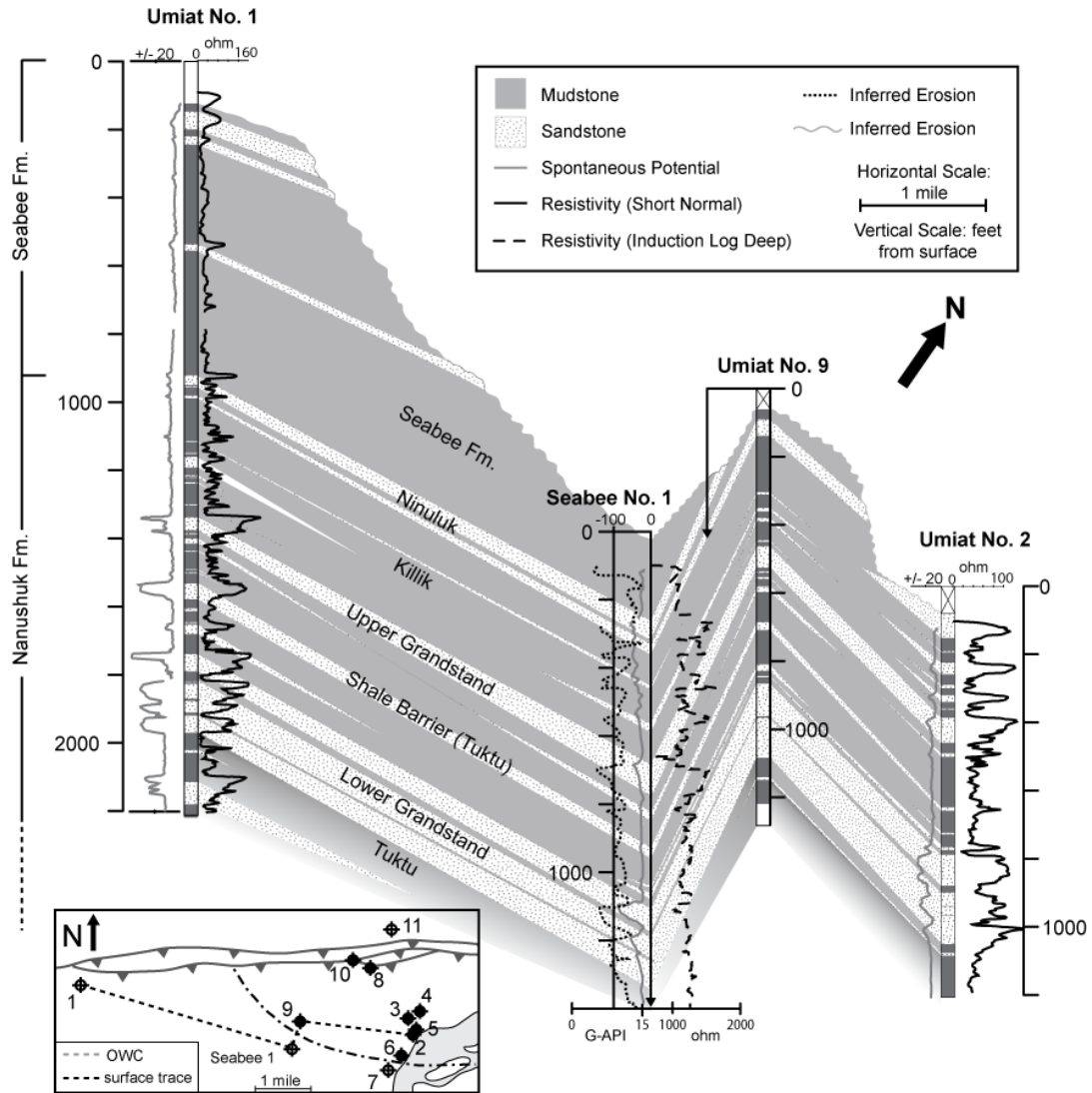


Figure 13. Fence diagram for Umiat field. Interpretations based on core description (this paper), cuttings (Collins, 1958), and well logs (Collins, 1958; Legg and Brockway, 1983). Base of Nanushuk Fm. (Tuktu) is undetermined. Primary reservoir rocks are the laterally extensive Lower Grandstand (shoreface) and Upper Grandstand (delta-front) units. The Ninuluk unit is also laterally extensive but is largely eroded in eastern part of Umiat field. It is difficult to correlate sandstones in the Killik and Shale Barrier (Tuktu) portions of the Nanushuk Fm., but some thin sands may represent the same surface. Inset map shows surface trace of fence diagram (dashed line). Umiat No. 9 is shifted slightly to the north in diagram to distinguish it from Seabee No. 1 well. Oil-water contact in Upper Grandstand passes between Umiat No. 9 and Seabee No. 1, as shown in the inset map (dash-dot line).

Lower Grandstand

In previous studies, the Lower Grandstand was considered a single reservoir unit (Watt, 2010). Core interpretation and permeability profiles, however, show that the Lower Grandstand actually consists of at least two upward coarsening sand bodies separated by a regionally extensive flooding surface (Figs. 6, 13). Resistivity and spontaneous potential logs are funnel-shaped or blocky in character (Fig. 14). The flooding surface and associated impermeable mudstones and sandstones represent a major flow barrier within the Lower Grandstand. The widespread distribution of the flooding surface, allows us to divide the Lower Grandstand into a basal reservoir unit (Lower Grandstand A) and upper reservoir unit (Lower Grandstand B; Fig. 14). The median thickness of the Lower Grandstand A is 150 ft (Table 4). Positive kicks in SP logs and drops in resistivity indicate further compartmentalization of Lower Grandstand A in Umiat No. 1, Umiat No. 2, and Seabee No. 1 (Figs. 11-12). The Lower Grandstand B is typically much thinner (~90 ft thick in the central reservoir). There is more between-well variation in Lower Grandstand B, which is very thin in Umiat No. 1 (50 ft) and much thicker in Umiat No. 11 (140 ft), but the well log character is more uniform (Fig. 13).

Table 4. Umiat Subsurface Unit Thicknesses By Well¹

	No. 1	No. 2	No. 3	No. 4	No. 5	No. 6	No. 7	No. 8	No. 9	No. 10	No. 11	Mean/ Median
Ninuluk ²	35 10	--	--	--	--	15 10 30	20 45	95	50	10 35	60 45	41/35 35/40
Killik	345	305	--	265*	300	325	340	310	330	320	295	319/ 320
Upper Grandstand	50	70	45	50	45	60	40	40	55	80	35	52/50
Shale Barrier (Tuktu)	290	330	280	305	325	--	290	335	310	--	325	310/ 310
Lower Grandstand B	45	90	--	85	95	--	100	40*	85	--	140	91/ 90
Lower Grandstand A	150 ²	155	--	--	160	--	--	--	120	--	130	143/ 150

¹All thicknesses in feet. ²In some wells the Ninuluk consists of two sandstone units. *Incomplete, not included in statistics

The top of Lower Grandstand B occurs at an abrupt transition from a fine-grained upper shoreface sandstone (FA-3) to a carbonaceous mudstone (FA-5a) deposited in interdistributary bays or lagoons. In most wells the carbonaceous mudstone layer is ~20-50 ft-thick and is part of a regressive succession associated with the Lower Grandstand B. In Umiat No. 1 mudstones of FA-5 are 70 ft thick, suggesting increased back-barrier accommodation to the west. In most of the wells a thin (10-20 ft-thick) sandstone truncates the carbonaceous mudstone (Fig. 14). We interpret this sandstone as a transgressive lag deposit at the base of the "Shale Barrier".

Shale Barrier (Tuktu) and Upper Grandstand

The Shale Barrier is 290-335 ft thick with an average thickness of 310 ft (Table 4). The unit consists of marine mudstone (FA-1) and distal shoreface sandstones (FA-2a). Sandstones are typically very fine-grained, with sand:mud ratios from 0.05-0.76 (Table 5). The maximum sand:mud estimate comes from Umiat No. 1, where the Shale Barrier is ~43% sand. However, Umiat No. 1 is located more than two miles west of the petroleum

trap in the Umiat anticline, and centrally-located wells have a relatively consistent sand:mud ratio of 0.10-0.30 (Table 5). A thick sand body in the middle of the Shale Barrier in Umiat No. 1 illustrates the reduction in sand content from west to east. The sand thins from 50 ft in Umiat No. 1 in the west to 20 ft in Umiat No. 9 and it is nearly absent in Umiat No. 2 (Fig. 13).

Table 5. Sand/Mud Ratios of Mud-Dominated Reservoir Units

	No. 1	No. 2	No. 3	No. 4	No. 5	No. 6	No. 7	No. 8	No. 9	No. 10	No. 11
Killik	0.19	0.85	--	0.71	0.88	0.33	0.33	0.17	0.14	0.28	0.40
Shale Barrier	0.76	0.10	0.10	0.21	0.10	--	0.09	0.05	0.29	--	0.10

The Upper Grandstand is a regionally extensive river-dominated deltaic sandstone (FA-4) found in all of the Umiat wells. The unit varies from 35 to 80 ft thick, with an average thickness of 52 ft. Well logs are funnel-shaped or serrated (Fig. 13). The Upper Grandstand lacks correlatable internal flooding surfaces, and there are no obvious directional trends in thickness (Table 4). The top of the Upper Grandstand is an abrupt, easily distinguished boundary between fine- or medium-grained sandstone of the Upper Grandstand and carbonaceous mudstone of the overlying Killik (Fig. 13).

Killik

We interpret the Killik as a marginal-marine to non-marine delta plain (FA-5) genetically related to the underlying Upper Grandstand. It is difficult to correlate sandstone layers within the Killik between wells (Fig. 9), and the sand:mud ratio varies considerably in each well (Table 5). It is also difficult to correlate thin coal layers, which we interpret as localized accumulations of organic matter swamps or marshes on the delta plain.

We attribute the irregular distribution of sandstone layers within the Killik to crevasse channel and crevasse splay deposits on the delta plain (FA-5b). Crevasse channel and splay deposits are found elsewhere in the Nanushuk Fm. (LePain et al., 2009), and are a typical component of the delta plain environment (Elliot, 1974; Bhattacharya and Walker, 1991). The geometry and extent of the crevasse splay sands, which can be tenuously correlated between Umiat wells in some instances (Fig. 13), is similar to modern crevasse splays that cover up to 7.5-9.5 mi² (12-15 km²) in deltaic environments (Coleman, 1988).

Ninuluk

The Ninuluk is poorly represented in the Umiat wells due to erosion on the southern limb of the Umiat anticline (Fig. 13). Facies variability within the Ninuluk is difficult to interpret because the primary data source for interpretation is the original cuttings descriptions (Collins, 1958). The best core data are from Umiat No. 11, in which there are two thick sandstone units we define as Ninuluk A and Ninuluk B. Ninuluk A is the lower unit, and is ~35 ft thick (Table 5). A similarly thick sand unit can be found in wells No. 6, No. 7, and No. 10. The upper unit, Ninuluk B, averages 40 ft thick (Table 5), though it is much thicker in wells No. 9 and No. 11. In Umiat No. 8 the Ninuluk is an apparently amalgamated sandstone nearly 100 ft thick. Unfortunately, these sandstone units are missing in much of the field due to erosion.

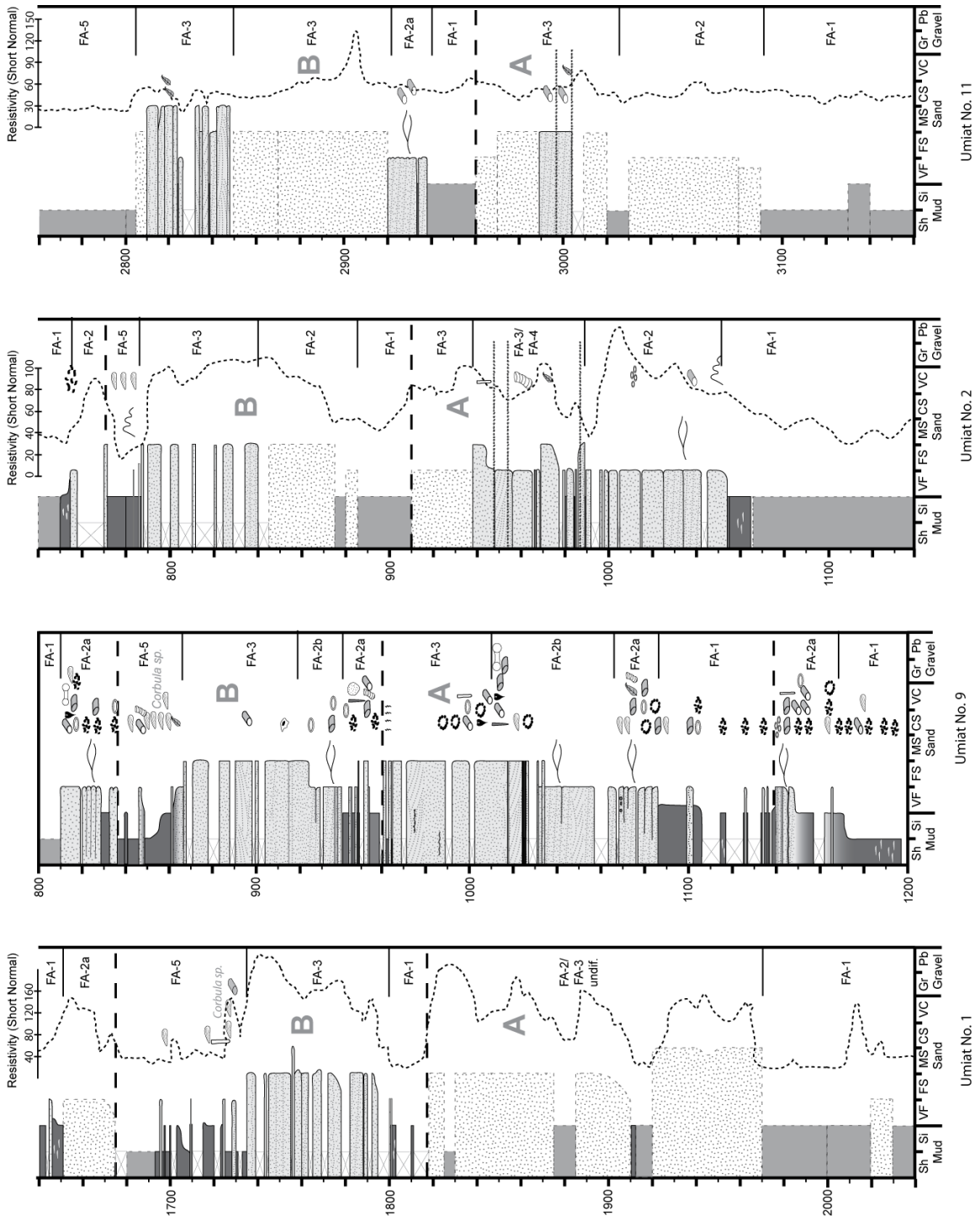


Figure 14. Segments of measured sections from Umiat wells 1, 9, 2 and 11 showing multi-storey shoreface deposits of the Lower Grandstand. These wells were selected for most complete core and well log records for the Lower Grandstand, and are arranged in rough west-east order from left-right. A flooding surface separates two major Lower Grandstand sand bodies (thick dashed line). The top of the Lower Grandstand includes delta plain mudstones and is capped by a transgressive sandstone in each well except Umiat No. 11. Lighter shaded areas with dashed lines are interpretations based on original cuttings data (Collins, 1958). See Figure 7 for symbol legend.

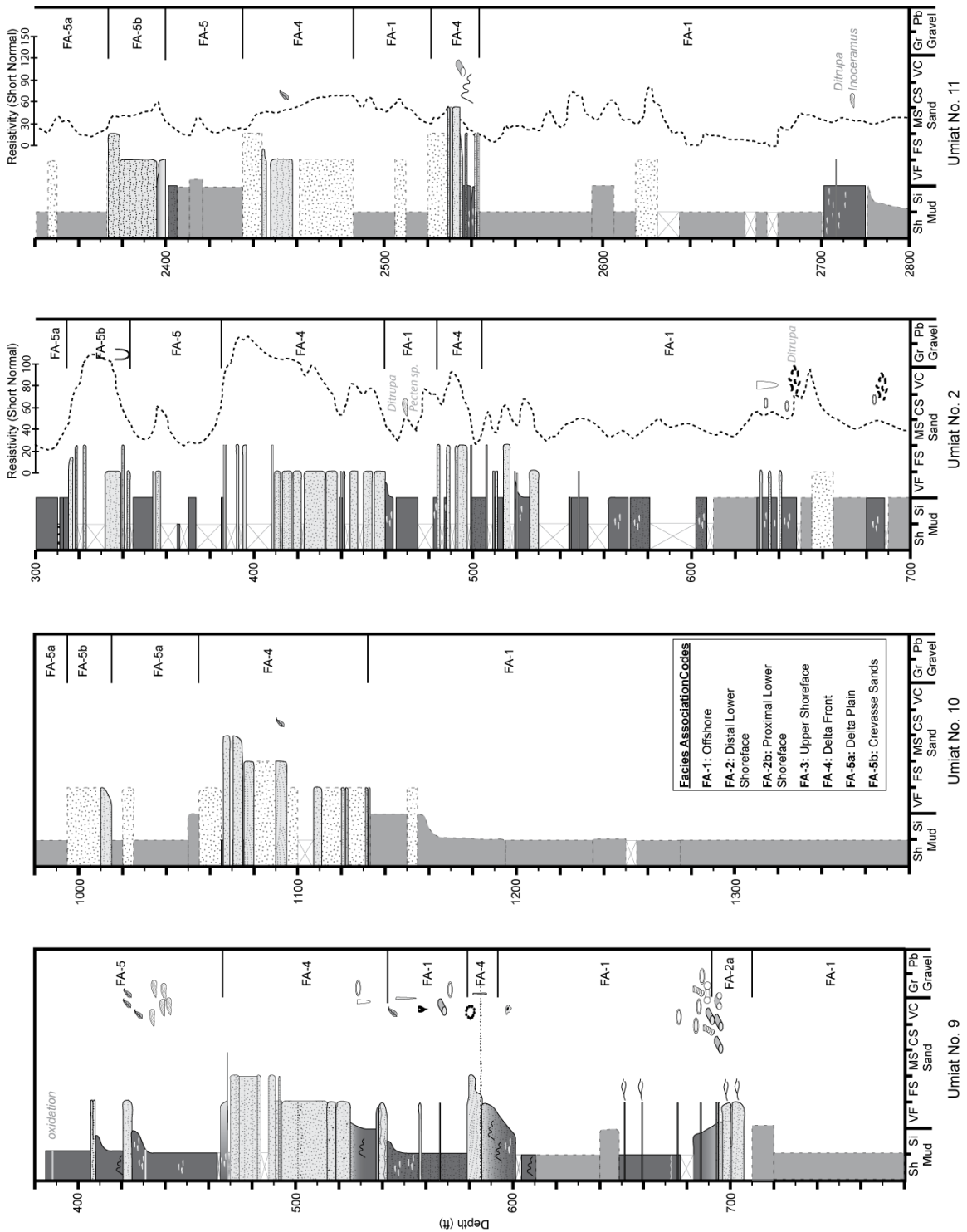


Figure 15. Segments of measured sections from Umiat wells 9, 10, 2 and 11 showing ~60-70 ft thick Upper Grandstand of the Nanushuk Fm.. These wells were selected based on core representation, and arranged in rough west-east order from left-right. The Upper Grandstand is interpreted as distributary mouth bar deposits of a river-dominated delta. Lighter shaded areas with dashed lines are interpretations based on original cuttings data (Collins, 1958). See Figure 7 for symbol legend.

NANUSHUK FORMATION DEPOSITIONAL SYSTEMS

In the Umiat area, the informal units of the Nanushuk Fm. can be grouped together to describe two distinct deltaic systems: an upward coarsening, progradational wave-dominated deltaic system comprised of the Tuktu and Lower Grandstand, and an upward coarsening, progradational river-dominated deltaic system comprised of the Shale Barrier, Upper Grandstand and Killik. These two major upward-coarsening, regressive systems are capped by the Ninuluk, which is interpreted as a back-stepping, transgressive system.

The Tuktu and Lower Grandstand: Wave-Dominated Shoreface

The facies successions described in the Tuktu and Lower Grandstand resemble the deposits of regressive wave-dominated shorefaces and wave-influenced deltas, where wave energy disperses sediment brought to the coast by distributary systems (Hampson and Storms, 2003; Bhattacharya and Giosan, 2003; Hampson and Howell, 2005; Fig. 16a). The wave-dominated shoreface successions coarsen upward from offshore mudstones (FA-1) of the Tuktu into lower shoreface (FA-2) and upper shoreface (FA-3) sandstones of the Lower Grandstand (Fig. 14). The type examples for the shoreface succession are from Umiat No. 9 (860-940 ft, 965-1085 ft: Fig. 6), which closely resembles the characteristic profile of a wave-dominated shoreface (Bhattacharya and Walker, 1991; Van Wagoner et al., 1990; Hampson, 2000; Hampson and Storms, 2003). The trace fossil assemblage of both *Cruziana* and *Skolithos* type ichnofacies further supports a shoreface interpretation (Frey, 1990; Pemberton and MacEachern, 1995).

In the Lower Grandstand A at both Umiat No. 2 (910-1050 ft) and No. 11 (2960-3090 ft: Fig. 14), thin lags marked by rip-up clasts interrupt hummocky cross strata. These features can be found in both shoreface and wave-influenced deltaic environments (Bhattacharya and Walker, 1991; Hampson and Howell, 2005). Though it is possible to distinguish non-deltaic shoreface deposits from wave-influenced deltas in core using physical and biogenic indicators of fluvial discharge (Dafoe et al., 2010), we do not identify any characteristic features that would permit this distinction in the Umiat wells.

The upper part of the Lower Grandstand A shows limited evidence for subaerial exposure beneath a minor flooding surface. There are root traces at the top of Lower Grandstand A in Umiat No. 9 (Fig. 5). Immediately above this layer are mudstones of FA-1 with trace fossils of the *Cruziana* ichnofacies including *Phycosiphon*, *Paleophycus*, and *Planolites* (Fig. 5). The abrupt deepening of facies above Lower Grandstand A marks the beginning of a second wave-dominated shoreface facies succession in all of the Umiat wells (Fig. 14). This second succession, which is capped by brackish water facies of the delta plain or coastal plain environments (FA-5a), makes up Lower Grandstand B.

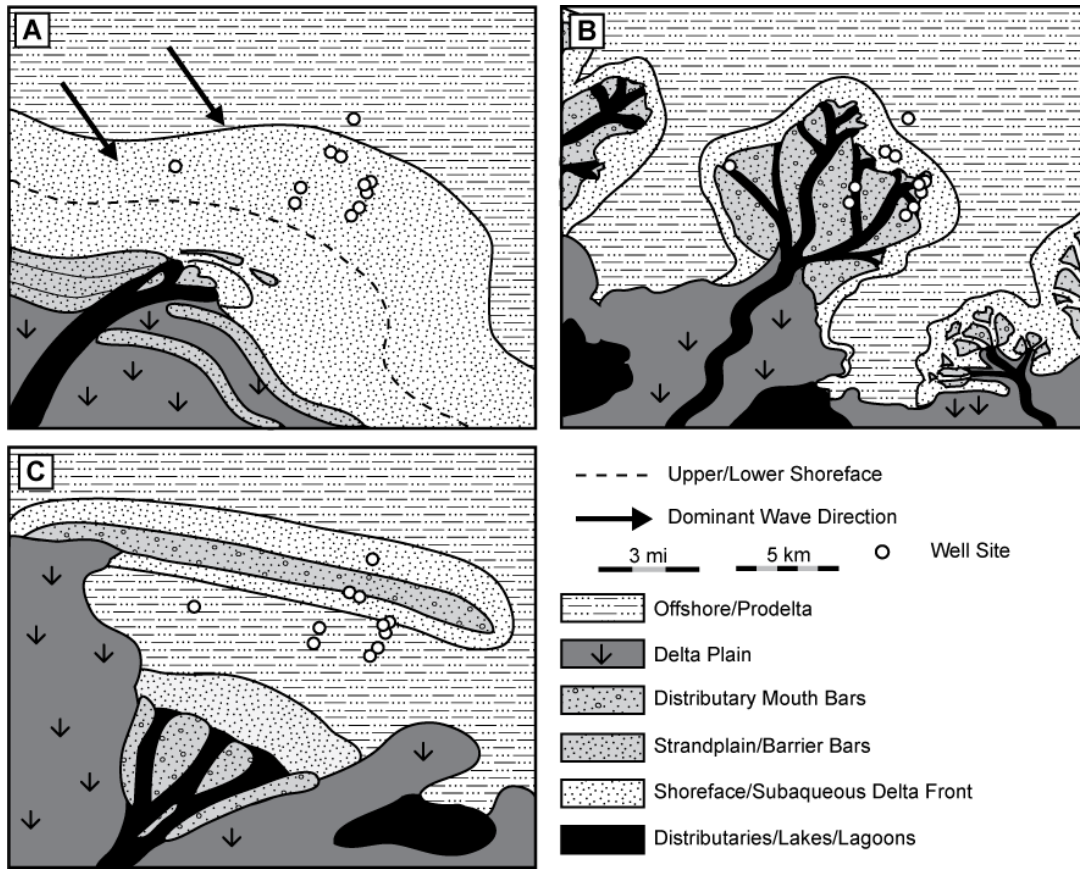


Figure 16. Schematic cartoons illustrating interpretations for Lower Grandstand (A), Upper Grandstand/Killik Tongue (B), and Killik/Ninuluk (C) depositional environments, with the locations of the Umiat wells for reference. The Lower Grandstand consists of shoreface sandstones, interpreted as being deposited in a wave-influenced deltaic setting. The inferred wave direction is based on modern shoreline currents. The Upper Grandstand and Killik were deposited in a river-dominated deltaic setting by delta front (Upper Grandstand) and delta plain (Killik) processes. The Ninuluk includes both tidally influenced delta front sandstones and overlying transgressive shoreface sandstones.

The top of the Lower Grandstand B lies beneath a ~20 ft thick sandstone in multiple wells (Fig. 14). The base of this sandstone, which consists of distal lower shoreface deposits (FA-2a) with trace fossils of the *Cruziana* ichnofacies, is interpreted to be a transgressive surface of erosion. Transgressive surfaces of erosion cap progradational parasequences and displace changes in bioturbation intensity and character (Gani et al., 2008). The ~20 ft thick sandstone represents wave reworking of the shelf during a slow rise in relative sea level associated with a back-stepping shoreline trajectory. The overlying offshore mudstones (FA-1) are part of the Shale Barrier and represent a major flooding surface at the top of the Lower Grandstand.

The Shale Barrier, Upper Grandstand, and Killik: River-Dominated Delta

The Shale Barrier consists of offshore marine mudstone (FA-1) with thin beds of distal lower shoreface sandstone (FA-2a). The abrupt deepening of facies from the Lower

Grandstand into the Shale Barrier is interpreted as a maximum flooding surface that represents a rise in relative sea level and an increase in accommodation. In this interpretation, the Shale Barrier, Upper Grandstand, and Killik are genetically linked marine shelf/prodelta (FA-1), delta front (FA-4), and delta plain (FA-5) components of a prograding deltaic system (Fig. 16b) that advanced out over the Lower Grandstand. Unlike the Lower Grandstand, the Upper Grandstand sandstone is a single-storey unit, and has a facies succession (Fig. 15) consistent with a river-dominated delta interpretation (*sensu* Bhattacharya and Walker, 1991) with no evidence of wave influence. The overlying delta plain mudstones of the Killik are over 300 ft thick, suggesting significant accommodation landward of the delta front. The dominance of brackish water conditions throughout the Killik (May and Shane, 1985), favors a broad, low-angle delta plain subject to influxes of marine water. Improved well control could be used to interpret minor transgressions within the Killik preceding the major transgression described below.

The Ninuluk: Back-Stepping Delta

The Ninuluk-Killik boundary is defined by a shift from mud-dominated delta plain deposits with non-marine microfossil assemblages to sandstones with marine microfossils similar to those found in the Lower and Upper Grandstand (Collins, 1958). In Umiat No. 11 the Ninuluk consists of two, thick sandstone units separated by a thin mudstone (Fig 8). The two units bear many similarities to a pair of sandstone units described in outcrop at Umiat Mountain (Houseknecht and Schenk, 2005), though the Ninuluk units in the Umiat wells are nearly twice as thick as those described in outcrop. In Umiat No. 11 we interpret the ~30 ft thick lower Ninuluk sand as tidally influenced distributary mouth bar deposits (FA-4: Fig. 16c). This interval is similar to the lower Ninuluk sandstone in outcrop that Houseknecht and Schenk (2005) interpreted as an estuary or flood-tidal inlet in a transgressive setting. The basis of their interpretation was the presence of possible herringbone cross-bedding. The decreasing frequency of spores and gymnosperm pollen and increasing frequency of dinoflagellates and acritarchs in the Ninuluk also supports the transgressive interpretation (May and Shane, 1985). The lower Ninuluk in Umiat No. 11 has trough cross stratification, with sideritized mud drapes, though there is no evidence for herringbone cross bedding in the cores. It is also relatively coarse-grained compared to the rest of the Nanushuk Fm. Consequently, we interpret the proximal distributary mouth bar deposits in the lower Ninuluk sandstone at Umiat field as part of a back-stepping delta system (Fig. 16c).

The upper Ninuluk sand unit in the Umiat No. 11 is 50 ft thick (Fig. 8), with massive, trough-cross laminated, and parallel laminated sandstones. A similar wave-influenced upper unit is exposed at Umiat Mountain (Houseknecht and Schenk, 2005). The facies succession in the upper Ninuluk sand is most similar to upper shoreface (FA-3) deposits, but may also be deltaic in origin. Unlike the other Nanushuk Fm. sandstones, the upper Ninuluk contains detrital and authigenic calcite (Collins, 1958; Fox et al., 1979), a possible sign of its transgressive shoreface origin. Calcareous cement can be associated with marine flooding surfaces and transgressive events at the top of highstand systems tracts (Taylor et al., 1995; Ketzer et al., 2002). We interpret the upper Ninuluk as a transgressive upper shoreface sandstone with lag deposits at the base, capped by a

flooding surface. The thickness of the Ninuluk supports a relatively slow relative sea level rise and corresponding transgressive event, where significant accommodation developed in pace with sediment supply. This contrasts with thinner (<20 ft) transgressive sandstones at the top of the Lower Grandstand.

RESERVOIR POTENTIAL OF INFORMAL UNITS

The major reservoir units at Umiat are the Lower Grandstand and Upper Grandstand sandstones, with additional potential petroleum accumulations in the sandstones of the Killik and Ninuluk. Both the Upper and Lower Grandstand are regionally extensive in the subsurface (Fig. 13). The Ninuluk is also extensive, but is eroded from the top of the Umiat anticline structure and is only found on the southern flank and in the footwall (Fig. 2). In contrast, sandstones in the Killik are not laterally extensive and are difficult to correlate between wells. Consequently, the Upper and Lower Grandstand are considered the primary reservoirs at Umiat.

Due to the regional extent of the Upper and Lower Grandstand (Fig. 13), and the similar thickness for the units within the predicted trap limits, it is likely that permeability trends are consistent across the site within each reservoir unit. The upward increase in permeability towards the top of reservoir units is apparent in both vertical and horizontal air permeability results. These trends suggest that permeabilities greater than 10 md are limited to the upper 20-40 ft of the Upper Grandstand and Lower Grandstand reservoir units (Figs. 6-7).

Permeability trends in both units of the Lower Grandstand and in the Upper Grandstand sand are consistent with increasing porosity related to improved sorting in increasingly high-energy deposits of regressive, upward coarsening shoreface and deltaic sandstones (Figs. 6-7). Previous authors hypothesized that winnowing of ductile phyllitic grains by high-energy shoreface deposits was responsible for an increase in porosity at the top of Grandstand sandstones (Bartsch-Winkler, 1985; Huffman et al., 1985; Fox et al., 1979). Preliminary petrographic results support this, and indicate that the percentage of metamorphic fragments present in sandstones is proportional to permeability (Fig. 17). This increase in permeability may also be related to a decrease in bioturbation intensity in upper shoreface settings (Fig. 6) and the lack of bioturbation in deltaic settings (Fig. 7). A similar relationship between energy and bioturbation intensity was observed in sandy deposits of the Cretaceous Ferron delta in southern Utah (Li et al., 2011). The trends in the Upper and Lower Grandstand contrast directly with the Ninuluk, a transgressive unit with upward decreasing permeability (Fig. 8).

Diagenetic factors that influence porosity include authigenic minerals and grain overgrowth that reduce porosity. SEM images clearly show quartz and feldspar overgrowths, as well as diagenetic clays and other authigenic minerals, such as pyrite (Figs. 11-12). The clays are found in delta front sandstones of the Upper Grandstand, while overgrowths are present in both the Upper and Lower Grandstand (Fig. 16). Grain coating clays are known diagenetic alterations in delta front sandstones, while extensive

cementation is common in wave-dominated environments (Morad et al., 2010). These generalities seem to hold within the Nanushuk Formation.

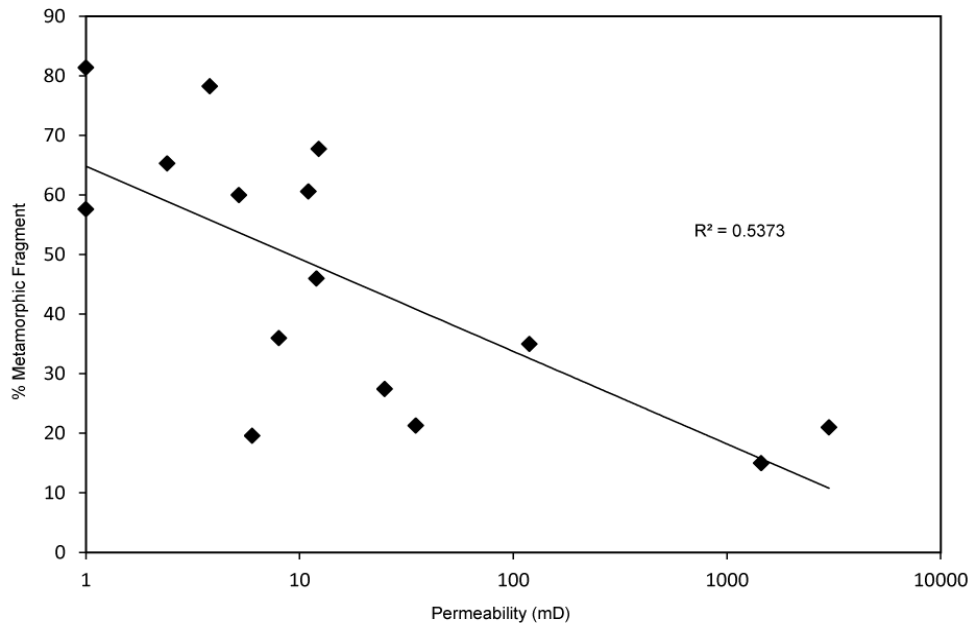


Figure 17. Metamorphic fragment content versus permeability. There is a negative covariant trend, indicating that metamorphic rock fragments reduce permeability.

Most of the oil produced from the Nanushuk Fm. at Umiat during the 1944-1953 drilling period came from the Upper Grandstand (Molenaar, 1982), but recent studies have revised reservoir estimates for Umiat field due, in part, to an improved understanding of the Lower Grandstand. Several of the wells crucial to original estimates did reach the Lower Grandstand, including the discovery well (Umiat No. 3). Ice formation and hole caving also prevented drillers from reaching the Lower Grandstand in Umiat No. 6 (Collins, 1958), which is important because the interpreted oil-water contact in the Upper Grandstand lies between Umiat No. 6 and Umiat No. 7 (Molenaar, 1982: Fig. 2b). The oil-water contact in the Lower Grandstand lies at 1500 ft, and new estimates that include the reservoir potential of the Lower Grandstand should increase the amount of producible oil from 70 million bbl (Molenaar, 1982) to 12-15% percent of the >1.2 billion bbl OOIP reported in recent assessments of the Umiat field (Watts, 2010; Levi-Johnson, 2010). This is a range of 180-225 million bbl. Furthermore, separation of the Lower Grandstand into two units adds to the complexity of the reservoir, though both Lower Grandstand A and B can be found in all the wells within the oil-water contact boundaries.

The Ninuluk is a low priority reservoir target, due to its absence in most of the field. Contrary to the Grandstand sands, the upper Ninuluk has an upward decreasing permeability profile (Fig. 8) that we interpret as an upward deepening succession of less-winnowed shoreface sand. The presence of calcite cement is a likely inhibitor of porosity, further reducing the reservoir quality of the Ninuluk sandstones.

CONCLUSIONS

New core-based interpretations of the sedimentology, stratigraphy, and permeability characteristics of the Nanushuk Fm. at Umiat field present a reservoir characterized by laterally extensive shoreface and deltaic sandstones. There are four primary reservoirs at Umiat, including two in the vertically compartmentalized, multi-storey shoreface sandstones of the Lower Grandstand, a river-dominated deltaic reservoir in the Upper Grandstand, and a limited transgressive deltaic/shoreface reservoir in the Ninuluk. Despite differences in depositional environments, the Lower Grandstand and the Upper Grandstand reservoir units have similar air permeability profiles. Permeability increases towards the top of these units, with the highest values within 20 ft of the top of each sandstone. Increases in permeability correspond to increases in grain size and transitions to more-well-sorted upper shoreface and distributary mouth bar facies with low bioturbation intensities. The lateral continuity of extensive shoreface and deltaic sandstones indicates that this trend should be consistent between existing wells in the central part of the field. This study demonstrates the utility of reassessing legacy wells in the National Petroleum Reserve–Alaska for improved understanding of facies-controlled permeability trends in the Nanushuk Formation.

Fracture distribution and character in exposed and subsurface Cretaceous rocks in the Umiat area

Introduction

Umiat oil field is located in the southeastern part of the National Petroleum Reserve in the foothills of the Brooks Range (Figure 1). The Brooks Range is the northern structural continuation of the backarc fold-and-thrust belt of the Cordilleran orogen (Hayes, 2008). Major contraction occurred during late Jurassic/Early Cretaceous time and involved the collapse of an extensive south-facing continental margin. The east-west-trending Colville basin is the foreland basin that developed during this orogeny and is filled with Cretaceous to Tertiary clastic sedimentary rocks derived from the Brooks Range. The Umiat structure is a shallow thrust-related anticline in the northern foothills of the Brooks Range fold-and-thrust belt and involves deformed Colville basin deposits (Figures 2, 3, 4).

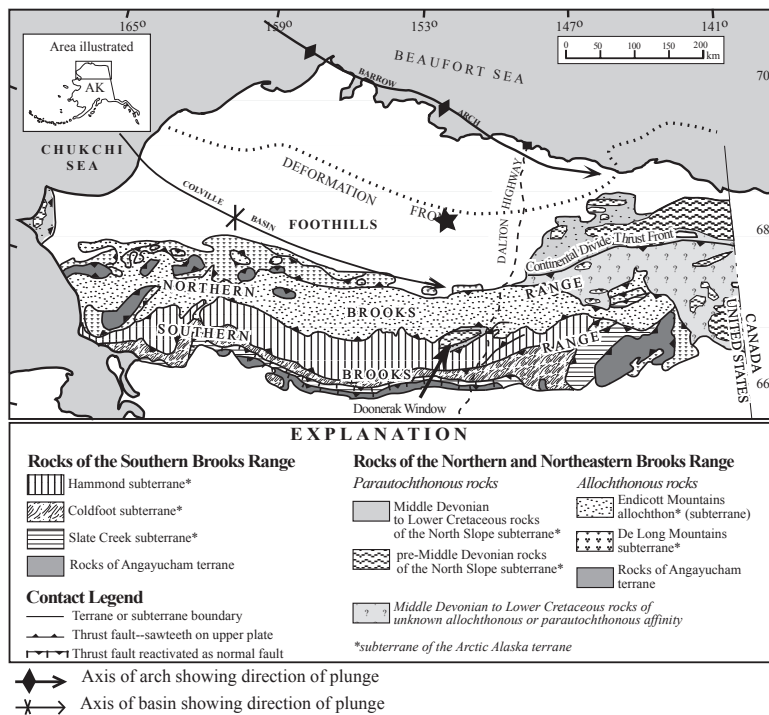


Figure 1. Geologic map of northern Alaska. Umiat field (star) is located at the leading edge of the Brooks Range fold-and-thrust belt. Map modified from Moore et al., 1994.

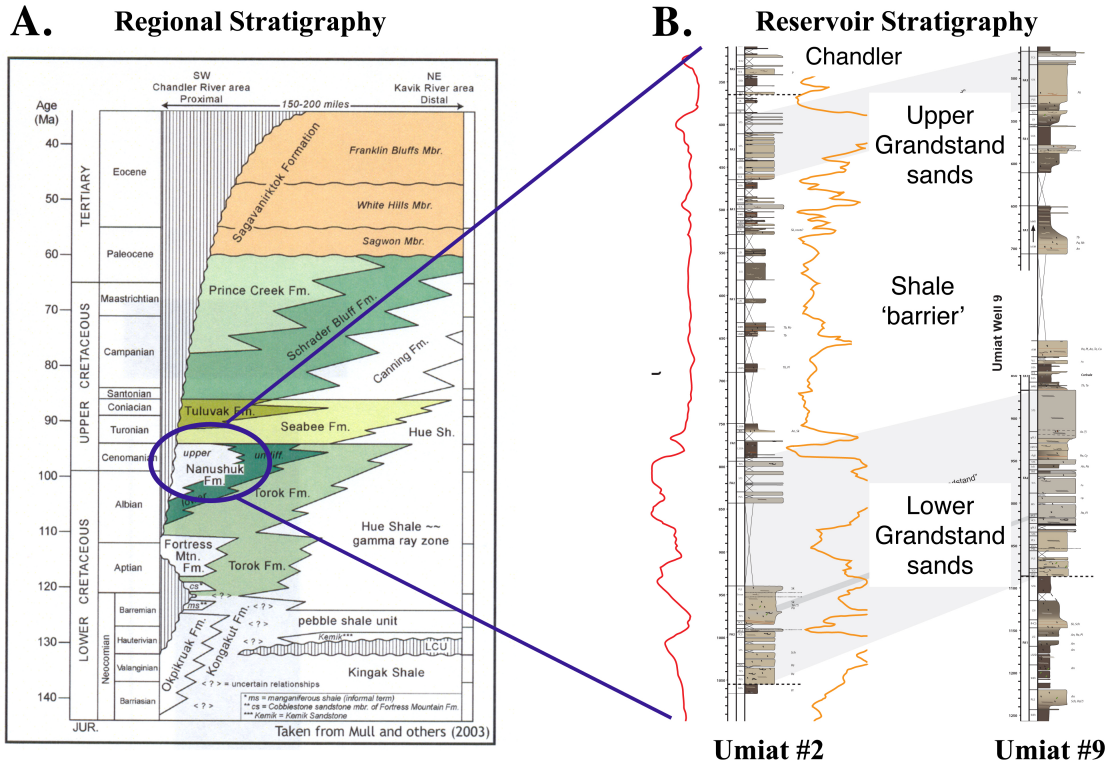


Figure 2. A. Regional stratigraphy of northern Alaska, showing the stratigraphic position of the Umiat reservoir in the Early Cretaceous Nanushuk Formation. Modified from Mull et al., 2003; B. Reservoir stratigraphic nomenclature used at Umiat field.

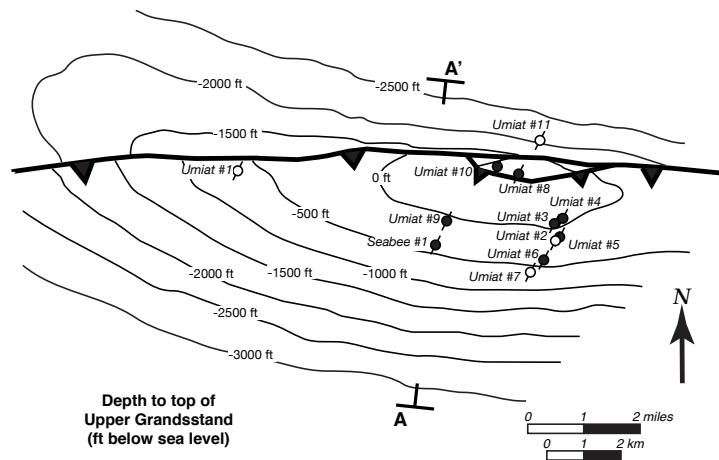


Figure 3. Structure contour map of top of Grandstand Sand, Umiat field showing location of legacy wells. A-A' shows location of seismic line in Figure 4. Contour intervals = 500 ft (153 m)

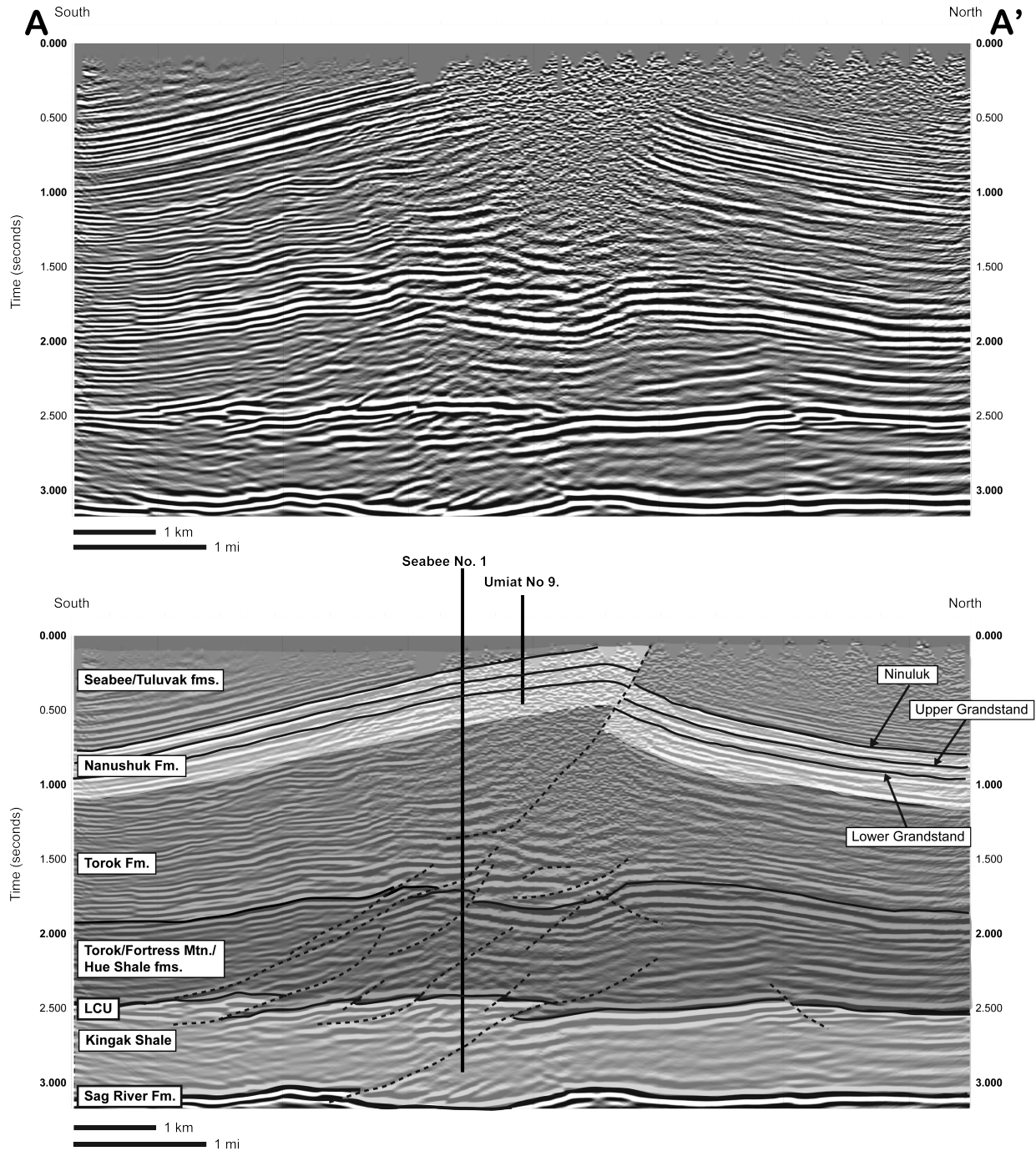


Figure 4. North-South seismic section through Umiat field. Top: uninterpreted; bottom: interpretation by G. Shimer. Location of seismic section shown on Figure 2. Seismic data courtesy of Renaissance Alaska Inc.

Regionally, fluid flow in a foreland basin can be enhanced by open fracture networks (Hanks et al., 2006). At the scale of an individual field, open fractures can enhance permeability while cemented fractures can impede fluid flow. Thus understanding the distribution, orientation and origin of fractures can yield important information regarding the evolution and reservoir

behavior of a field. At Umiat field, this is particularly important given that the development scenario calls for several horizontal wells in order to access the shallow reservoir.

The purpose of this study is to document the fracture orientation, distribution and character at exposed age-equivalent rocks in both the subsurface at Umiat and in exposed structures in the vicinity of Umiat field. While the surface studies focused on a potential analog to the Umiat structure (Figure 5: Big Bend Anticline) several other exposures were also visited in the area (Figure 5: Colville Incision and Fossil Creek). These three structures involve rocks at different stratigraphic levels within the reservoir interval at Umiat, the Cretaceous Nanushuk Formation (Figure 6). This character and distribution of fractures in these locations will ultimately be incorporated into a model of fracture distribution for the Umiat anticline.

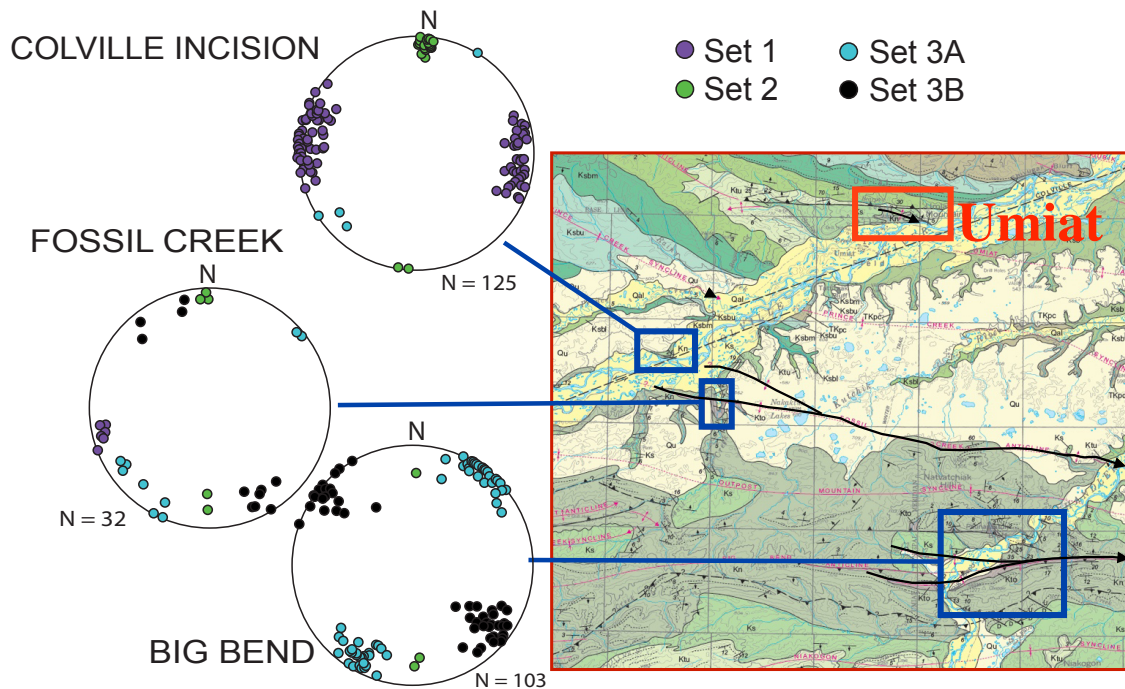


Figure 5: Map showing Big Bend anticline, Fossil Creek anticline and the Colville Incision and their relationship to the Umiat anticline to the North. Modified from Mull et al., 2004.

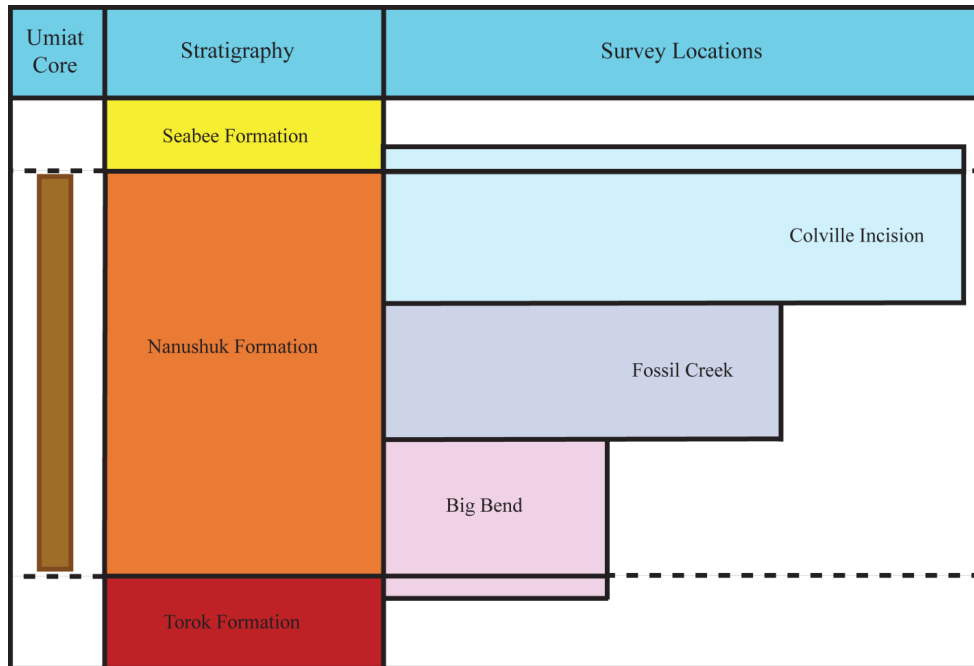


Figure 6: Schematic diagram showing stratigraphic level at each fracture survey location.

Methodology

Cores taken during initial exploration of the Umiat field during the 1940’s and 50’s were examined for evidence of natural fractures. Information such as orientation with respect to bedding, aperture, fracture fill and/or surface ornamentation was documented. These early cores were not oriented, so fracture orientation could not be determined.

Fracture data from surface exposures were collected using the straight scan-line fracture survey method at the four previously mentioned locations during June and early July 2010. A flexible tape measure was laid along an outcrop surface and characteristics of every fracture that intersected the tape line was recorded. The following information was recorded: orientation of fractures, spacing between adjacent fractures, height of fracture (perpendicular to bedding), length of fractures (parallel to bedding), fracture aperture (width of opening normal to fracture wall), fracture fill and composition (quartz or calcite, nature of fracture terminations and the fracture type (shear or extension). Samples were collected of fracture fill (where observed) for future fluid inclusion analysis.

Observations

Umiat core

Natural fractures were identified in Umiat Well #1, Umiat Well #2 and Umiat Well #11 (Figure 7, Table 1). Characteristics of these natural fractures include: planar geometry, high dip with respect to bedding, calcite cementation and/or open with apparent surface staining. None of the

wells examined had core from the actual thrust faults, so fractures related to thrusting were not observed.



Figure 7: Fracture with an 82° dip in Umiat Well #11 , depth of 709 – 729’.

Well number	Well depth (ft)	Amount of recovered core (ft)	Amount of core examined (ft)	Number of natural fractures identified
1	6,005	1,294	1,294	2
2	6,212	592.75	500	3
11	3,303	740.45	740	6

Table 1: Tabulation of well depth, amount of recovered/examined core, and the number of natural fractures identified.

Exposed structures in the vicinity of Umiat anticline

Fracture Sets 1A&B and Set 2 were identified at the Colville Incision locality (Figure 5). Set 1 fractures are N-S striking and are interpreted to be extensional fractures. These fractures perpendicular to bedding, can be vertically extensive and either terminate within bedding or at lithology changes. Fracture apertures range from <1 mm to 1 cm. Set 1A is filled or partially filled with calcite cement; Set 1B is unfilled.

Three fracture sets were identified on the south limb of the Big Bend anticline—Sets 2 and 3A & B. (Figure 5, Table 2). Sets 3A & 3B are the dominant fracture orientations and strike NE-SW (Set 3A) and NW-SE (Set 3B). These fractures are perpendicular to bedding with average dips

of 72° and 76° , are vertically extensive and were either open or partially filled with calcite cement. The average aperture for these fracture sets are <1 cm to 5 cm and are interpreted to be shear fractures based on surface features. Fractures in both sets are perpendicular to bedding and vertically extensive.

Fracture Set 2 is also present at Big Bend anticline, but is less common (Table 2). This fracture set strikes E-W, is vertically extensive and usually unfilled. The lack of fracture cement suggests that this fracture set postdates Sets 3 A&B.

All three fracture sets were documented at Fossil Creek (Figure 5, Table 2). The dominant fractures strike NW-SE and NE-SW and are interpreted to be fracture Set 3. These fractures are vertically extensive and are open with apertures ranging from <1 mm to 5 cm and are interpreted to be shear fractures. Fractures from Set 1 and Set 2 were also documented at Fossil Creek and have been interpreted to be extensional fractures.

Fracture Set	Orientation & Type	Fracture Characteristics	Fracture Distribution			Relative Age with Respect to Folding			
			Big Bend	Fossil Creek	Colville Incision	Pre-Folding	Early-Folding	Late-Folding	Post-Folding
1A North-South Filled	*Perpendicular to fold axis *Perpendicular to bedding *Extensional	Extension fracture: small apertures, calcite filled; terminate at bedding planes; evenly distributed	Stratigraphy			■ ■ ■	■ ■ ■		
			lower Nanushuk/Torok	lower Nanushuk/Torok	upper Nanushuk				
1B North-South Open	*Perpendicular to fold axis *Perpendicular to bedding *Extensional	Open extension fracture: small apertures, terminate at bedding planes; evenly distributed		■ ■ ■ ■ ■		■ ■ ■ ■ ■		■ ■ ■ ■ ■	
2 East-West Open	*Parallel to fold axis *Perpendicular to bedding *Extensional	Apparent extension fractures; open, vertically extensive	■ ■ ■ ■ ■ ■ ■ ■ ■ ■				■ ■ ■ ■ ■ ■ ■ ■ ■ ■		
3A Northeast-Southwest Open	*Acute bisectors perpendicular to fold axis *Perpendicular to bedding *Shear	Unfilled shear fractures with conjugate geometry, small apertures; vertically extensive	■ ■ ■ ■ ■ ■ ■ ■ ■ ■			■ ■ ■ ■ ■ ■ ■ ■ ■ ■	■ ■ ■ ■ ■ ■ ■ ■ ■ ■	■ ■ ■ ■ ■ ■ ■ ■ ■ ■	
3B Northwest-Southeast Open	*Acute bisectors perpendicular to fold axis *Perpendicular to bedding *Shear	Unfilled to partially filled shear fractures with conjugate geometry, small apertures; vertically extensive	■ ■ ■ ■ ■ ■ ■ ■ ■ ■			■ ■ ■ ■ ■ ■ ■ ■ ■ ■	■ ■ ■ ■ ■ ■ ■ ■ ■ ■	■ ■ ■ ■ ■ ■ ■ ■ ■ ■	

Table 2: Characteristics, orientations, and relative age of fracture sets observed at the Big Bend anticline, Colville Incision and the Fossil Creek anticline.

Interpretation of fracture orientation and timing and implications for fractures in the subsurface

Three sets of fractures were identified in outcrop near the Umiat anticline and are interpreted to have formed due to burial, folding and/or unroofing.

Fracture Set 1 is present in the upper and lower Nanushuk and Torok Formations at the Colville Incision and at Fossil Creek (Table 2). Set 1A hinge-perpendicular fractures are interpreted to be the oldest fracture set, predating folding that formed at depth as a result of burial and elevated fluid pressures due to an extensive amount of overburden. As burial of sediments continued, there was enough stress, combined with elevated fluid pressures to propagate extension fractures. The principal stress direction (σ_1) would be oriented NS with a vertical intermediate stress (σ_2). Due to the large amount of overburden, high fluid pressures and the orientation of the principal stress direction, fractures would open parallel to σ_1 . Set 1B fractures are interpreted to form prior to or during early stages of folding as a result of in-situ regional stress and/or reactivation of earlier Set 1A fractures with similar orientations.

Fracture Set 2 is recorded at all three localities (Table 2). Set 2 fractures are oriented parallel to the fold hinges of Big Bend anticline, Fossil Creek anticline and the Colville Incision and are interpreted to be extension fractures. These fractures are interpreted to have formed during late stages of folding to accommodate outer arc extension of folding mechanical competent layers and would correspond to Type 1 extension fractures in Stearns (1967) model (Figure 8). In this interpretation, the principal stress direction would be parallel to the fold axis.

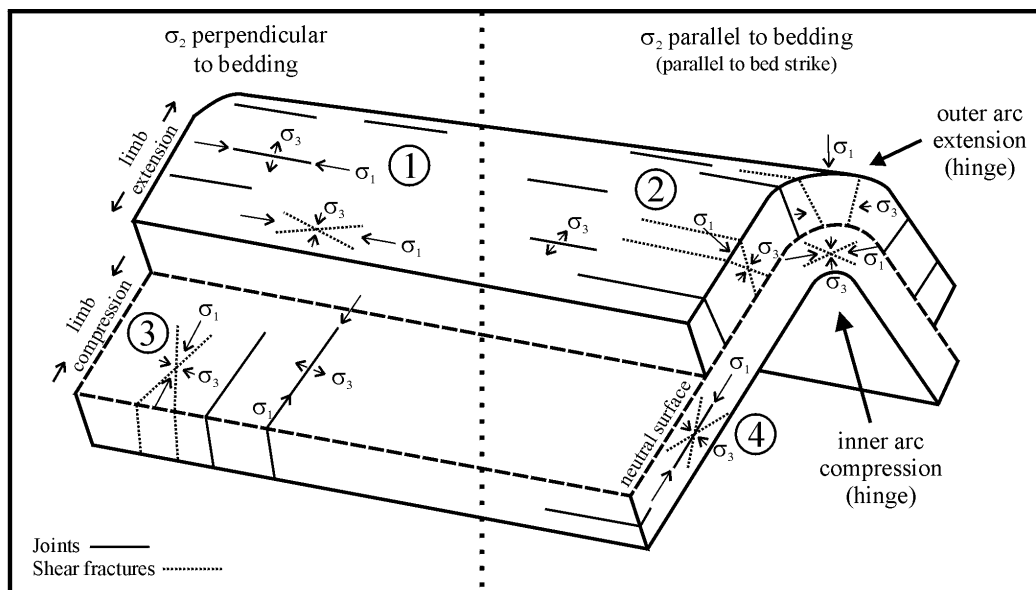


Figure 8. Four fracture sets associated with cylindrical folds and the neutral surface. Each set consists of joints parallel to σ_1 and shear fractures that are conjugate to σ_1 . Note that σ_1 is parallel to bedding on the left hand of the diagram and perpendicular to bedding on the right hand of the diagram. 2 sets represent limb extension above the neutral surface (type 1 and 2) and 2 represent limb compression below the neutral surface (type 3 and 4). Modified from Price and Crossgrove, 1990; Stearns, 1967.

Fracture Set 3 is present in the lower Nanushuk Formation at Fossil Creek and the lower Nanushuk Formation and Torok at the Big Bend anticline and are uncemented conjugate shear fractures (Table 2). Set 3 shear fractures exhibit an apparent conjugate relationship with the bisector perpendicular to fold axes. This observation is consistent with, and interpreted as, fold-related fractures that formed due to inner arc limb compression (Figure 8, Type 3 shear fractures). The local principal stress direction would be perpendicular to the fold axis. Fracture set 3A and 3B are interpreted to have developed continuously during folding due to tangential longitudinal strain near fold hinges.

The orientations of fractures at the Colville Incision, Fossil Creek anticline and the Big Bend anticline are similar to those documented by Duncan (2007) and Hayes and Hanks (2008). In these fracture studies, fractures striking perpendicular to fold hinges are related to pre-folding while fractures oriented parallel and oblique to fold hinges are interpreted to be fold-related (Duncan, 2007; Hayes and Hanks, 2008).

The variation in fracture orientation data from three different surface locations in the Umiat area can be interpreted in two different ways:

1. Fracture distribution and character varies spatially with respect to the range front. Open folds further from the thrust front (e.g., Umiat, Colville Incision) exhibit low intensity fracturing that occurred prior to and during folding under low differential stresses. Tighter folds closer to the range front exhibit higher intensity fractures that developed under higher differential stresses. This more intense fracturing masks any early prefolding fractures.

In this interpretation, the fractures observed at Colville Incision are most likely to represent the fracture distribution in the subsurface at Umiat field.

2. Fracturing occurred prior to and/or during folding but appears to vary spatially because the three fracture locations expose different structural levels and different parts of the stratigraphy.

In this interpretation, the fracture character, distribution and spacing at Umiat field would vary with structural and stratigraphic level, as shown in Figure 6. Fractures in the upper Nanushuk (e.g., Upper Grandstand) would be most similar to those observed at the Colville Incision; middle Nanushuk fractures (Shale barrier) would be most similar to those seen at Fossil Creek; and lower Nanushuk fracture character (Lower Grandstand and upper Torok) would be most similar to Big Bend.

Spacing of fractures in exposed rocks and implications for fracture distribution in the subsurface

The relative low number of natural fractures in Umiat core (Table 1) is most probably related to the fact that these fractures are spaced, vertical phenomena; shallow vertical, low diameter wells are not likely to encounter many vertical or near vertical fractures.

The density of fractures observed in surface exposures can be used to predict fracture spacing in core. Figure 9 is a schematic representation of a vertical well bore with the surrounding formations and fractures. In this diagram, Y represents the fracture spacing parallel to bedding calculated for fractures in surface exposures; and α is the average dip of fractures in the subsurface. The average dip of bedding from Big Bend anticline, Fossil Creek and the Colville Incision is approximately 12° . X represents the calculated fracture spacing that would be observed in a vertical section through the fractured rocks and is calculated using the following formula:

$$X = Y/\cos(\alpha)$$

Calculated values of fracture spacing for the locations visited are summarized in Table 3. Based on this analysis, if the distribution and spacing of fractures in the subsurface is the same as that observed in surface exposures in the upper Nanushuk Formation at Colville Incision, fractures would be encountered approximately every 398.0 cm in a vertical well. Fractures would be encountered approximately every 175.7 cm in middle stratigraphic levels and would be encountered approximately every 149.0 cm in the lower Nanushuk Formation. However, as well trajectories approach horizontal, the possibility of encountering fractures would approach the observed fracture spacing parallel to bedding (Y; Figures 9 & 10, Table 3).

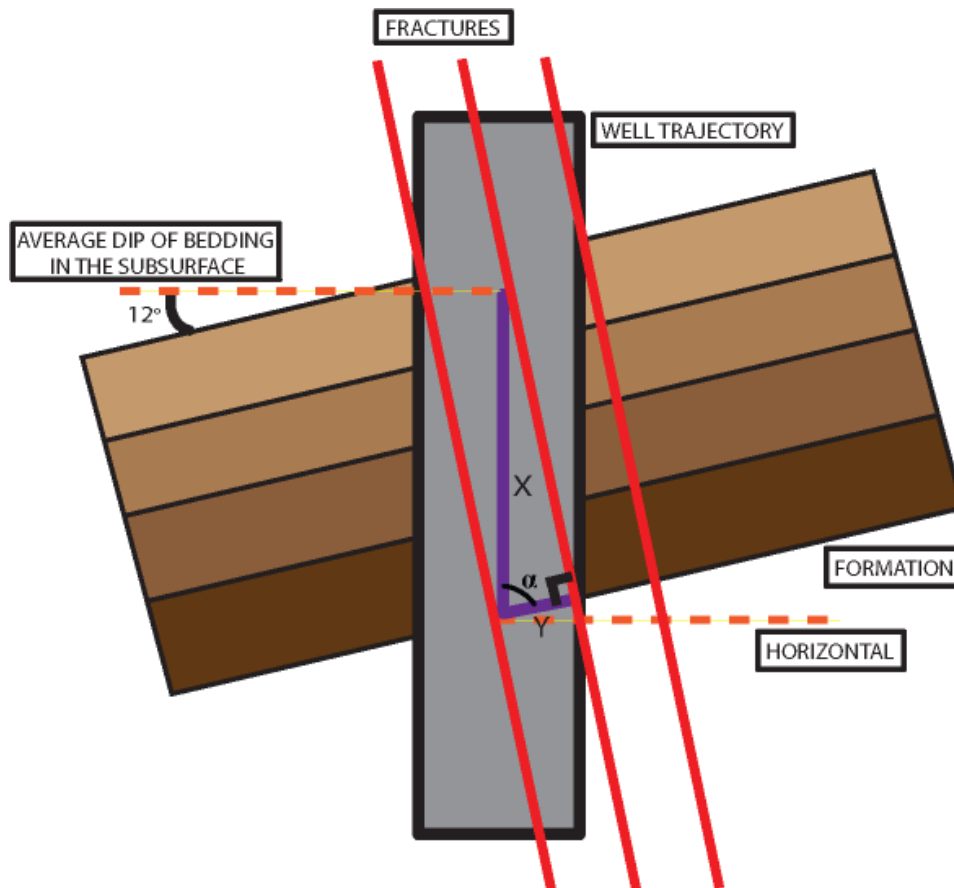


Figure 9: Y is the fracture spacing parallel to bedding calculated from fractures in surface exposures; X is the calculated fracture spacing that would be observed in a vertical core using outcrop data and α is the average

dip of fractures in the subsurface. The average dip of bedding from Big Bend anticline, Fossil Creek and the Colville Incision is approximately 12°.

Location:	Transect:	Y (horizontal fracture spacing) (cm)	α (dip of fractures in outcrop)	$\text{Cos } \alpha$	X (vertical distance between fractures) (cm)
Big Bend	1-6	43.0	73.28	.288	149.0
Fossil Creek	8	25.0	78.53	.199	125.70
Colville Incision	7	58.5	81.53	.147	398.0

Table 3: Average horizontal fracture spacing and vertical distance between fractures calculated for the outcrop locations. Y is the fracture spacing parallel to bedding in each outcrop. α is the dip of fractures measured in outcrop. X is the calculated vertical distance between fractures and would correspond to the distance between fractures that could be expected in a vertical borehole in similarly fractured rocks in the subsurface.

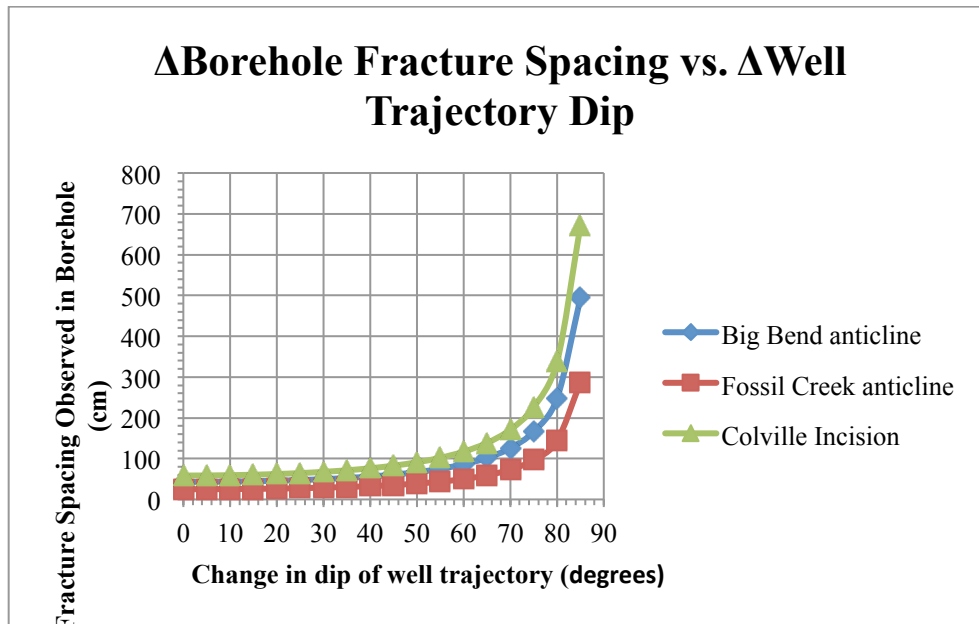


Figure 10: Graph showing the relationship between the observed fracture spacing in a borehole with changing borehole angle with respect to bedding, assuming the well trajectory of well is perpendicular to the trend of the fractures. Different curves represent fracture spacing observed at three field locations: the Big Bend anticline, Fossil Creek anticline and the Colville Incision.

Conclusions

Examination of legacy core from Umiat field indicate that fractures are present in the subsurface, but don't provide information on their orientation and density. Nearby surface exposures in similar stratigraphy indicate there are at least three possible fracture sets: an early, N/S striking set that probably predates folding and two sets possibly related to folding: an EW striking set of extension fractures that are parallel to the fold axes and a set of conjugate shear fractures oriented NE and NW.

There is a spatial variation in fracture character, orientation and spacing, with the prefold NS extension fractures and the EW syn fold extension fractures occurring nearest Umiat field, in rocks representative of the upper parts of the Nanushuk Fm. and in the higher structural levels. The later set of fold-related conjugate shear fractures dominate fracture patterns seen in exposures further south involving lower Nanushuk/upper Torok stratigraphy and deeper structural levels. This spatial variation could be explained by two possible models:

1. Fracture distribution and character varies spatially with respect to the range front, with open folds in the north preserving low intensity fracturing that occurred prior to and during early folding under low differential stresses. Tighter folds in the south exhibit higher intensity fractures that developed under higher differential stresses and masked any early pre-folding fractures. In this interpretation, the fractures observed in the northern, open folds are most likely to represent the fracture distribution in the subsurface at Umiat field.
2. Fracturing varies with structural and stratigraphic level, with higher structural levels exhibiting the early NS and EW extension fractures and lower structural levels showing conjugate shear folding. In this interpretation, the fracture character, distribution and spacing at Umiat field could vary with structural and stratigraphic level.

More field information is needed in order to distinguish between these two models.

Distribution and spacing analysis suggests that these natural fractures are fairly widely spaced (25-59 cm depending upon the fracture set), but could provide improved reservoir permeability in horizontal legs drilled perpendicular to the open fracture set.

Measurement of gas-oil relative permeability for frozen rock systems¹

Introduction

In the early 1900s, field geologists from the United States Geological Survey (USGS) explored the National Petroleum Reserve of Alaska (NPR-A), a roadless area located 321.9 km (200 miles) north of the Arctic Circle (Gates and Caraway, 1960-A; Baptist, 1960). The geologists discovered several good shows of oil that prompted the establishment of the Naval Petroleum Reserve No.4 (NPR4) in 1923. The area remained largely untouched until the conclusion of the Second World War. From 1944 through 1953 the Department of Navy, Office of Naval Petroleum and Oil Shale Reserves organized an exploration program to evaluate the oil resources of NPR4 and surrounding area (Gates and Caraway, 1960-B; Baptist 1959). The largest oil accumulation discovered by this program was in the Umiat field.

The initial estimates of recoverable reserves range from 30 to over 100 million bbl (Gaffney, Cline & Associates, 2006; Baptist 1959). The field lies entirely within the continuous permafrost region. The depth to the bottom of the permafrost ranges from 234.7 to 321.6 m. The oil was found at a depth of 83.8 to 335.3 m and therefore most of the oil is in the permanently-frozen zone. For this reason, the field is considered unconventional. The oil is 36°-37° API with a -15°C (5°F) pour point, which allows it to flow even in a permafrost environment.

The main oil-producing zones in the Umiat field are marine sandstones in the Grandstand Formation of the Cretaceous Nanushuk Group (Baptist, 1960). The upper sandstone is usually 15.2 to 22.9 m thick and is separated from the lower one by 91.4 m of gray shale. The thickness of the lower sandstone is much greater but only the top 30.5 m has good reservoir quality. The range of reservoir pressures is about 344.7 kPa in the upper sand and about 2413.2 kPa in the lower one. Most of the primary production will be based on solution gas drive mechanism.

Because of the extraordinary reservoir conditions, the Federal Bureau of Mines was asked to carry out laboratory tests of the reservoir sand (Baptist, 1960). One of the goals of the research was to estimate oil recovery from frozen reservoir rocks under solution gas drive mechanism. For this purpose, experiments were carried out on core samples to determine the effect of freezing of connate water on oil recovery and on relative permeability, which is of most interest for the work presented in this paper. To research the reduction of oil permeability and oil recovery due to freezing of interstitial water, Baptist (1960) ran a set of experiments both at room conditions 23.9°C (75°F) and simulated permafrost conditions -3.3°C (26°F). Permeabilities of the samples at 23.9°C and -3.3°C were found to be $2.96 \times 10^{-14} \text{ m}^2$ and $2.27 \times 10^{-14} \text{ m}^2$ for the first sample (23.3% reduction) and $1.87 \times 10^{-14} \text{ m}^2$ and $1.28 \times 10^{-14} \text{ m}^2$ for the second sample (31.5% reduction). Thus the average reduction in effective oil permeability due to freezing of irreducible water is about 27%.

¹ To be submitted to *Transport in Porous Media*

Although Umiat contains valuable light oil, the field's remote location, far away from the Prudhoe Bay infrastructure and the Trans-Alaska Oil Pipeline, has precluded the development of the field for many years (Bailey, 2009). In 2004, as oil prices started to climb from \$30s into the \$40s, Renaissance Alaska, LLC saw Umiat as one of several Alaska opportunities. Based on 2008 3-D seismic survey and new assessment of field reserves, Renaissance thinks that modern production technology, such as horizontal wells, will grow the field's economically recoverable oil reserve up to 250 million bbl. That is much higher than an old USGS assessment which assumed the use of vertical wells only.

Considering the decline in the production of conventional oil resources from Alaska North Slope, the development of unconventional oil fields such as Umiat becomes attractive. Development of the Umiat oil field could prove to be a useful addition to the inventory of producing fields in northern Alaska. For this purpose it is necessary to build a good reservoir model in order to test different production methods and predict the field's future performance using various reservoir simulators. This objective dictated the problem that had to be addressed in this experimental research. Particularly, the problem implies obtaining critical information about the rock and fluid properties of the reservoir by means of conducting the core flooding experiments and studying two-phase fluid flow properties both at room temperature and in simulated permafrost conditions.

In order to get economically viable oil flow rates while producing hydrocarbons from Umiat field, it will be necessary to artificially support the reservoir energy because the natural energy of the reservoir is fairly low due to low reservoir pressures. For this purpose, injection of cold gas is being considered as one of the EOR techniques (Joshi Technologies International Inc., 2008). Moreover, as Baptist (1960) stated in his work, primary recovery will be based on solution-gas drive mechanism. All of this implies two phase, gas-oil flow through the Umiat porous media and hence obtaining relative permeability data becomes imperative as a means to predict reservoir behavior. Herein lies the purpose of this work with the primary objectives of (1) designing and building up an experimental set-up suitable for conducting two-phase core flooding experiments under ambient and simulated permafrost conditions, (2) developing pertinent experimental procedures, (3) conducting core flooding experiments on representative Umiat core samples and study two-phase fluid flow properties through lab-scale tests, both at room temperature and in simulated permafrost conditions, and (4) determining gas-oil relative permeabilities for unfrozen and frozen rock systems. To the best of the authors' knowledge complete gas-oil relative permeability sets as a function of multiple saturation ranges of frozen rocks have not been reported before and thus makes a unique contribution to the literature on flow through porous media.

Experimental Setup

Figure 1 shows the schematic of the experimental setup which was indigenously designed, developed and assembled in the Petroleum Development Laboratory at the University of Alaska Fairbanks. The major constraint while designing the setup was to provide the flow of three different phases, water, oil and gas through the core samples both at room temperature and at simulated permafrost conditions. As seen from this figure, some of the apparatus is inside the freezing chamber and the rest is outside. Hence, the setup can be conditionally subdivided into inside and outside parts. The apparatus consists of two pumps, four accumulators, a core holder, four pressure gauges, a hydraulic hand pump, an electronic balance, a glass accumulator, a nitrogen gas cylinder, a gas flow meter, a back pressure regulator, a computer and a freezing chamber. Overall, with all the components integrated

into the system, the setup is capable of handling pressures upto 34473.8 kPa (5000 psi) and -10°C .

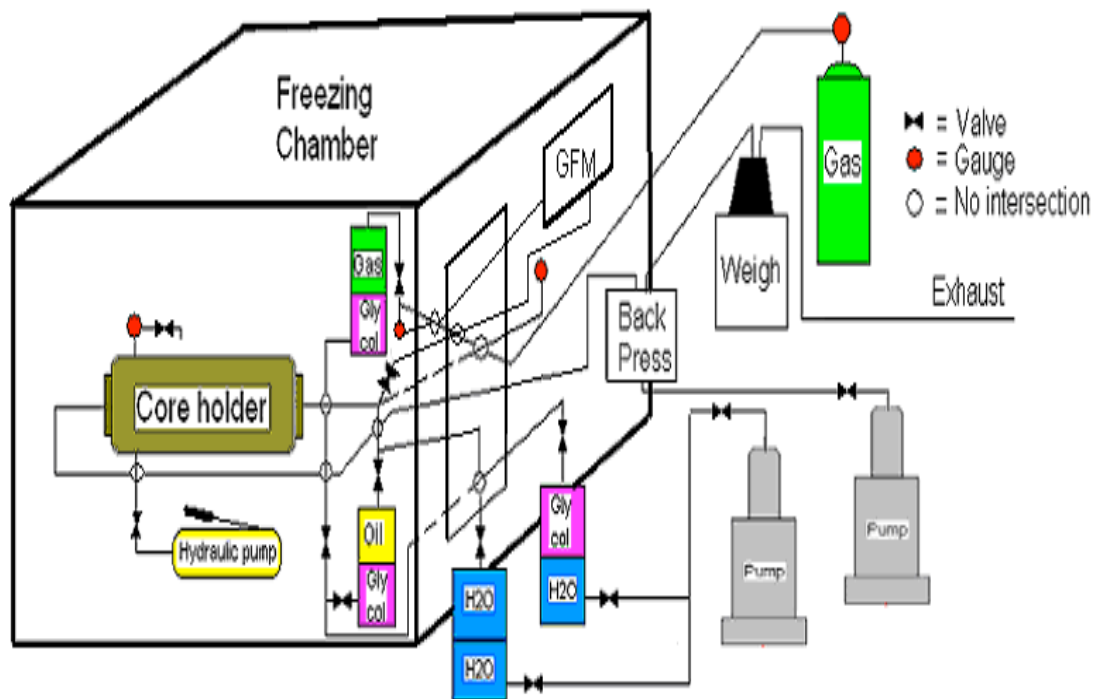


Fig. 1 Schematic representation of the experimental setup.

The salient features of the key components of the setup are briefly described below.

Core holder. The Temco RCHR-1.5 series core holder is located inside the freezing chamber, and can accommodate cores 0.0381 m (1.5 inches) in diameter and up to 0.3047m (12 inches) long.

Pumps. Two Isco Series pumps 500D and 100DX are used to control the flow of fluids at either constant flow rate or constant pressure and maintain constant pressure at the outlet of the core holder. Both pumps are installed outside the freezing chamber.

Accumulators. Three cylindrical accumulators are used for storage of brine/deionized water; oil (kerosene), and injection gas. A fourth accumulator is used as an intermediate accumulator full of glycol between the pump and kerosene and gas accumulators. The oil and gas accumulators are inside the freezing chamber and the glycol and water accumulators are outside the chamber. Each accumulator has a floating piston inside which pushes the fluid towards the outlet of the accumulator. Glycol was used in order to push the piston and remain unfrozen during low temperatures floods.

Hydraulic hand pump. Enerpac P-141 hydraulic hand pump is used for pumping the hydraulic oil in the annular space between the rubber sleeve and the metal jacket of the core holder. The purpose of the pump is to simulate the overburden pressure and to make sure that all the fluid goes through the core sample without bypassing it. The hydraulic hand pump is placed inside the freezing chamber.

Freezing chamber. Tenney T30C-2 freezing chamber is used for freezing the core sample at connate water saturation inside the core holder to simulate the reservoir rock in the permafrost region. The chamber has a small insulated window to establish the connection between the inside and outside parts of the experimental setup.

Electronic balance. One AND GF-4000 electronic balance (accuracy $\pm 0.002\text{g}$) is used to measure the mass of produced oil as a function of time during the gas injection process. The balance is connected to a computer for logging the data using defined time intervals.

Glass accumulator. An enclosed glass accumulator, located on the electronic balance is used to collect the produced oil and separate it from the nitrogen during the gas injection.

Gas flow meter. Aalborg gas flow meter (GFM) is used to measure the volume and flow rate of injected nitrogen during the gas injection process. The GFM transfers the data to a computer for logging with specified time intervals.

Back pressure regulator. A Temco BP series back pressure regulator is used to apply constant pressure at the outlet of the core holder.

Computer. A Dell computer for logging experimental data and its analysis to determine the gas-oil relative permeabilities using the JBN method (Johnson et al, 1959).

Figures 2 and 3 show additional details of the experimental setup.

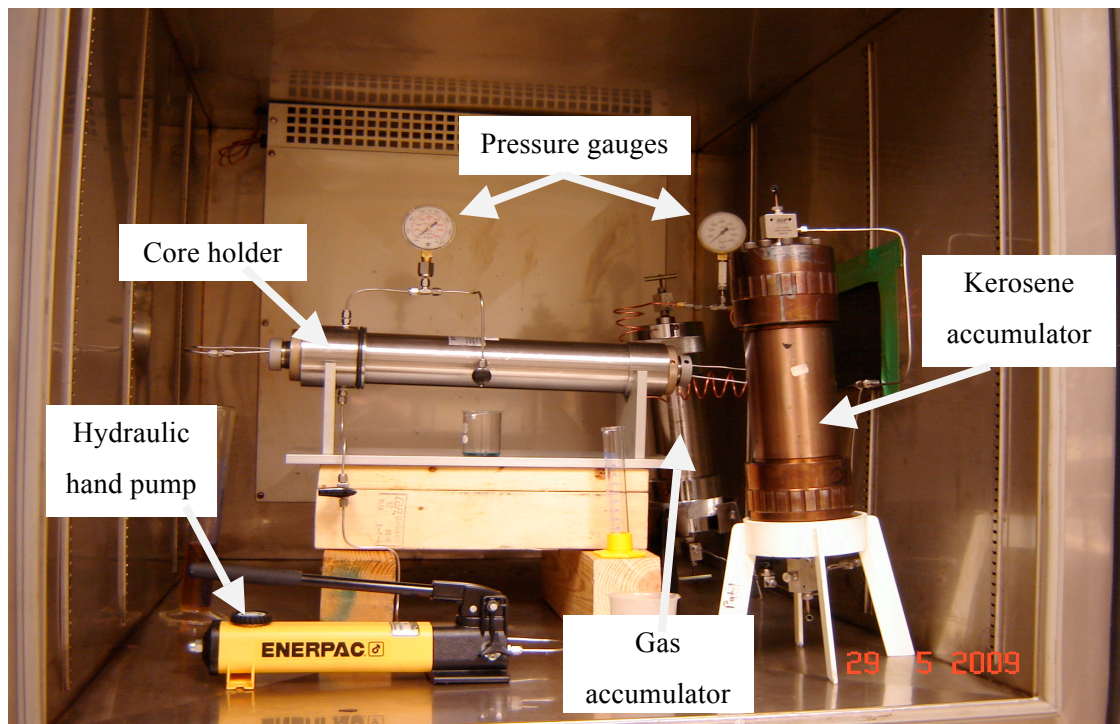


Fig. 2 Internal pictorial representation of the experimental setup.

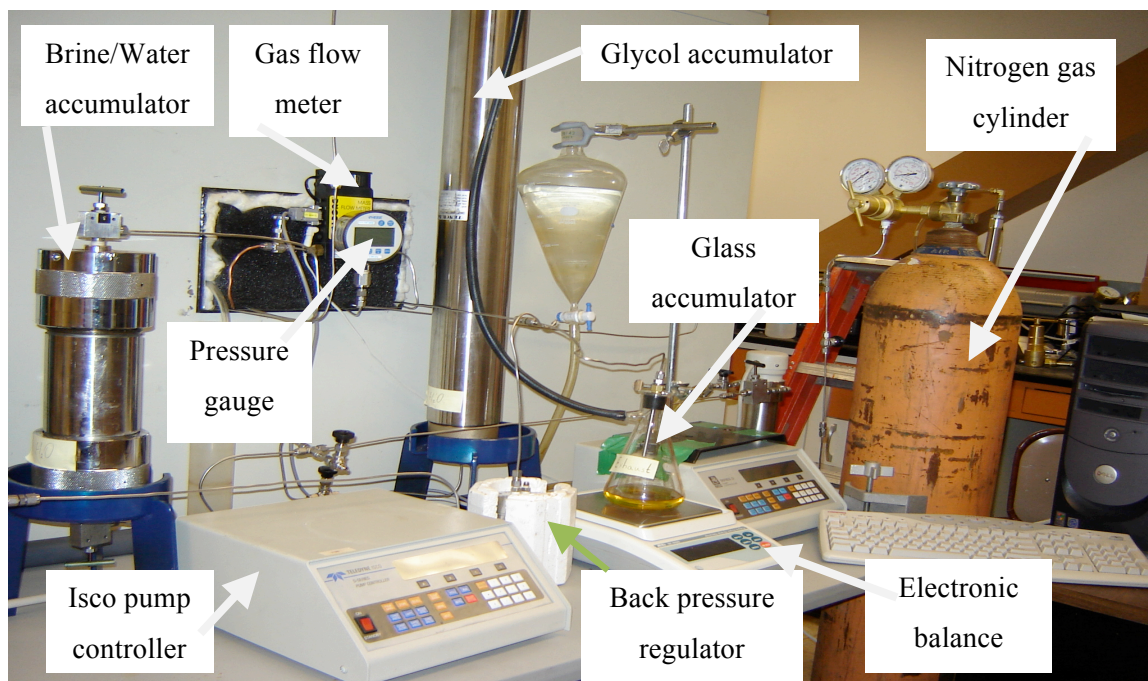


Fig. 3 External pictorial representation of the experimental setup.

Experimental Procedures

Flow experiments were carried out on six representative Umiat core plugs (see section 4 for details), according to the different steps that are briefly described here. All core plugs were cleaned, dried, dimensioned, 100% saturated with representative brine samples and dry and weight masses measured from which their porosities were determined. Following brine saturation, core plugs were flooded with brine at a flowrate of $5.0 \times 10^{-9} \text{ m}^3/\text{s}$ (0.3 ml/min)

under a confining pressure of 3447.38 kPa (500 psi) at 22°C. The stabilized pressure obtained during this flood, core dimensions and brine viscosity is used to determine the absolute permeability from Darcy equation (these are the values reported in Table 2). Subsequently, the core plugs were flooded with oil (kerosene) at the same flowrate and confining pressure to irreducible water saturation (S_{wi}) and again using the stabilized pressure drop, core dimensions and oil viscosity the effective permeability to oil at S_{wi} is determined. The S_{wi} values were determined using volume as well as mass balance, which showed good agreement. In the final step, core plugs are placed back inside the core holder and gas (nitrogen) injection procedure begins at constant flow rate as an unsteady state displacement process. Gas flowrates in the range of 8.0×10^{-9} to 2.75×10^{-6} m³/s (0.008-2.75cm³/s) were used for different core plugs. Cumulative oil production, cumulative gas injection, gas flow rate and pressure differential across the core plug are recorded every 2 seconds by the electronic balance and the gas flow meter. The recorded data are transferred to the computer and processed according to the JBN method. Gas injection process ends at residual oil saturation. The above described steps are repeated at the freezing conditions of -10°C.

Core and Fluid samples

Core samples. Conventional core samples from Umiat well #11 were collected from the Geological Materials Center repository, Eagle River, Alaska. With the intention to find samples from high quality reservoir sands, core samples with potentially high porosity and permeability were selected based only on visual observations of grain size and sorting due to the absence of engineering tools on site. Altogether eight core samples were selected representing Ninuluk, Chandler, Upper Grandstand and Lower Grandstand formations present in Umiat well #11. Figure 4 shows the lithology log of well #11 and the core samples taken from each formation.

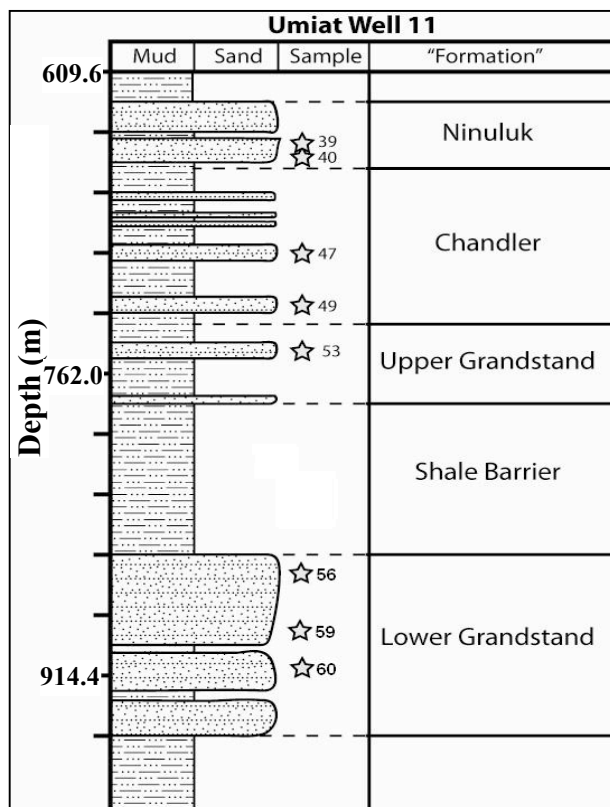


Fig. 4: Lithology log of Umiat well 11 showing the location of core samples (Shimer, G, 2010).

All cores had the diameter of 0.0778 m (7.78 cm) and lengths in the range of 0.0818 to 0.1349 m (8.18 to 13.49 cm). Depth of the samples ranges between 647.39 and 912.27 m (2124 and 2993 feet). All cores were visually inspected and their vertical and horizontal permeabilities were measured using a probe permeameter. Six core plugs each having a diameter of 0.0381 m (1.5 inch) were cut from conventional core samples and are numerically identified as 40, 49, 53, 39, 47 and 60. These core plugs were employed in the relative permeability experiments. Core 59 collapsed during the cutting process and core 56 was considered unsuitable due to high fracture density.

Fluid samples. Three different formation water samples were reconstituted in the lab according to the composition data from Umiat well #11 which are presented in Table 1.

Table 1. Water analyses from Umiat well 11 (Collins, 1958).

Water compositions (ppm)	Test 8 723.6-734.9 m	Test 9 745.8-750.1 m	Test 11 863.2-868.7 m
Barium	-	1	-
Calcium	30	8	14
Magnesium	9	3	4
Sodium	2190	2030	2190
Carbonate	96	390	126
Bicarbonate	2960	3120	2240
Sulfate	21	28	19
Chloride	1600	865	1950
Total solids	6906	6434	6543
Specific gravity at 60 ⁰ F	1.004	1.003	1.003

Based on these data, water composition from Test 8 was used for the core plugs drilled from the cores 40, 49, 39, and 47, while the water compositions from Test 9 and Test 11 were used for core plugs cut from the cores 53 and 60 respectively. Upon preparation, water samples were filtered in order to avoid clogging of the core plugs while conducting the flow experiments on them.

Sufficient volumes of representative oil samples from Umiat were not available hence kerosene was used as a substitute oil phase in all the core flooding experiments. Additionally, kerosene has a very low freezing point (less than -30°C), thus precluding the potential of freezing during the low temperature core floods.

Nitrogen was used directly from a gas tank to conduct the gas flooding tests.

Fluid properties. Density and viscosity of the formation water or brine and kerosene samples at the representative test temperatures were measured by the Anton-Paar densitometer (DMA-4500) and viscometer (AMVn) respectively. Formation water densities and viscosities for the three samples ranged from 1002-1003 kg/m³ and 1.15-1.16 mPa.s respectively at 22°C, whereas kerosene density was 780 kg/m³ and viscosity was 1.15 mPa.s (22°C) and 1.78 mPa.s (-10°C). Nitrogen viscosity was 0.0176 mPa.s at 22°C (not measured). Freezing point for each water sample was also determined by placing it at 0°C inside the Tenney chamber and subsequently reducing the temperature by 1°C until the sample froze. These values for the formation water samples ranged from -3 to -5°C (accurate to within ±1°C).

Results and discussion

This section presents the results obtained in this study on routine (porosity, absolute permeability, irreducible water saturation) and special (relative permeability, capillary pressure) core analyses of the tested Umiat core plug samples. These results are discussed in the subsequent section.

Routine core analysis

The results from routine core analysis for all the tested samples are presented in Table 2. The values obtained in this work are also compared with the ones reported by Baptist (1960) for Well 11.

Table 2. Routine core analyses results for the tested Umiat cores.

Core plug #	40	49	53	39	47	60	
Depth (m)	650.1	725.7	748.3	647.4	700.7	912.3	
Length of core plug (m)	0.055	0.042	0.034	0.054	0.042	0.032	
Depth range for Baptist data (m)	649.2-652.3	723.9-726.9	No data	646.2-649.2	699.5-704.1	No data	
This work ϕ (%)	12.65	16.1	14.75	12.83	17.23	12.97	
Baptist ϕ (%)	11.1-14.7	14.2-23.3	No data	12.4-14.7	13.6-19	No data	
This work K_{abs} (m ²)	9.2×10^{-16}	3.96×10^{-15}	6.55×10^{-13}	4.45×10^{-16}	2.73×10^{-14}	4.03×10^{-16}	
Baptist K_{abs} (m ²)	<4.93- 61.2×10^{-16}	0- 2.57×10^{-15}	No data	2.57- 6.12×10^{-15}	<4.93- 740.2×10^{-16}	No data	
This work S_{wi} (%)	Mass balance	41.1	41.7	42.5	34.3	43.4	39.5
	Volumetric	39.8	37.3	38.8	32.2	42.1	36.2
Baptist S_{wi} (%)	No data	26-50	No data	? to 32	15-49	No data	

The data shown in Table 2 indicates that our measurements on porosity, absolute permeability and irreducible water saturation fall within the ranges reported by Baptist in 1960. Additionally, the volumetrically and gravimetrically determined S_{wi} values reported in this work are in good agreement indicating the reliability of these measurements.

Special core analysis

The gas-oil relative permeabilities calculated by the JBN method from the data collected during the core flooding experiments for core 40 (as an example) are given in Table 3 at both 22°C (K_{ro} and K_{rg}) and -10°C ($K_{ro(ice)}$ and $K_{rg(ice)}$). Depending on experimental conditions these values are given at different liquid saturations (S_{Liq}) because the total liquid saturation at any time step depends on gas injection flowrate as well as on phase status of irreducible water. The gas-oil relative permeability data for core 40 are also presented graphically in

Figure 5 and 6. The results as seen in Figure 5 were consistently obtained for all the tested samples (not shown here, but presented in Godabrelidze, 2010); a significant reduction in both the gas as well as oil relative permeabilities was observed due to freezing of the interstitial water.

Table 3: Oil and gas relative permeabilities for core 40.

S_{Liq} (%)	K_{ro} (dimensionless)	K_{ro} (ice) (dimensionless)	S_{Liq} (%)	K_{rg} (dimensionless)	K_{rg} (ice) (dimensionless)
100.00	478×10^{-3}	290×10^{-3}	100.00	0	0
80.16	387×10^{-3}		80.16	133×10^{-5}	
78.97		234×10^{-3}	78.97		508×10^{-6}
78.15	288×10^{-3}		78.15	291×10^{-5}	
74.67	206×10^{-3}		74.67	418×10^{-5}	
73.98		117×10^{-3}	73.98		156×10^{-5}
72.03		939×10^{-4}	72.03		178×10^{-5}
70.10		705×10^{-4}	70.10		199×10^{-5}
69.32	101×10^{-3}		69.32	564×10^{-5}	
68.14		572×10^{-4}	68.14		204×10^{-5}
67.50	833×10^{-4}		67.50	613×10^{-5}	
66.46		457×10^{-4}	66.46		214×10^{-5}
62.53	402×10^{-4}		62.53	653×10^{-5}	
58.74	213×10^{-4}		58.74	725×10^{-5}	
57.17	100×10^{-4}		57.17	742×10^{-5}	

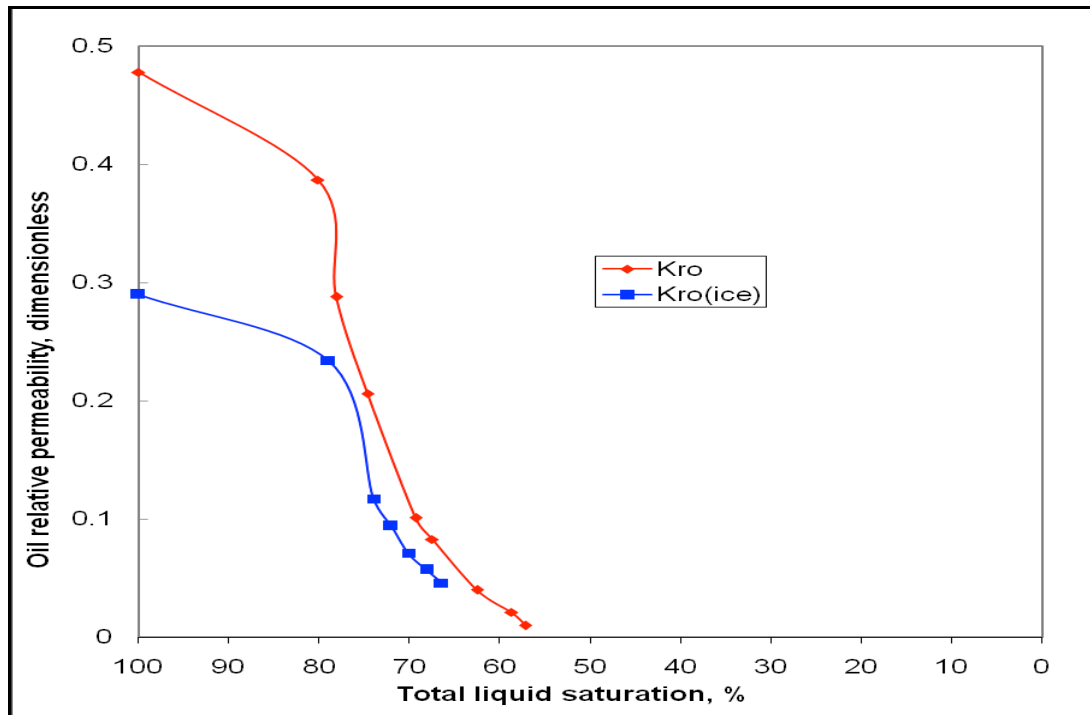


Fig. 5: Oil relative permeabilities at 22°C (Red) and -10°C (Blue) for Umiat Core 40. Note – base permeability is absolute.

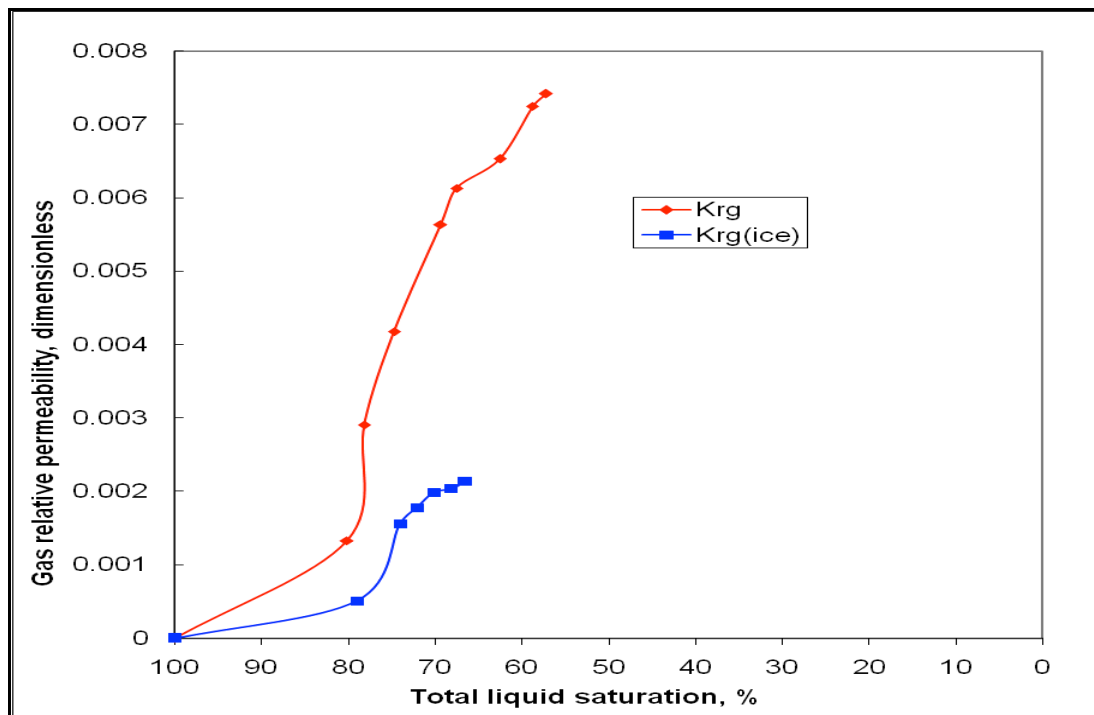


Fig. 6: Gas relative permeabilities at 22°C (Red) and -10°C (Blue) for Umiat Core 40. Note – base permeability is absolute.

Discussion

The results of the core flooding experiments exhibit the reduction of oil relative permeability at irreducible water saturation (which is same as oil relative permeability at 100% total liquid saturation, see Figure 5) for all six Umiat core plugs, caused by freezing of connate water. Table 4 shows the extent of oil relative permeability reduction for the studied core plugs, which is in the range of 39.3%-91.5% with an average decline of 60.97%. This average decline is significantly higher than the average 27% reduction obtained by the Federal Bureau of Mines studies (Baptist, 1960). So the average decline of relative oil permeability at irreducible water saturation has increased more than two times by changing temperature from -3.3°C (Baptist, 1960) to -10°C (this work), see Figure 7.

Table 4: Reduction in oil relative permeability at S_{wi}

Core #	K_{ro}	$K_{ro}(\text{ice})$	Reduction in K_{ro} , %
40	478×10^{-3}	290×10^{-3}	39.3
49	622×10^{-3}	128×10^{-3}	79.4 [1 st run] 62.0 [2 nd run]
53	453×10^{-3}	196×10^{-3}	56.7
39	714×10^{-3}	335×10^{-3}	53.1
47	568×10^{-3}	480×10^{-4}	91.5 [1 st run] 83.8 [2 nd run]
60	450×10^{-3}	244×10^{-3}	45.8

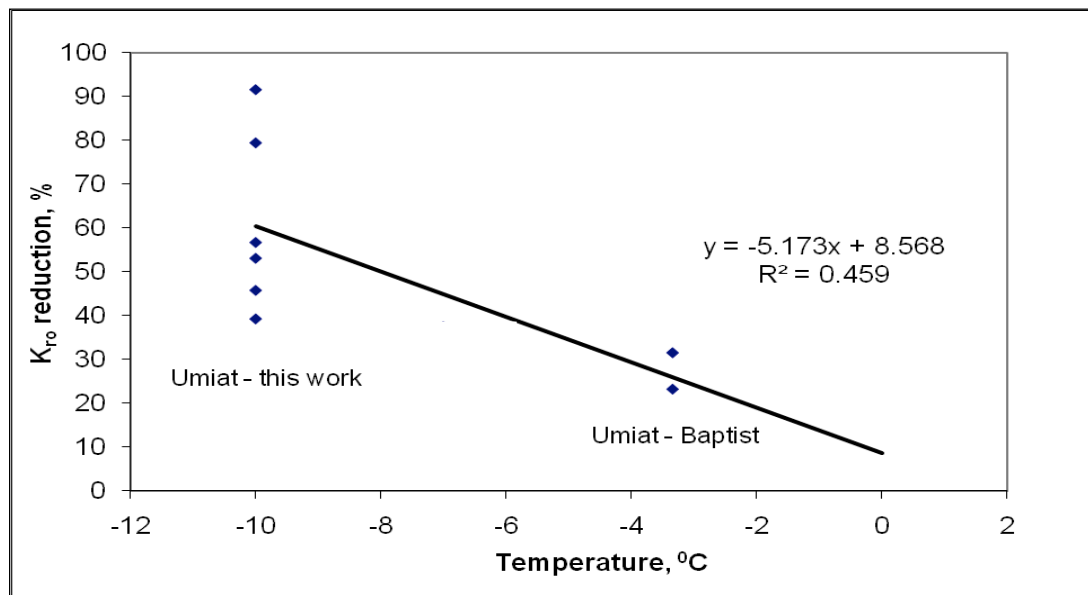


Fig. 7: Relationship between the freezing temperature and oil relative permeability reduction.

In order to better analyze the results obtained in this study, the oil relative permeability reduction was also plotted against absolute permeability and irreducible water saturation.

These plots are shown in Figures 8 and 9 respectively and also include data obtained by Baptist in 1960.

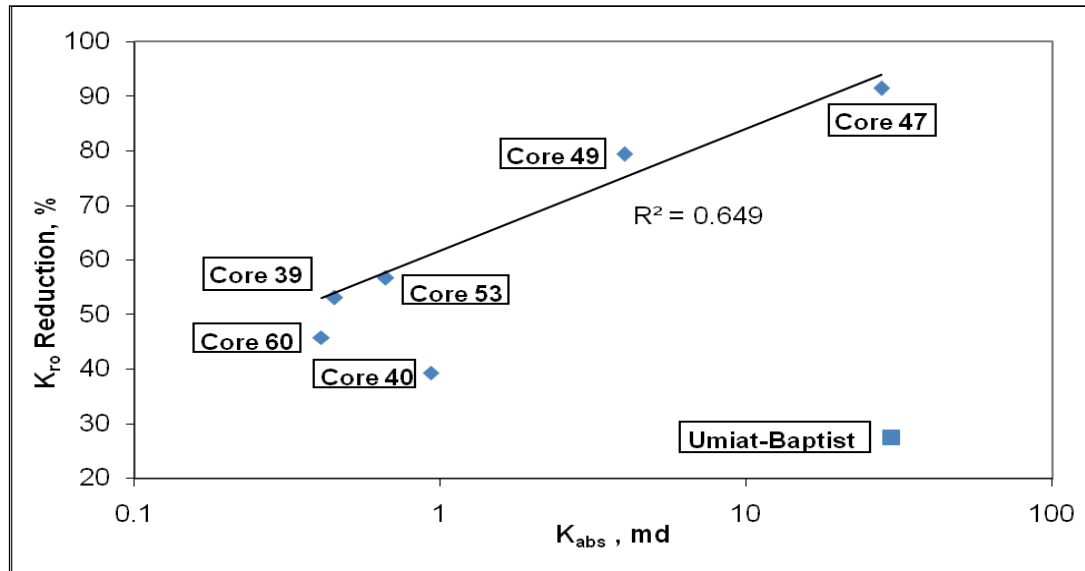


Fig. 8: Relationship between the absolute permeability and oil relative permeability reduction.

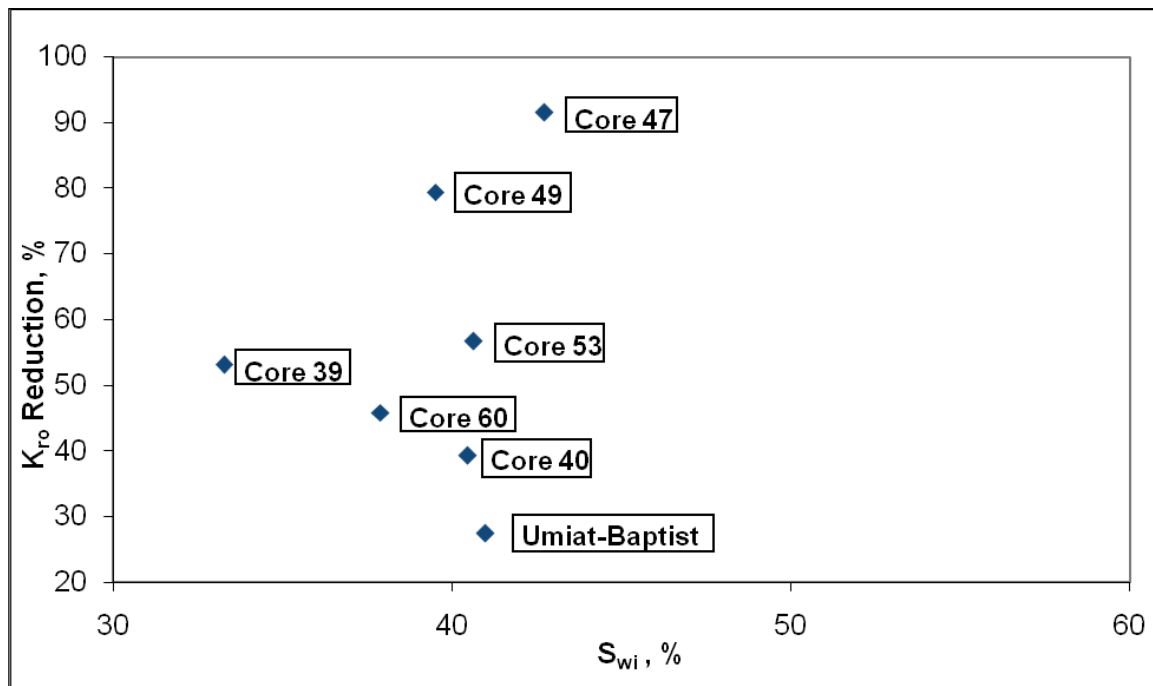


Fig. 9: Relationship between the irreducible water saturation and oil relative permeability reduction.

As seen in Figure 8, the data does show some scatter and indicates a weak correlation between reduction in K_{ro} and absolute permeability. However, excluding the data points on

Baptist's core and core 40, the correlation is somewhat stronger and shows increasing reduction in effective oil relative permeability with increasing absolute permeability. Hypothetically, the core plugs with higher permeabilities most likely have larger pores and pore-throats which results in smaller water-to-ice ratios (Smith and Low, 1996). Therefore, at the same temperature the core plug with higher permeability will have lower unfrozen water content and the reduction of oil relative permeability will be greater. However, this needs to be verified by core imaging techniques.

The plot of irreducible water saturation and reduction in oil relative permeability shows significant scatter. As a matter of fact Baptist appropriately commented on this based on just two core samples that he tested, noting that freezing results in about 9% volume expansion thus correspondingly increasing the "magnitude" of S_{wi} . This increased S_{wi} then results in additional constriction of connections between the pore spaces, in a way "cementing" them, which causes a dramatic reduction in K_{ro} (Baptist, 1960). However, the effect of S_{wi} on reduction in K_{ro} should not be considered in isolation but together with other key rock properties such as porosity and absolute permeability.

Godabrelidze (2010) also measured the capillary pressures for three of the core plug samples (47, 53 and 60) using mercury injection, in order to characterize the pore size distribution (PSD), because this in turn influences the amount of unfrozen water in the pore spaces. The PSD revealed that in all three core plugs a significant portion of total pore volume consists of medium-size pores, about 58% for core 53 with pore radius range of 0.69-2.13 μm , 54% for core 47 with pore radius range of 1.59-3.14 μm and 40% for core 60 with pore radius range of 0.2-0.5 μm . Based on the correlations proposed by Andersland and Ladanyi (2004), Godabrelidze (2010) also determined the amount of unfrozen water as a function of temperature for two different types of soils, i.e., Fairbanks silt and West Lebanon gravel that represent relatively smaller and larger pore sizes respectively. At -10°C, the unfrozen water content in Fairbanks silt was found to be more than 2%, whereas it was less than 1% for West Lebanon gravel. This qualitative and quantitative comparison is indicative of the fact that relatively larger the pore size the smaller the unfrozen water content, which will have a direct impact on the fluid permeability (reduction). Therefore, as far as the relation between pore size distribution and oil relative permeability reduction is concerned, obviously the average radius of medium-size pores is very important because, medium-size pores constitute a high portion of total pore volume. Consequently, larger pores (and therefore in core 47 which has the biggest average radius of medium pores) will have a lower unfrozen water content, which explains the fact that the highest reduction of oil relative permeability occurs in core 47, see Table 4. Applying the same logic, the higher reduction of oil relative permeability in core 53 compared to core 60 was quite predictable.

Conclusions

Experimental study was undertaken on six representative core plugs to investigate two-phase fluid flow properties both at room temperature and at simulated permafrost conditions for Umiat porous media. The experiments were successful in generating unique gas-oil relative permeability data for frozen rocks, which the authors believe to the best of their knowledge, is the first such data ever published in the open literature on flow through porous media. The following key conclusions can be made based on the findings of this work:

1. The routine core analysis data obtained in this work compares favorably with the one reported by Baptist (Baptist, 1960) for similar Umiat cores.
2. For all six Umiat core plugs, oil relative permeability declines on an average by 61% as a result of freezing irreducible water at -10°C .
3. Comparison between Baptist's data and the outcomes of this work suggests that lowering the temperature of porous medium significantly below 0°C results in further reduction of oil relative permeability.
4. Data obtained from this experimental study gives insights about the influence of absolute permeability, irreducible water saturation, and pore size distribution on oil relative permeability reduction. Although these correlations are somewhat weak, it can be observed that reduction in oil relative permeability tends to be higher for the core plugs which have higher absolute permeability, higher irreducible water saturation and higher average pore size radius. However, none of these factors should be considered separately; rather they should be considered in combination with others.

Effect of below 0°C reservoir temperature on relative permeability to oil: a theoretical and experimental approach

Introduction

In conventional oil and gas reservoirs reservoir temperature is of limited importance modifying only fluid properties such as viscosity, density etc. For heavy oil, reservoir temperature becomes increasingly important as the recovery strategy depends on decreasing the oil viscosity sufficiently to allow the oil to flow. For shallow reservoirs located in the permafrost, the reservoir temperature may also modify the pore structure through partial freezing of the water phase. Above 0°C, all of the water phase is considered to be liquid and, for a water wet system, exists as a film on the pore surface. For a reservoir temperature below zero, the issue is more complicated. Extensive research in soils (e.g. Anderson et al. (1971)) has shown that water can be in an unfrozen state until the ambient temperature reaches as low as -60°C. The experimental results derived by Christ et al. (2009) revealed that the amount of unfrozen water in silt decreased with decreasing temperature and stabilized at temperatures below -10°C. The fraction of the water phase that is frozen and its location in the pores may exert a strong control on the relative permeability to oil.

The occurrence of unfrozen water in porous media below can be attributed to some or all of the following phenomena

- Salts present in the water
- Surface melting on pore walls reduces free energy.
- Capillary forces due to the location of the water in a porous media

As water freezes, it expands by approximately 9%. This in itself reduces the pore space available for the oil and decreases the oil saturation thereby reducing the relative permeability to oil relative to standard conditions.

Kleinberg et al. (2004) performed an NMR experiment on two samples taken from a sandstone reservoir and a mud stone reservoir at below 0°C temperatures and allowed them to thaw to 18°C. His experiments showed that the unfrozen water was in contact with the grain surface, while the ice tended to reside in the interior of the pore space. As the temperature increased, ice was shown to melt in successively larger pore spaces (Kleinberg et al., 2005). The location of ice in the center of the pores would tend to act as an obstruction to flow, decreasing the relative permeability to oil. Additional surface tension effects as oil moves over ice might also magnify this effect.

The aim of this study is to better understand the factors which reduce the relative permeability to oil for a frozen reservoir. The better we can quantify the extent to which temperature, salinity, fraction of ice formed and ice-oil surface tension affect the relative permeability to oil, the better we can devise production strategies to overcome the impaired relative permeability.

Experimental Approach

This study investigates the effect of temperature on relative permeability to oil as a function of salinity in Berea sandstone cores. Berea sandstone was used as the base material because of its frequent use in core studies. We hope to be able to leverage some of those studies to better understand our own results.

Basic Rock and Fluid Properties

The absolute permeability and porosity of the two cores was measured using a conventional setup at room temperature with kerosene as the non wetting phase. Air-permeability tests were also made on these samples using a probe permeameter.

Viscosity measurements were performed on the kerosene at each experimental temperature using a Brookfield viscometer.

Relative Permeability to Oil

In order to determine the sensitivity of relative permeability to oil with temperature and salinity, a set of core flooding experiments was performed at the following temperatures 23°C, 0°C, -5°C, and -10°C using a cold chamber on two clean Berea sandstone cores. The cores used are cylindrically shaped, 6 inches in length (L) and 1.4 inches in diameter. These experiments were performed in the conventional way except for placing in a cold chamber with a controlled temperature. The original set of experiments used deionized water. Additional experiments were performed with water salinities of 6467 ppm and 5626 ppm. These were chosen based on the salt composition of Umiat formation water, a known oil reservoir located in the permafrost in Alaska (Table 1).

Table 1. Water Sample Salt Composition (Collins, 1958)

Used salts	Salinity #1 g/6L	Salinity #2 g/6L
Calcium Chloride (CaCl ₂)	0.11	0.09
Sodium Sulfate (Na ₂ SO ₄)	0.25	0.13
Sodium Bicarbonate (NaHCO ₃)	25.78	21.63
Sodium Chloride (NaCl)	8.4	4.91
Magnesium Chloride (MgCl ₂)	0.07	0.11
Calcium Carbonate (CaCO ₃)	0.02	.02
Sodium Carbonate (Na ₂ CO ₃)	4.11	6.83
Magnesium Carbonate (MgCO ₃)	0.003	.003
Barium Carbonate (BaCO ₃)	0.009	.009
Total Salinity (ppm)	6467	5626

Freezing Point Depression due to solute and capillary pressure

Due to the addition of nine different salts to the pure solvent (water), the final solution had a lower freezing point than pure water. The depressions in the freezing points of saline water used for this study were calculated using

Equation 1

$$\Delta T = K_F \cdot m \cdot i$$

Where,

ΔT = Freezing point depression, K

K_F = Cryoscopic constant, K·kg/mol

For water, $K_F = 1.853$ K·kg/mol.

m = molality (mol solute per kg of solvent)

i = Van 't Hoff factor (number of ions per mole of solute)

The depression of the melting point by capillary forces is:

Equation 2

$$\Delta T = -T_m \frac{2\gamma_{si} \cos\theta}{\rho_s \Delta H_m D}$$

Where:

ΔT = Depression of the melting point, K,

T_m is the normal melting point, K,

γ_{sl} is the surface tension of the liquid water-ice interface, J/m²,

θ is the contact angle between ice and the pore wall,

ΔH_m is the enthalpy of melting per unit mass, J/kg,

ρ_s is the density of the solid, kg/m³, and

D is the diameter of the cylindrical capillary (Pore throat), m,

Using literature values,

$T_m = 273.15$ K,

$\Delta H_m = 3.34 \times 10^5$ J/kg,

$\rho_s = 916.2$ kg/m³.

The surface tension of the water–ice interface is $\gamma_{si} = 3.2 \times 10^{-2}$ J/m² and $\Theta = 0$

Capillary Pressure

A Pycnometer experiment was performed on Core 1 at room temperature to estimate capillary pressure with respect to wetting phase saturation (air). The resulting capillary pressure curve can be transposed into a pore size distribution function.

Theoretical Approach

In an attempt to separate out the effect of the structural placement of ice in the center of the pores from interfacial tension effects etc, we use a modified Kozeny -Carman model which allows us to estimate how large the ice in the center of the pore would have to be to have the same impact on the relative permeability to oil as we observe in the experiments.

The commonly used Kozeny–Carman equation assumes that the pore structure can be represented by a series of N parallel tubes of given radius b where τ is the tortuosity giving rise to a permeability k .

Equation 3

$$k = b^2 \frac{\phi}{8\tau^2} = \frac{N}{A\tau} \frac{\pi b^4}{8}$$

Dvorkin (personal communication, 2010) proposed an modified Kozeny–Carman equation which we adopt for the below 0°C case where the effective pore structure can be modeled as a concentric tube with a solid kernel which we assume to represent the structural placement of ice in the pores

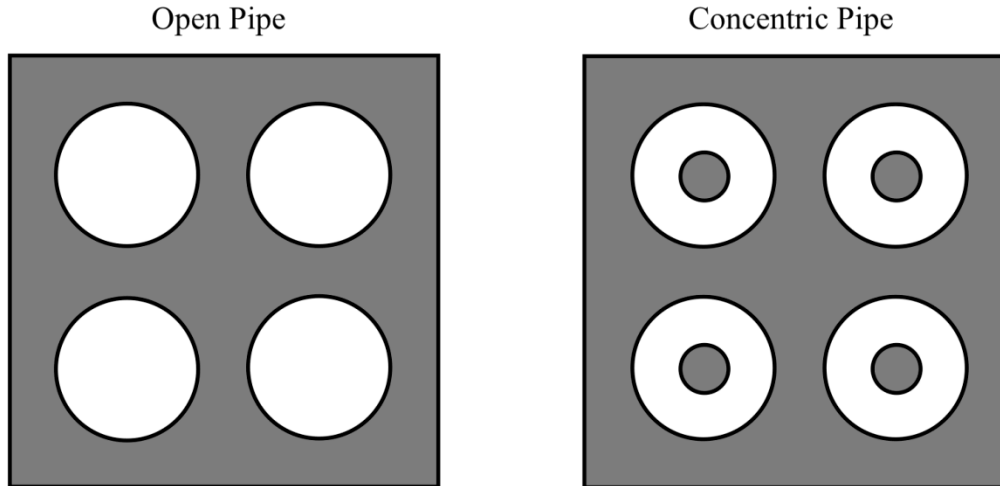


Figure 1 Schematic of Open and Concentric Pipe

In applying the modified Kozeny-Carman equation, we assume the following:

1. Water upon freezing occupies the center of the pore.
- Kleninberg (2004) indicated that the unfrozen water is in contact with the grain surface, and ice tends to reside in the interior of the pore space.
2. The average pore radius calculated from capillary pressure measurements can be used as the open tube radius
 3. The only mobile phase in the interstices of the pore is oil.
- Since the relative permeability to oil has been determined at the irreducible wetting-phase saturation. The mobility of unfrozen water should be zero.
4. Tortuosity does not change.

In fact we would expect tortuosity to increase with the presence of ice in the pore space but we are unable to separate the effects of this from the presence of ice in the pores. Our aim with the theoretical approach is to separate structural effects, of which tortuosity is one, from interfacial effects.

Flow through a concentric pipe (Dvorkin)

Consider the flow of fluid through a pipe of radius 'b' with a concentric pipe of radius 'a'. For boundary conditions: $u = 0$ at $r = a$ and $r = b$, the fluid velocity is given as

Equation 4

$$u = -\frac{1}{4} \frac{dP}{dx} b^2 \left[\left(1 - \frac{r^2}{b^2} \right) - \left(1 - \frac{a^2}{b^2} \right) \frac{\ln(b/r)}{\ln(b/a)} \right]$$

Upon integration on both sides, from the definition of volumetric flow rate

Equation 5

$$q = -\frac{\pi}{8\mu} \frac{\Delta P}{l} b^4 \left(1 - \frac{a^2}{b^2}\right) \left[1 + \frac{a^2}{b^2} + \left(1 - \frac{a^2}{b^2}\right) \frac{1}{\ln(a/b)}\right]$$

The total flux through N pipes is given as,

Equation 6

$$Q = Nq = -N \frac{\pi}{8\mu} \frac{\Delta P}{l} b^4 \left(1 - \frac{a^2}{b^2}\right) \left[1 + \frac{a^2}{b^2} + \left(1 - \frac{a^2}{b^2}\right) \frac{1}{\ln(a/b)}\right]$$

Resulting in the following equation for permeability

Equation 7

$$k = -\frac{N}{A\tau} \frac{\pi b^4}{8} \left(1 - \frac{a^2}{b^2}\right) \left[1 + \frac{a^2}{b^2} + \left(1 - \frac{a^2}{b^2}\right) \frac{1}{\ln(a/b)}\right]$$

The porosity of the block is

Equation 8

$$\phi = \frac{N\pi(b^2 - a^2)l}{AL} = \frac{N\pi(b^2 - a^2)\tau}{A}$$

Resulting in the modified Kozeny-Carman equation

Equation 9

$$k = -\frac{\phi}{8\tau^2} b^2 \left[1 + \frac{a^2}{b^2} + \left(1 - \frac{a^2}{b^2}\right) \frac{1}{\ln(a/b)}\right]$$

Equation 3 represents the flow of fluid through the porous media before freezing. Equation 9 represents the flow of fluid through a frozen porous structure. The value of b has been determined using the Mercury Pycnometer experiment, and value of 'a' for each salinity will be calculated using Equation 9 and substituting the observed reduced relative permeability to oil.

Results

Capillary Pressure

The capillary pressure data for Core 1 is shown in Figure 2. The average pore radius is calculated using a volume weighted average method. The average pore radius was calculated to be $1.60 \mu\text{m} \pm 0.004 \mu\text{m}$. The distribution of pore sizes based on the capillary pressure data is shown in Figure 3.

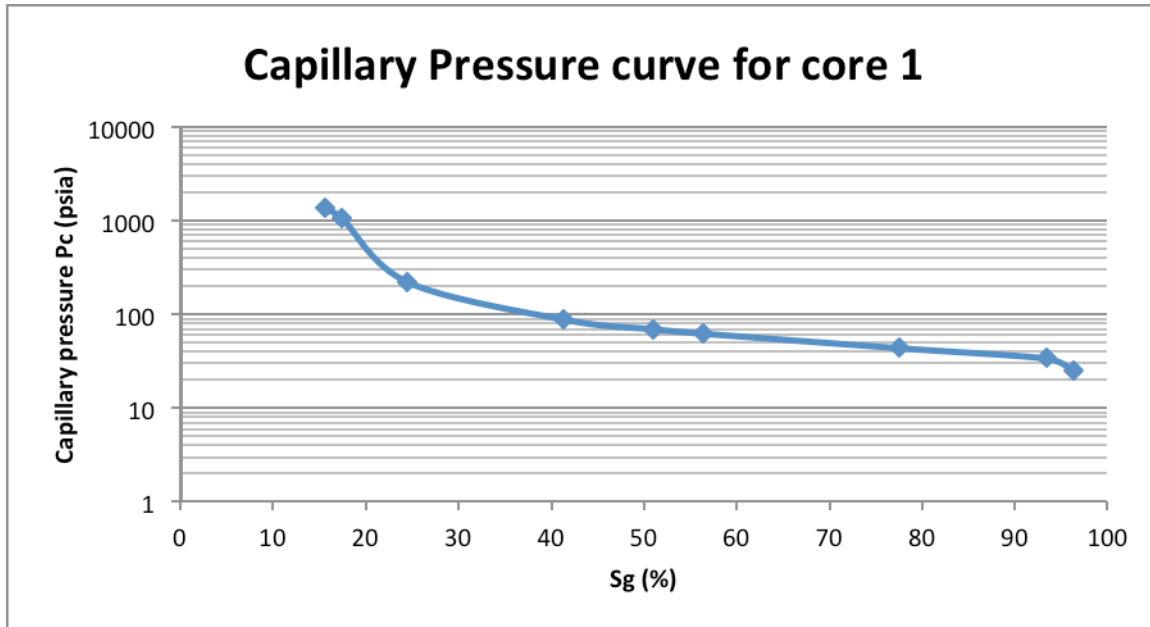


Figure 2 Air-Hg Capillary Pressure Curve for Core 1

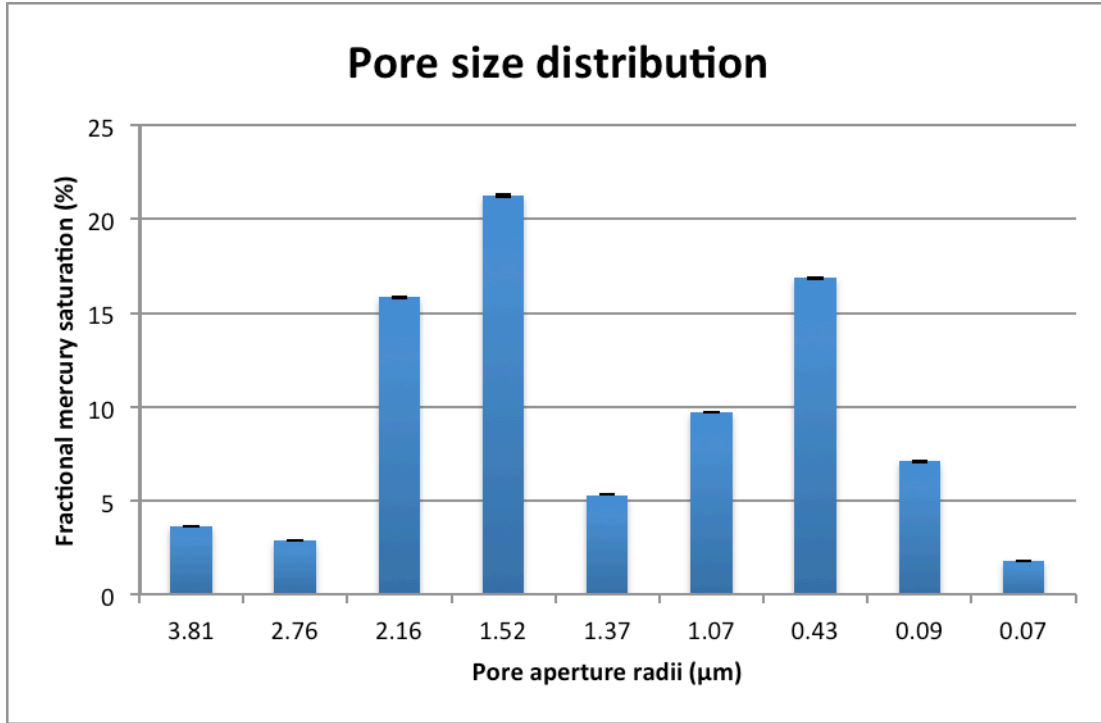


Figure 3 Pore Size Distribution corresponding to Capillary Pressure curve for Core 1

Theoretical Approach

Several calculations were made to determine the radii of ice formed within the center of the pore. The radius of the open tube was assumed to be equal to the volume weighed average radius derived from the capillary pressure curve transform, 1.60 μm . The effective permeability to oil for each salinity were also used as inputs. The results for the radius of ice kernel formed upon freezing of interstitial water of different salinities at -10°C are listed in Table 2.

Table 2 Radius of ice kernel assuming only structural effect for Core 1 at -10°C

Salinity (ppm)	Radius of ice kernel formed within the center of the pore (μm)
0	0.145± 0.004
5626	0.098± 0.004
6467	0.069± 0.004

The size of ice formed within the center of the pore decreased as salinity increased in the water sample.

Frozen/Unfrozen Water Ratio

Depression in freezing point due to solutes:

Depression in freezing point of salinity 01, $\Delta T_F = -1.92^\circ\text{C}$.

Depression in freezing point of salinity 02, $\Delta T_F = -1.71^\circ\text{C}$.

Depression in freezing point due to capillary pressure:

Table 3 shows the depression in freezing point values at each incremental increase in pressure used in the capillary pressure experiment.

Pc air-Hg(psi)	Pore radius (μm)	ΔT_F ($^\circ\text{C}$)
25	3.81	0.007
34	2.76	0.01
44	2.16	0.013
63	1.52	0.019
70	1.37	0.02
89	1.07	0.027
223	0.43	0.07
1067	0.09	0.32
1372	0.07	0.41

Table 3 Freezing Point Depression due to Capillary pressure in Core 1

Basic Rock and Fluid Properties

Vertical air permeability of Core 1 and Core 2 were respectively 187 md and 180 md.

Core	Porosity (%)	Absolute permeability (mD)	K_{ro} at S_{wirr}	Irreducible Water Saturation (%)		
				Deionized (0 ppm)	Salinity 1 (6467 ppm)	Salinity 2 (5626 ppm)
Core 1	18.9	134.1	?	$53.7 \pm <1$	$50.4 \pm <1$	$50.4 \pm <1$
Core 2	20.7	153.3	?	$51.7 \pm <1$	$51.7 \pm <1$	$51.7 \pm <1$

Table 4 Basic Properties for Core 1 and Core 2

Effect of temperature on relative permeability to oil

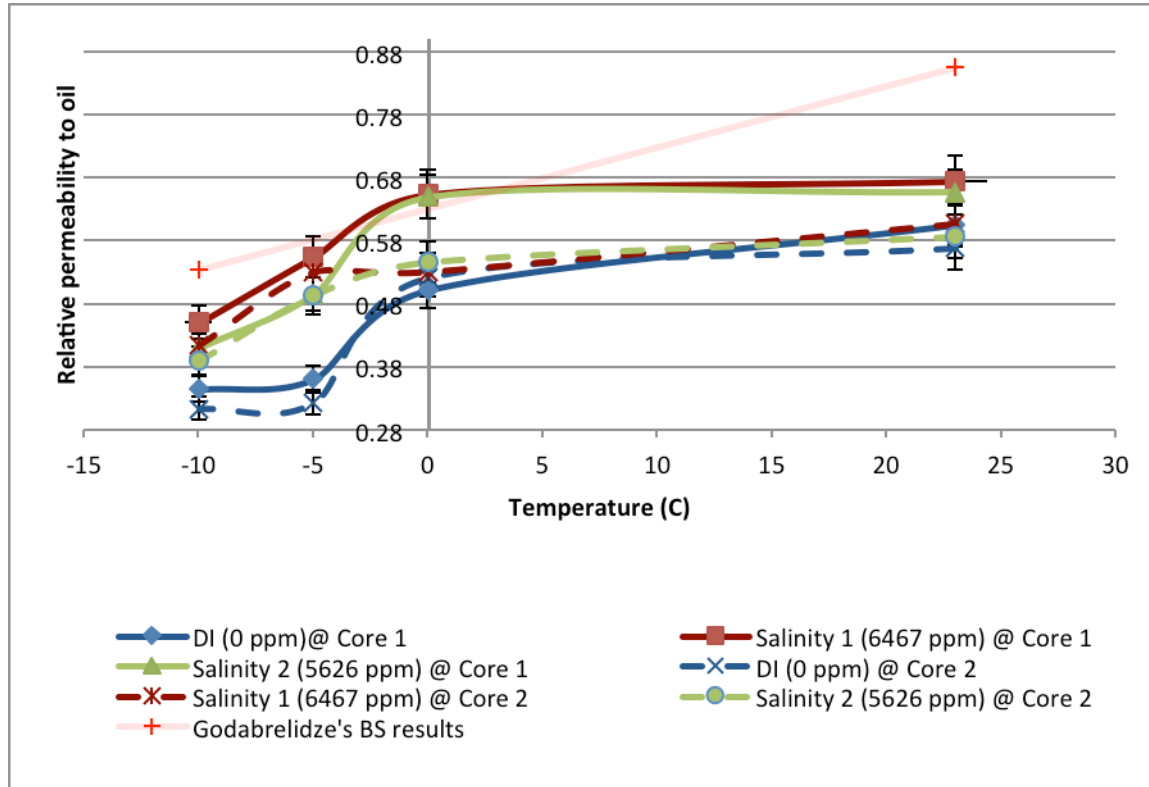


Figure 4 Relative Permeability to oil vs temperature as a function of salinity

Table 5 presents the percentage decreases in relative permeability for both of the cores. Percentage reductions in the relative permeability to oil were calculated for all three salinities, taking values from 23°C as the reference point (Table 8).

Deionised Water

Core 1 with deionised water case showed a reduction of 40.5% ($\pm 5.94\%$) at -5°C and 43.2% ($\pm 5.94\%$) at -10°C relative to room temperature conditions.

Salinity 1

Core 1 with salinity 1 case showed a reduction of 17.8% ($\pm 5.94\%$) at -5°C and 33.3% ($\pm 5.94\%$) at -10°C relative to room temperature conditions.

Salinity 2

Core 1 with salinity 2 case showed a reduction of 24.5% ($\pm 5.94\%$) at -5°C and 37.5% ($\pm 5.94\%$) at -10°C relative to room temperature conditions.

Table 5 Percentage reduction in relative permeability to oil with temperature

Temperature °C	Reduction in Relative Permeability to oil relative to room temperature (%)		
	Deionized	Salinity 1	Salinity 2
Core 1			
23	-	-	-
0	17.1±5.94	3.1±5.94	1.0±5.94
-5	40.5±5.94	17.8±5.94	24.5±5.94
-10	43.2±5.94	33.3±5.94	37.5±5.94
Core 2			
23	-	-	-
0	8.3±5.94	12.5±5.94	6.9±5.94
-5	43.2±5.94	12.6±5.94	15.9±5.94
-10	44.9±5.94	31.7±5.94	33.6±5.94

Effect of salinity on relative permeability to oil

The effect of salinity on relative permeability to oil is analyzed in two cases. Case 1 investigates the effect of salinity from 23°C to 0°C, and Case 2 investigates the effect of salinity from 0°C to -10°C.

Effect of salinity from 23°C to 0°C:

For Core 1, a reduction in relative permeability of 17%, with an uncertainty of 5.94%, was observed for deionized water (Table 5). For the same temperature range, the reduction was observed to be 3% for Salinity 1 (6467 ppm) and 1% for Salinity 2 (5626 ppm) (Table 5). Even factoring in error bars, reductions in relative permeability for deionized water were much larger than those for the saline water. This means that relative permeability values of deionized water do not overlap the values of saline water.

Core 2 differs from Core 1 above 0°C, with the trends of all salinities overlapping each other (Table 5). In relative permeability to oil, deionized water showed a reduction of 8.3% ($\pm 5.94\%$), Salinity 1 (6467 ppm) showed a reduction of 12.5% ($\pm 5.94\%$), and salinity 2 (5626 ppm) showed a reduction of 6.9% ($\pm 5.94\%$). Factoring in their error bars, these three salinities overlap each other.

Effect of salinity from 0°C to -10°C:

For Core 1 at -10°C, a maximum reduction of 43.2% ($\pm 5.94\%$) was observed for deionized water. A minimum reduction of 31% was observed for Salinity 1 (6467 ppm) (Figure 3). Core 2 showed a reduction of 44.9% for deionized water and a reduction of 31.7% for Salinity 1 (6467 ppm).

Discussion

Experimental Considerations

Irreducible water saturation of more than 50% was observed due to the unstable displacement characteristic of kerosene. The kerosene used in the experiment had low viscosity at room temperature, too low to adequately push the water out of the core sample. Thus, the irreducible water saturation showed a higher value than it normally would.

Figure 3 illustrates that, regardless of salinity, relative permeability values tend to decrease with temperature from 23⁰C to 0⁰C. Since the effect of decreased oil viscosity is already accounted for, we suspect that the decrease may be due to an increase in interfacial tension.

Another anomalous behavior that needs to be addressed is the relative permeability values of the deionized water of Core 1 shown in Figure 3. The reason for divergence of the curve of deionized water with the values of saline water can be explained by core's irreducible water saturations. Table 4 shows the values of connate water saturations of different salinities. For Core 1, S_{wi} of saline water is 50.7%, whereas S_{wi} of pure water is 53.7%, which indicates the increased mobility of oil phase in the case of saline water. Thus, the relative permeability to oil values for saline water were more than those for deionized water. Therefore, relative permeability values in case of deionized water did not overlap with the relative permeability values for saline water (unlike Core 2). Core 2 has the same connate water saturations for all salinities.

Relative permeability to oil below 0°C

The experimental data indicate that relative permeability to oil generally decreases with decreasing temperature.

Fluid Saturation

The first parameter that could alter relative permeability directly is fluid saturation. If the wetting phase (water) saturation increases, the relative permeability of the non-wetting phase (oil) normally decreases. If the frozen water is considered as water phase, then the net water phase saturation increases as the temperature decreases. Consequently, the non-wetting phase (oil) saturation decreases concurrent with a reduction in relative permeability.

Salinities

The salinity trends follow what we would expect given the freezing point depression associated with solutes. At -5°C, the greater decreases in relative permeability to oil are seen for the deionized water case which would presumably have a larger frozen fraction than the saline cases which have the benefit of a freezing point depression of -1.92°C for 6467 ppm and -1.71°C for 5626 ppm.

We might expect that the maximum reductions in relative permeability should be observed for a temperature which combines the effect of the maximum capillary pressure and the effect of solutes for the respective salinities, but in contrast, we observed continuity in reductions even below the freezing temperatures, Figure 3. This phenomenon indicates the presence of unfrozen

water even below the theoretical freezing point of the in situ water. A possible reason for this could be that water freezes first at the center of the pore, expelling salts that may exist in the pore water. This would cause unfrozen water closer to the particle surfaces to have a higher concentration of salts than previously existed and a lower freezing point.

Discussion of theoretical approach

In general, rocks with large pores have low irreducible water saturations and therefore a relatively large amount of pore space available for the flow of fluids. This condition allows high relative permeability end points to exist. Correspondingly, rocks with small pores have high irreducible water saturations that leave little room for the flow of hydrocarbons. This condition creates low values of oil relative permeability.

In a frozen reservoir, larger pores are occupied by ice, leaving only a narrow path for the flow of fluids. Early freezing of water in larger pores is mostly due to lower values of capillary pressure. This results in lower values of relative permeability. Smaller pores tend to be ice free due to their higher capillary pressures. Moreover, pore throats are certainly smaller in size compared to the average pore size obtained from capillary measurements. These pore throats are also occupied by unfrozen water.

Conclusions

The main aims of this study were to investigate the reasons for reduction in relative permeability to oil and to propose a possible production mechanism for frozen reservoirs. Core flooding experiments were performed on two clean Berea sandstone samples to examine the behavior of relative permeability with respect to temperatures 23°C, 0°C, -5°C, and -10°C and salinities of 0 ppm, 6467 ppm, 5626 ppm.

Continuous reduction in relative permeability was observed for both cores with reduction in temperature from 23°C to -10°C for all three salinities. The magnitude of the reduction in relative permeability was inversely related to water salinity. At -10°C, the reduction in relative permeability could be modeled as a kernel of ice of radius 0.069 μm for 6467 ppm saline water versus a radius of 0.145 μm for deionized water residing in tube of radius 1.6 μm . Other factors affecting reductions in relative permeability to oil were fluid saturation and pore structure.

Efficacy of saline water and antifreeze as flooding fluids in a frozen reservoir

Introduction

For reservoir temperatures below 0°C, conventional secondary recovery techniques such as water flooding need to be carefully examined. This study considers a range of flooding fluids which might be used to maintain pressure in the reservoir. Deionized water, saline water (6467 ppm) and antifreeze (60% ethylene glycol (EG) + 40% water) were used as injection fluids in a conventional flooding experiment designed to estimate ultimate recovery.

Experimental Method

The core was initially saturated with water initially and then flooded with oil (kerosene) until the pressure differential (ΔP) across the core stabilized. The core was then flooded with one of the test fluids until no further production of oil was observed. This process was repeated for temperatures 23°C, 0°C, -5°C, and -10°C for each test fluid. The collected volume of oil at each temperature was measured and tabulated.

Results

For each fluid tested, recovery factors were calculated based on the amount of oil recovered with respect to total oil saturation of the pore volume. Table 1 and Table 2 show recovery factors for each flooding fluid for Core 1 and Core 2, respectively.

Table 1. % Oil Recovery for Core 1

Flooding fluid	Temperature (°C)			
	23	0	-5	-10
	Recovery factor %			
Deionized water	78	No Production	No Production	No Production
Saline water (6467 ppm)	78	57	No Production	No Production
Antifreeze (60% EG +40% water)	-	67	57	50

Table 2. % Oil Recovery for Core 2

Flooding fluid	Temperature °C			
	23	0	-5	-10
	Recovery factor %			
Deionized water	62	No Production	No Production	No Production
Saline water (6467 ppm)	62	50	No Production	No Production
Antifreeze (60% EG +40% water)	-	62	50	31

Discussion

The Umiat reservoir is located in shallow depths of 275 ft to 1,100 ft and has very low reservoir pressure of 50 psi to 350 psi (Baptist, 1960). The Umiat reservoir is an under saturated reservoir containing no aquifer support. The primary production mechanism for pressure support is supplemented by solution gas drive mechanisms that enabled the reservoir to produce for only 3 months. A lack of aquifer support and poor pressure support of the reservoir make the search for a best production mechanism necessary.

A U.S. Bureau of Mines report states that solution gas drive could result in sensible recovery factors of 29% and 45%. However, secondary recovery techniques are required to economize field development and production from low-pressure frozen reservoirs. One assumes that keeping the formation cold and stable would result in higher recoveries than to thaw and refreeze the formation through water injection. Based on this assumption, cold gas injection has been suggested by the U.S. Bureau of Mines as a secondary recovery mechanism in frozen reservoirs.

The common belief is that water injected into the formation tends to freeze and block the formation from further injection. Similarly, either gas or water injected above reservoir temperatures tends to thaw then refreeze the formation. This results again in freezing of the interstitial water. These factors improve the chances of producing reservoir with cold gas injection as a secondary recovery. Moreover, the abundance of gas on the North Slope also supports the idea of cold gas injection.

One of the challenges of a frozen formation is that its ice resides in the interstices of pores. Minimizing the blockage of pores due to freezing may resolve the problem of poor recovery, as stated by Baptist (1960). One aspect of the present study focused on production techniques using fluids other than cold gas. Fluids like deionized water, saline water (6456 ppm), and antifreeze (60% ethylene glycol or propylene glycol + 40% water) were used as flooding fluids for secondary recovery.

The performance of these flooding fluids and recovery factors are shown in Table 1 and Table 2. No production was observed in the case of deionized water for Core 1 and Core 2. This is solely because of freezing of the interstitial water below freezing temperatures. The idea of melting the existing ice and keeping the formation fluids unfrozen might result in good recoveries.

Consequently, saline water was used as a flooding fluid. Adding salts decreases the rate of freezing. The rate of melting is unchanged by the presence of these foreign materials, so melting occurs faster than freezing. When saline water was used as a flooding fluid, 57% of oil was recovered at 0°C. This was due to the salts melting the frozen water existing within the pores. When ice melts, a larger space becomes available for the flow of fluids. In addition, unlike deionized water, saline water does not freeze while flowing within the interstices of the reservoir. The higher viscosity value of this saline water as compared to deionized water at 0°C also helps in better recovery of oil. This encourages the use of saline water as an injection fluid for frozen reservoirs that have subsurface temperatures near 0°C. Depending on its salinity, saline water helps to keep interstitial water unfrozen until a certain temperature. For a particular concentration of salts, as the temperature decreases well below 0°C, salt begins to crystallize out of the solution (as NaCl₂.H₂O), until the solution completely freezes. Therefore, what is an appropriate flooding fluid for frozen reservoirs that have temperatures much lower than 0°C?

Further increase in the salinity concentration of salinity might be the answer. However, the selected concentration and components of the saline water must be a close match with the formation–water salinity. Flooding with antifreeze is another option. From Table 1 and Table 2, it is clear that with antifreeze (60% ethylene glycol +40% water) as a flooding fluid, the reservoir produces, even at much lower temperatures. At -10°C, we can see 50% and 31% recovery rates, respectively for core 1 and core 2 (Table 1 and Table 2). Like the ethylene glycol/water mixture, 60% propylene glycol/40% water is also a commonly used antifreeze mixture. Similar to saline water, these fluids melt the existing ice within the interstices and also keep the fluids unfrozen throughout the flooding process. These fluids provide a freer channel for the flow of fluids through the pores and pore throats by melting the frozen interstitial water. Water will not refreeze while these fluids reside in the formation.

These two fluids (60% ethylene glycol or propylene glycol and 40% water) are relatively cheap at \$0.50-\$0.90/lb (www.icis.com). They also possess a lowest freezing point of -54°C and can be considered best for flooding techniques.

The viscosity of these fluids is a major factor in determining the best production strategy. Viscosity profiles with respect to temperature of the ethylene mixture and propylene mixtures are shown in Figure 1.

The propylene glycol mixture showed a higher value of viscosity than the ethylene glycol mixture. Higher viscosity of propylene glycol mixture results in better flooding capability than does the ethylene glycol mixture. However, high-powered machinery certainly would be required to pump the propylene glycol mixture into the formation. The viscosity of ethylene glycol may be low enough to pump in a more cost-effective way. The low cost of these mixtures and their ability to replace oil even at -10°C, make it a better flooding fluids that should be considered as best production strategy for frozen reservoirs.

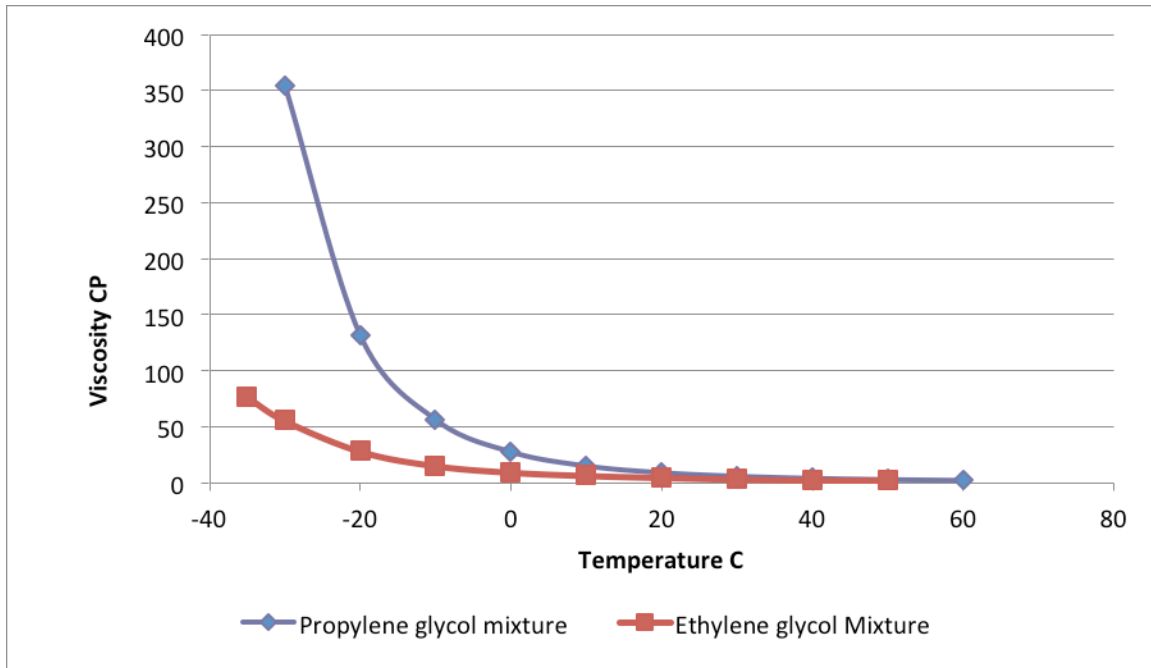


Figure 1. Viscosity vs. temperature profiles for a mixture of 60% ethylene glycol and 40% water and mixture of 60% propylene glycol and 40% water (Sahoo et al., 2009)

Baptist (1960) showed a recovery of 20% to 34% at -3°C using gas drive as a recovery technique for core samples that had a permeability of greater than 100 mD. The present study of production mechanisms showed nearly 50% recovery using saline water, and 60% recovery using antifreeze at -5°C for both cores. Further production is also observed at -10°C with a recovery factor of 50% for Core 1 and 30% for Core 2.

The main aim of the production strategy experiments was to explore the use of water injection, in the hope of using saline water as a flooding fluid (depending on formation temperature). Saline water could possibly melt the frozen interstitial water and provide higher recovery factors than those of cold gas injection. Thus, it is advisable to invest in saline water injection if the produced oil through water injection generates more revenue than cold gas injection.

Fluid Characterization and Phase Behavior Studies of Oil from Frozen Reservoir of Umiat Oil Field, Alaska¹

Introduction

Umiat is one of the light oil frozen reservoir located in arctic region of northwestern Alaska. It is the largest oil accumulating reservoir discovered on Naval Petroleum Reserve-4 of Alaska (NPR-4) during the initial exploration program conducted by Department of Navy, Office of Naval Petroleum and Oil Shale Reserves from 1944 through 1953 (Baptist, 1960). However, despite drilling 11 wells, the field was not developed during that period due to economic and technical challenges associated with it. According to the initial estimates recoverable reserves in the Umiat field ranged from 30 to over 100 million bbl with an average of 70 MMB of oil and 1.415 billion m³ (50 billion ft³) of gas (Baptist, 1960).

Even though Umiat field had such a great potential for oil and gas, it was never considered viable and its development was precluded because of the unusual reservoir conditions and challenges associated with it. It is very shallow reservoir with reservoir depths of 84-335 m (275-1100 ft) and most of the oil is in continuous layer of permafrost. The base of the permafrost ranges from 235-322 m (770-1055 ft). The reservoir pressures 344.7-2413.2 kPa (50-350 psi) and temperatures 266.5-274.8 K (20-35°F) are very low with small quantity 12.57 sm³/m³ (70.6 scf/stb) of solution gas (Baptist, 1960). However, the Umiat oil is high API gravity (36-37°API) and it is not bio-degraded despite being at very shallow depths, which allows it to flow even in a permafrost condition. The low reservoir pressure and GOR system contribute very limited in primary recovery and a secondary recovery mechanism will have to be introduced to maintain the reservoir pressure for optimal production. Even though the oil is high API gravity but it may behave like viscous oil under low temperature reservoir condition. Other EOR techniques such as thermal or VR-WAG (viscosity reducing water alternating gas) methods may also not be suitable for the Umiat field. If thermal methods are used then it would melt the permafrost, causing the potential collapse around the well-bore, and if VR-WAG is used then it would potentially freeze the water and reduce the permeability substantially. Additionally, the field is located far away from immediate oil transportation infrastructure such as the Trans Alaska Pipeline System (TAPS). The present challenges associated with developing or producing Umiat oil field are captured in Fig. 1.

¹ To be submitted to *Fluid Phase Equilibria*

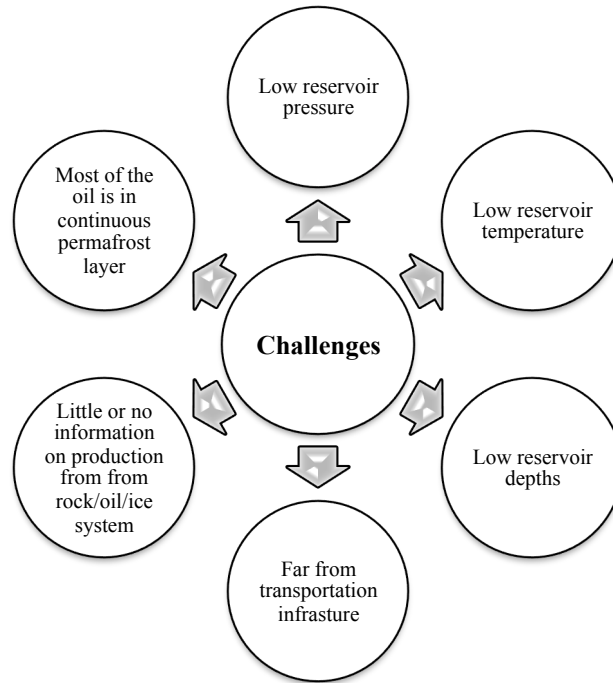


Fig. 1. Challenges associated with Umiat oil field development.

In 2006 and 2008, Renaissance Alaska, (Umiat leaseholders at the time) commissioned two different studies to undertake an independent overview of the technical and commercial aspects of Umiat oil field. Although both studies independently confirmed that Umiat is an attractive production target, production issues still need to be overcome. For economical development and to overcome the production issues of Umiat reservoir, a reliable full scale reservoir simulation model is required to study and investigate various EOR options to simulate oil under permafrost conditions and determining effective production strategy. Therefore, critical reservoir fluid properties and understanding of fluid phase behavior is essential to form the basis of the reservoir engineering model. Given the conspicuous lack of complete fluid characterization and phase behavior data on Umiat oil, the primary objective of this study is to characterize and quantify oil from Umiat reservoir experimentally and through EOS modeling, and henceforth provide the essential data for reservoir engineering model. Herein lies the purpose of this study. To the best of the authors' knowledge the type of comprehensive novel approach successfully adopted in this study has not been done and reported before and thus makes a unique contribution to the literature on petroleum reservoir fluid studies. This includes: to:

- (1) characterization of the weatherized old dead oil sample;
- (2) estimation of the amounts of the *missing/evaporated* light components;
- (3) synthetic recreation of the *pseudo representative* dead oil sample and subsequently the live oil sample;
- (4) performance of laboratory PVT studies on the live oil sample and modelling the fluid phase behavior using an EOS model;

Brief background and previous fluid studies on Umiat oils

Oil and gas samples were collected from the produced test wells of Umiat field. The collected oil sample from each well was analyzed by U.S. Bureau of Mines. From the fluid analysis, it was observed that the field contains light oil of 36-37.2°API, pour point in the range of 258.2 – 241.5 K (5°F to -25°F), and the Saybolt viscosity in the range of 36-44 seconds at 310.9 K (100°F) [2,3]. Umiat test well 8 (one of the wells drilled out of the total of 11) was considered for comparison purpose with the experimental values obtained through this study. According to the fluid analysis reported by Collins [2], oil from Umiat has specific gravity of 0.842 (36.6°API), Saybolt Universal viscosity of 36 seconds or 2.9 mPa.S (2.9 cp) at 310.9 K (100°F), and pour point of -25°F. Collins (1958) also reported distillation data of dead oil that shows the composition of each fraction at respective cut temperature and their measured specific gravities.

During production tests that date back to the 1940's and 1950's only small quantity of produced gas was observed with the oil by field personal, suggesting the absence of gas cap. Therefore, it was concluded that saturation pressure or bubble point of Umiat oil is the same as, or lower than, the reservoir pressure. The reservoir pressures were not accurately measured or predicted, but all the observed data from various tests indicate that the range of reservoir pressure is about 344.7 kPa (50 psi) in the higher upper sand to 2413.2 kPa (350 psi) in the lower sand near the oil-water contact (Baptist, 1960).

The only reservoir engineering PVT data, by far, was reported by Baptist in 1960, which included the solution gas-oil ratio (GOR) of 12.57 sm³/m³ (70.6 scf/stb) at the temperature of 269.3 K (25°F) and the bubble point pressure of 2261.5 kPa (328 psi).

In July 2008, historical atmospheric pressure oil samples of the Umiat field that were nearly 60 years old at the time of testing, were provided to Schlumberger Oilphase-DBR laboratory for density and viscosity measurements. These measurements indicated a significantly lower API gravity and viscosity 2-3 times higher when compared with the values reported in the previous government reports (Alaska Geologic Materials Center, 2008). Schlumberger (Alaska Geologic Materials Center, 2008) stated that the probable cause of this vast difference in the density and viscosity values is the likely vaporization of the light ends from the oil samples, or handling of the samples in a manner that would have elevated their density and viscosity. They concluded that the Umiat oil samples did not appear to be representative of the original oil and consequently, the measured analytical data are not considered to represent the fluid properties of the Umiat field accurately.

The foregoing clearly indicates that this level of knowledge of the characteristics of the Umiat oil is woefully inadequate for any type of reservoir engineering analyses, which is one of the main motivating factors behind this study.

Methodology adopted in the study

The dead Umiat oil sample of about $5 \times 10^{-5} \text{ m}^3$ (50 cm^3) was provided by the Alaska Geological Materials Center (GMC) repository, in a small plastic container. The provided oil sample was from well-5 and it was collected about 60 years ago. The preliminary task was to measure the initial fluid properties such as density, viscosity, molecular weight, and composition of chemical constituents present in the oil sample and compare them with all the available experimental data from previous studies.

After initial analysis and comparison with previous work, it was observed that the API gravity and viscosity (at 310.9 K or 100°F) of provided oil sample was lower and higher respectively when compared with the previous government reports, which was in agreement with the measurements reported by Schlumberger (Alaska Geologic Materials Center, 2008), thus again confirming severe weatherization having lost some of the lighter fractions. To further confirm this, the next step was to compositionally characterize the given oil sample by using simulated distillation by gas chromatography (GC). The analyzed composition by GC was compared with composition obtained by theoretical analysis using Pedersen's characterization method (Pedersen et al., 1989). For theoretical compositional analysis, specific gravity of original Umiat oil (36.6 °API) defined in literature (Collins, 1958) was considered as representative and molecular weight was calculated using the distillation data provided by Collins (1958); this essentially represents the properties of a C_{7+} fraction that is characterized using the Pedersen method. The comparison of the composition pointed out that some of the lighter fractions from the single carbon number (SCN) C_7 - C_{12} had been evaporated, which possibly resulted in the reduction of API gravity and increase in the viscosity of the GMC provided oil sample.

Therefore, given the non-representativity of the GMC sample and the lack of fresh dead oil samples from Umiat, a novel approach was employed to recreate the original/representative dead oil sample from given Umiat sample from GMC. Based on simple mass balance, the mass of each component that was potentially *lost* due to weatherization was estimated by comparing the GC measured and the Pedersen characterized compositions. The mass difference thus gave the amount of each evaporated lighter fraction required to be added to achieve the representative dead oil sample. The calculated volume for pure component (n-alkanes used in this case) of each evaporated lighter fraction was added to the given oil sample. The dead oil sample recreated in this manner was subsequently used for recombination with solution gas according to reservoir GOR to produce the live oil sample, as no such sample currently exists anywhere and there is no possibility of acquiring either new dead oil or live oil samples from Umiat in the near future. The experimental PVT studies were conducted on this laboratory created live oil sample. The experimental PVT and phase behavior studies were followed by EOS modeling to develop a tuned EOS model to predict the various reservoir fluid properties for reservoir engineering model. The flowchart provided in Fig. 2 depicts the general methodology adopted in this study, while the specifics of the experimental procedures, EOS modeling and results and discussions appear in the following sections.

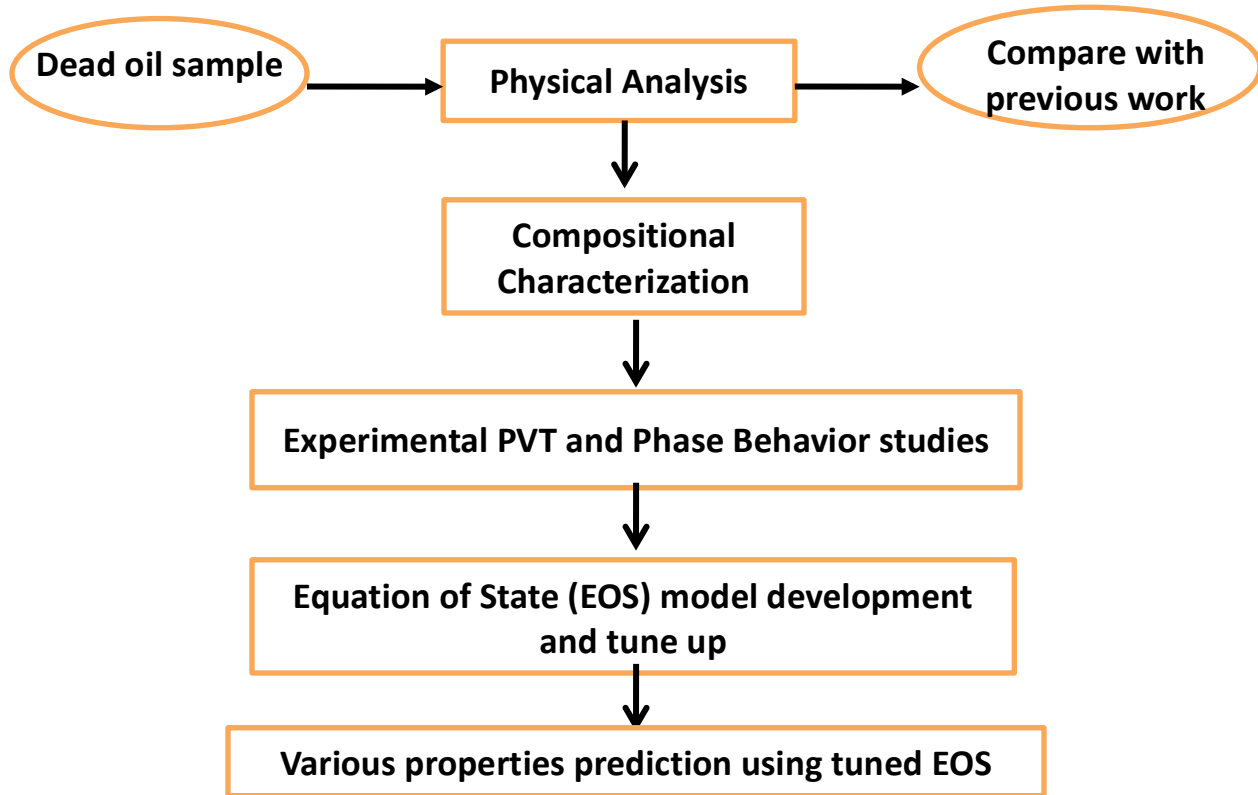


Fig. 2. Flowchart of the general methodology adopted in this study.

Overview of the experiments conducted and experimental set-ups and protocols

Overview of experiments conducted

As mentioned earlier, the provided oil sample was initially characterized both physically and chemically. Furthermore, to understand the fluid phase behavior and to simulate the oil in permafrost condition, it is necessary to measure the pressure-volume (PV) relationship at constant reservoir temperature condition. The representative dead oil sample was then recombined with Umiat gas of specified composition at reservoir GOR of $12.57 \text{ sm}^3/\text{m}^3$ (70.6 scf/stb) to achieve representative live oil sample.

The experiments performed for fluid characterization and phase behavior study consisted of:

- Measurement of physical properties of the GMC provided dead oil sample
- Compositional analysis of GMC provided dead oil sample using simulated distillation by gas chromatography
- Recreation of a physical *pseudo representative* Umiat dead oil sample and measurement of its physical properties
- Recombination of recreated dead oil and solution gas
- Constant composition expansion (CCE) of the recreated live oil sample to measure bubble point pressure at reservoir temperature

- Recreated live oil density and viscosity measurement at elevated pressures and reservoir temperatures using CCE

Experimental set-ups and protocols

The density and viscosity of the oil samples at atmospheric pressure and various temperatures were measured using the oscillating tube Anton-Paar densitometer (model no. DMA-4500) and rolling ball Anton-Paar Micro viscometer (model AMVn) respectively. Both units have the distinct advantages of requiring very small sample volumes, which was one of the limitations in this study. Prior to measuring the actual oil densities and viscosities, the DMA-4500 and AMVn were calibrated with reference fluids in the required measurement range. The recreated live oil densities at elevated pressures and reservoir temperatures were measured using the DMA 512 Anton-Paar densitometer in conjunction with the mPDS 1000 digital display processing unit. The DMA512 was calibrated using nitrogen and n-pentane in the desired measurement range. Cambridge scientific SPL-440 viscometer in conjunction with the ViscoPro 2000 digital display meter was used to measure viscosity of live oil sample at elevated pressures. The viscometer was factory calibrated; therefore viscosities of the reference standards were measured and found within acceptable range. The experimental set-up and procedures used for live oil density and viscosity measurements is described at the end of this section.

The molecular weight of the GMC dead oil sample was measured using the CRYETTE A apparatus which operates under the principle of freezing point depression. The unit was calibrated using a dilute solution of n-decane (molecular weight 142.28 kg/kg-mole) in benzene (solvent) of known concentration.

The GMC dead oil compositional analysis was performed on Thermo Electron Corporation Trace Ultra GC using simulated distillation (SimDist) technique that is used to produce boiling point distribution curves of petroleum fractions. The Trace GC is equipped with an oven, injector and detectors. It also has digital pressure flow control system to control the gas flow rate and pressure as specified. The data system is Chromo Quest 4.1. The ASTM D2887-04 method is used for the characterization of petroleum fraction having boiling point range between 328.15 K (131°F) and 811.15 K (1000°F) or carbon number fraction from C₆-C₄₄. Boiling point temperatures are related to the retention times through a calibration curve, obtained by running a standard mixture of hydrocarbons; generally n-alkanes under the same chromatographic conditions. For calibration of GC, various concentrations of solution were prepared by diluting "SUPELCO" ASTM D2887 quantitative calibration mix with methylene chloride solvent. All prepared different concentration solutions were run on GC and response of flame ionization detector (FID) was recorded on the chromatograms. The components and related peaks were identified using their retention time and area of each identified peak was calculated by Chromo Quest software. Average retention time calculated from all the calibration runs of each component present in calibration mix was correlated with its atmospheric equivalent boiling point (AEBP). Retention time range of single carbon number (SCN) fraction was calculated using the correlation obtained from the plot of AEBP vs. average retention time for AEBP range defined in generalized single carbon number property table (Katz and Firoozabadi, 1978). The wt% of the components in the unknown oil sample was calculated from the response factor of component calculated by calibration.

The recreated dead oil sample (procedure for obtaining this sample is described in the results and discussion section) was recombined with the Umiat gas in a floating piston accumulator per the GOR of $12.57 \text{ sm}^3/\text{m}^3$ (70.6 scf/stb) to produce the Umiat live oil sample. The Umiat gas composition that was reported in Masterson's work (2001) was used as recombination gas. Obviously, owing to the non-existence of the physical or actual samples of this gas, the specified composition (Masterson, 2001) was supplied to Air Liquide Gas Company who blended the gas sample matching this composition, which was used in the recombination process. The two compositions are compared in Fig. 3, which shows a very close match with average differences in the molar % compositions of less than 0.0035.

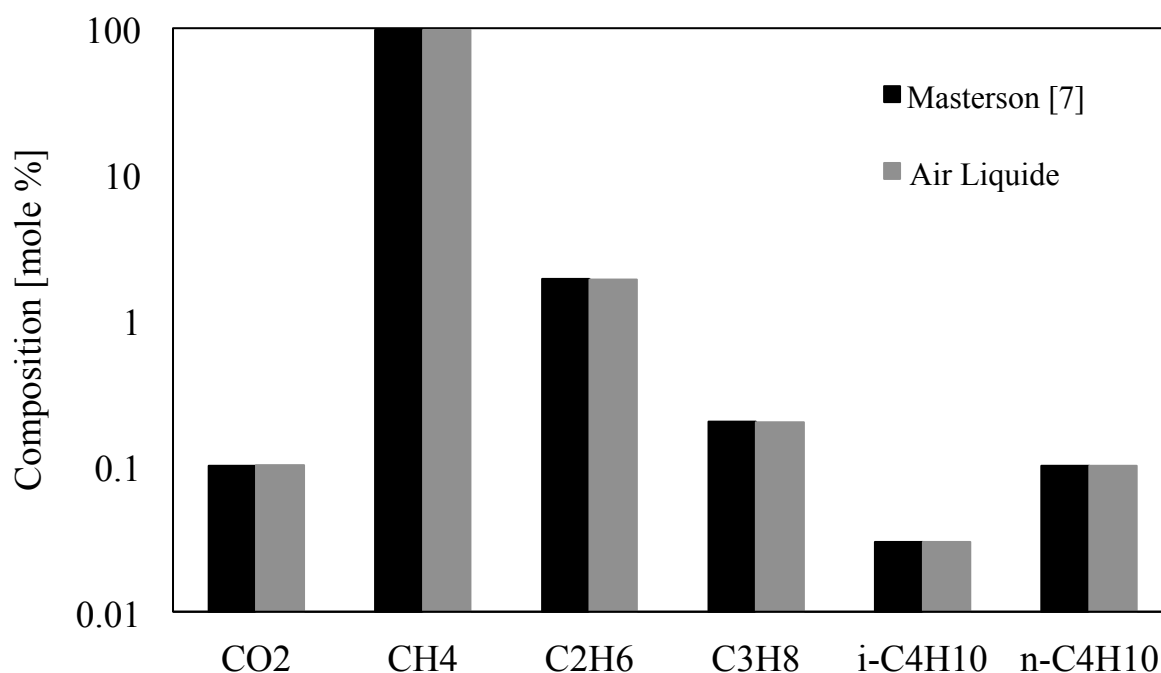


Fig. 3. Comparison of Umiat gas composition reported by Masterson (2001) and the blend prepared by Air Liquide.

The setup for conducting the CCE tests was designed and developed in this work and the schematic and the actual picture are shown in Figs. 4 and 5 respectively. The setup consists of a set of accumulators, a positive displacement pump, and constant temperature bath. Both the accumulators are capable of handling pressures up to 68,947.6 kPa (10,000 psi) and temperature up to 449.8 K (350°F), and having capacity of $25 \times 10^{-5} \text{ m}^3$ (250 cm³). The constant temperature bath is able to maintain subzero temperatures required specifically to mimic Umiat reservoir temperature conditions. The positive displacement pump is used to expand or contract the process side fluid volume of the accumulator 2. The volume and pressure readings are recorded by Pump LabView software at set time intervals. The entire setup was checked for any gas or liquid leaks using air and water as medium. The accumulators, pumps, gas cylinder etc. were connected using stainless steel tubing, Swagelok fittings, and valves. Oil recombination was carried out in accumulator 2 and the reconstituted oil sample was pressurized to 4136.8 kPa (600

psi) and the temperature was adjusted to the reservoir temperature of 269.8 K (26°F) and 273.15 K (32°F). The system was maintained at these conditions by using the constant pressure option on the ISCO pump in order to stabilize the sample to ensure single phase conditions on the basis of no change in the ISCO pump volume reading as a function of time. After stabilization of the system the sample was expanded upto 1241.1 kPa (180 psi) and bubble point pressures determined on the basis of the break in the pressure-volume curve.

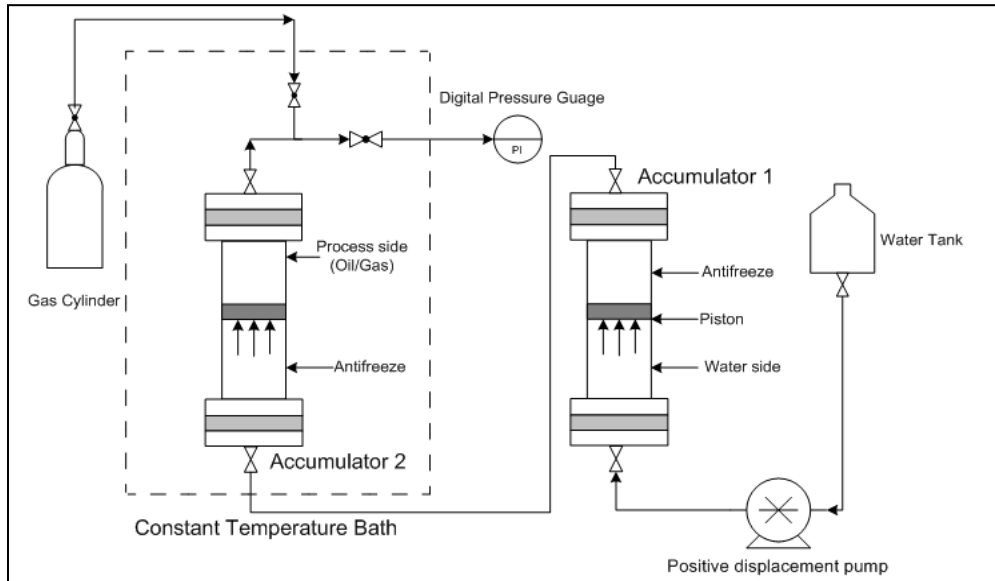


Fig. 4. Schematic of the experimental setup for conducting CCE tests.



Fig. 5. Picture of the actual experimental setup for conducting CCE tests.

The previously described CCE set-up was slightly modified to accommodate online densitometer and viscometer at the outlet of accumulator 2, for live oil density and viscosity measurements at elevated pressure conditions and reservoir temperatures. Figs. 6 and 7 respectively show the schematic and the actual picture of the set-up used for live oil density and viscosity measurements. As shown in the schematic, the entire system from outlet of accumulator 2 to outlet of viscometer was connected as one single closed system via the densitometer, thus allowing simultaneous measurements of both density and viscosity at the specific pressure and temperature.

Other specific elaborate details on the experimental set-up and protocol can be found in Shukla (2011).

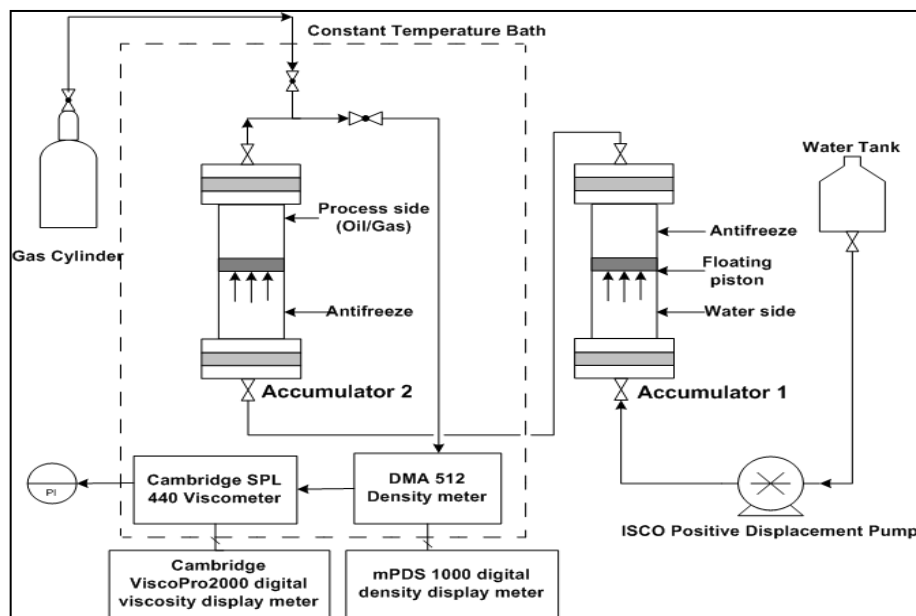


Fig. 6. Schematic of the modified CCE set-up for live oil density and viscosity measurements.

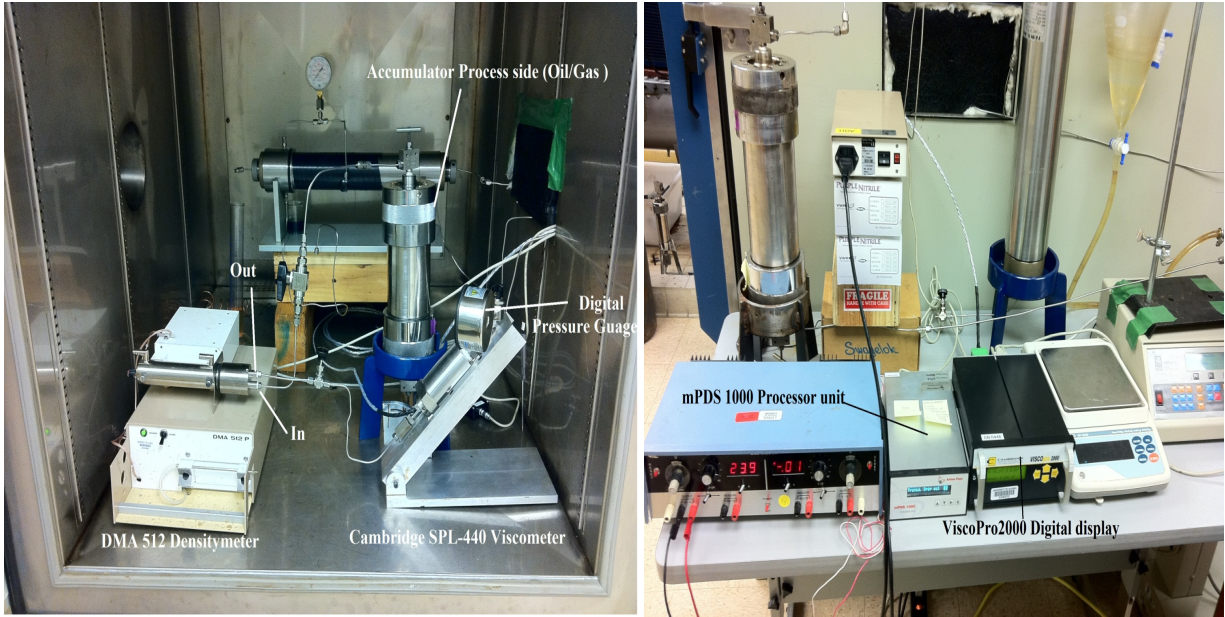


Fig. 7. Picture of the actual modified CCE set-up for live oil density and viscosity measurements.

Empirical equations for bubble point pressure estimation and equations of state (EOS) tuning

Empirical equations for bubble point pressure estimation

The bubble point pressure of Umiat oil was also estimated using correlations found in literature to compare with the experimental values. The correlations used are Standing (1947) and Vasquez and Beggs (1980) respectively.

Standing correlation [9]:

$$P_b = 18.2 \left[\left(\frac{R_s}{\gamma_g} \right)^{0.83} (10)^a - 1.4 \right] \quad (1)$$

Vasquez and Beggs (1980) correlation:

$$P_b = 29.782 \left[\left(\frac{R_s}{\gamma_{gs}} \right)^{0.8425} \exp \left[\frac{-20.161 \gamma_{API}}{T+460} \right]^a \right] \quad (2)$$

where, P_b is the bubble point pressure in psia; R_s is the solution gas-oil ratio in scf/STB; γ_{gs} is the solution gas gravity (dimensionless); $a = 0.00091T - 0.0125(\text{API})$; T is the temperature in $^{\circ}\text{F}$ and γ_{API} is the API gravity.

EOS model development and tuning

A compositional PVT simulator (WinPropTM), developed by Computer Modeling Group (CMG) was used for this study. The Peng-Robinson EOS (Robinson and Peng, 1978) was selected for simulating and predicting fluid phase behavior of Umiat oil. It is the most widely used EOS for various fluid types. The prediction of EOS cannot be relied upon directly and differs from experimental values due to insufficient characterization of plus fraction, inadequate hydrocarbon-hydrocarbon or hydrocarbon-non-hydrocarbon components interaction etc. Therefore to predict fluid properties and phase behavior accurately at different conditions, some amount of tuning of these EOS parameters is required to match the experimental data. The experimental values available for tuning were density and viscosity of recreated dead oil sample, bubble point pressures and live oil densities and viscosities above bubble point for reservoir temperatures of 269.8 K (26°F) and 273.15 K (32°F) respectively. In this study we used all the measured properties at 269.8 K (26°F) to tune the EOS model, which was later applied in a predictive mode to simulate differential liberation at 269.8 K (26°F) and all other calculations at 273.15 K (32°F) to generate the data required in reservoir simulation.

In EOS modeling, the plus fraction for Umiat oil was defined as C₁₈₊. As far as tuning is concerned, initially the bubble point pressure was matched, followed by the recreated live oil densities using Peneloux (Peneloux et al., 1982) volume translation techniques and finally the viscosity values were matched separately using modified Pedersen's viscosity correlation (Pedersen and Fredenslund, 1987). The viscosity correlation only affect molar volume, therefore EOS was unaltered while matching viscosity. Table 1 lists the various parameters selected for regression of experimental data and Table 2 shows the % change required to match the various experimental values.

Table 1. Parameters selected for EOS regression to match the experimental data at 269.8 K (26°F).

Experimental data	Parameters selected
Saturation Pressure/Bubble Point Pressure	Critical pressure (P _c), Critical Temperature (T _c), Acentric Factor (AF) of plus fraction (C ₁₈₊)
Density or volumetric data	Volume Shift (SH) C ₁₈₊ Modified Pedersen's Viscosity Correlation
Viscosity	MU1: MW mixing rule coefficient
	MU2: MW mixing rule exponent
	MU3: Coupling factor correlation coefficient
	MU4: Coupling factor correlation density exponent
	MU5: Coupling factor correlation MW exponent

Table 2. Percentage change in each EOS and viscosity correlation variable selected for regression at 269.8 K (26°F).

Variable	Initial Value	Final Value	% Change
P _c C ₁₈₊	1.3025E+01	1.4608E+01	12.16
T _c C ₁₈₊	8.6837E+02	9.1852E+02	5.78
AF C ₁₈₊	8.9006E-01	8.9006E-01	0.00
SH C ₁₈₊	1.2456E-01	1.2296E-01	-1.28
MU1	1.3040E-04	1.3062E-04	-23.31
MU2	2.3030E+00	2.3463E+00	-20.00
MU3	7.3780E-03	7.7701E-03	-20.00
MU4	1.8470E+00	1.4808E+00	-20.00
MU5	5.1730E-01	5.6410E-01	-4.85

Results and discussion

Physical properties of the GMC provided dead oil sample

The physical properties of the GMC dead oil sample measured in this work are presented in Table 3, which also compares the values measured by Schlumberger (Alaska Geologic Materials Center, 2008) and those reported by Collins (1958). Clearly, as the comparison shows, values measured in this study and by Schlumberger are quite similar, whereas those reported by Collins are much different; i.e., density, viscosity as well as molecular weight are high in the former while they are substantially lower in the latter thus indicating severe weatherization and loss of light ends over the period of 60 or so years that the sample had been stored.

Table 3. Comparison of physical properties of Umiat dead oil samples.

Property	This work (GMC provided Umiat dead oil sample)	Schlumberger (Alaska Geologic Materials Center, 2008)	Collins, 1958	This work (recreated Umiat dead oil sample)
Density at 288.7 K (60°F) and 101.3 kPa (14.7 psia)	877.8 kg/m ³ or 29.7°API	874.9 kg/m ³ or 30.2°API	842.0 kg/m ³ or 36.6 °API	836.0 kg/m ³ or 37.6 °API
Viscosity at 310.9 K (100°F) and 101.3 kPa (14.7 psia)	9.16 mPa.S	7.60 mPa.S	2.90 mPa.S	2.75 mPa.S (at 313.1 K)
Molecular weight (kg/kg-mole)	245.00	Not measured	184.17*	183.38**

* Estimated from the TBP distillation data provided in Collins, 1958.

** Not measured, but calculated from the molar composition of recreated Umiat dead oil sample.

GC analysis of the GMC provided dead oil sample

The composition of the GMC provided dead oil sample was analyzed using the GC which gave the individual component concentrations in wt% (obtained from areas) for SCN C_6 through C_{25+} (lumped). These compositions in wt% were converted to mole% using the generalized molecular weight and specific gravities (Katz and Firoozabadi, 1978) of SCN fractions C_6 through C_{24} , whereas for C_{25+} the values were back calculated using balance equations from the overall sample molecular weight of 245 kg/kg-mole and density of 877.8 kg/m^3 . The GC determined molar composition (normalized after excluding the C_6 , since Pedersen characterization starts with C_7) is shown in Fig. 8, which clearly indicates majority of components in the vicinity of the middle SCN range of C_{15} and a significant proportion of C_{25+} ; this is yet another evidence of the loss of lighter ends from the GMC dead oil sample.

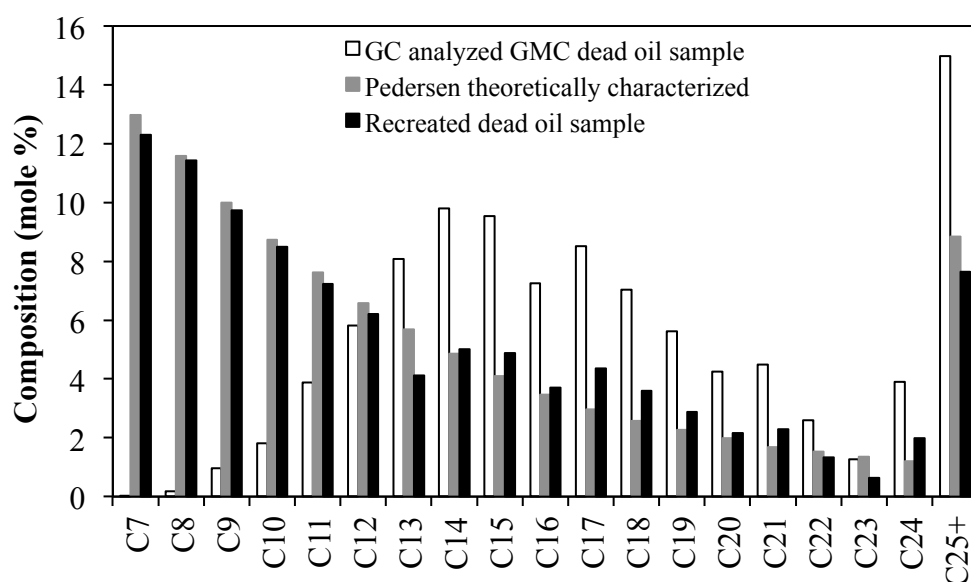


Fig. 8. Comparison of Umiat dead oil molar compositions.

Theoretical characterization of C_{7+} by Pedersen method

The Pedersen characterization method, as described by Danesh (1998) was applied to split the C_{7+} fraction. The C_{7+} molecular weight of $184.17 \text{ kg/kg-mole}$ and density of 842 kg/m^3 was used in the splitting calculations, as this was considered to be representative of the original Umiat dead oil. The splitting included SCN fractions from C_7 through C_{45} ; however, components from C_{25} through C_{45} were lumped as a C_{25+} fraction for comparison with the GC determined compositions. Again, generalized molecular weight and specific gravities (Katz and Firoozabadi, 1978) of SCN fractions C_6 through C_{45} were used in the calculation of C_{25+} molecular weight and specific gravity. The GC characterized composition is shown in Fig. 8.

C₂₅₊ molecular weight and specific gravity

The molecular weights of C₂₅₊ as determined for the GC analysis method and the Pedersen characterization methods were 374.07 and 405.64 kg/kg-mole respectively; i.e., a difference of less than 8%. Similarly the specific gravities of C₂₅₊ as determined for the GC analysis method and the Pedersen characterization methods were 1.0120 and 0.9097 respectively; i.e., a difference of about 11%. Ideally, in a perfect case, one would expect components C₂₅ and above due to their heavy nature to be relatively unaffected and thus resulting in similar molecular weights and specific gravities from both approaches since mass balances are applied. However, we consider the observed differences as reasonable and acceptable as they may be attributed to the severe weatherization of the GMC oil sample and to some extent given the approximate nature of the characterization method. The Pedersen characterized composition is compared with the GC composition in Fig. 8.

Estimation of the amounts of lost lighter ends from GMC provided dead oil sample

When the GC analyzed and theoretically determined compositions (both normalized to 100%) are compared (see Fig. 8), the differences in the compositions of SCN fractions C₇ through C₁₂ are readily noticed, i.e., the mole% of these components in the GMC provided dead oil sample are much less compared to the theoretically determined values and in particular they are orders of magnitude less for C₇ through C₉. However, when compositions of components C₁₃ through C₂₅₊ are compared, the opposite is the case, i.e., higher in the GMC sample than in the theoretically characterized; obviously this is to be expected because lower amounts of C₇ through C₁₂ will naturally increase the mole% of the heavier ones as all compositions are normalized to 100%.

Given the differences in the components C₇ through C₁₂, a simple component mass balance calculation was performed on both the compositions. The total volume of the GMC provided Umiat oil sample was converted to mass by using the measured density of 877.8 kg/m³. Using the compositions in wt% of the GMC provided dead oil sample, masses of individual components was calculated. Similar procedure was applied to the theoretically characterized composition, i.e., the same overall sample mass as earlier was used and compositions of all components in wt% was calculated (generalized SCN properties for C₇ through C₂₄ and C₂₅₊ molecular weight used was 405.64 kg/kg-mole) from which masses of individual components was obtained. The comparison of the masses of individual components in the GMC provided dead oil sample and the one characterized by the Pedersen method enabled the determination of the mass of each component, i.e., C₇ through C₁₂ that would be required to be added to the former in order to *makeup* or *compensate* for the evaporated light ends.

The individual masses obtained as described above were converted to volumes using the generalized SCN densities. Given the fact that there is no such thing as a SCN that can be readily ordered from a chemical supplier, we chose to use normal alkanes instead, i.e., n-heptane through n-dodecane and in any case the SCN fraction properties are somewhat biased toward paraffinicity. After determining the required volumes of n-heptane through n-dodecane, they were individually added to the GMC provided dead oil sample in order to recreate and achieve the *pseudo representative* Umiat dead oil sample for the remaining studies.

Composition and physical properties of recreated dead oil sample

After addition of n-heptane through n-dodecane, total masses of individual components SCN C₇ through C₁₂ were calculated (C₁₃ through C₂₅₊ remaining the same), which were converted to moles using generalized SCN molecular weights for C₇ through C₂₄, while the molecular weight of C₂₅₊ used was 374.07 kg/kg-mole. The individual component moles were then normalized to mole% in order to obtain the molar composition of the recreated dead oil sample, which is compared in Fig. 8. As seen in Fig. 8, by using the previously described methodology, we have successfully recreated a physical as well as a numerical *pseudo representative* Umiat dead oil sample, the composition of which matches very well with the theoretically characterized composition.

The density and viscosity of the recreated physical dead oil sample were also measured at a temperature of 288.7 K and 313.1 K respectively but at atmospheric pressure. These values are provided in Table 3, which are in close agreement with those reported by Collins (1958), with difference of 0.7% and 5% in density and viscosity respectively. We also computed the average molecular weight of the recreated dead oil sample based on the composition and the molecular weights of the SCN fractions and the C₂₅₊ fraction as described above, resulting in a value of 183.38 kg/kg-mole, which compares very well (difference less than 0.5%) with 184.17 kg/kg-mole estimated from the TBP distillation data provided in Collins, 1958. Clearly, this is yet another demonstration of successfully recreating a representative Umiat dead oil sample.

CCE of Umiat live oil sample

After achieving a representative Umiat dead oil sample, it was recombined with the solution gas to obtain a live oil sample. As part of the CCE test, the bubble point and density and viscosity of the live oil sample were measured at 269.8 K (26°F) and 273.15 K (32°F) respectively. The bubble points were determined using the break in the PV relationships. Two sets of bubble point measurement at single reservoir temperature were performed to check for repeatability and were found to be within 1%. Due to a relatively high compressibility volatile or lights oils typically to do not exhibit a sharp break in the PV curve, which makes it somewhat challenging to accurately determine the bubble point pressure, moreover in the case of Umiat oil this is further compounded by the significantly low solution gas.

After bubble point pressure measurement, live oil density and viscosity data were measured for single phase Umiat oil sample at two reservoir temperatures and at various pressures above bubble point. These results shown later follow the typical trend of increasing density and viscosity with increasing pressures. Similarly, when these values are compared at isobaric conditions, both density and viscosity slightly decrease with increase in temperature from 269.8 K (26°F) and 273.15 K (32°F).

Bubble point pressure estimation from empirical correlations and EOS modeling and tuning

The Standing correlation (Standing, 1947) and Vasquez and Beggs correlation (1980) were applied to estimate the bubble point pressures at 269.8 K (26°F) and 273.15 K (32°F), with gas

gravity computed from the molar composition of the Umiat gas (Masterson, 2001); API gravity of 37.6 based on the recreated dead oil sample and solution GOR of 70.56 scf/STB (Baptist, 1960). The estimated bubble point pressure values are compared with the experimentally determined values in Fig. 9, which show a reasonably good agreement with the latter lying between the two estimates. Also shown on this plot is the bubble point reported by Baptist at 269.3 K (25°F), which also compares favorably with other values.

Prior to tuning the PR EOS model, raw predictions of bubble point pressures were also obtained. The Umiat live oil fluid composition used in the raw predictions is shown in Table 4. Note that instead of C₂₅₊, the plus fraction was lumped to C₁₈₊. Default correlations available in WinProp™ were used for obtaining the critical properties and acentric factors of SCN fractions and C₁₈₊. The *untuned* PR EOS predicted bubble point pressures at the two temperatures are compared in Fig. 9, which again show a fairly reasonable match with the ones measured and estimated using correlations.

Table 4. Molar composition of recombined Umiat live oil sample.

Component	Mole %
CO ₂	0.010
CH ₄	10.215
C ₂ H ₆	0.199
C ₃ H ₈	0.021
i-C ₄ H ₁₀	0.003
n- C ₄ H ₁₀	0.010
C ₆	0.000
C ₇	11.064
C ₈	10.288
C ₉	8.760
C ₁₀	7.639
C ₁₁	6.499
C ₁₂	5.578
C ₁₃	3.713
C ₁₄	4.499
C ₁₅	4.383
C ₁₆	3.333
C ₁₇	3.913
C ₁₈₊	19.873
Total	100.000

Molecular weight of C₁₈₊ = 317.82 kg/kg-mole; specific gravity of C₁₈₊ = 0.915. Generalized SCN properties are used for C₆ through C₁₇.

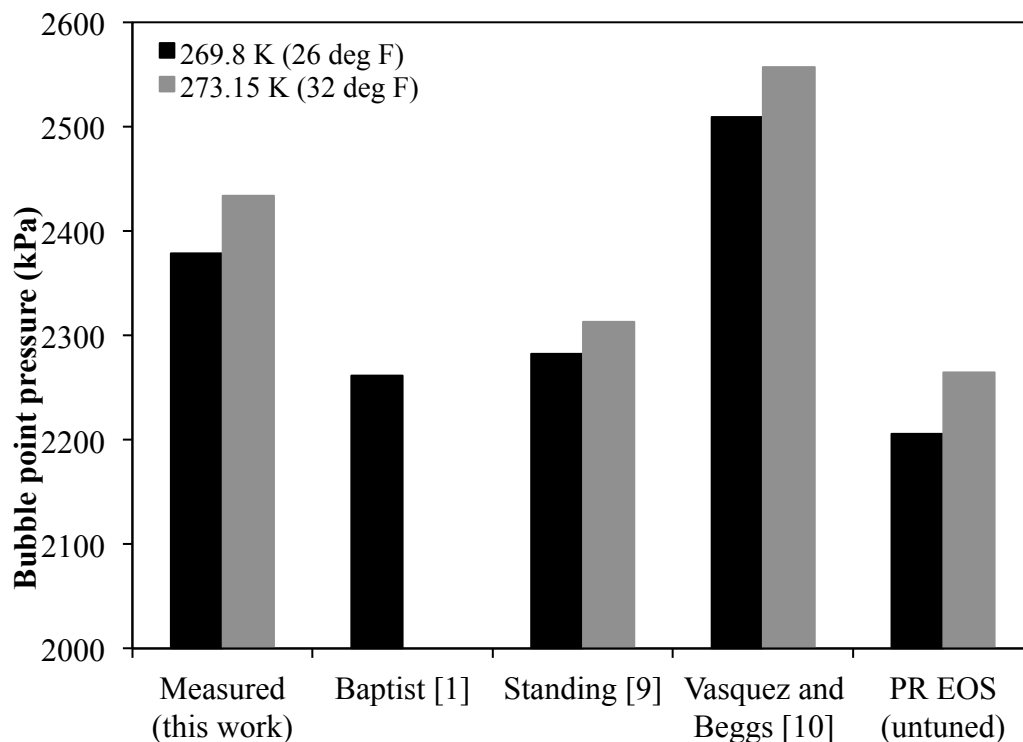


Fig. 9. Comparison of Umiat live oil bubble point pressures.

With the altered critical properties and acentric factor of C_{18+} as shown in Table 2, the bubble point pressure at 269.8 K (26°F) was exactly regressed at the measured value. With the volume shift parameter of C_{18+} altered by 1.28%, the densities were regressed reasonably well at 269.8 K (26°F) as shown in Fig. 10. Although all measured density values were used in the regression some of the high pressure density values could not be regressed well; however, the differences are rather small. The regression of live oil viscosities at 269.8 K (26°F) is shown in Fig. 11; however, a significant alteration in the Pedersen viscosity correlation coefficients MU1 through MU5 was necessary (see Table 2).

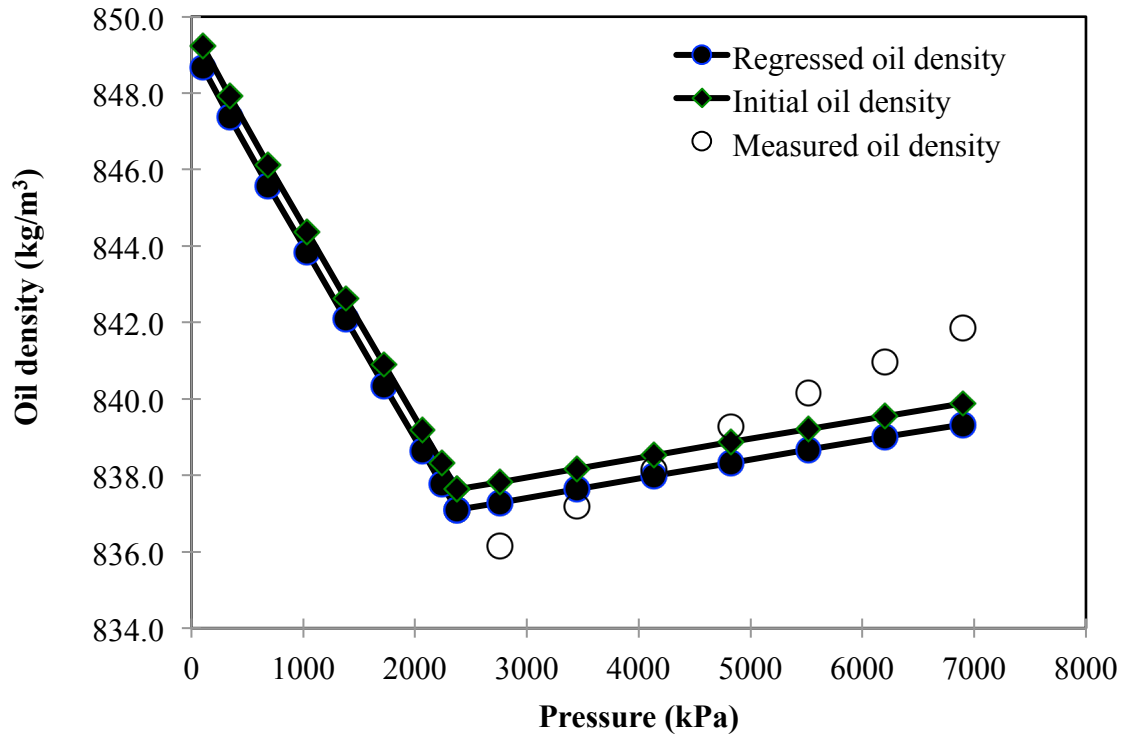


Fig. 10. Regression of live oil densities at 269.8 K (26°F).

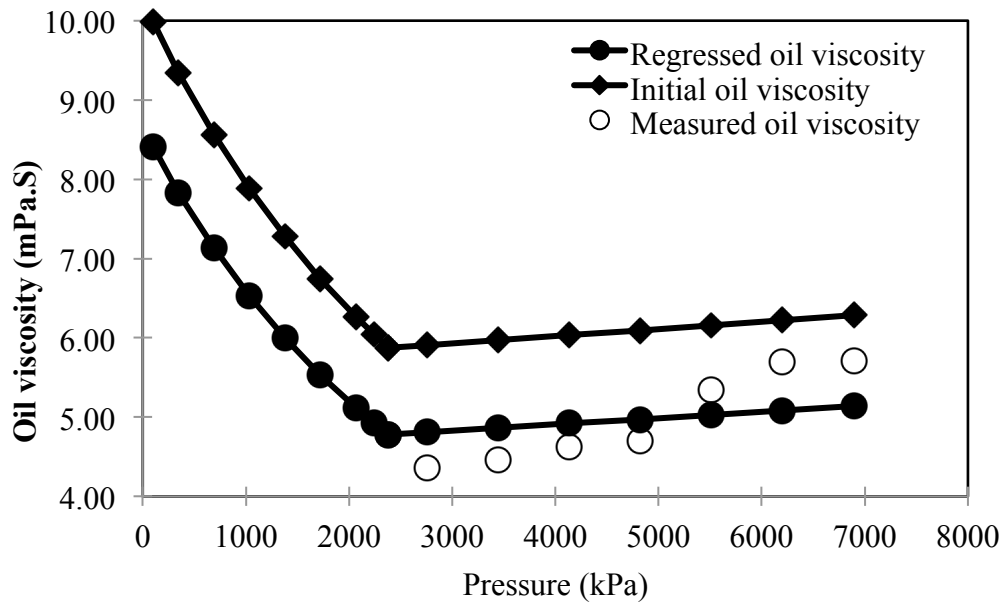


Fig. 11. Regression of live oil viscosities at 269.8 K (26°F).

The tuned EOS model predicted a bubble point pressure of 2442.1 kPa (354.2 psia) at 273.15 K (32°F), which compared very well with the measured value of 2433.7 kPa (353.0 psia). The predictive performance of the tuned EOS model for density and viscosity calculation at 273.15 K (32°F) is shown in Figs. 12 and 13 respectively, which shows a very good match with the measured values. Figs. 14 and 15 show the predicted oil formation volume factors and solution GOR as a function of pressure for the two temperatures for a differential liberation simulation. One peculiarity to notice in Fig. 14 is the fact that oil formation volume factors at certain lower pressures are less than 1, which actually is an anomaly but is due to the low Umiat reservoir temperatures that are less than the standard temperature of 288.7 K (60°F). Finally, Fig. 16 illustrates how the fluid characterization and phase behavior study described and presented in this work will be used in conjunction with the reservoir engineering and geologic model to create a full scale reservoir simulation model for ultimate use in determining an optimum production method for Umiat.

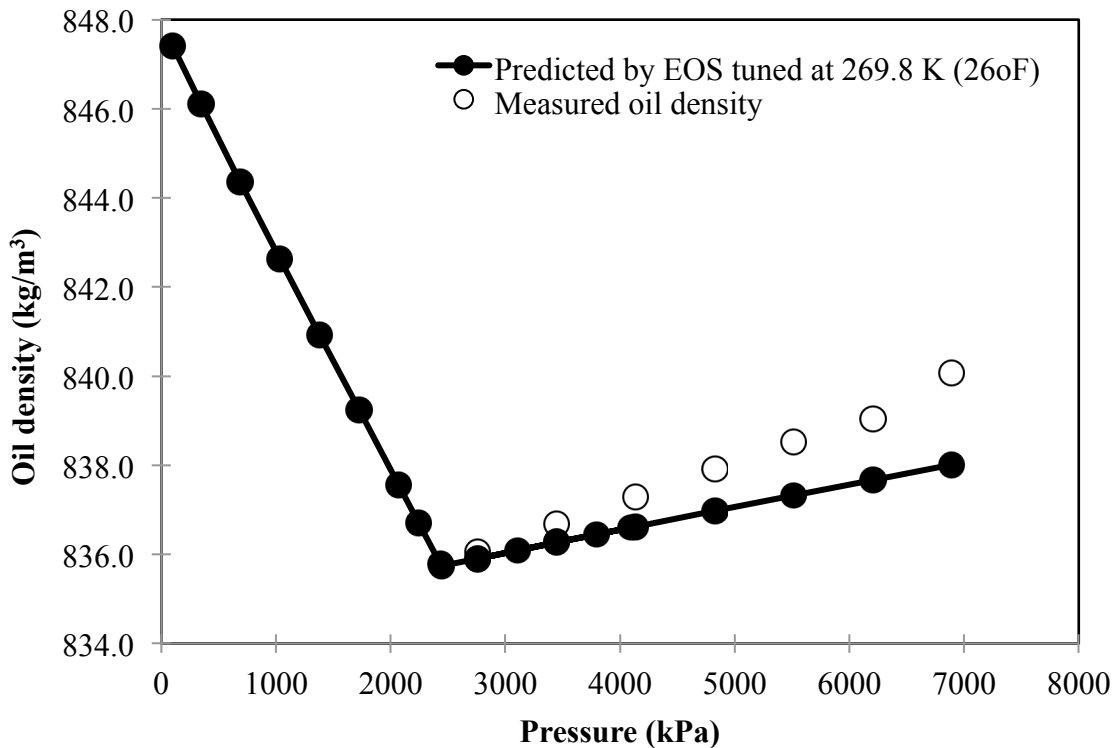


Fig. 12. Comparison of predicted and measured live oil densities at 273.15 K (32°F).

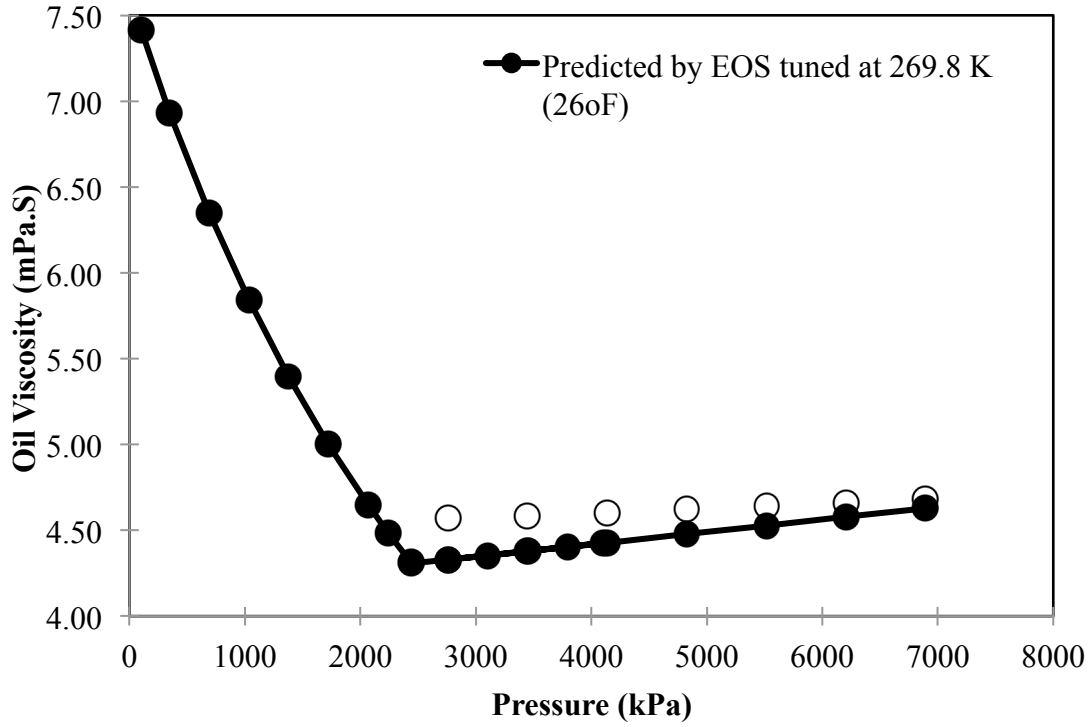


Fig. 13. Comparison of predicted and measured live oil viscosities at 273.15 K (32°F).

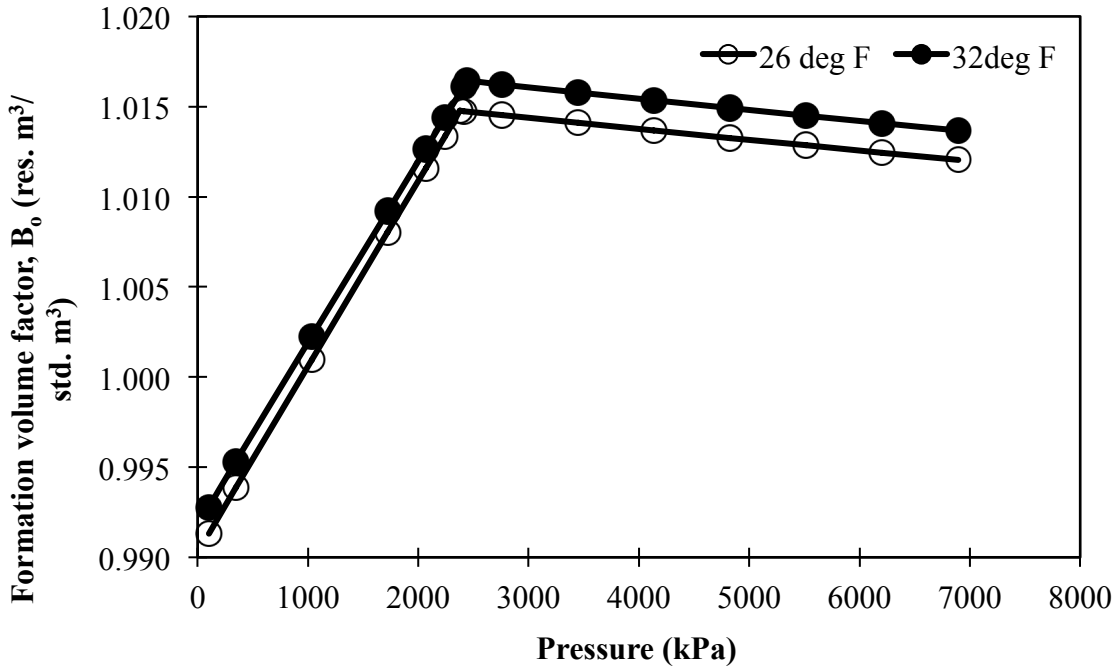


Fig. 14. Prediction of oil formation volume factor for Umiat oil.

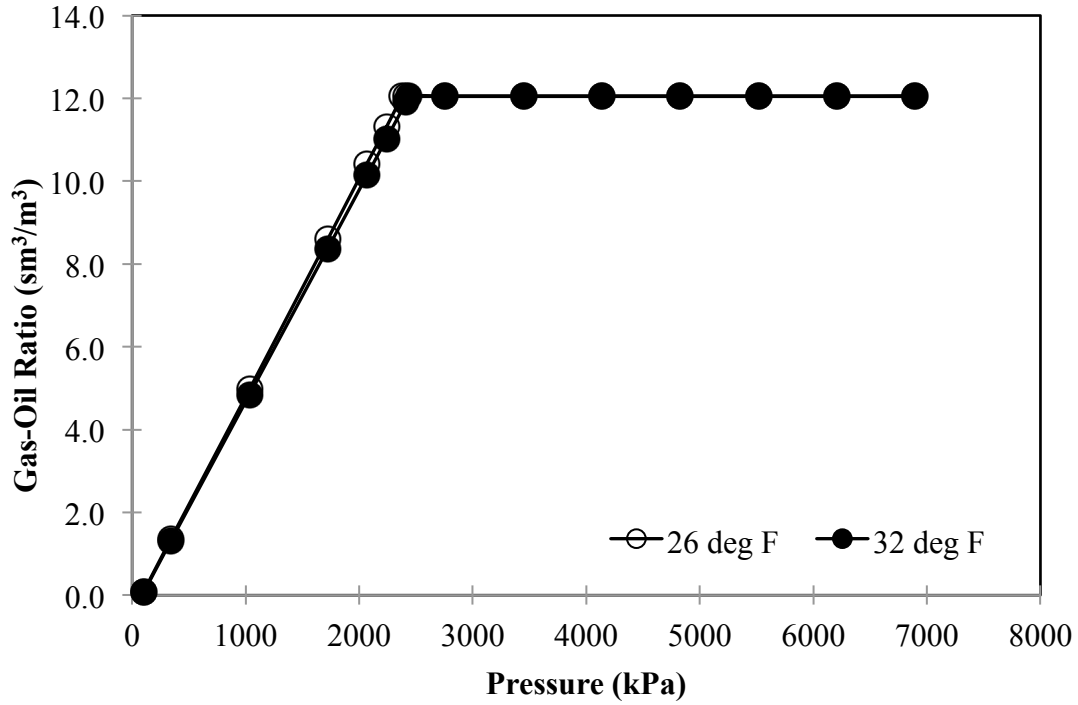


Fig. 15. Prediction of solution GOR for Umiat oil.

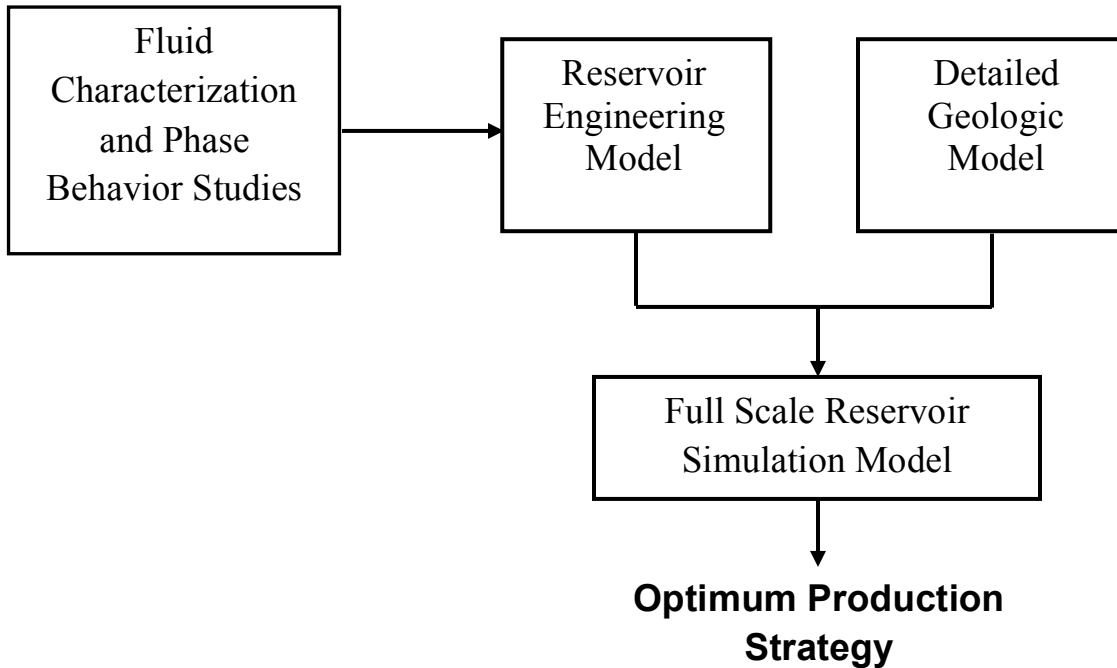


Fig. 16. Importance of fluid characterization and phase behavior data for Umiat oil field development.

Conclusions

The only currently available dead oil sample, collected some 60 years ago was physically and chemically characterized to ascertain its resemblance with the original representative reservoir oil from Umiat. Given the non-representativity of the available sample and the lack of new oil samples from Umiat, a novel and unique approach was adopted in this study by which the Umiat oil was theoretically characterized and was used in estimating the lost light ends from the available Umiat oil sample. This was used to recreate the representative Umiat dead oil sample, which also was characterized and later used in producing the live oil sample for phase behavior studies, which included experimental bubble point pressure and density and viscosity measurements at the two low reservoir temperatures. The experimental phase behavior measurements also formed the basis of EOS modeling and tuning. The results presented in this paper clearly demonstrate that a comprehensive fluid characterization and phase behavior study for a light oil from frozen reservoir of Umiat oil field in Alaska has been successfully executed, which the authors believe will greatly aid in determining an optimum production method for this challenging reservoir.

Effect of Drilling Fluid characteristics on Rock Properties of Umiat Field formations

Introduction

Umiat field is unique in the fact that most oil reserves are within the permafrost, which extends from surface to about 800 or 1,100 ft below. The reservoir pressure ranges from 50 to 350 psi depending on depth and gas dissolved. The reservoir temperature is about 26 °F at a depth of 100 ft and it gradually increases until the bottom of the permafrost is reached. Current industry estimates indicate that the oil in place at Umiat field may be as high as 1.0 BBL. The crude oil is of a good quality; it has an API of 36°, a pour point of -5 °F, sulfur of less than 0.1% and no H₂S. This makes it a very promising field, if drilling and production issues could be overcome. The main oil producing zones are two marine sandstone beds (upper and lower sands) in the Grandstand formation (Baptist, 1960; Gates and Carroway, 1960).

The development of such oil and gas reserves in permafrost areas requires a new drilling and well completion technology. Horizontal drilling techniques have opened the possibility of economically developing such a shallow reservoir. However, drilling through low pressure and low temperature reservoirs in the permafrost poses some difficulties that may drastically alter the reservoir rock properties. Permeability in the area near the wellbore may be severely reduced by direct contact between drilling/completion fluids and bare formation. This is even more pronounced in drilling long horizontal sections (Hanks et al., 2011).

Formation damage as a result of drilling/completion fluids in conventional overbalance drilling can reduce the permeability near the wellbore and presents an extra resistance to the fluid flow. Formation damage is a result of various mechanisms. Differential pressure between borehole and formation causes mud to filtrate to the formation. This filtrate is basically the liquid phase of mud. This leaves large-size solid particles in mud to form a filter cake around the walls of the borehole. However, the small-size solid particles invade the formation with the filtrate and, eventually start to precipitate and thus partially or completely plug the pores and reduce the formation absolute permeability. Meanwhile, relative permeability is reduced as well as a result of change in fluid saturation near the wellbore. Another mechanism of reducing formation permeability is clay swelling where filtrate hydrates the clay found in the formation and increases its volume. In permafrost, in addition to the conventional mechanisms of formation damage, a unique mechanism reduces permeability near the wellbore even more and may completely plug the pores. That is the freezing of the filtrate. While circulating the warm mud, filtrate invades the sand and water saturation increases. Once circulation is ceased, this filtrate may freeze and form a barrier that is impermeable to oil (Kljcec et al., 1974; Samarskiy, et. al., 2008).

To tackle this problem, a study was conducted to investigate the effect of drilling fluid properties on formation rock properties of Umiat field in the permafrost. Although various fluids are available, the proposed fluids should have specific properties to reduce their interaction with the formation. These properties may include: low solid content, depressed freezing point, highly

inhibitive, low fluid loss, excellent filter-cake quality, shear-thinning, high yield point to plastic viscosity ratio, better borehole stability, environmentally acceptable and cost effective. Another factor to be considered when selecting a suitable drilling fluid for permafrost is the in situ ice itself. It is known that ice disintegrates if it is exposed to brines, even at very low temperatures (below 32 °F).

With no fluids originally designated by Renaissance or Linc, two preliminary base fluids were made to get a more basic understanding of how they interact with the subsurface formations. The first fluid tested was simply a water-based-mud composed of water and 9 [lb/bbl] bentonite. The second fluid was brine, composed of water, 10 [lb/bbl] KCl, and 9 [lb/bbl] bentonite. The mud weights were 8.5 and 8.8 ppg, respectively.

From the Umiat field point of interest, it is clear that the main mechanisms for reducing formation permeability are clay swelling because of filtrate interaction, pore plugging because of filtrate freezing and solid precipitation. Therefore, drilling fluids are basically evaluated based on the above three mechanisms. A Fann 35 viscometer and Gemini II Rheometer were used for rheological behavior measurement under various temperatures, from ambient through freezing temperature. An API Low Pressure Filter Press was used to define fluid filtration properties in terms of spurt loss, filtrate volume and filter cake thickness while an OFITE swell meter was used to measure clay swelling properties. The results are discussed hereafter.

Results

Fluid Rheology

Rheological properties of drilling fluids are major players in controlling the filtration process and formation damage. Viscous fluids exhibit resistance to flow, especially in the pores near the wellbore and thus limit its effect. Gel strength and apparent viscosity were measured at ambient temperature and the results in Fig. 1 conclude that both fluids exhibit shear-thinning behavior. Water-based-mud has more viscosity than brine. Further investigation of the rheological properties using the state-of-the-art Gemini Rheometer under low temperatures is planned.

Fluid Filtration Properties

The thickness of filter cake built on the walls of the wellbore provides extra resistance to filtrate invasion, especially if it has a permeability value lower than that of the formation. However, increased thickness may offer other problems like differential pipe sticking. Another parameter is the volume and nature of the filtrate. It can damage both absolute and relative permeability. Filtration properties were measured for both fluids using an API low-pressure filter press under a pressure of 100 psi.

The results in Table 1 show that, although thickness of the filter cake is almost identical, 2/32-in., water-based-mud has better filtration properties than brine. It has small filtrate volume, 56 mL/30 min and a spurt loss of 2 mL compared to 94 mL/30 min and 5.2 mL, respectively for brine. However, the nature and properties of the filtrate is another important factor to determine

its damaging effect. A small volume of water filtrate can hydrate clays and reduce formation permeability. Therefore, the swell test results have to be considered for an overall conclusion.

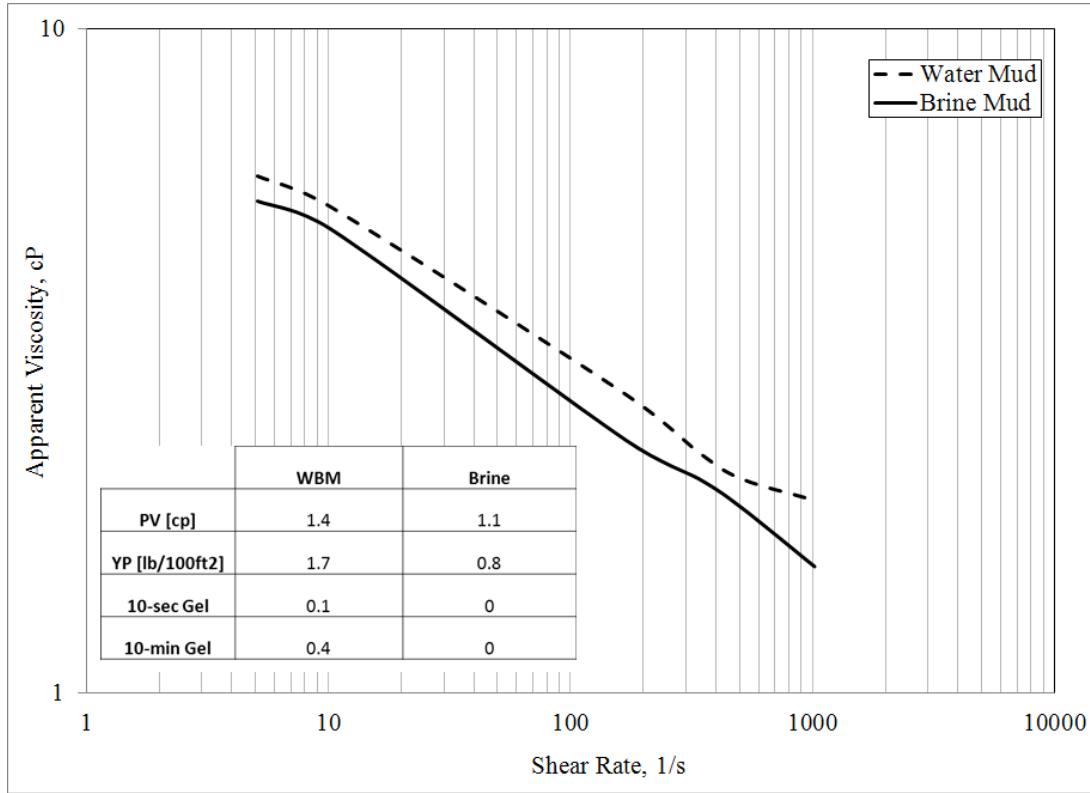


Fig. 1: Rheogram for Drilling Fluids

Table1: Filtration Properties of Drilling Fluids

	<i>Water Mud</i>	<i>Brine Mud</i>
<i>30 min volume [cc]</i>	55.5	93.5
<i>Filter Cake [inch]</i>	2/32	2/32
<i>Spurt Loss [cc]</i>	1.97	5.17

Formation-Fluid Reactivity (Swell tests)

An OFITE linear swell meter can be used to test how the formations would interact with the fluids and measure the percent swell. Therefore, formation rock samples from each sandstone layer were acquired from well No. 9 for Upper and Lower Grandstand and well No. 11 for Ninuluk formation. Rock wafers were prepared by crushing the samples to an unconsolidated form, where they were compacted in ~17g wafers at 10,000 psi for an hour. These consolidated wafers would allow for testing of critical formation-fluid interaction properties.

From the test results shown in Table 2, it can be concluded that water-based-mud has resulted in more swelling than brine. The percent swell for water-based mud, after about one hour test, was 1.1% with Ninuluk formation while it was 0.4% for Upper and Lower Grandstand. With brines,

the percent swell was 0.3, 0.2, and 0.1% for Ninuluk, Lower, and Upper Grandstand formations, respectively. This confirms the fact that salt inhibits clay swelling and reduces formation damage, despite its large filtrate volume.

Table1: Percent Swell for Different Formations

	<i>Water Mud</i>	<i>Brine Mud</i>
<i>Formation</i>	<i>Swell %</i>	<i>Swell %</i>
<i>Upper Grandstand</i>	<i>0.4</i>	<i>0.1</i>
<i>Lower Grandstand</i>	<i>0.4</i>	<i>0.2</i>
<i>Ninuluk Formation</i>	<i>1.1</i>	<i>0.3</i>

Different interaction behavior is seen between the three formation layers (Figs. 2 and 3). This may be due to different formation composition. The Upper Grandstand is marine sandstone, mostly absent of microfossils. The grains are fine to very fine, with inter-bedded clay shale making up approximately 50%. The next layer is the Lower Grandstand, which is made of mostly sandstone with small amounts of shale/claystone. This layer contains abundant microfossils and it is medium to fine grained. Lastly, there is the Ninuluk Formation, with fine to very fine grained sandstone. In the top portion of this layer there are abundant microfossils, while they are absent in the lower half. The lower half also contains silty grains, with some claystone present near the bottom. However, a longer swell test is planned to define the maximum percent swell (Hanks et al, 2011).

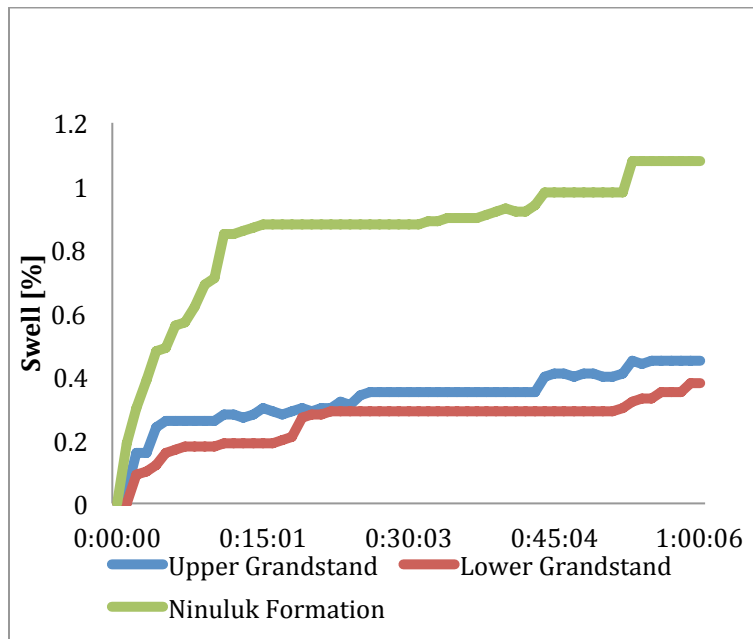


Fig. 2: Effect of Formation Type on Swell Percent with Water Mud

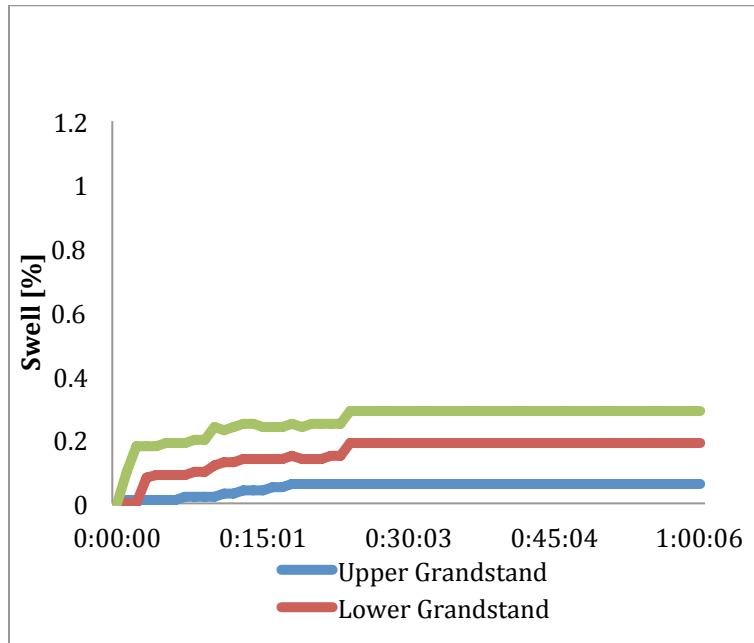


Fig. 3: Effect of Formation Type on Swell Percent with Brine Mud

Again, it is worth recalling that in addition to clay swelling and filtrate invasion, formation damage and permeability reduction can be caused by frozen filtrate and ice blocking. Therefore, depressed freezing point is of utmost importance.

Conclusions

From the data gathered it can be easily concluded that the water-based-mud has better filtration properties, with less fluid loss, while the brine has lower apparent viscosity at high flow rates, which reduce the pumping pressure required to circulate the fluid. Brine also has the ability to inhibit clay swelling in the formation where water-based-mud does not. However since the freezing filtrate is another cause of formation damage, a simple water-based-mud may not a viable option.

It is recommended that new fluids should be tested. This may include different salts, brines, and polymers as well as oil-based-mud for sensitive producing zones. These fluids should be tested at low temperatures in order to determine the properties under such conditions and to ensure the freezing point is below that experienced in the reservoir. A more detailed classification of formation composition may be a key factor for drilling fluid selection. This would require more collaborative work between engineers and geologists at UAF. In future, an evaluation based on the friction pressure losses and equivalent circulating density, ECD may be conducted using a flow loop to get accurate measurements of the pressure losses. Also, potential washout and wellbore stability problems could be investigated.

Geological Modeling and Reservoir Simulation of Umiat: A Large Shallow Oil Accumulation in Northern Alaska¹

Introduction

The Umiat oil field is situated in the folded and thrust-faulted sedimentary rocks at the leading edge of the Brooks Range foothills of northern Alaska. Discovered in 1947, the main oil reservoirs are the Upper Grandstand (UGS) and the Lower Grandstand (LGS). They are between 500–1400 feet deep and mostly in permafrost. Geographic location of the Umiat oil field is shown in Figure 1.

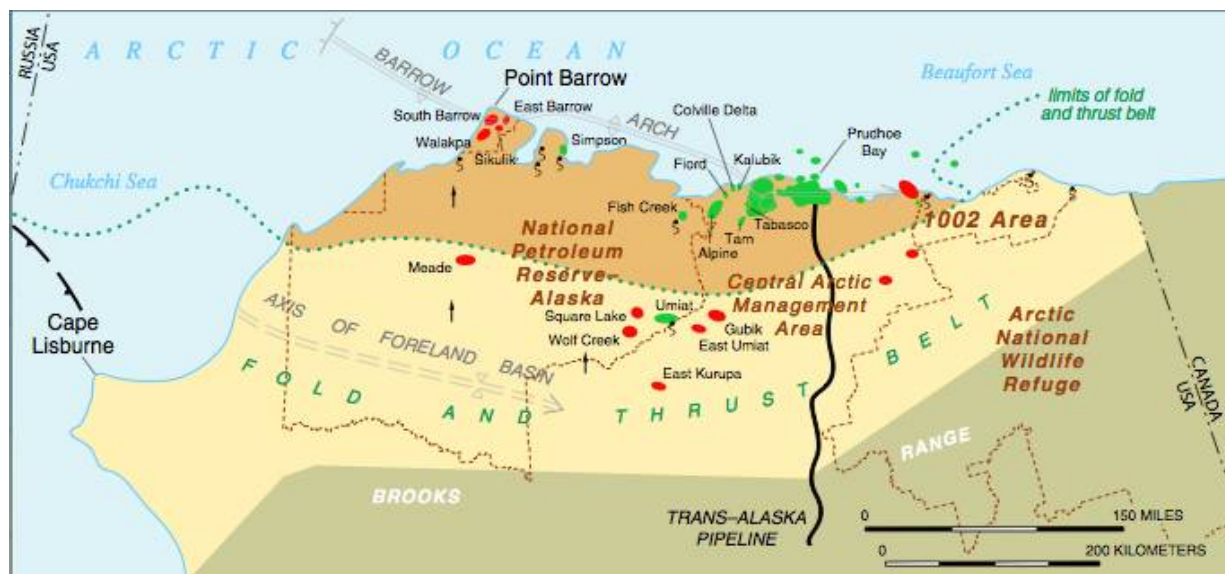


Fig. 1. Umiat field location (Modified from Kumar et al., 2002)

The Umiat field lies mostly within the continuous permafrost region. Permafrost depth ranges from 770 to 1055 feet. Oil was found at depths of 275 to 1100 feet (Baptist, 1960); therefore, some of the oil is believed to be in the permanently frozen zone. For this reason, the Umiat field is considered unconventional. The oil has an API gravity of about 37 with a 5 °F pour point, which allows it to flow even in a permafrost environment (Levi-Johnson, 2010).

There are two main sandstone oil-producing formations which vary in thickness and quality across the Umiat area. The main oil-producing zones in the Umiat field are marine sandstones in the Grandstand Formation of the Cretaceous Nanushuk Group (Baptist, 1960). With an areal extent of 7,500 acres, the Upper Grandstand sand (UGS) has bodies of sandstones usually 50 to 75 feet thick. The UGS is separated from the Lower Grandstand sand (LGS) by 300 feet thick gray shale (Shale Barrier). The LGS has smaller area of 5,600 acres, but its thickness is much

¹ prepublication draft of manuscript to be submitted to Petroleum Science and Engineering.

greater than the UGS, though only the top 100 feet has good reservoir quality (Shimer et al., this report).

The average of reservoir pressures is about 50 psi in the UGS and about 350 psi in the LGS (Baptist, 1960). Most of the primary production will be based on a solution gas drive mechanism. However, since the bubble point of the oil is 345 psi in the LGS formation (Shukla, 2011), the field is considered an undersaturated black oil field that needs immediate pressure support for efficient oil production.

The objectives of this simulation study are to obtain the ultimate oil recovery and oil production profile for the gas injection development plan and highlight the input parameters with highest impact on the oil recovery. The study is focused on the LGS, which has been identified as having the best reservoir properties. Cold gas injection has been proposed as a potential pressure maintenance method (Watt et al., 2010). Pure methane will be injected at reservoir temperature of 26°F in order to avoid disturbing the permafrost. Thawing of the permafrost around the wellbore would lead to the failure of the cement seal and put the integrity of the well at risk. As part of the simulation, sensitivity analyses are conducted for permeability anisotropy (k_v/k_h) ratio, relative permeability end points, horizontal well length, producing GOR constraints and injection bottom-hole pressures.

Materials and methods

Reservoir modeling is the process of building and maintaining a reservoir model (Roxar, 1994-2008). A petrophysical property model for Umiat field was built using IRAP RMS geostatistical software designed and marketed by Roxar Inc. (acquired by Emerson in 2011). The modeling software has a workflow management which allows for the easy access to all the procedures saved in it. A geologic model had already been built with large scale cell dimensions (600 ft * 600ft) and is shown in Figure 2. It used a single value for the water saturation ($S_w=0.41$) and set the WOC depth at 783 ft in the volumetric calculations.

Based on new permeability trends and geologic information, the LGS formation was divided into three sub-formations known as: the Upper LGS, the Middle LGS, and the Lower LGS. The Lower LGS is mostly mudstone impermeable layer with about 20 feet thickness across the reservoir (Grant Shimer et al., this report). The new geometry was also included in the volumetric calculations.

The new geometry was also included in the volumetric calculations to give how much OOIP is accumulated in each zone. The workflow used in the new geologic modeling is illustrated in Figure 3.

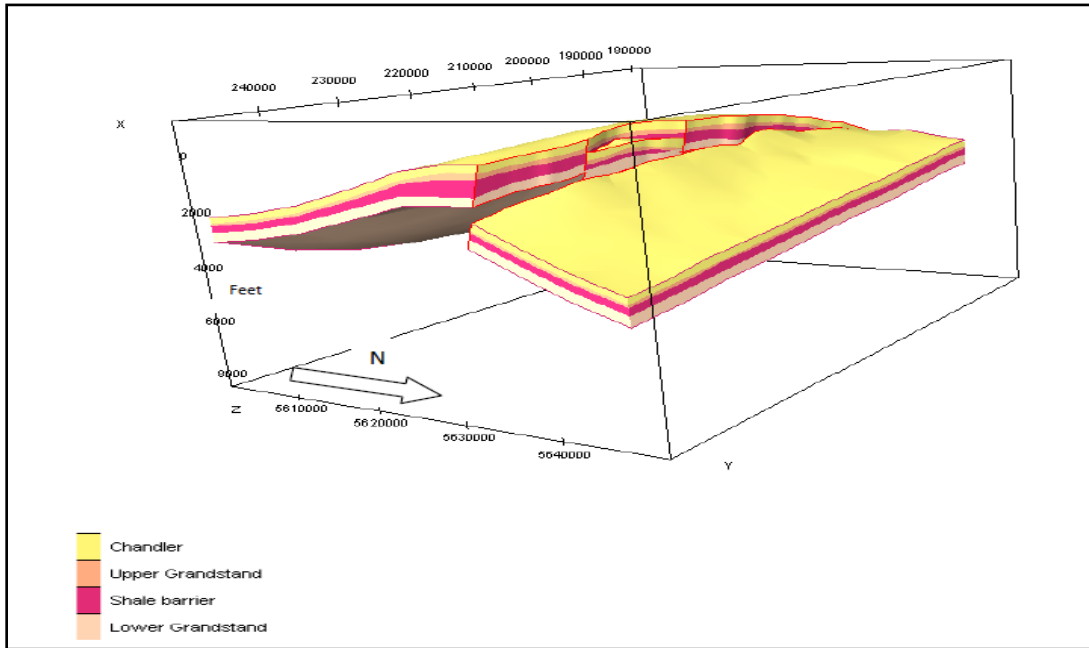


Figure 2. Horizon model of the previous Umiat geologic model (Levi-Johnson, 2010)

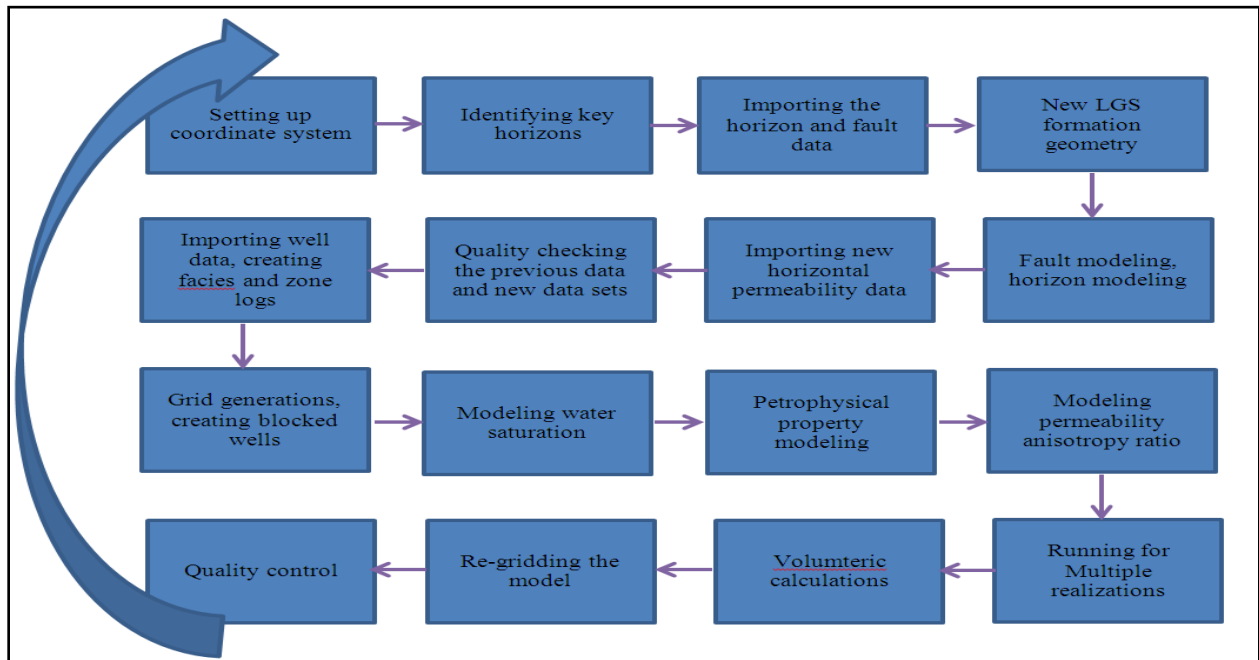


Figure 3. The workflow used for the entire modeling procedure

Petrophysical property modeling

The new 3D petrophysical properties as well as reservoir structure were generated and are shown in Figures 4 through 6. The histograms for the permeability and porosity in the LGS formation

are presented in Figures 7 and 8, respectively. As it can be seen, the mean value for permeability in the LGS formation is about 43 md and the mean value for porosity is 12 percent.

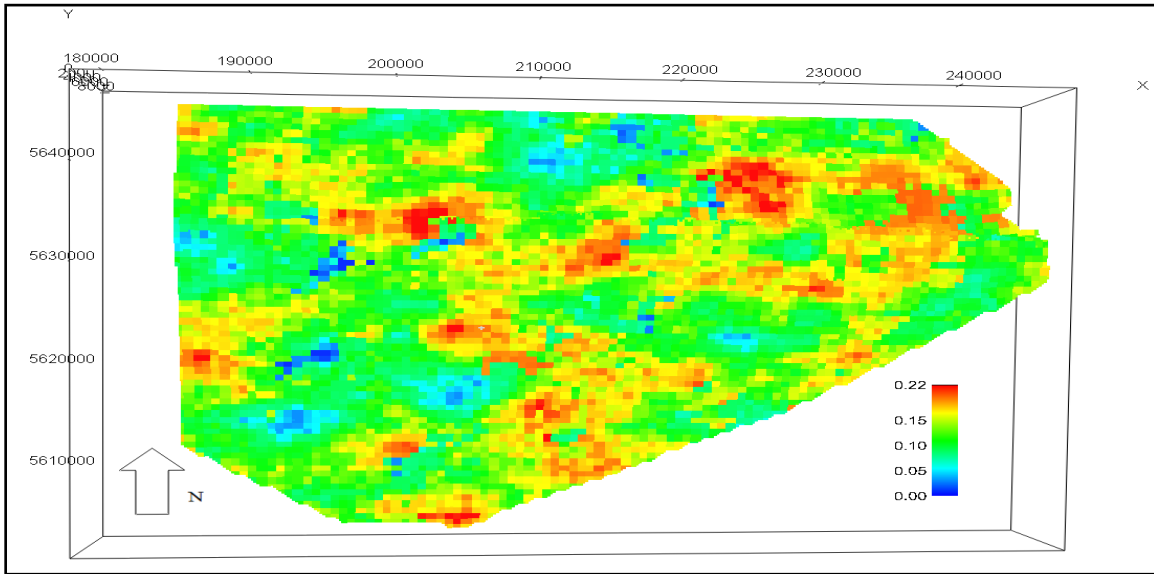


Figure 4. 3D distribution of porosity in uppermost layer of LGS formation

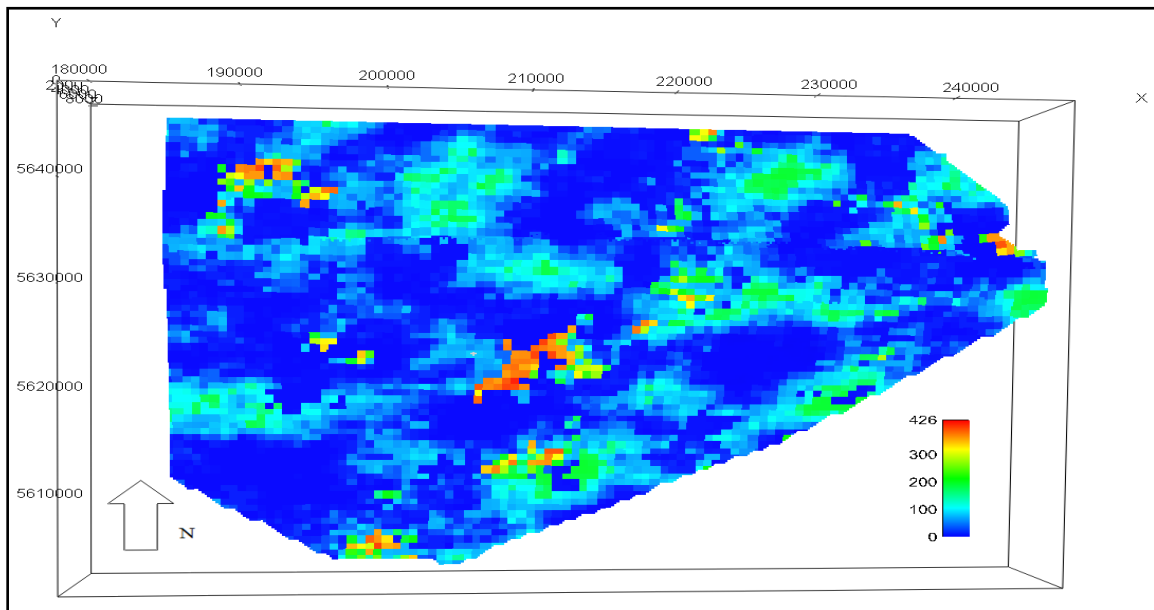


Figure 5. 3D distribution of horizontal permeability in uppermost layer of LGS formation

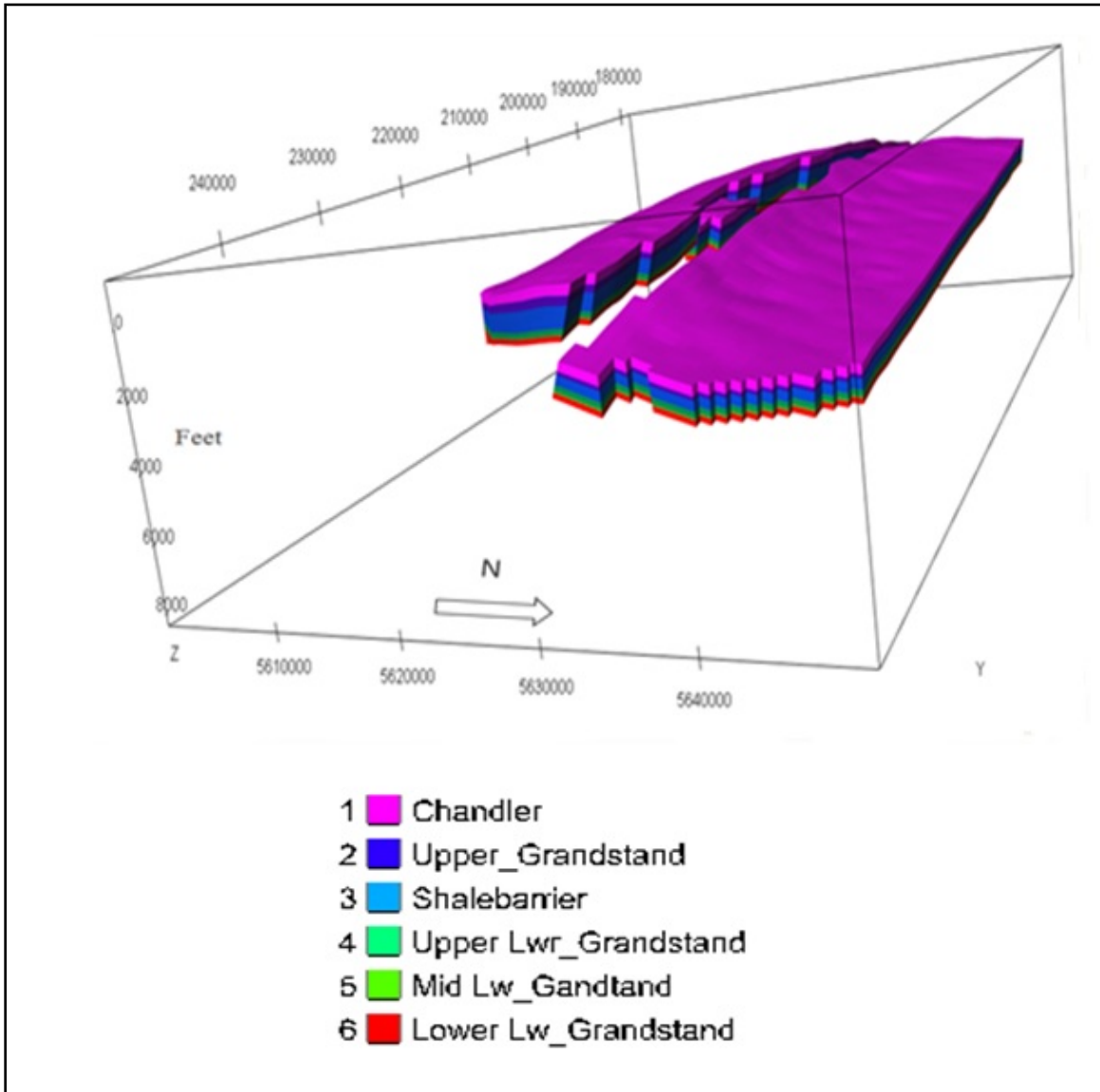


Figure 6. Horizon model of the new geologic model with LGS divided into three sub-formations

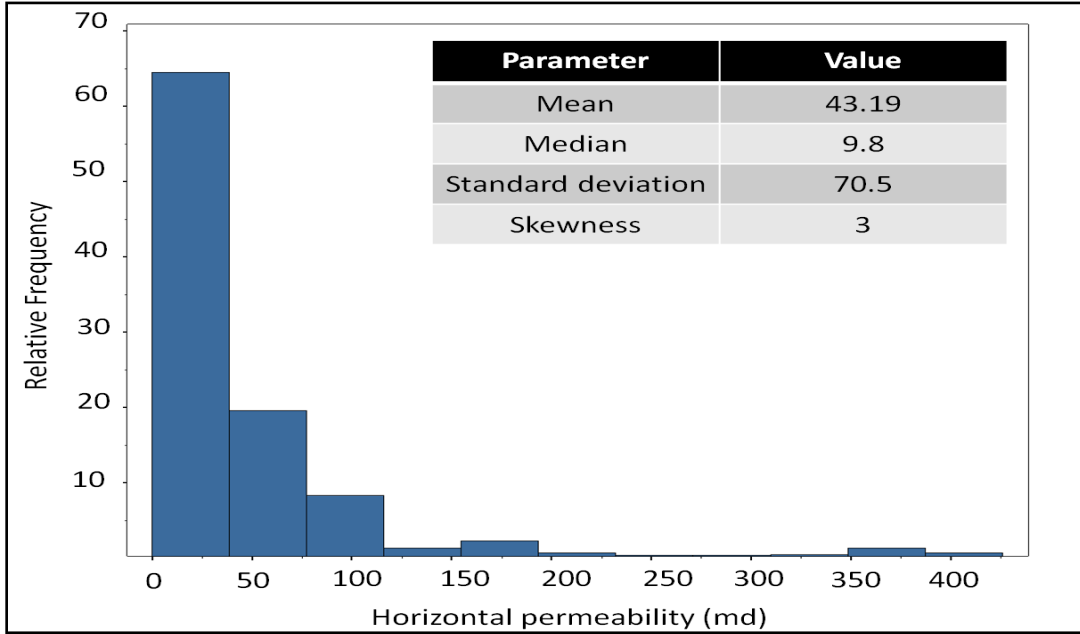


Figure 7. Histogram analysis for the permeability in the LGS formation

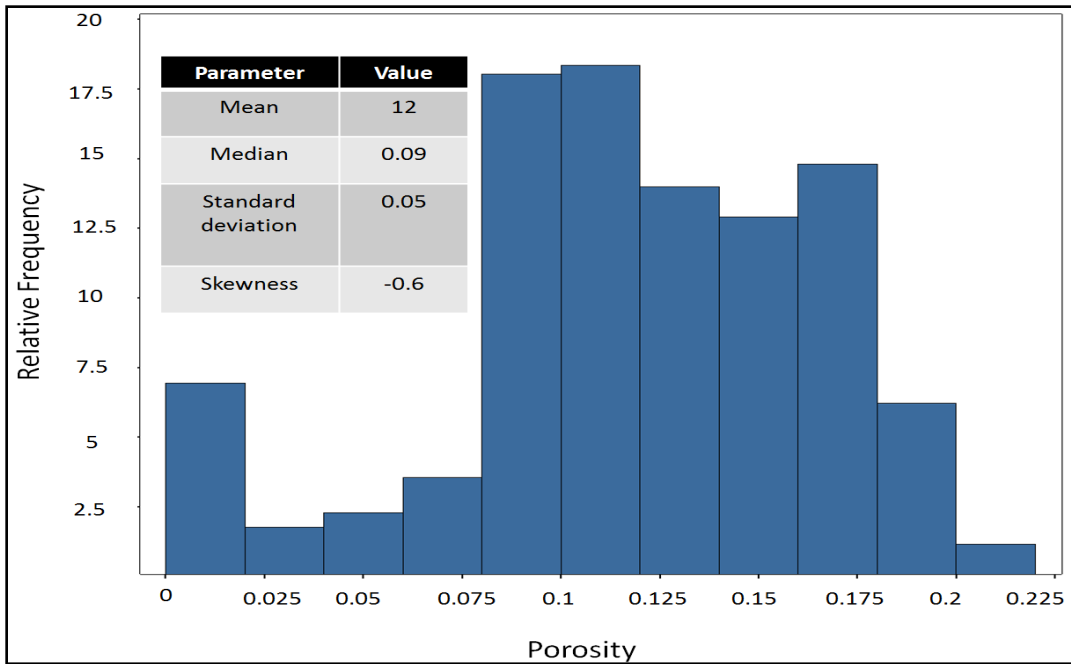


Figure 8. Histogram analysis for the porosity in the LGS formation

Permeability anisotropy

The previous model had to be updated with new permeability measurements. A team of geologists and engineers traveled to Eagle River to measure absolute permeability and observe if there is any trend of presence of natural fractures in the core level. We cut the cores into flat surfaces and measured the air permeability on as many cores as possible. They were mostly from Wells #9 with a few ones from Well #11. Then the data were calibrated and examined to measure anisotropy ratio. For some cases, unreasonable permeability anisotropies were observed and assumed to be due to permeameter and human error. Horizontal permeabilities were more accurate than vertical permeabilities (personal communication with geologist Grant Shimer). After smoothing out the available data, an average value of 0.45 was chosen as the base case permeability anisotropy value. A set of higher and lower values was included in the sensitivity analysis in the reservoir simulation. Figure 9 shows a graph of anisotropy ratio versus depth from the Well #9. The 3D distribution of modeled vertical permeability is shown in Figure 10. Impact of permeability anisotropy on reservoir simulation results are presented later in the simulation section.

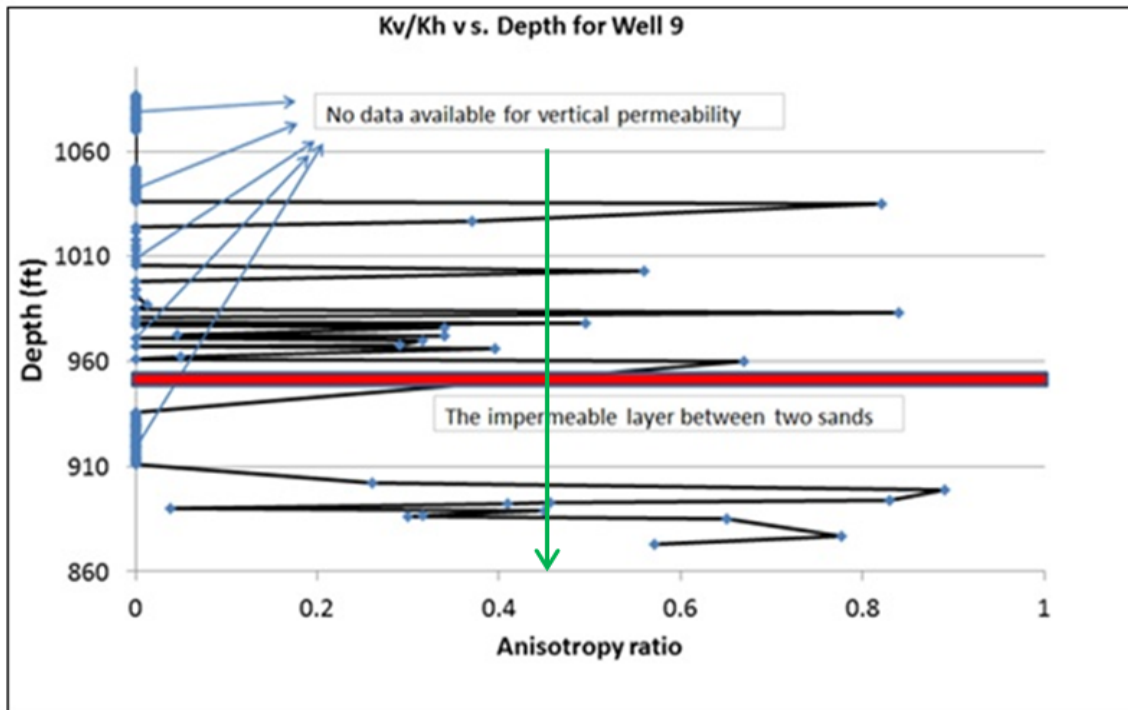


Figure 9. Permeability anisotropy ratio data versus depth for Well #9

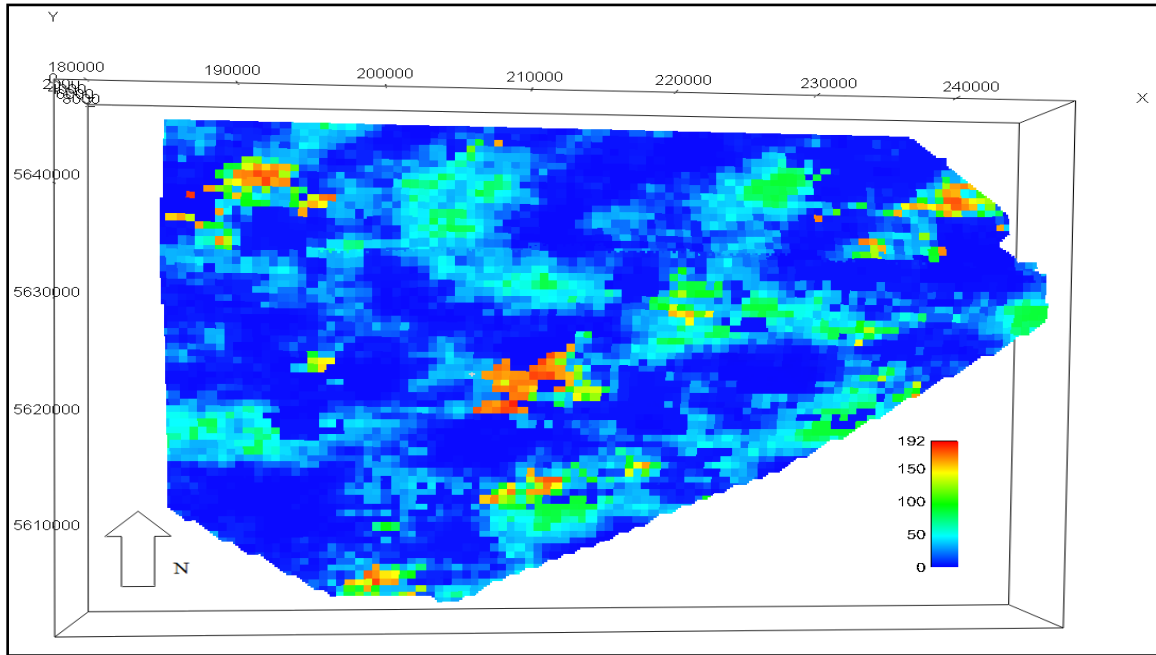


Figure 10. Permeability distribution in vertical direction, K_z (md) in layer #1

Modeling of Water Saturation, Concept and Challenges

Water saturation is the fraction of water in a given pore space. In reservoirs, Water Oil Contact (WOC) represents a surface where oil-water capillary pressure is zero or the minimum depth where below it water saturation is 100%. Three phases of gas, oil and water may exist in reservoir. These phases are separated due to density difference with a transition zone caused by capillary forces. The height of the transition zone depends on factors like permeability, porosity, and capillary pressure (Roxar, 1994-2008).

Accurate modeling of water saturation variation in the transition zone is important to reservoir simulation (Ghedan et al. 2006) and determination of original oil in place. Water saturation in the reservoir is commonly determined by interpretation of electrical resistivity measurements using the Archie's law (Masoudi et al., 2011). Use of the Archie equation entails having adequate resistivity logs and S_w -log-derived data. In most cases, even the Archie's law may not comply with physical bounds and may create significant bias in the computed hydrocarbon saturation (Shang et al., 2008). Plotting the Resistivity Index (RI) (measured from SCAL) vs. the water saturation results in a line with the slope of n , the saturation exponent. However, most of the points are scattered, and usually one slope cannot be drawn for a whole range of water saturation. Conventionally, a value of about 2 would be used as an average saturation exponent for the whole reservoir, regardless of the level of heterogeneity and various rock typing. Field performance data have shown that this approach could have huge impact on calculated volumes, hydrocarbon recovery, and hence project economics (Masoudi et al. 2011).

Extensive laboratory studies have shown that Non-Archie behavior could be attributed to multiple rock types, heterogeneous formations and anisotropic properties, multi-modal pore size, intergranular or micro-porosity, wettability, saturation history, and hysteresis effect (drainage vs. imbibition) in the reservoir (Masoudi et al., 2011).

The reservoir descriptions did not suggest a clear trend to identify different sand subcategories (SS) in the Umiat reservoir with wide variation in permeability (0-500 md). A semi-log plot of (K/Φ) vs. Φ is shown in Figure 11. For any range of porosity there is a wide range of permeability which could be due to varying degree of shale in the reservoir. Since there are no distinguishable trends in the porosity and permeability data, three sand subcategories were chosen based on three ranges of permeability (Table 1). With no available resistivity log, a methodology was developed to use the air-kerosene capillary pressure data to derive the saturation-height functions for each subcategory in the model. The fact that the capillary pressure-saturation curves of nearly all naturally porous materials have many features in common have led to attempts to devise some general equation describing all such curves (Ahmed, 2001). Since the P_c data was available for the sand subcategory 1 (SS-1) from the core #60, the Leverett J-function was used to correlate capillary pressure data for other sand subcategories based on average their permeability. The Leverett J-function is defined as:

$$(3) \quad J = \frac{P_c * \text{Sqrt} \left(\frac{K}{\Phi} \right)}{\sigma * \text{Cos} \theta}$$

Where:

K= Absolute permeability (md)
 Φ = Porosity (%)
 σ = Interfacial tension (dyne/cm)
 P_c = Capillary pressure (psi)
 Θ = Capillary angle

$$P_c = P_{c_{60}} * \text{Sqrt} \left(\frac{K_{60}}{K} \right) \quad (4)$$

Where:

$P_{c_{60}}$ = Capillary pressure for core# 60
 K_{60} = Absolute permeability for core #60
K= Absolute permeability average for other sand subcategories

If we assume that the porosity range is the same in each subcategory, by neglecting the interfacial tension forces, the capillary pressure is inversely proportional to square root of permeability (Equation 4). Then by using Equation 5 and oil and water densities at reservoir conditions (Table 2), the obtained capillary pressure data were transformed to the respective capillary heights in the reservoir and a look-up function for each subcategory was built in IRAP to account for different trends of S_w versus depth (Figure 17).

Table 1. Different sand subcategory for wide permeability ranges in the Umiat reservoir

Sand Subcategory	Permeability range (md)	Representative K for Pc class (md)
1	$K < 1$	0.408
2	$1 < K < 50$	22.5
3	$K > 50$	100

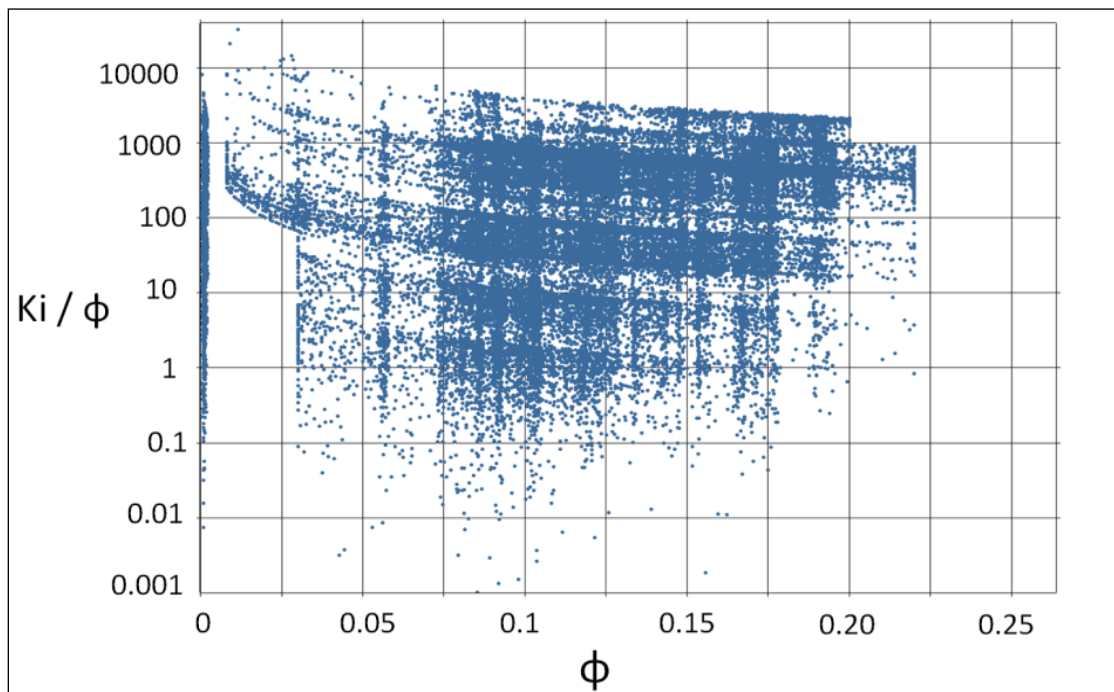


Figure 11. Plot of $\text{Log}(K/\Phi)$ vs. Φ in the LGS formation

As it can be seen in Figure 12, water saturation data changes with respect to depth for different sand subcategories. As expected, the SS #1 which has the lowest permeability range has the

highest transition zone height compared to other sand subcategories in the reservoir. Figure 13 shows the 3D distribution of the water saturation after executing the workflow. It should be mentioned that the model accuracy was tested against the available core water saturation data and anomalous data were excluded from the data domain. The final accuracy was within a reasonable engineering range.

$$h = (144 * Pc) / (\rho_w - \rho_o) \quad (5)$$

Where:

H= Capillary height (ft)

Pc= Capillary pressure (psi)

ρ_w = Water density (lbm/ft³)

ρ_o = Oil density (lbm/ft³)

Table 2. Oil and water density at reservoir conditions

Water density (lbm/ft³)	Oil density (lbm/ft³)
62.4	52.6

The water-kerosene data were mathematically converted to oil/brine system at the reservoir condition (350 psi, 26 F). Typical interfacial-tensions ($\sigma_{\text{air-mercury}}=487$ dynes/cm, $\sigma_{\text{water-kerosene}}=48$ dynes/cm) were used while possible difference in the contact angles were ignored as input to simulator.

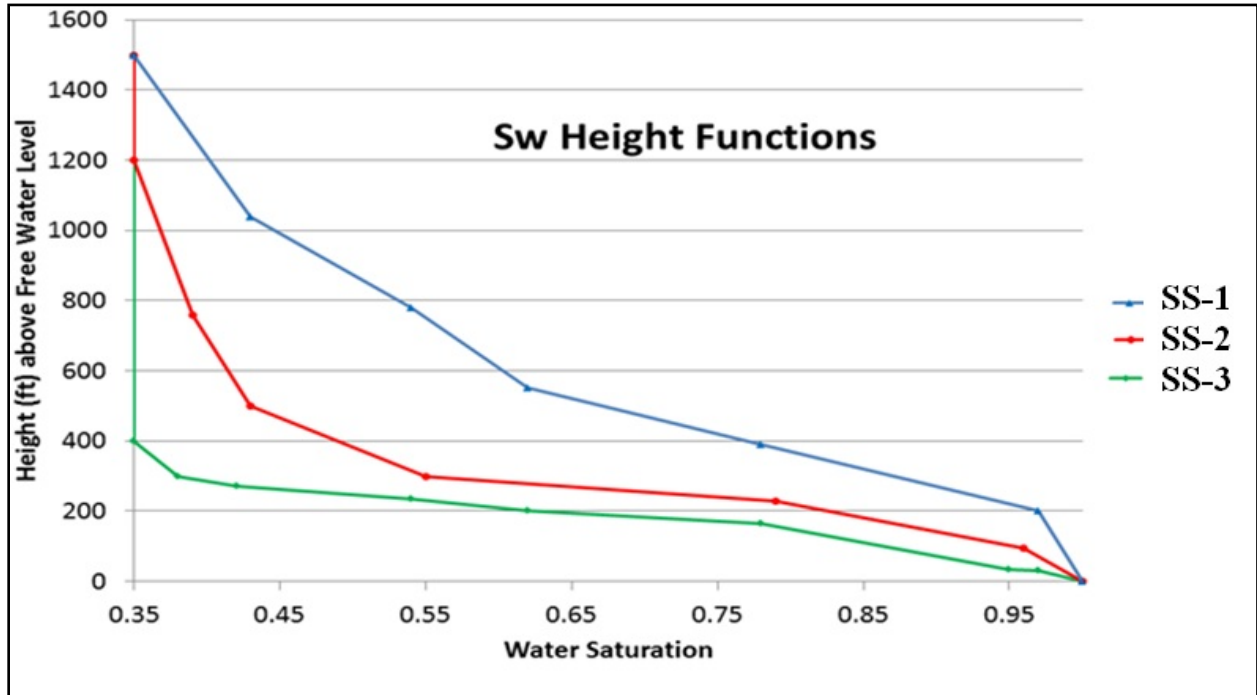


Figure 12. Water saturation height functions for different sand subcategories

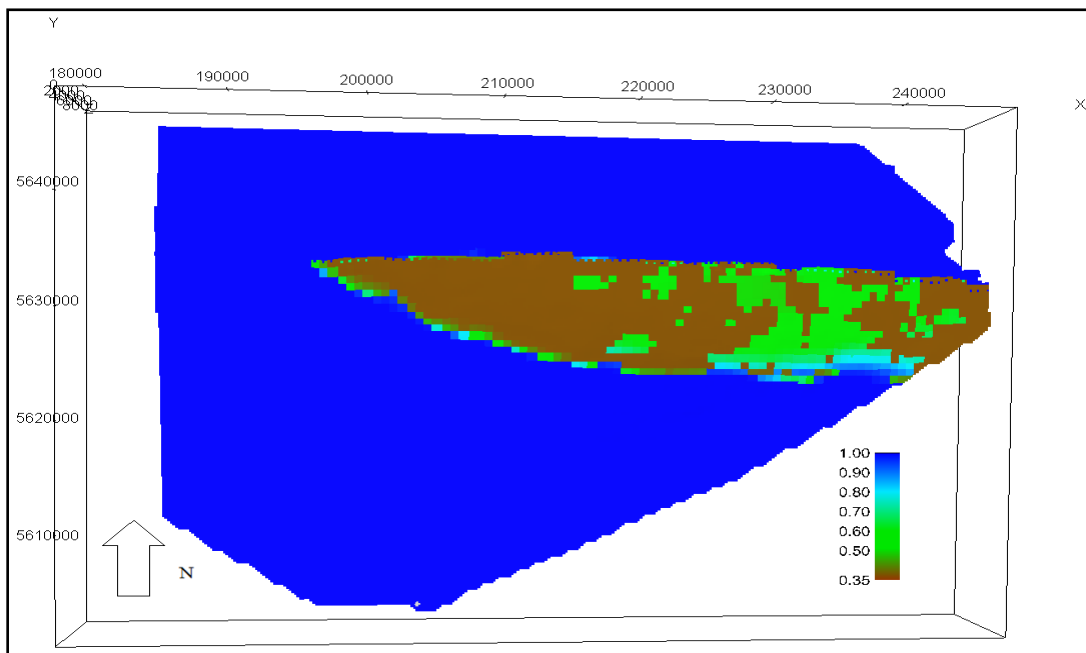


Figure 13. Modeling of water saturation in the Umiat reservoir by use of capillary height functions (layer #18)

Monte Carlo Method for STOOIP Estimation

The estimated original hydrocarbon in place is one of the most important factors when considering an accumulation for development. The estimates provided in previous reports were based on a single realization of the geological model that honored the range of data reported from wells. Having different realizations for combinations of different volumetric factors helps one understand this element better and make better decisions. A Monte Carlo (MC) simulation was done by considering different ranges of 5 input variables in 10,000 runs. The range of input variables used in MC simulation and the results are provided in Tables 3 and 4 for three sub-formations in the LGS. Given the P10, P-50, and P-90, the results show that both the previous and new reserve estimations are in the range of probable occurrence. The result of this simulation yielded STOOIP estimations ranging from P90 of 739 million barrels to a P10 of 2437 million barrels. The P50 value for STOOIP was 1527 million bbls (Figure 14).

Table 3. Different variable ranges used as input to Monte Carlo simulation

Input	Range
Swi	0.35–0.45
NTG ratio	0.1–0.7
Bulk volume (E+9 ft ³)	36–56
Porosity (%)	5.00–22.00
WOC depth (ft)	700–1500
Oil formation volume factor (Rbbl/stbbl)	1.015

Table 4. STOOIP estimations for each zone in the LGS formations

Zone	STOOIP (MM barrel)
Upper LGS	779
Middle LGS	7.8
Lower LGS	741
Total	1527

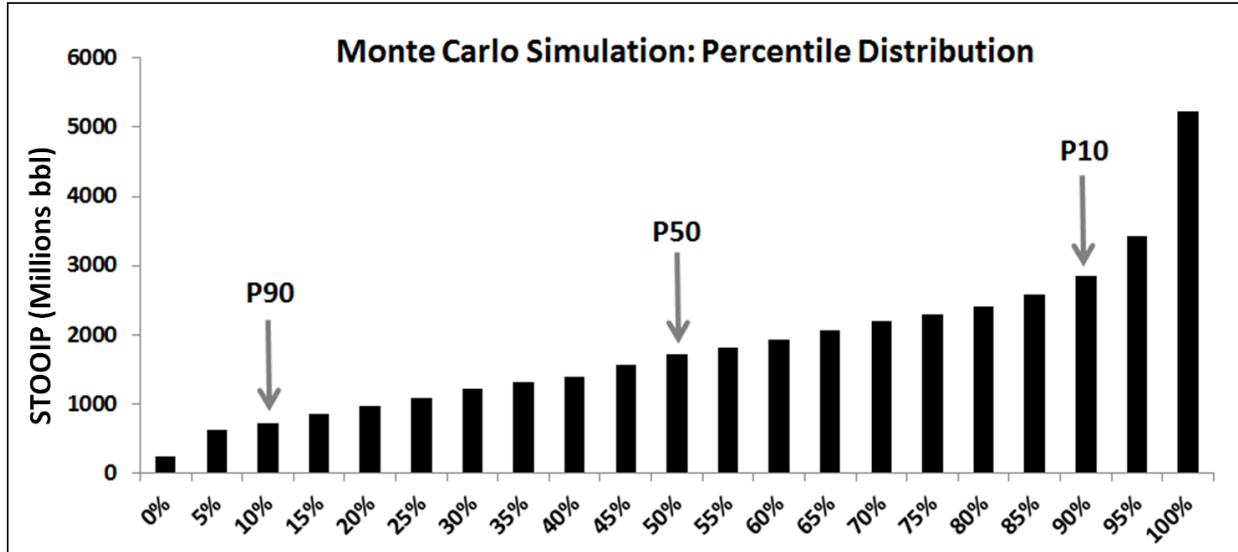


Figure 14. Graphical representation of Monte Carlo simulation for 10,000 runs

Preparation of Input data for simulation model

In this study the performance of LGS reservoir under immiscible gas injection was evaluated by building a reservoir model using CMG IMEX.

Relative permeabilities to oil and gas in presence of ice were measured in laboratory by unsteady state method (Godabrelidze, 2010) for 6 Umiat core plugs. Only Core #60 was from the LGS formation. A semi-log plot of relative permeability data for Core #60 is shown in Figure 15 (Godabrelidze, 2010). As it can be observed, the values of the measured relative permeability to gas for the core plug #60 are extremely small compared to the conventional values.

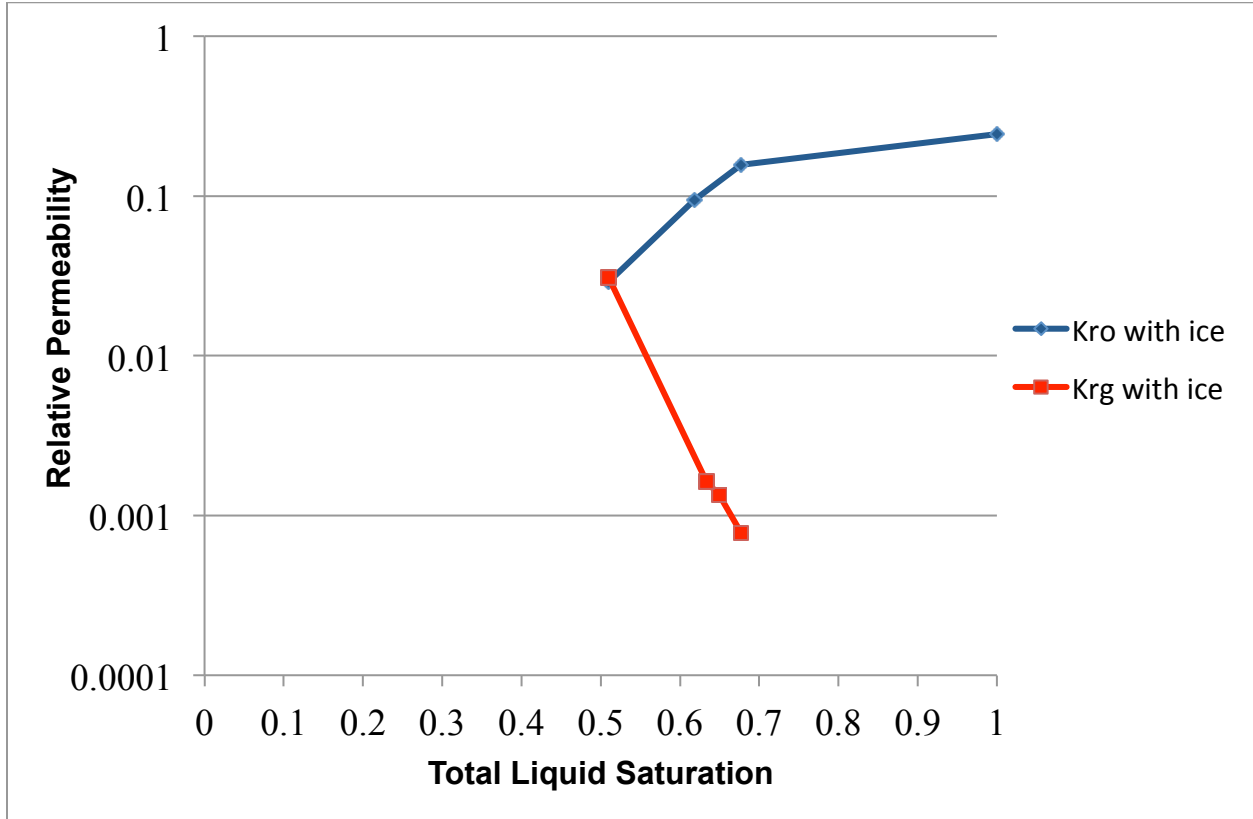


Figure 15. Relative permeability to oil & gas in presence of ice

Each sand subcategory, 3 here, needs a set of capillary pressure and gas-oil relative permeability curves. Generated capillary pressure curves are explained later. Relative permeability data presented in Fig. 23 can be used for the subcategory covering lowest range of permeability including permeability of core #60. To generate relative permeability data for other subcategories, a capillary pressure-based correlation (Schneider, 2003) was utilized based on the pore size distribution for each class of capillary pressure. Brooks and Corey observed that a log-log plot of S_w^* vs. P_c results in a straight line with a slope $-\lambda$ which is characteristics of the pore structure (Brooks and Corey 1964). They proposed the following relationship between the drainage capillary pressure and the wetting phase saturation:

$$P_c = P_{ce} \times (S_w^*)^{-1/\lambda} \quad (8)$$

Where P_{ce} is the capillary entry pressure (or in other words this is the minimum pressure required for non-wetting phase to invade the largest pore) S_w^* is the normalized wetting phase saturation defined as:

$$S_w^* = \frac{S_w - S_{wi}}{1 - S_{wi}} \quad (9)$$

Where S_{wi} denotes irreducible wetting phase saturation. The gas-oil relationship can be defined with the following equations:

$$K_{ro} = (S_{wo}^*)^{(2+3\lambda)/\lambda} \quad (10)$$

and

$$K_{rg} = (1 - S_{wg}^*)^2 * (1 - S_{wg}^*)^{(2+\lambda)/\lambda} \quad (11)$$

Where:

$$S_{wo}^* = \frac{(S_L - S_{or} - S_{wr})}{(1 - S_{or} - S_{wr})}$$

$$S_{wg}^* = \frac{(S_L - S_{wr})}{(1 - S_{wr} - S_{gc})}$$

K_{rg} = gas phase relative permeability

K_{ro} = oil phase relative permeability

S_o = oil saturation

S_{or} = residual oil saturation

S_{wr} = irreducible water saturation

$S_L = S_{wr} + S_o$

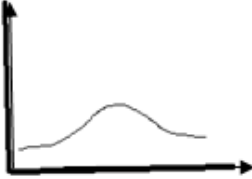
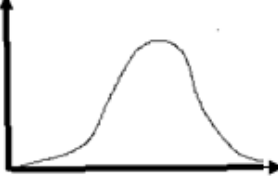
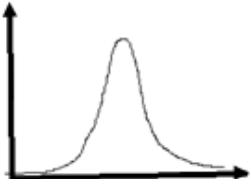
S_{gc} = critical gas saturation

λ = Lithology factor obtained from capillary pressure curve

We have assumed the S_{wi} in all three subcategories is constant at 0.35. This is not a correct assumption as tighter cores are expected to have higher irreducible water saturation. It was used because we were not able to find a quantitative correlation between permeability and irreducible water saturation. Three lithology factors were obtained by calculating the slope of the capillary pressure curves for each sand subcategory and they are presented in Table 5. A small λ indicates a very wide distribution of pore size, while larger λ value indicates uniformity of pore size. Since water freezes in higher percentages in larger pores than small pores and the water to ice ratio is higher in smaller pores than larger pores (Godabrelidze, 2010), the critical gas saturation which conventionally occupies the largest pores in a medium due to lowest capillary pressure, is influenced by distribution of ice in each subcategory. The percentage of ice may vary across the reservoirs depending on distribution of three different sand subcategory with different pore sizes and distributions. The presence of ice can significantly impact the quality of the oil flow (Venepalli, 2011). It is however recommended to run NMR (Nuclear Magnetic Resonance) experiments on Umiat cores in order to examine the relationship between the pore size

distribution and unfrozen water content at different temperatures in order to accurately model the distribution of ice within the pore structure.

Table 5. Different sand subcategory and their corresponding lithology factor

Rock type	1	2	3
λ	0.62	0.84	1.23
Pore size frequency			

With no other option to construct relative permeabilities for other sand subcategory, we performed sensitivity analysis on the relative permeability end points in the simulation. The relative permeabilities to oil and gas for different sand subcategory versus gas saturations are depicted in Figures 16 through 18.

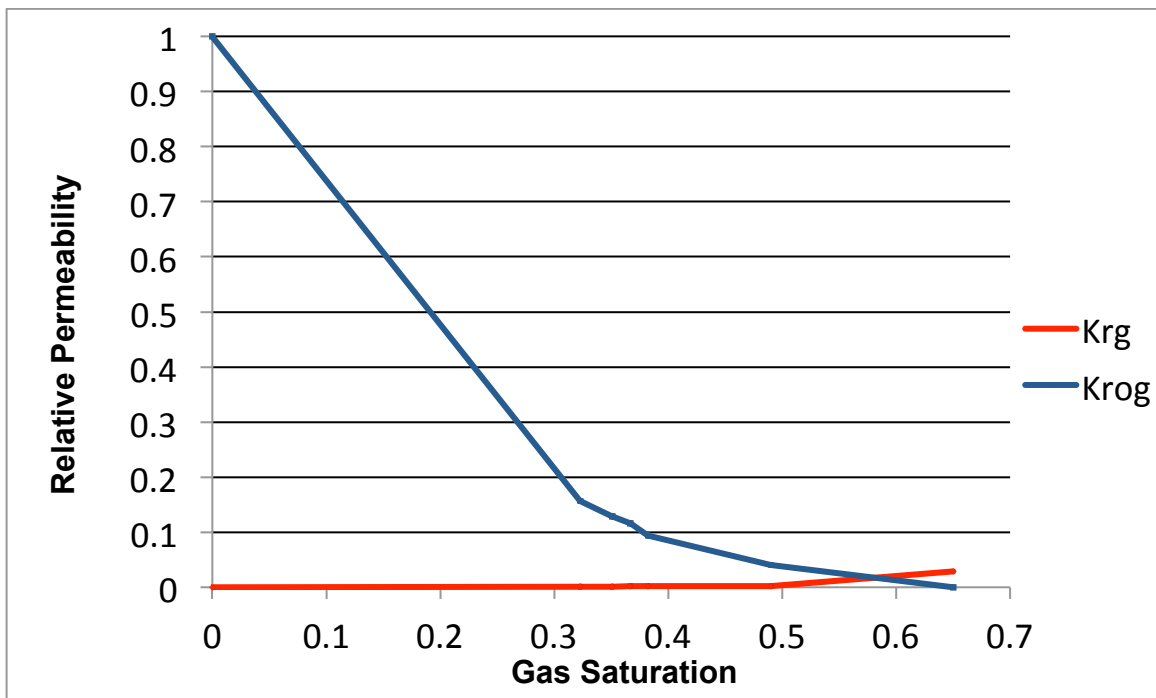


Figure 16. Relative permeability to oil and gas for SS #1 as input to the simulation

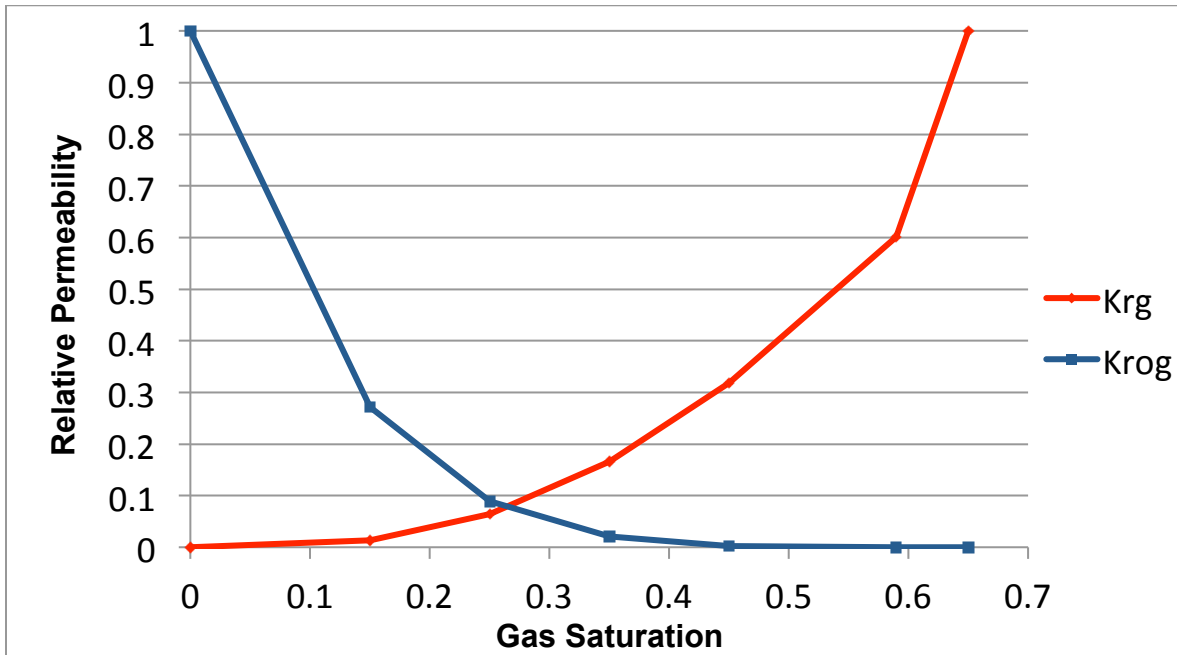


Figure 17. Relative permeability to oil and gas for SS #2 as input to the simulator

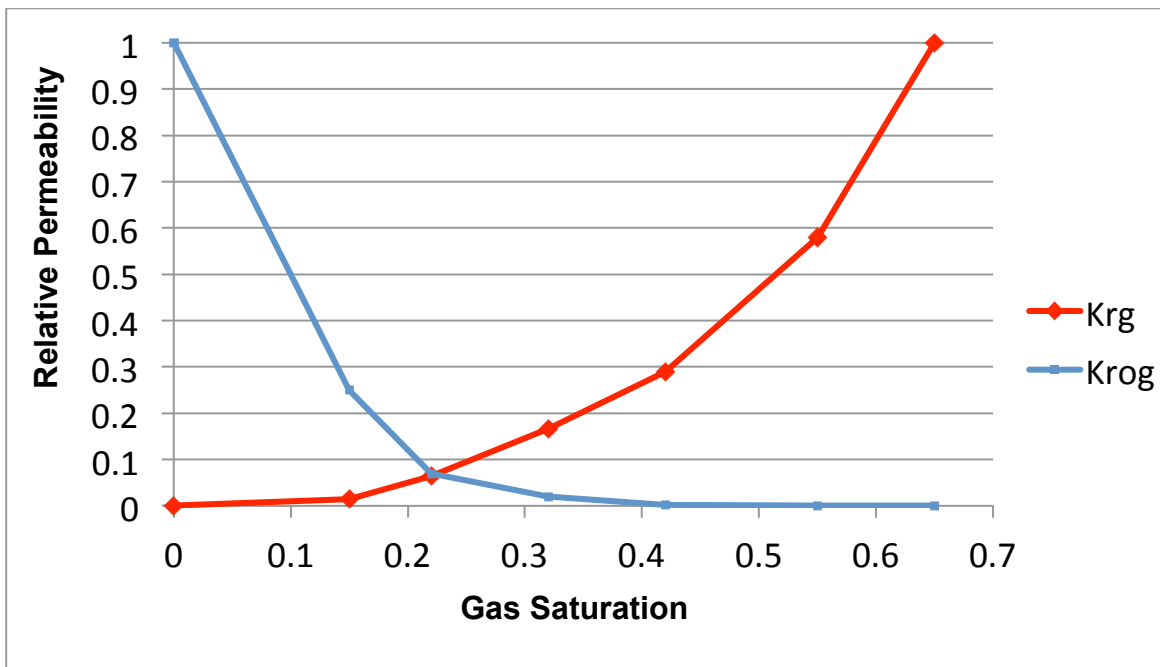


Figure 18. Relative permeability to oil and gas for SS #3 as input to the simulator

For the relative permeabilities to oil and water, due to flooding issues at water freezing temperatures, there was no measured water-oil relative permeability data available for input to simulator. The only available information was the end point to oil relative permeability (K_{row})

at the reservoir temperature of 26°F (Venepalli, 2011). Therefore, existing correlation (Corey, 1954) was adapted and modified to account for the presence of ice. A constant multiplier was used to customize the K_r data to the freezing temperature. Since there is no active aquifer considered in the model, we assume effect of the water relative permeability to be insignificant on the simulation results. Irreducible water saturation normally increases as permeability decreases. In low-permeability sandstones, the water saturation may be very high. However, Chilingar (Chilingar et al., 1972) demonstrated that in some low permeability cases, water saturation can be low. We have assumed that the irreducible water saturation is the same for all the three sand subcategories. The oil-water relative permeability data that was used for all the sand subcategories is presented in Figure 19.

For the capillary pressure data, there were only three core plugs with known capillary pressure obtained by mercury injection method, but only one core plug (#60) was from the LGS formation (Figure 20). A close examination to the core plug properties revealed that it has a very low absolute permeability of 0.408 md. Given a wide variations of permeability in Umiat (0-500 md), capillary pressure from this core plug only represents low range of permeability, SS #1. Therefore, the capillary pressure data were correlated based on the absolute permeability using Leverret J-function. Table 6 shows a categorization scheme used for obtaining capillary pressure data. The original P_c data of the core plug #60 along with other generated P_c data were used to initialize the simulation model. Figure 21 shows the capillary pressure versus the water saturation. The associated height for the core plug #60 with the low permeability data is the highest among three sand subcategories. It should be noted that the P_c data are only shown for oil and water. The capillary pressure between oil and gas is generally ignored because of large density differences between them and there is no initial gas cap in the reservoir.

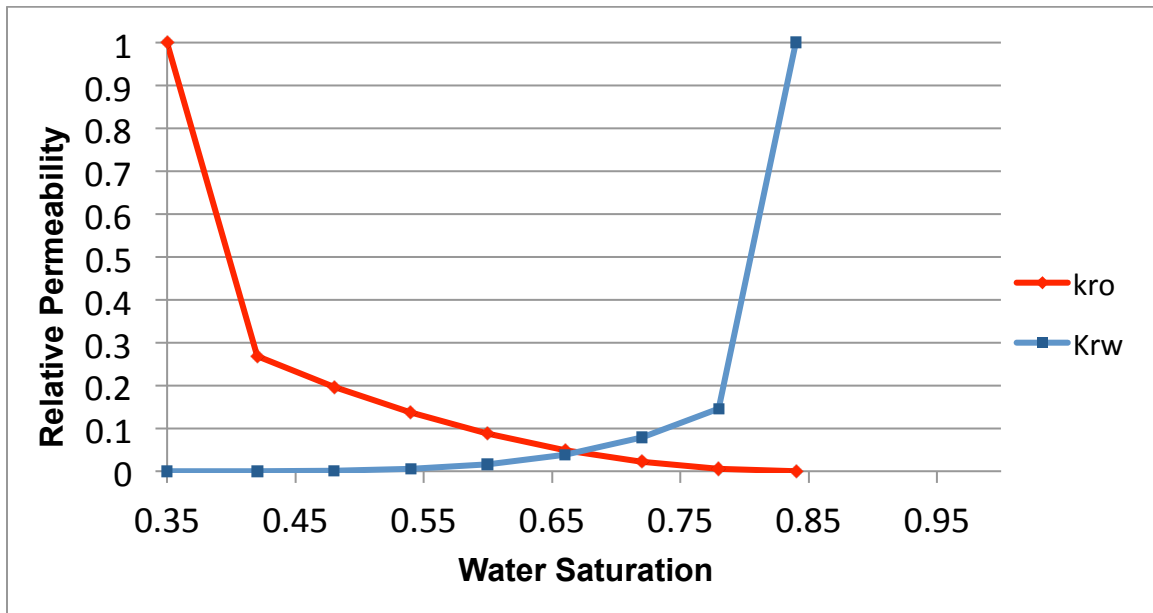


Figure 19. Oil-water relative permeability curve as input to simulator for all three sand subcategories

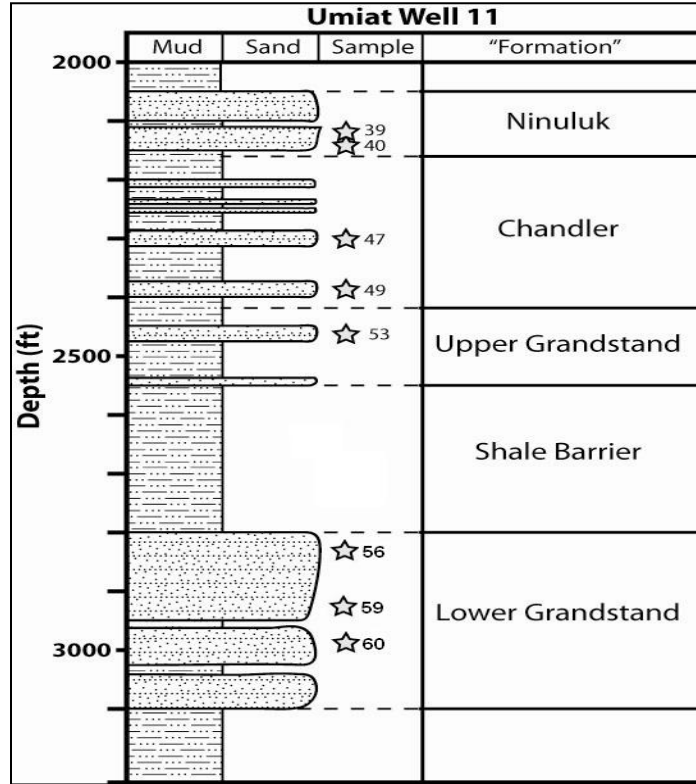


Figure 20. Lithology log of Umiat Well# 11 (Godabrelidze, 2010)

Table 6. Capillary pressure categorizations based on absolute permeability data

Absolute permeability ranges (md)	Representative K (md)	Pc categorization
$K < 1$ md	0.408	Pc-1
$1 < K < 50$	24.5	Pc-2
$K > 50$	100	Pc-3

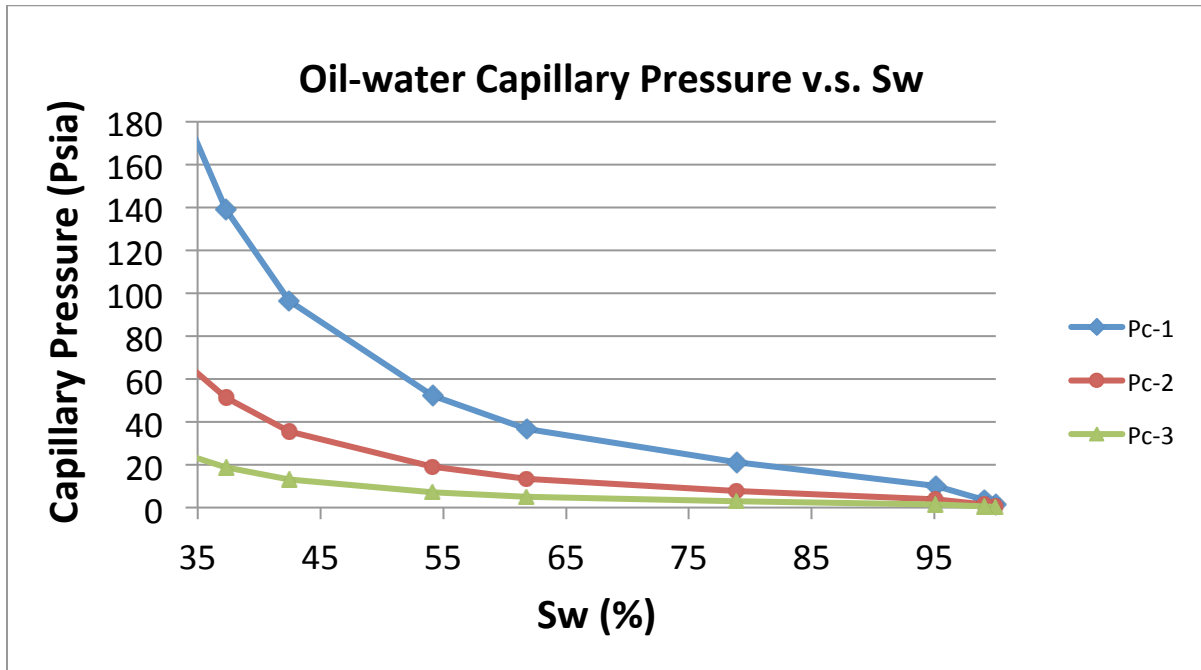


Figure 21. Oil-water capillary pressure data based on absolute permeability

The small sample of Umiat oil was severely weathered and inappropriate for traditional PVT analysis. Shukla (2011) developed a method to physically recreate a pseudo-live reservoir oil sample by comparing the composition of the weathered Umiat fluid, collected in 1940's, with a theoretical Umiat composition derived using the Pedersen method (Pedersen et al. 1989). CMG WinProp was used to simulate the phase behavior of the live oil using the Peng-Robinson equations of state (EOS). The EOS model was then tuned with measured experimental data to accurately simulate the differential liberation tests to obtain the necessary data for reservoir simulation model (Chinmay, 2011). The generated PVT data was directly entered into the simulator (Table 7). Average reservoir pressure increases by injecting gas into the reservoir, the properties were also correlated for pressures higher than the initial reservoir pressure. It should be mentioned that only one PVT region has been defined in the model assuming that the oil API gravity is the same across the reservoir.

Table 8 lists other simulation data that were used to initialize the simulation model.

Table 7. Fluid properties input data to the simulator

P (psi)	Rs (scf/stb)	Bo (rbbl/STB)	Bg (rcf/scf)	Viso (cp)	Visg (cp)
14.7	0.4339	0.9913	0.9313	8.3342	0.01022
50	7.7047	0.9939	0.2718	7.7874	0.01029
100	18.2051	0.9990	0.1456	7.1047	0.01036
150	28.0095	1.0009	0.0888	6.5106	0.01043
200	38.853	1.0054	0.0661	5.9876	0.0105
250	48.3216	1.0080	0.0522	5.5253	0.01058
300	58.5032	1.01158	0.04307	5.1151	0.01065
350	67.7079	1.0147	0.03655	4.7848	0.01073
400	67.7079	1.01453	0.03165	4.8140	0.01082
500	67.7079	1.0141	0.02481	4.8672	0.01100
600	67.7079	1.01369	0.02026	4.9207	0.01120
700	67.7079	1.01327	0.01702	4.9744	0.01143
800	67.7079	1.01287	0.01461	5.0283	0.01167
900	67.7079	1.01246	0.01274	5.0824	0.01193
1000	67.7079	1.01206	0.01126	5.1366	0.01222

Table 8. General fluid properties at initial reservoir conditions and initialization parameters used in simulation model

Parameter	Value	Source
Oil density	52.1873 lb/ft ³	Chinmay, 2011
Oil bubble point pressure	345 psi	Chinmay, 2011
Gas density	0.04539 lb/ft ³	Chinmay, 2011
Water phase density	62.4 lb/ft ³	http://www.simetric.co.uk
Water FVF	1.002	McCain, 1990
Water compressibility	3.06e ⁻⁶ 1/psi	https://www.fekete.com
Water viscosity	1.78 cp	Beal, 1964
Reservoir temperature	26	Baptist, 1960
Reservoir pressure	350 psia	Baptist, 1960
Reference depth	900 ft	Arbitrary
WOC depth	1500 ft	Third party (Linc Energy)

A wagon-wheel pattern was considered as the most efficient means of accessing the maximum amount of the Lower Grandstand reservoir interval while minimizing the surface footprint. In the proposed pattern, one vertical well in the center along with two dual lateral injectors in the north and south at the top of the Lower Grandstand sand supports pressure for a combination of four dual lateral producers at the bottom of the interval, each one angled at 36 degree in a square mile spike configuration. The wells had about 1500 ft length of 4.5” wide open hole completion across the productive area with a total well length of 3500 ft. To reduce surface impact and the cost of infrastructure, only 6-10 pad locations are being considered. A total combination of 80 producers and 25 injectors, controlled by flowing bottom hole pressures of 80 and 450 psia, respectively, were used in the simulation model. Figures 22 and 23 show the well configuration used in the simulation runs. Table 9 includes the well parameters used in the simulation model.

Table 9. Well model parameters used in the simulation base case model

Well Parameter	Producer	Injector
Total depth (ft)	3000	3000
Length of lateral (ft)	1500	1500
Wellbore radius (inch)	2.5	2.5
Completion type	Open-hole	Open-hole
Minimum Flowing Bottom-hole Pressure (psi)	80	-
Bottom-hole Gas-injection pressure (psi)	-	400
Skin Factor	0	0

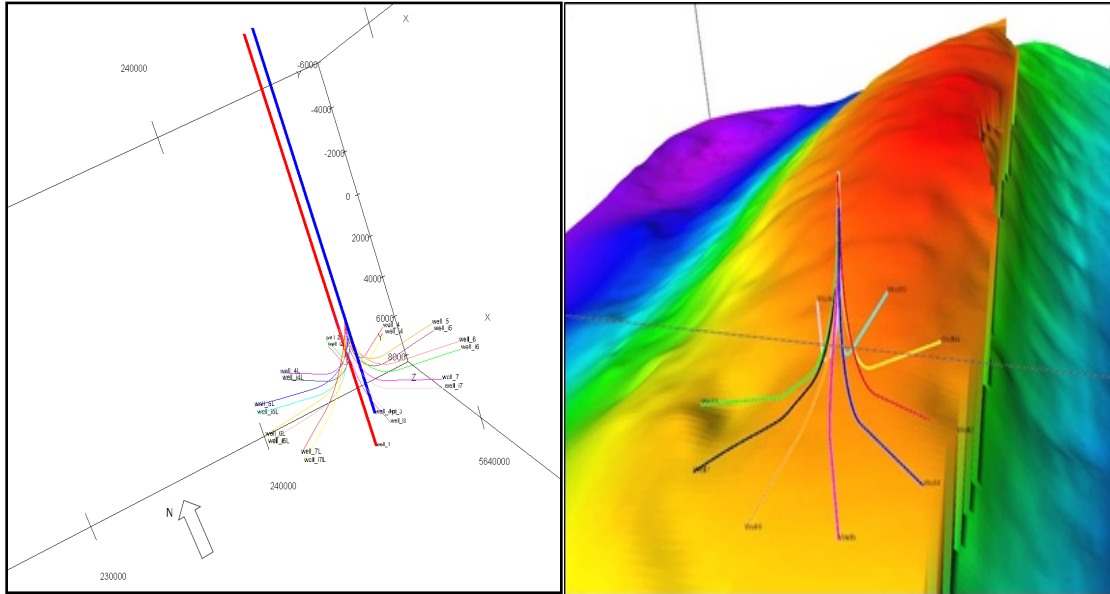


Figure 22. Dual lateral well model, note the red line in the left picture, shows the injection well representative and the blue line shows the production well representative

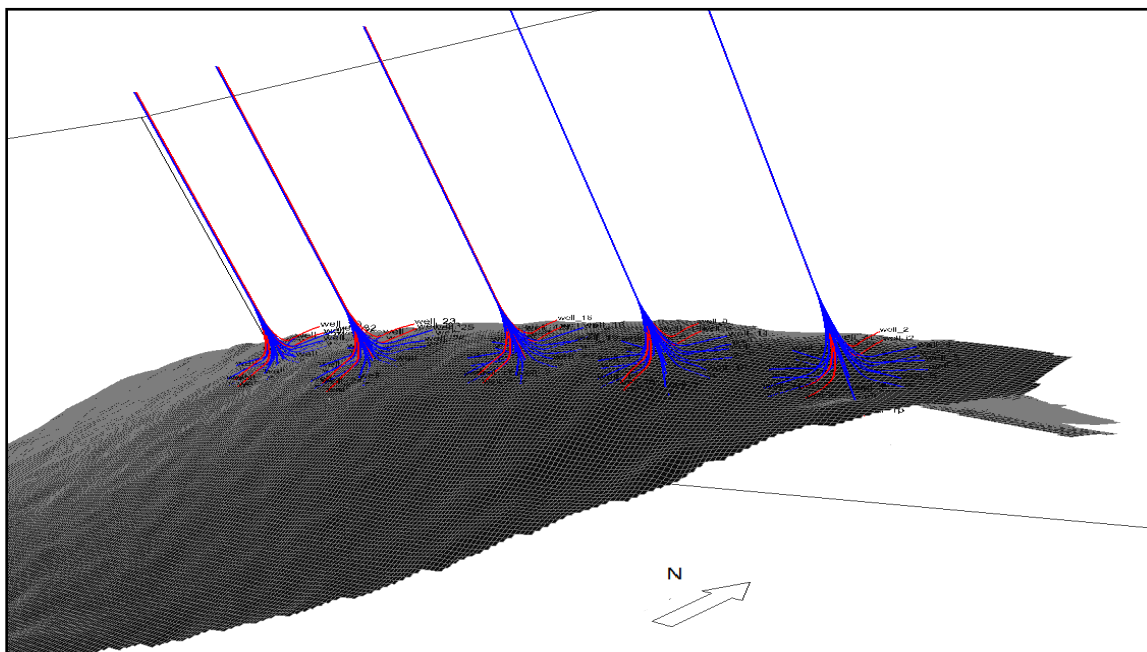


Figure 23. The final well profile used in the reservoir simulation. Note the blue lines show the production wells and the red lines show the injection wells

The approach developed in this study is based on two points: 1) optimization such as well length, operating condition, injection pressures and 2) sensitivity analysis on uncertain parameters such as permeability anisotropy and relative permeability end-points.

A base case model was defined to observe the performance of the reservoir under gas injection. Table 10 provides the parameters used in the base case simulation model. The model was run with all the wells producing and injecting against pressure limitations only, no limit on GOR.

The injection of 100% methane (CH₄) and production commenced at the same time. The producers and injectors were operating under minimum and maximum bottom hole pressure of 80 and 400 psi, respectively.

Table 10. Simulation parameters used in the base case model

Parameter	Description
Upper production wells	Completed open hole at layer 18
Lower production wells	Completed open hole at layer 32
Upper injection wells	Completed open hole at layer 1
Lower injection wells	Completed open hole at layer 21
Simulation dates	01/01/2013 to 01/01/2063
Economic limit for each well	5 STBD
Gas lift	Not applicable
Permeability anisotropy ratio	0.45
Horizontal well length	1500 ft
Grid size dimensions	200 ft * 200 ft
Flowing bottom-hole pressure (FBHP)	80 psi
Bottom-hole injection pressure (BHIP)	400 psi
Initialized Reservoir Pressure	350 psi
Oil bubble point pressure	345 psi
Reservoir Temperature	26° F
WOC Depth	1500 ft

Results and discussion

There are influential parameters that can be easily controlled such as injection pressure, within the range dictated by safety and avoiding unwanted fracturing, and length of horizontal legs. Using simulation study the impact of each of these parameters can be explored and the optimum values can be determined. For all simulation results, four sets of plots are presented, field cumulative oil production vs. time, field monthly oil rate vs. time, producing GOR vs. time, and average reservoir pressure vs. time. The result of modeling will be used to evaluate the “if’s” and to work out the “how’s” of the multi-million development investment.

Horizontal Well Length

In addition to the horizontal well length of 1500 ft used as base case, a case with horizontal length of 3000 ft was also simulated. We did not investigate if such length is reachable or not. The result for field cumulative oil recovery, oil rate, pressure response, and the producing GOR are shown in Figure 24 and 25. The cumulative oil production in model with smaller well length (the base model) is 4 MM STB smaller than the cumulative oil production in the model with longer horizontal well length which is not significant. This could be due to drainage area of the well model and its relation to the vertical fluid flow in the vicinity of the wellbore. It is important to note that the pressure drops along the horizontal leg have not been included in this study. Nevertheless, friction losses for different well lengths and flow regimes were investigated by use of Hagdorn and Brown correlation (1964) for a constant borehole size of 2.5 inch and are presented in Figure 26. Based on literature (Novy 1995), if the loss of oil rate is less than 10%, then the pressure loss should be ignored. That means if we design our horizontal well in a way that pressure drops are high that they cause our production to drop more than 10%, we should consider a new design. Such well length corresponding to this critical pressure drop is called: Length of Significant Pressure Drop (L_{sf}). It can be mathematically shown that when friction reduced flow rate (q) by at least 10%, the wellbore pressure drop is more than 15% of drawdown. Given the low reservoir pressure in Umiat, we concluded that 1500 ft of horizontal well length is the best case scenario applicable to Umiat reservoir conditions.

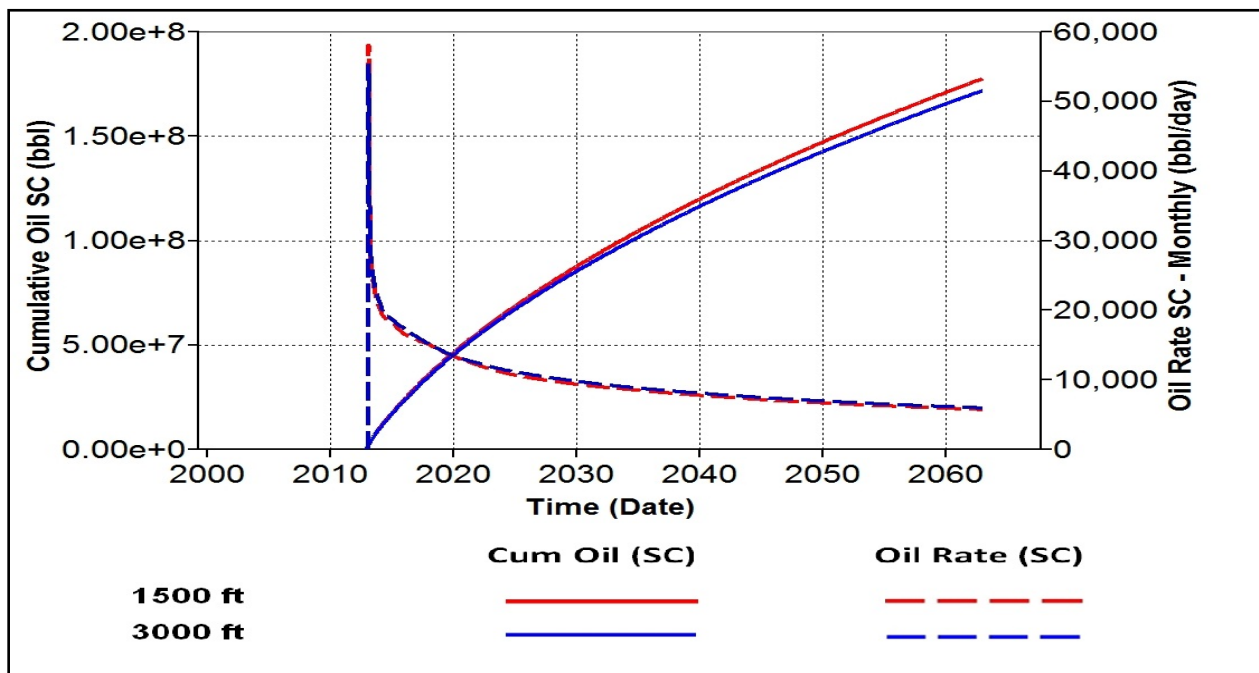


Figure 24. Field cumulative oil production and field oil rates for two different horizontal well lengths

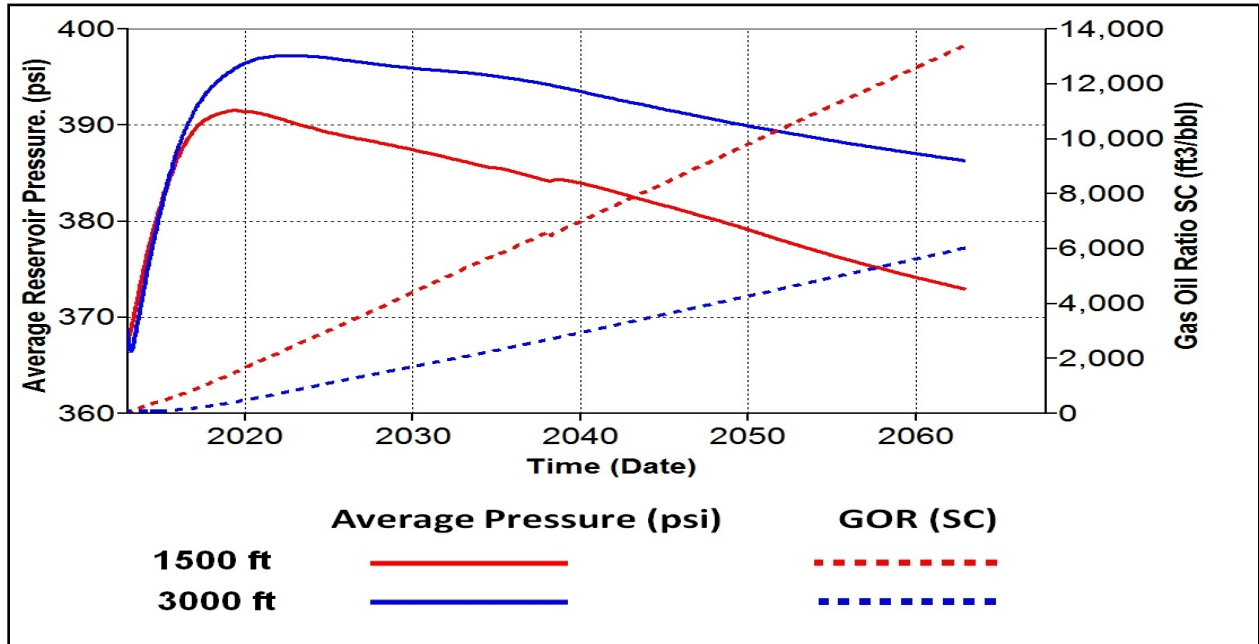


Figure 25. Average reservoir pressure and field producing GOR for two different horizontal well lengths

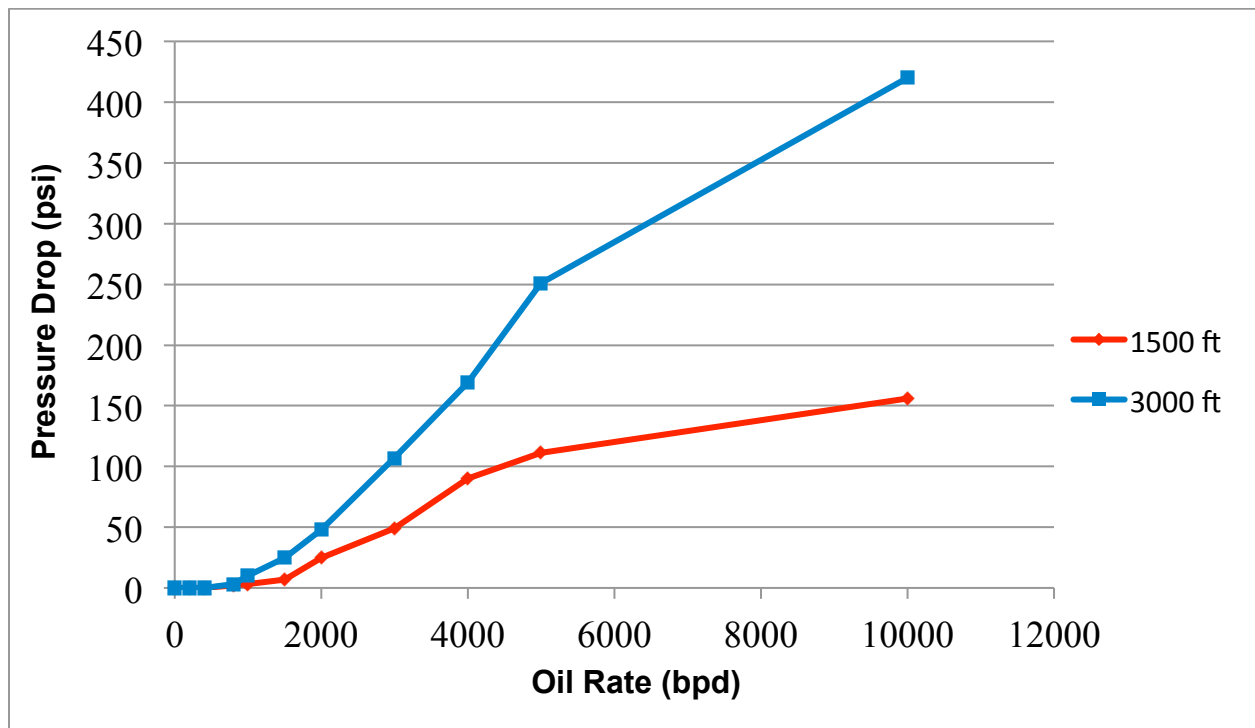


Figure 26. Pressure drop versus oil rates for two different horizontal well lengths

Injection Pressure

Gas injection was considered as an optimization parameter because the sweep efficiency is a function of injection pressure (Roebuck 1987) keeping all other parameters constant. Higher gas injection rates can increase oil production rate by increasing pressure draw down. A good gas injection operation can result in increased oil recovery and reservoir production characteristics such as decreasing depletion time and increasing well productivity (Roebuck 1987). Three models with different gas injection pressures were designed and run. Figures 27 and 28 show the simulation results. The case with no gas injection gives the lowest oil recovery. In terms of average reservoir pressure, as expected, the case with higher gas injection maintains a higher reservoir pressure compared to the other cases. Although the case with BHIP of 600 psi gives the highest oil recovery, since there was no information about the fracture gradient, the best case was selected as the one with BHIP 400 psi as the safest option. Exceeding the fracture gradient could have catastrophic consequences on well integrity and the actual fracture gradient will need to be determined to enable the design of the injection plan.

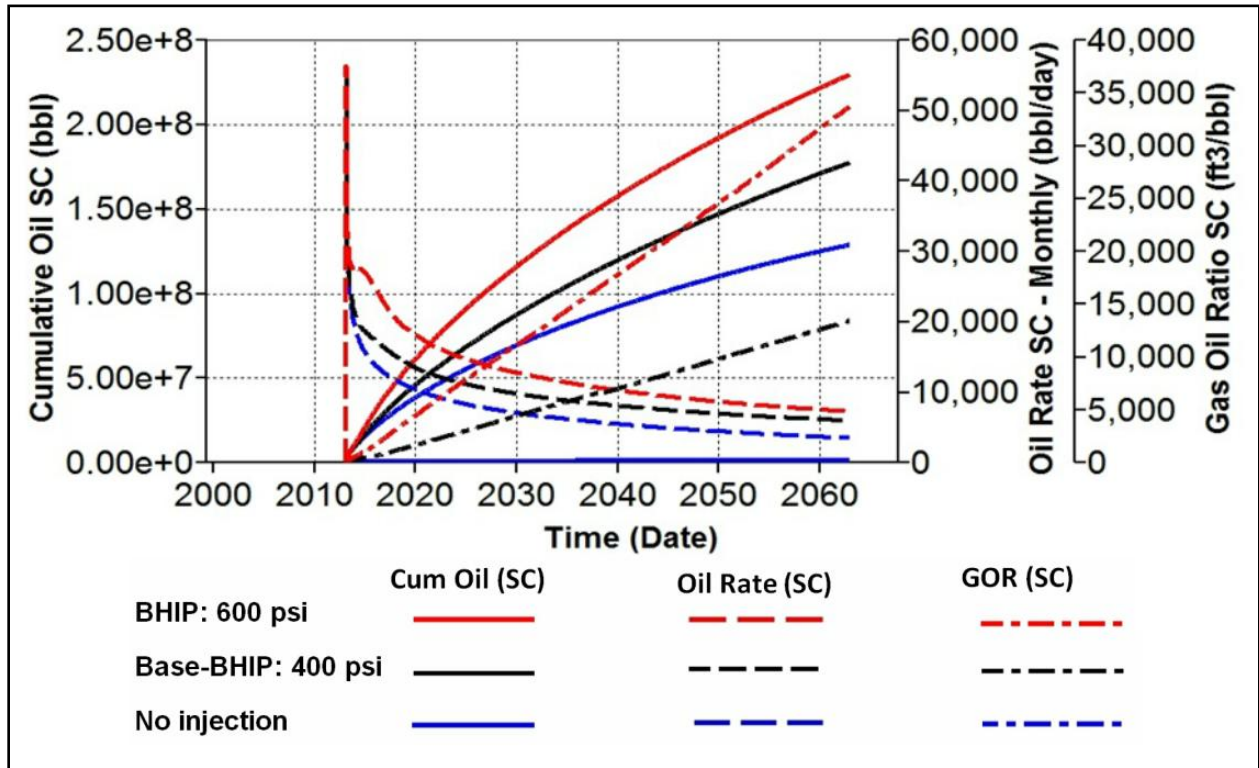


Figure 27. Field cumulative oil production, field oil rate, and field producing GOR for different gas injection pressures

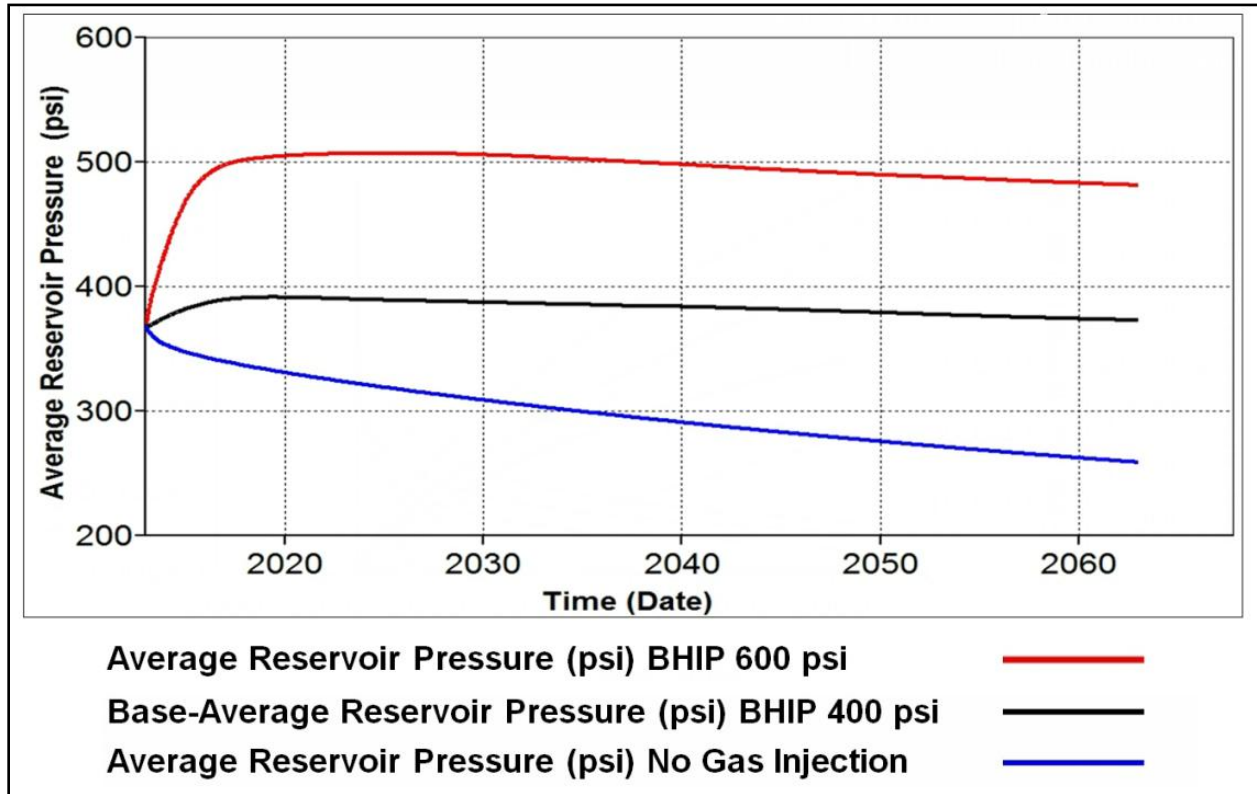


Figure 28. Average reservoir pressure for different gas injection pressures

Sensitivity Analysis

Since several input data such as relative permeability and permeability anisotropy have been estimated based on limited data, sensitivity analysis is a helpful tool in defining the impact of their variation on the oil recovery. Sensitivity to some end point relative permeabilities to oil and gas as well as different ranges of permeability anisotropy ratios are presented here.

Permeability Anisotropy

New data indicated the reservoir has six facies associations with distinctive permeability trends. Regional and local observations suggest that three sets of fractures may occur at Umiat. These trends combined with diagenetic effects and natural fractures impart strong vertical and horizontal permeability anisotropy to the reservoir. Presence of natural fractures and their orientation with respect to horizontal well plane (Figure 29) can enhance the flow if open or can block if filled with ice or cement (Hanks et al., 2012).

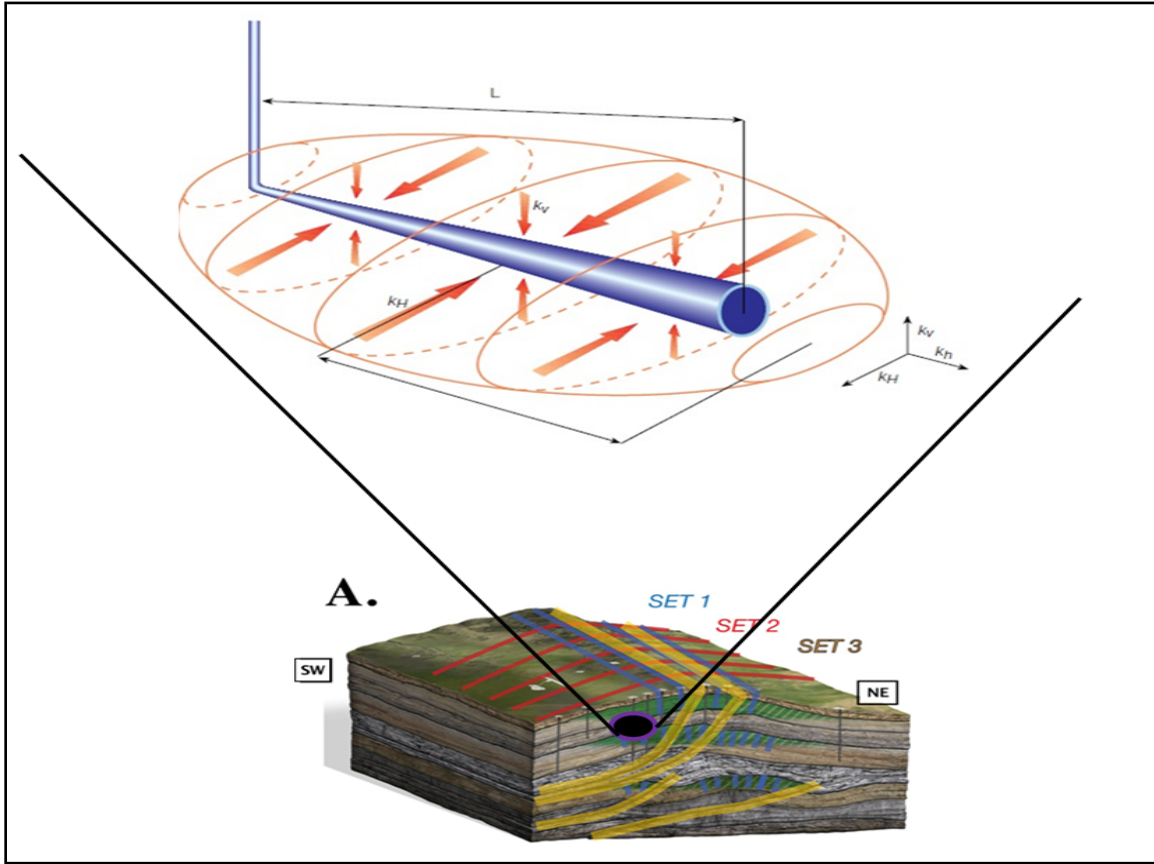


Figure 29. Natural fractures and their orientation with respect to permeability anisotropy in horizontal wells (Modified after Hanks et. al 2012, Ayan et al. 1994)

Since there was no data on flow characteristics of these fractures such as their effective permeability, spacing, shape factor, etc., we assumed that permeability anisotropy ratios could mimic the effect of the fractures and their contribution to flow. The author is aware that this is not the best assumption and the effect of natural fractures should be investigated in a different study. In addition to the base case permeability anisotropy ($k_v/k_h = 0.45$), a set of six permeability anisotropy ratios were selected and incorporate into the geologic model. The ratios were selected as low as 0.05 to account for little exhibition of vertical natural fractures in the system, to as high as 1.25 for extreme vertical communications between layers. The grid system for each case was populated and imported to the simulator. All the other parameters were kept identical to the base case model. Figures 30 and 31 show the simulation results. The results show that higher anisotropy ratios although leads to less average reservoir pressure, but result in higher oil production. Smaller anisotropy ratios although have increased average reservoir pressure, their gas injection performance is further limited by ability of gas to move and displace the oil. The field producing gas oil ratio for all the cases increases. For the case with smallest anisotropy ratio, the producing gas is restricted by limited vertical flow of gas towards the horizontal producers. The plots show that there is no significant change in the oil recovery, oil rates, and average reservoir pressure when the anisotropy ratio changes from 1 to 1.25.

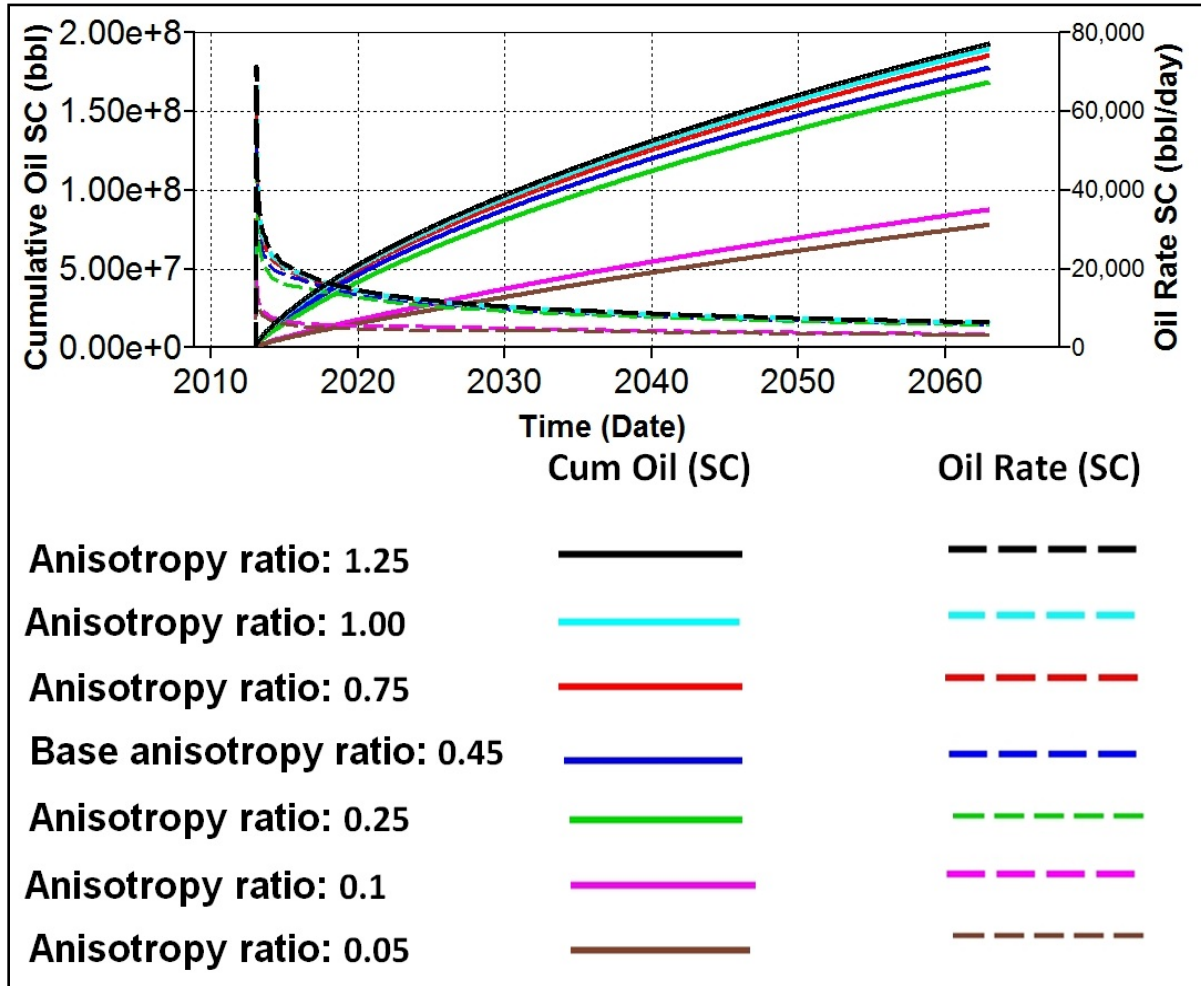


Figure 30. Field cumulative oil production and field oil rate for different permeability anisotropy ratio

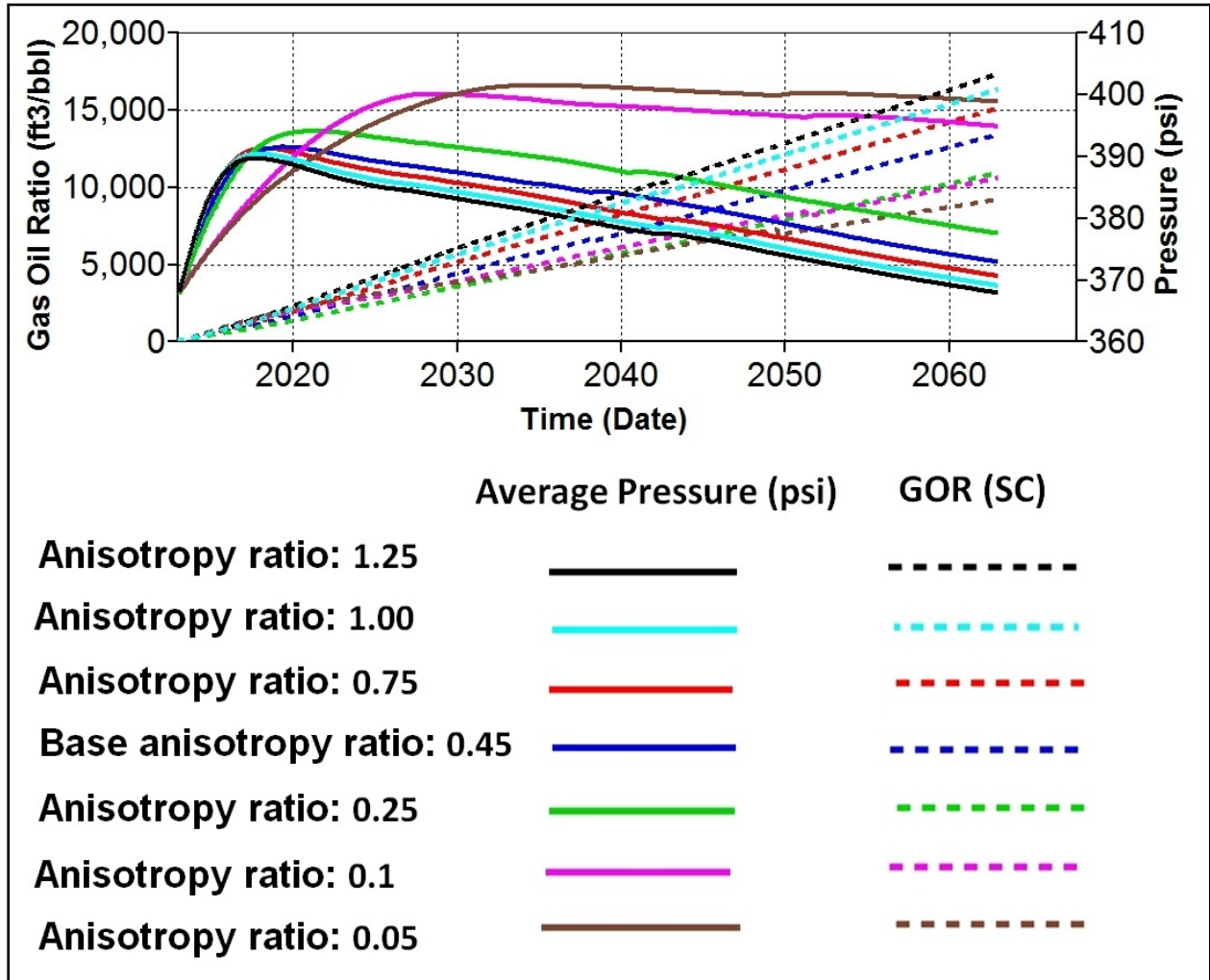


Figure 31. Average reservoir pressure and field producing gas oil ratio for different permeability anisotropy ratios

End Point Relative Permeability and Residual Saturation

For a given simulator and known reservoir geology, endpoint saturations and relative permeabilities strongly affect the results. Inaccurate consideration of relative permeability data can result in underestimation or overestimation of oil recovery. The relative permeability to gas at the residual oil saturation for the SS #1 was significantly low. Thus, sensitivity to the K_{rg} at the residual oil saturation was considered. Because the only relative permeabilities to oil and gas was available for SS #1, Brooks and Corey (1964) correlation was used to estimate the relative permeabilities to oil and gas for SS #2 and #3. Table 11 gives the data for the end points used in the base case simulation model. Residual oil saturation, critical gas saturation, and end point relative permeability to gas at residual oil saturations were considered for sensitivity analysis. The residual oil saturation is important in knowing what percentage of the oil is mobile and what percentage of it remains behind in swept zone. Usually, the sand subcategory with smaller pore size has higher residual oil saturation (Brooks and Corey, 1964). The critical gas saturation and

the end point relative permeability to gas at the residual oil saturation also play an important role in the mobility of gas, gas breakthrough and producing GORs.

Table 11. End point relative permeability and residual saturations in the base case model

Sand Subcategory	S_{or}	S_{gc}	K_{rg}
1	0.16	0.32	0.0028
2	0.25	0.15	0.56
3	0.20	0.02	0.60

Table 12 presents the parameters used in the sensitivity analysis for different cases. The values were chosen in a way so that the shape of the relative permeability curve changes significantly compared to the base case. The following cases were considered:

- Case 1: Change in S_{or} for all the sand subcategories
- Case 2: Change in S_{gc} for SS #2 and #3
- Case 3: Change in end point K_{rg} for SS #1
- Case 4: Change in end point K_{rg} for SS #2 and #3

Each case was run separately and compared with the base case model. The results are shown in Figures 32 through 39.

Table 12. End point relative permeability and residual saturations used in sensitivity runs

Sand Subcategory	S_{or} (case #1)	S_{gc} (case #2)	K_{rg} (case #3)
1	0.24	0.32	0.03
2	0.20	0.10	0.56
3	0.16	0.05	0.60

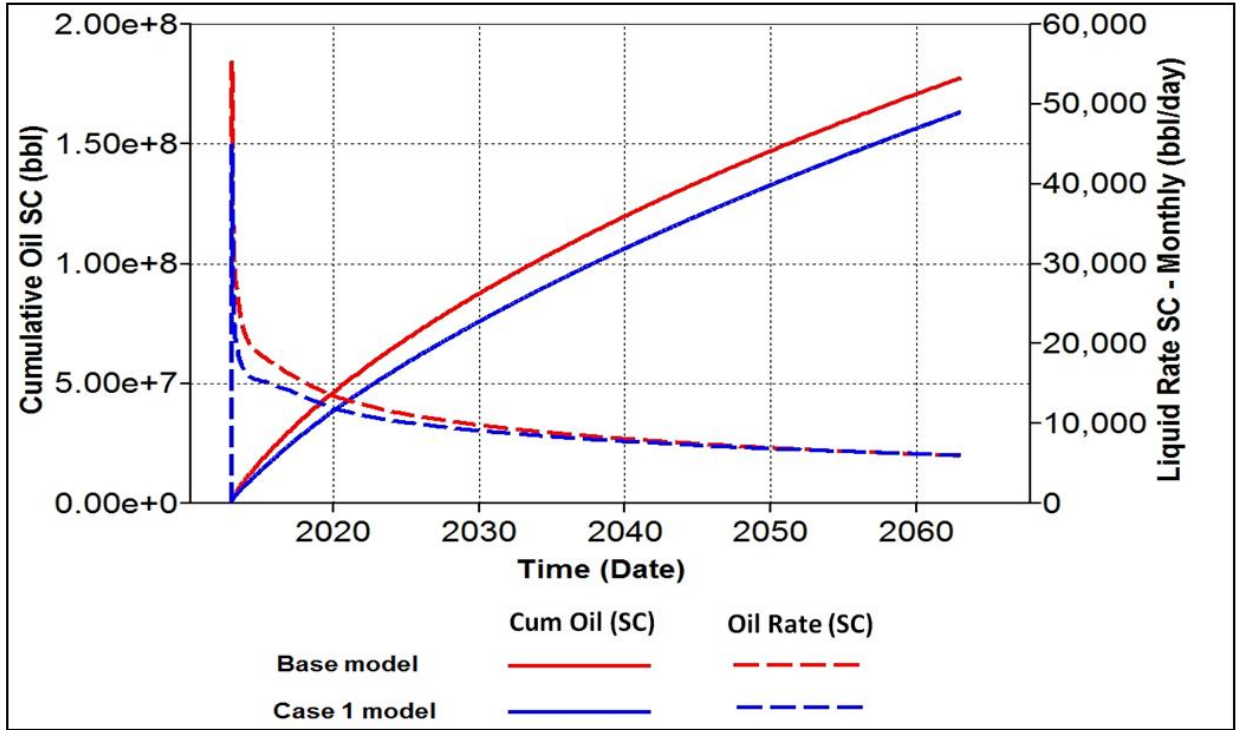


Figure 32. Field cumulative oil production and field oil rate for case #1

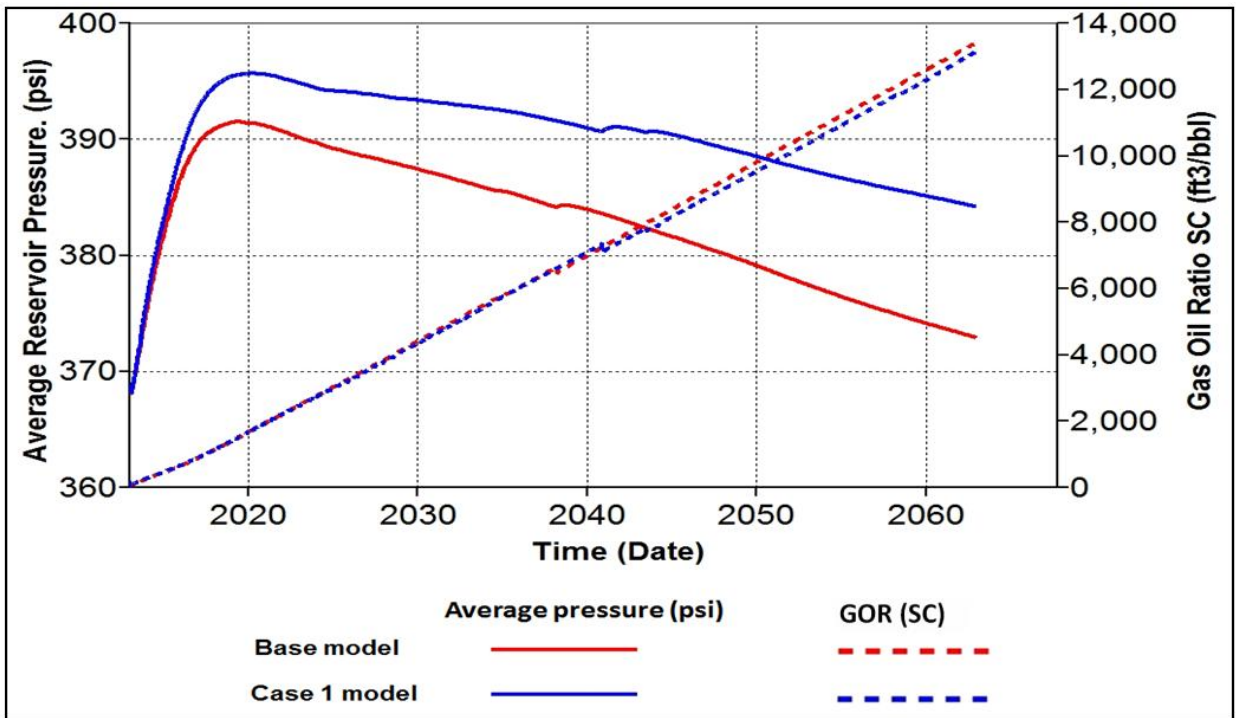


Figure 33. Average reservoir pressure and field producing gas oil ratio for case #1

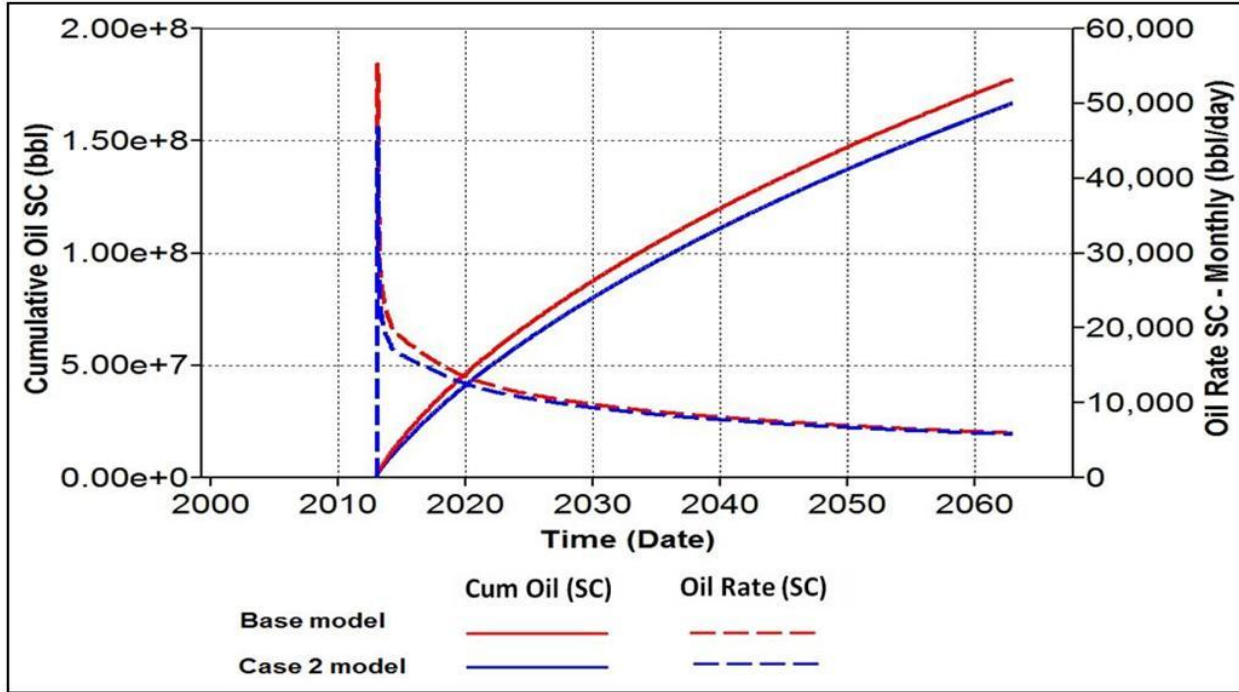


Figure 34. Field cumulative oil production and field oil rate for case #2

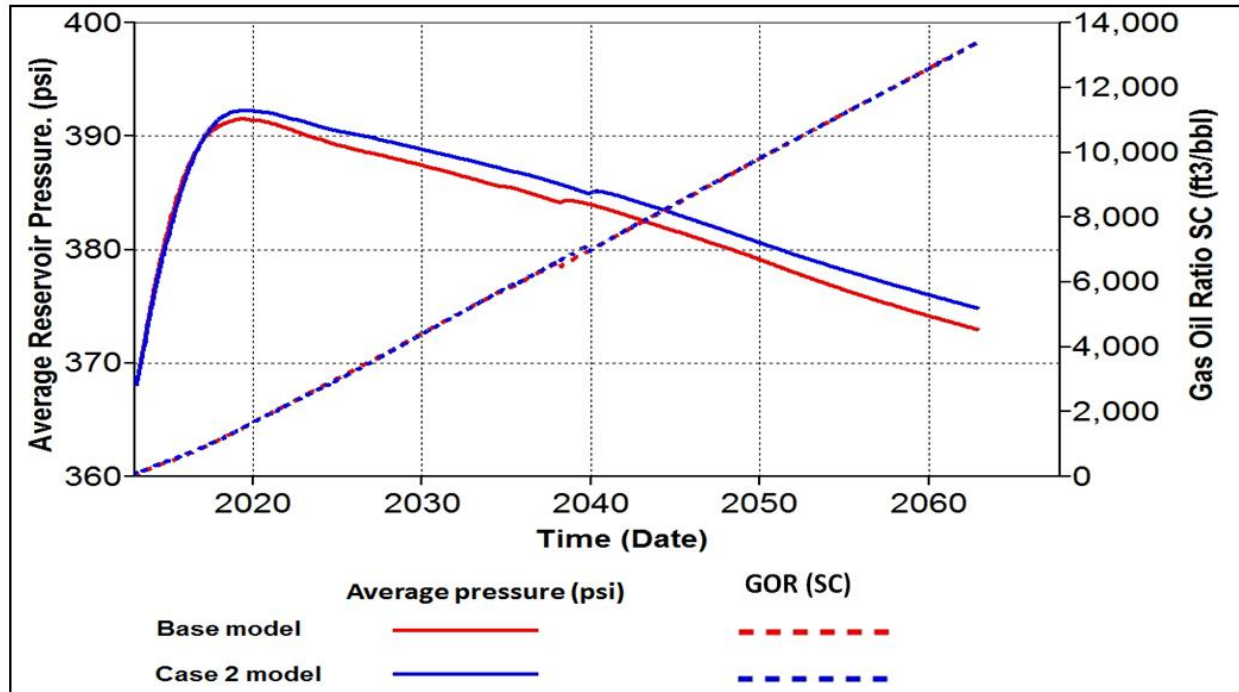


Figure 35. Average reservoir pressure and field producing gas oil ratio for case #2

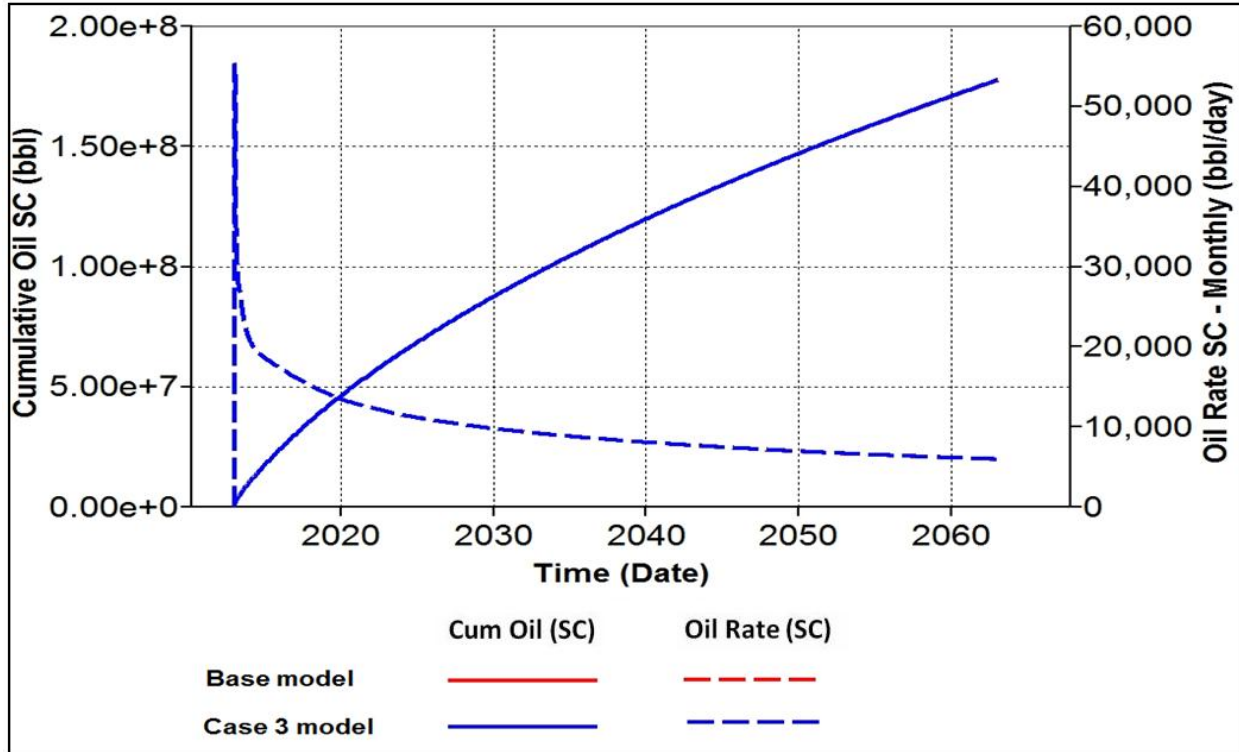


Figure 36. Field cumulative oil production and field oil rate for case #3

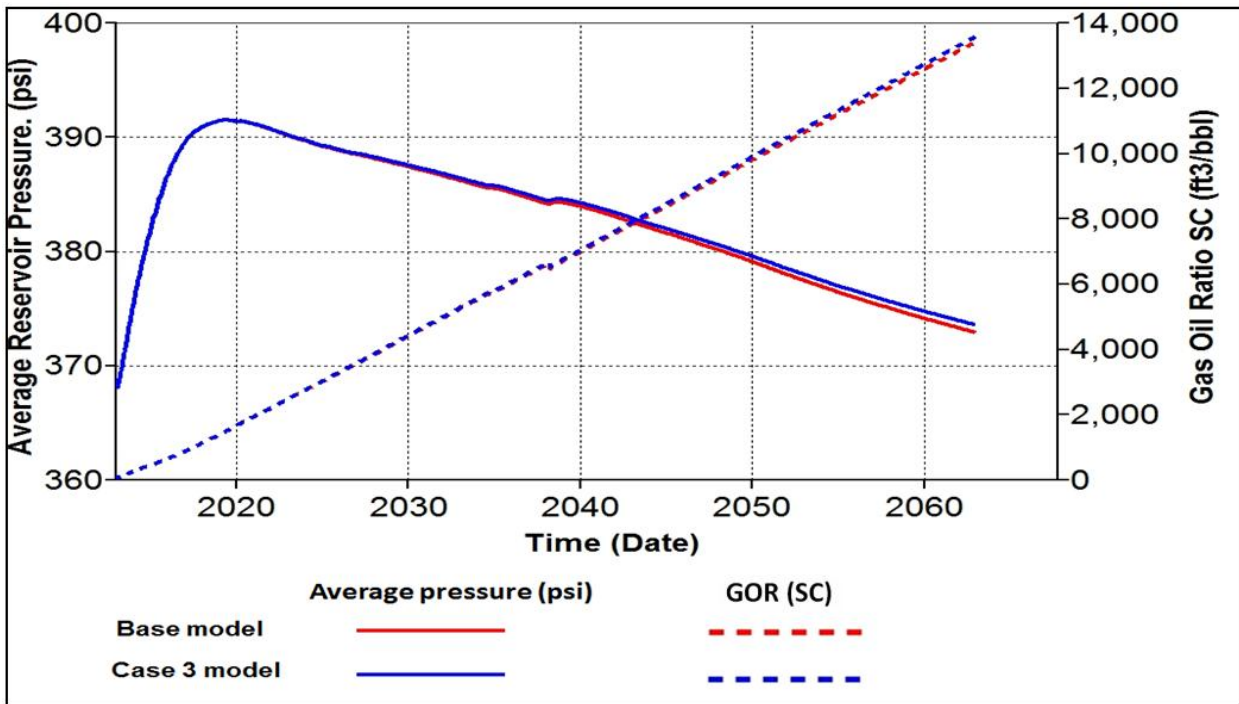


Figure 37. Average reservoir pressure and field producing gas oil ratio for case #3

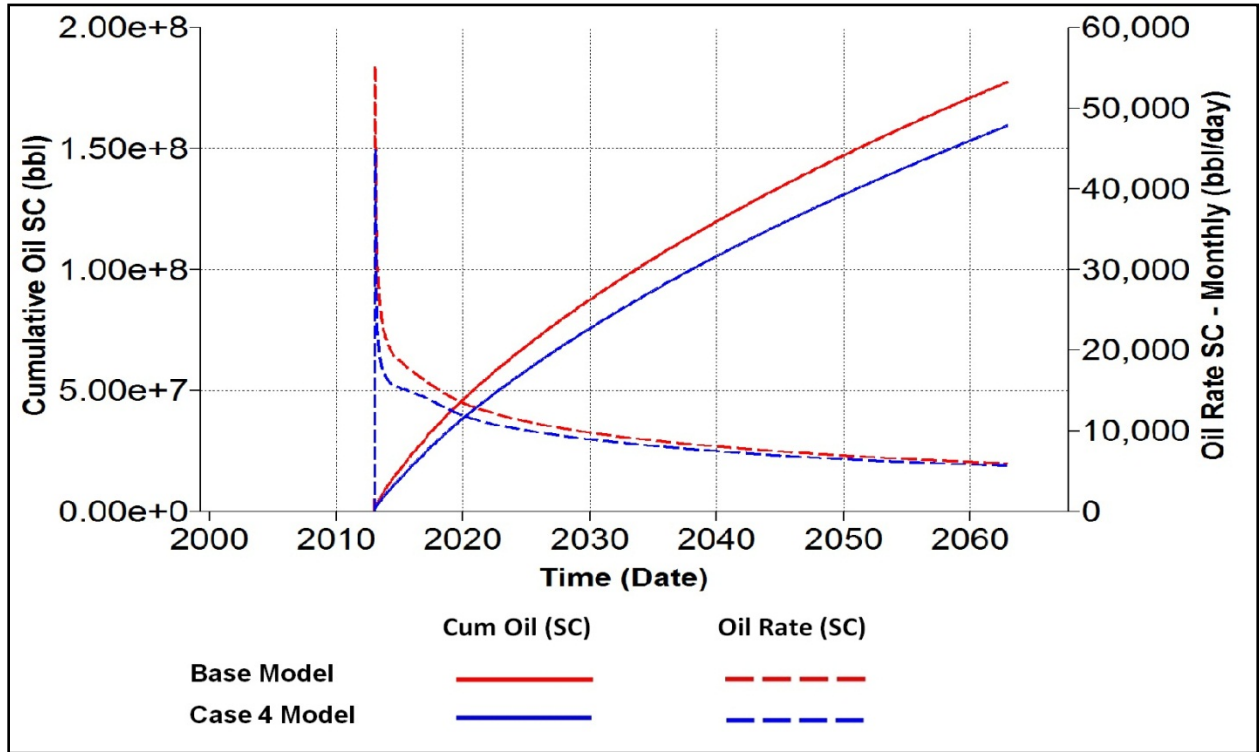


Figure 38. Field cumulative oil production and field oil rate for case #4

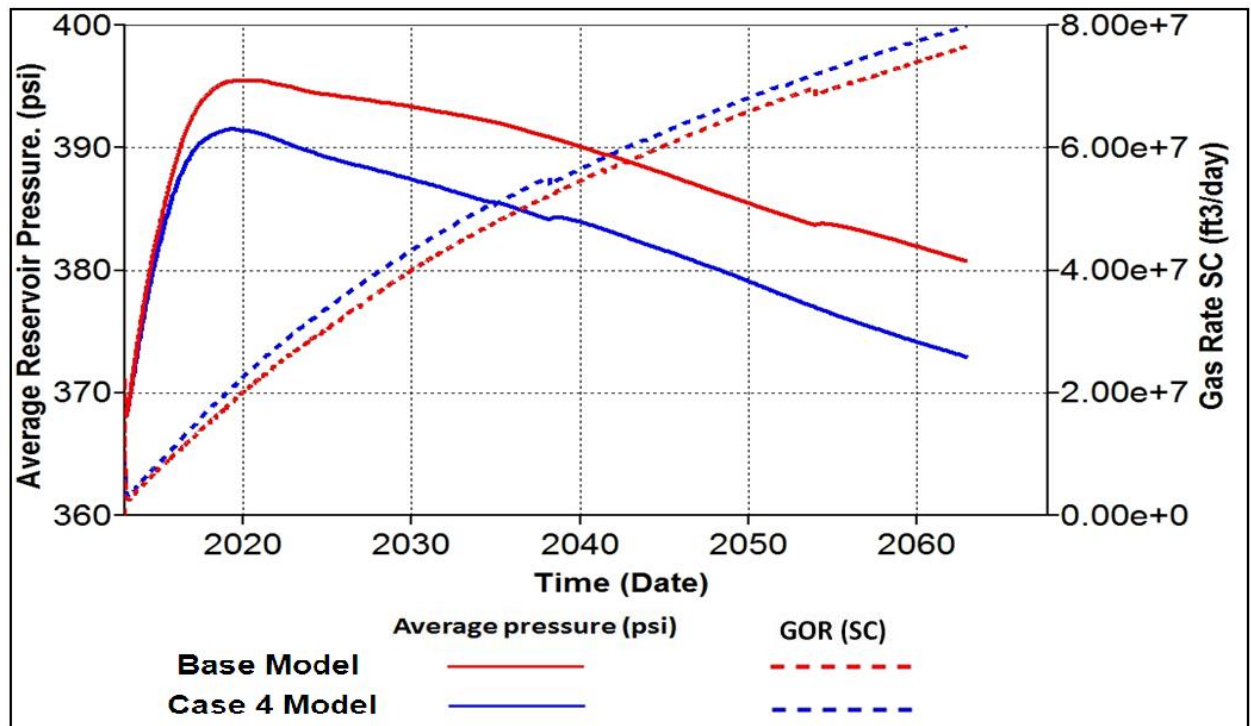


Figure 39. Average reservoir pressure and field producing gas oil ratio for case #4

Figure 32 shows that when the residual oil saturation in rock type #1 is increased by about 50% and residual oil saturation in SS #2 and #3 are decreased by 20% in the model, then the cumulative oil production decreases by about 10 MMSTB (7% reduction in the ultimate recovery factor). This shows that although the residual oil saturation in SS #2 and #3 have been reduced, an increase in the residual oil saturation of SS #1 has caused the oil recovery to drop by 7%. There is no major change in the producing GOR, but the average reservoir pressure increases by the aforementioned changes in the residual oil saturation of three rock types. The pressure trend is the same but the final average reservoir pressure increases by 3% (about 10 psi) in the case #1 than the base case (Figure 33). Figure 34 shows that the oil recovery is also sensitive to changes in critical gas saturations. When the critical gas saturation in rock type #2 is decreased by 33% and increased by about 150% in rock type #3, the ultimate oil recovery is decreased by 6%. There is no significant change in the producing GOR (Figure 35). The reason for this might be the producing gas migrates upward into formation of a gas cap. Figures 36 and 37 demonstrate that the changes in relative permeability to gas at the residual oil saturation in SS #1 does not have significant impacts in oil recovery, average reservoir pressure, and the producing GOR. This might be due to extremely low permeability of SS #1. However, when the relative permeabilities to gas at the residual oil saturation in SS #2 and #3 are increased by 25% and 33% respectively, there is a significant increase in the oil recovery and a sensible reduction in the average reservoir pressure. The ultimate oil recovery decreases by 9% (Figure 38) and the final average reservoir pressure decreases by 3% (about 8 psia) (Figure 39).

Conclusions

A static property model of Umiat reservoir was built that incorporated new geologic data, including porosity and permeability anisotropy trends and structural geometry. A Monte Carlo simulation of the range of STOOIP in the most prospective reservoir interval, the Lower Grandstand, yielded a range of STOOIP from a P90 (low) estimate of 739 million barrels to a P10 (high) estimate of 2437 million barrels. The P50 value for STOOIP was 1527 million bbls

A cold gas injection method was proposed as the development plan and simulation studies focused on the LGS formation that contained the better quality rocks. With no distinguishable trends in the porosity and permeability data and wide variations in permeability, three sand subcategories were defined and used to assign capillary pressure curves. Rock and fluid data in presence of ice were either measured or calculated and were imported into a simulation model.

In order to minimize the surface footprint, the development plan uses a wagon wheel dual lateral well configuration with 80 producers and 25 injections from 5 surface pads. This well design was incorporated into the simulation model. Horizontal well length and injection pressure were optimized to be 1500 ft and 400 psi respectively.

For the base case with bottom-hole injection pressure 400 psi and a 5 bpd production constraint, simulation results indicated the oil recovery will be about 12%. For the bottom-hole gas injection pressure 600 psi, the recovery would be 15%. The higher pressure at which we inject gas, the higher the average reservoir pressure and the more oil production. When the BHIP was set to 600 psi, the results show about 30% increase in the cumulative oil production compared to the case with BHIP 400 psi. When there is no gas injection, the recovery factor for the base case was

about 8%, but with BHIP 400 psia the recovery increased to about 12%. This shows an incremental oil recovery of about 50 MMSTB in the base model. However, using a higher injection pressure depends on matrix fracture gradient. Overpressuring the reservoir rock may result in fracturing the reservoir that may cause reduction in oil recovery due to early breakthrough of gas.

The simulation results demonstrate a reduction in oil recovery by 18% compared to the base case when producing GOR is limited to 5000 scf/STB. This suggests that the operator needs to plan for gas producing facilities in order to handle large volumes of produced gas.

The impact of potential fractures was incorporated into the simulation by testing the sensitivity of the reservoir performance to permeability anisotropy (K_v/K_h). Models with different permeability anisotropy ratios were built in order to account for vertical flow due to open natural fractures. As expected, higher anisotropy ratios resulted in higher oil production and lower average reservoir pressures after 50 years of gas injection. The findings show that there is no significant change in the oil recovery, oil rates, and average reservoir pressure when the anisotropy ratio changes from 1 to 1.25. The case with anisotropy ratio 0.75 gives about 4 MMSTB higher oil production compared to the base case. When the anisotropy ratio drops from 0.25 to 0.1, the cumulative oil production significantly decreases by more than 45%. There is a similar trend in the average reservoir pressure. When the anisotropy ratio falls from 0.25 to 0.1, the average reservoir pressure increases by more than 6%. This suggests that less fluid has been displaced in the reservoir.

Compared with the base case model, when the residual oil saturation changes in all sand subcategories (SS) (an increase of 50% in SS #1 and a decrease of 20% in SS #2 and #3), cumulative oil production decreases by about 10 MMSTB (i.e., a 7% reduction in the cumulative oil production).

A sensitivity analysis of the reservoir performance to end point relative permeabilities showed the profound impact of accurate relative permeability data on projected oil recovery and reservoir pressure. Simulation results indicate that oil recovery and average reservoir pressure are very sensitive to the end point relative permeability to gas in the SS #2 and #3, but not for the SS #1. This result emphasizes to the need for accurate relative permeability data (especially the relative permeability to oil and gas) for accurate projections

Project summary and Conclusions

Introduction

Shallow oil production in arctic regions must contend with a variety of unique production issues, including low, potentially sub-freezing, reservoir temperatures. Consolidated reservoirs located in permafrost (ground that has remained below 0°C for at least two years) may have production challenges even if the oil is light and not biodegraded. While deemed uneconomic in the past, horizontal drilling technology and higher oil prices may make these shallow accumulations economic if the reservoir character and rock and fluid behavior under these low temperature and pressure conditions can be adequately understood and managed.

Umiat field of the National Petroleum Reserve-Alaska (Figure 1) is an example of such a shallow, light oil accumulation where most of the reservoir is within permafrost. Umiat field was discovered during the initial exploration of northern Alaska in the 1940's and 50's (Collins, 1958). Eleven Umiat wells were drilled between 1946-1953 (Figure 2); initial estimates of primary recoverable reserves ranged from 30 to over 100 million bbl, with an average of about 70 million bbl (Baptist, 1960). Oil quality is high (37°API), but the reservoir is very shallow (275-1055 ft), with part of the reservoir within the permafrost. Moreover, reservoir pressures are very low, with small quantities of solution gas. These factors along with the remote location and the lack of a drilling technology to economically extract oil from a shallow, frozen reservoir, have thus far precluded Umiat development.

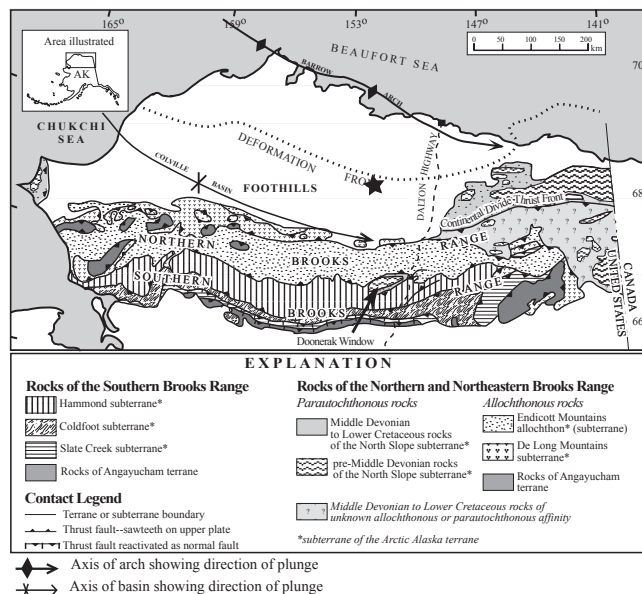


Figure 1. Geologic map of northern Alaska. Umiat field (star) is located at the leading edge of the Brooks Range fold-and-thrust belt. Map modified from Moore et al., 1994.

The advent of modern drilling and production techniques has made Umiat and similar fields in northern Alaska attractive exploration and production targets (Watt et al., 2010). Modern horizontal drilling techniques have opened the possibility of developing such a shallow reservoir by drilling long horizontal wells which allow for producing at an economic rate and in some cases reducing the required number of wells and the surface footprint. However, the unusual reservoir conditions pose a significant challenge and source of uncertainty. Little is known about how to produce light oil from a frozen, albeit lithified, reservoir and there is no information on the flow behavior of a rock/ice/light oil system at low pressures.

This paper summarizes the work of an interdisciplinary team of geoscientists and petroleum engineers to build an accurate geologic model of the reservoir and collect low temperature rock and fluid property data that were then used to develop a robust simulation model of the field where potential production techniques could be evaluated. The original cores from the Umiat legacy wells (Collins, 1958) provide a valuable subsurface database with which to evaluate the reservoir interval. Detailed analysis of nearby surface exposures of the reservoir interval were combined with modern core descriptions to develop a high-resolution facies model of the reservoir in order to assess both vertical and lateral variability within the reservoir. Cores and outcrops were evaluated to determine if natural fractures could play a role in reservoir permeability. Experimental work on existing samples of Umiat reservoir sandstones and on Berea sandstone samples determined the relative permeability of oil and gas in the presence of ice. Experimental and modeling work on the only remaining sample of Umiat fluid provided information on the potential fluid properties of the Umiat oil at reservoir conditions. These data were integrated into a simulation model to test the performance of cold-gas injection as a recovery technique.

Geology of Umiat field

Umiat is a thrust-related anticline at the leading edge of the Brooks Range fold-and-thrust belt (Figure 1 & 2), with the reservoir consisting of multiple shallow marine and deltaic sands of the Cretaceous (Albian-Cenomanian) Nanushuk Formation (Molenaar, 1982; Figure 3). The main reservoir interval at Umiat lies within the Albian-Cenomanian Nanushuk Formation, a unit that is widespread in the subsurface of the North Slope and in outcrop along the Brooks Range fold-and-thrust belt (LePain et al., 2009). Regionally, the Nanushuk Fm. consists of topset deltaic facies associated with deep marine mudstones of the Torok Fm. (Houseknecht and Schenk, 2005). Though the Nanushuk Formation has been considered largely deltaic, the formation varies considerably from west to east, reflecting changing source areas and the relative influence of wave and storm processes on coastal deposition (Huffman et al., 1985; LePain et al., 2009).

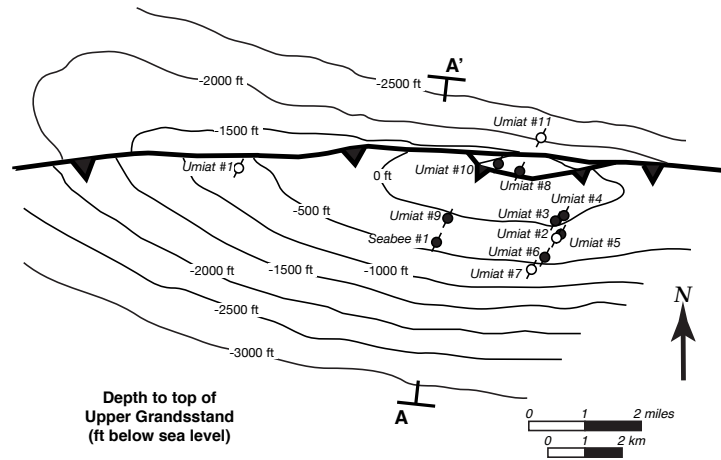


Figure 2. Structure contour map of top of Grandstand Sand, Umiat field showing location of legacy wells. A-A' shows location of seismic line in Figure 7. Contour intervals = 500 ft (153 m)

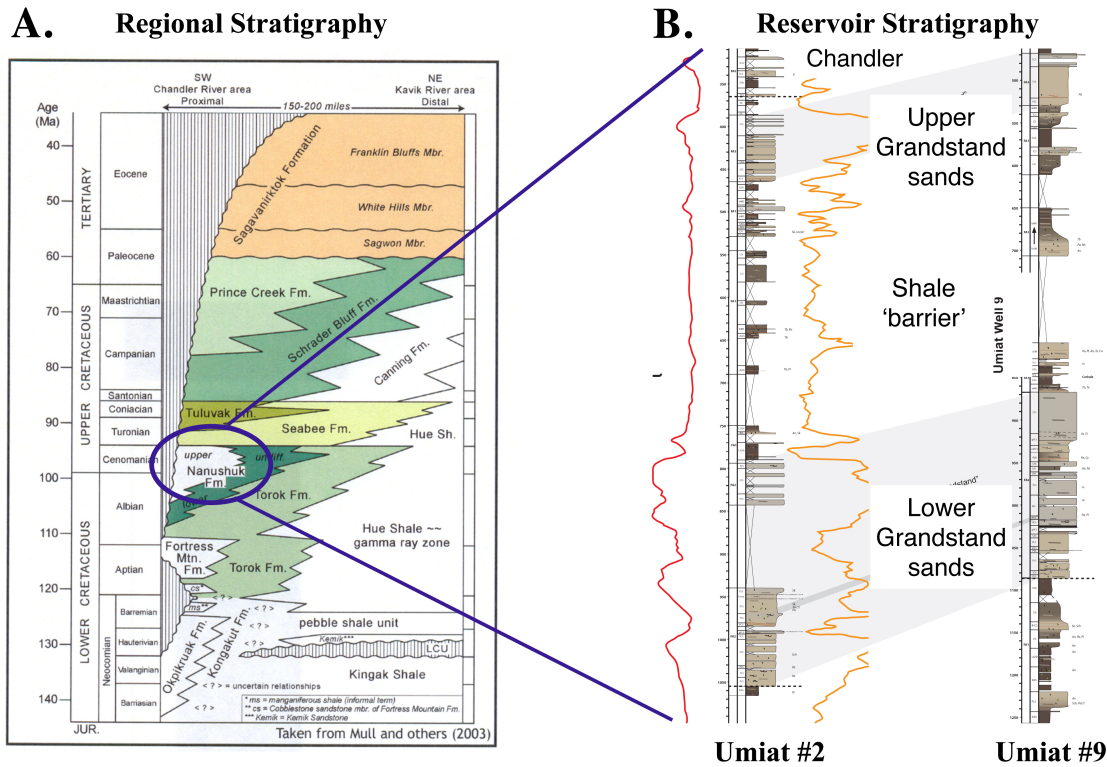


Figure 3. A. Regional stratigraphy of northern Alaska, showing the stratigraphic position of the Umiat reservoir in the Early Cretaceous Nanushuk Formation. Modified from Mull et al., 2003; B. Reservoir stratigraphic nomenclature used at Umiat field.

In the subsurface at Umiat field, the Nanushuk has been divided into 5 informal units: the

Ninuluk sand, heterolithic sand and mud Chandler, Upper Grandstand sand, mud-rich Shale Barrier, and the Lower Grandstand sand (Figure 3; Collins, 1958). These units, while informal, will be used in the following discussion of facies observed at and in the vicinity of Umiat field.

Characterization of reservoir interval

Key to understanding the flow behavior of the Umiat reservoir is determining the permeability structure of the sands within the reservoir interval. Legacy cores, combined with surface observations, provide a valuable means of examining sedimentologic, compositional, diagenetic and structural controls on the character of the reservoir.

Sedimentology

The Nanushuk Formation at Umiat can be characterized as a mixed shallow marine and deltaic system subdivided into 5 informal units: the Lower Grandstand sand, the Shale Barrier, the Upper Grandstand sand, the heterolithic Chandler and the Ninuluk sands (Figure 4). Six facies associations are recognized in core and outcrop (Figure 4 and Table 1). These facies associations best describe vertical facies relationships in cores and have unique horizontal and vertical permeability profiles.

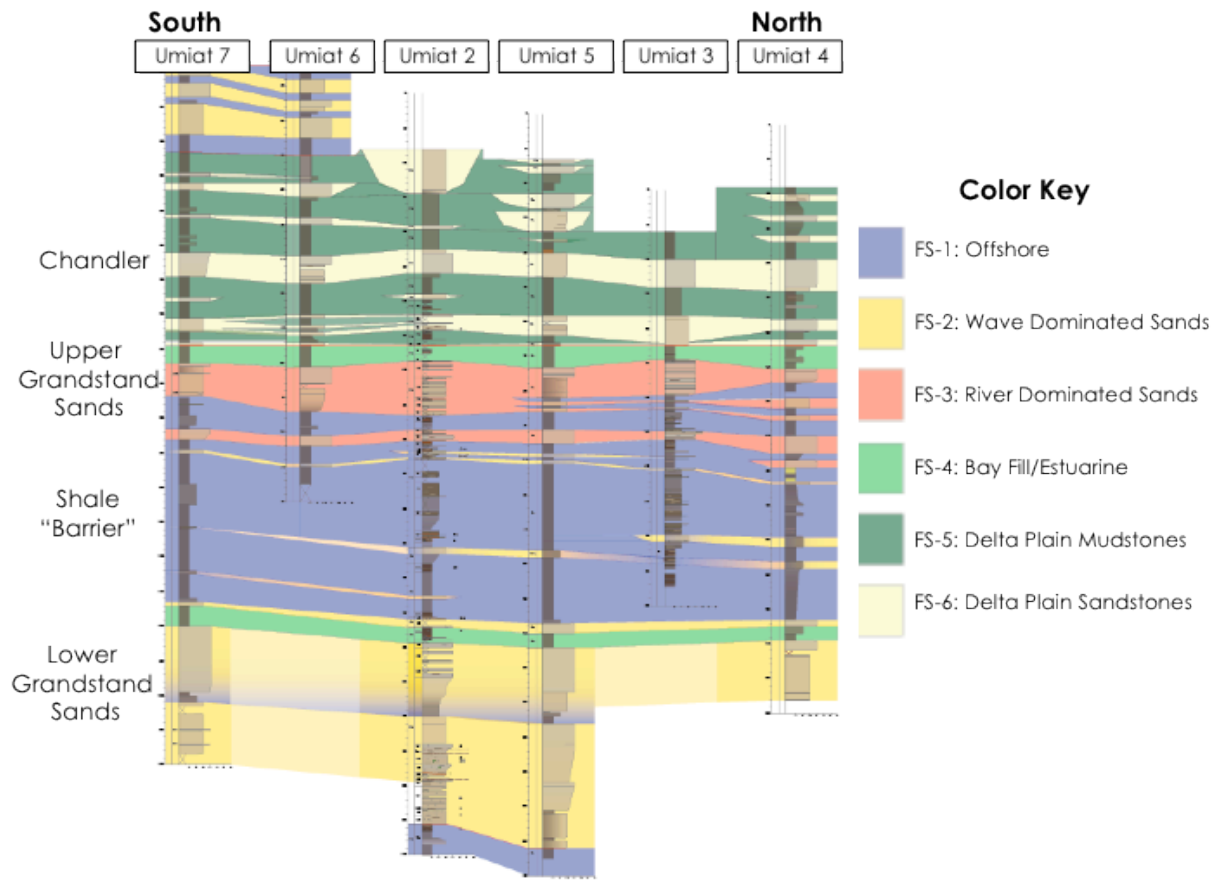


Figure 4. North-south stratigraphic cross section showing the vertical and lateral distribution of facies successions at Umiat field.

Table 1. Facies associations identified in legacy core and in outcrop.

	Diagnostic Features	Environmental Interpretation	Depositional Processes
Facies Associations	1	Laminated shale or bioturbated mudstone (<i>Cruziana</i> ichnofacies)	Offshore/Prodelta Suspension settling in the prodelta or the marine shelf near storm wave base
	2	Interbedded bioturbated mudstone (<i>Cruziana</i> ichnofacies) and upward coarsening hummocky and swaley cross-stratified sand (<i>Skolithos</i> ichnofacies), with some sand beds obliterated by bioturbation. Increasing amalgamation up well, with highly bioturbated beds (<i>Skolithos</i> ichnofacies)	Lower Shoreface Mixed-energy shelf, above storm wave base but below fair-weather wave base. Deposition by suspension settling and storm-wave redistribution of sand and silt originally delivered to the coast by deltaic systems.
	3	Low-angle, trough cross-stratified, and plane-laminated fine-grained sandstone. Rare bioturbation (<i>Skolithos</i> ichnofacies)	Upper Shoreface/Foreshore Subaqueous bar migration above fair-weather wave base, with some swash zone deposits.
	4	Wavy and lenticular bedding with occasional soft sediment deformation coarsens up into ripple cross-laminated and massive sand. Bioturbation intensity and diversity low	Delta Front Progradation of distributary mouth bars into muddy prodelta. Rapid deposition associated with massive sand, soft sediment deformation, low BI.
	5	Carbonaceous mudstone with brackish water bivalve assemblage (<i>Corbula</i>), volcanic ash deposits, and plant fossils.	a. Delta Plain Suspension settling in protected interdistributary bays or lagoons, with some tidal influence, organic matter accumulation in marshes or swamps.
		Wavy bedding coarsens up into flaser bedding and ripple cross-laminated sandstone. Beds are 5-10 ft thick. Mud-drapes are common in some sandstone beds, and are often sideritized, especially in Umiat No. 11. Rare mudstone rip-up clasts.	b. Crevasse Sands Crevasse channel and splay deposits that form during flood or avulsion into interdistributary bays or the delta plain. Some tidal influence indicated by mud drapes.

The Lower Grandstand sand is considered the primary reservoir interval and consists of two thick (90-150 ft), upward-coarsening wave-influenced deltaic associations with an intervening 20-50 ft thick shale (Figure 5). Permeability is highest in the upper 20-40 feet of each succession, probably due to increased wave energy and a lower degree of bioturbation. Permeability anisotropy (K_v/K_h) in the two sands averages 0.70. These sands are consistent in thickness and character across the field, with the shale interval acting as an internal flow barrier.

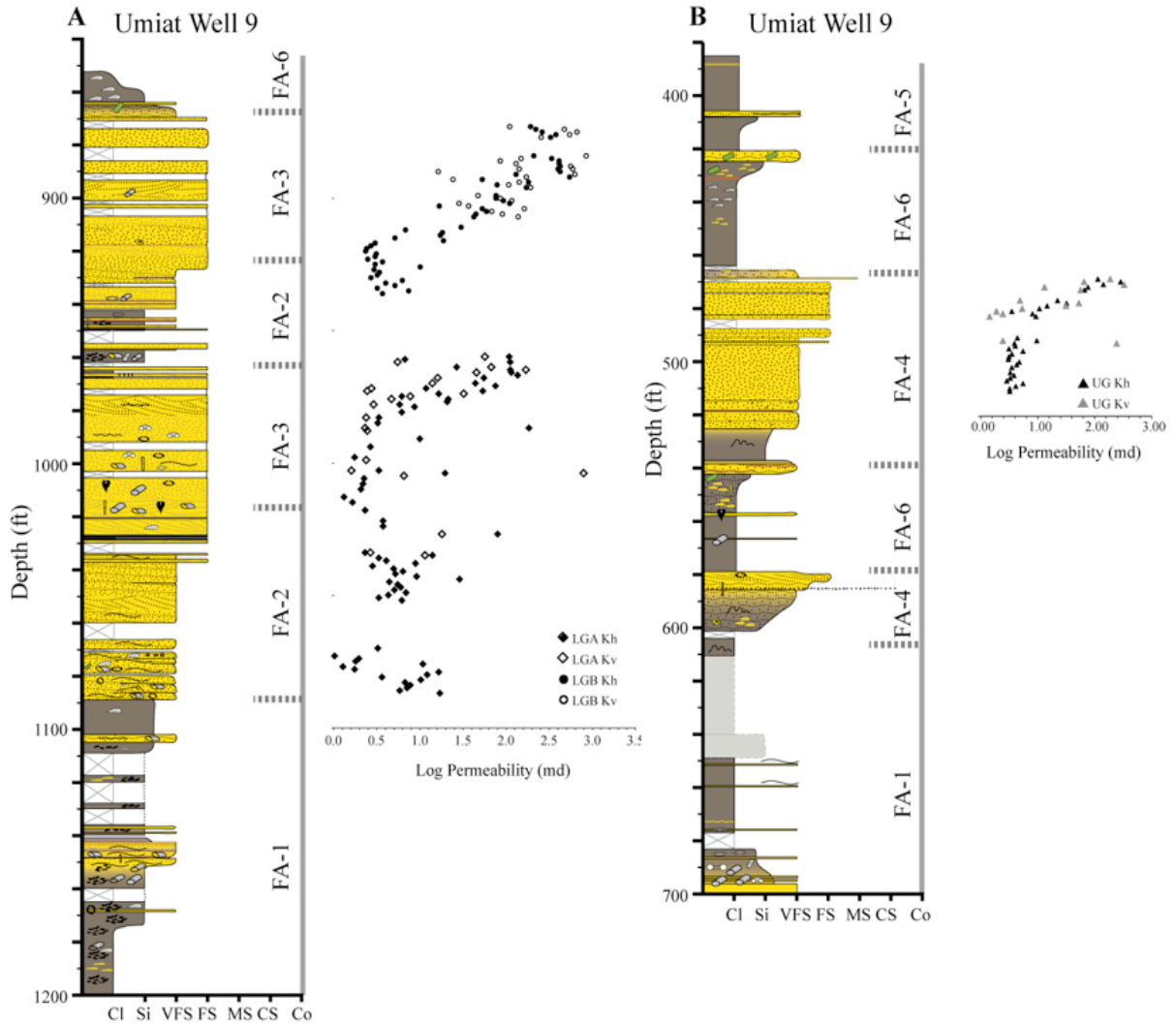


Figure 5. Permeability profiles from major sands in Umiat well #9. A. Lower Grandstand sands; B. Upper Grandstand sands. Note that both horizontal and vertical permeabilities increase significantly towards the top of facies associations FA-3 and FA-4. This effect may be partially controlled by diagenesis and lithic grain composition.

The Lower Grandstand sands are overlain by a thick (290-335 ft) shale informally known as the Shale Barrier (Figure 4). This shale consists of offshore shallow marine mudstones with thin, isolated sands. While individual sands within this interval have good porosity and permeability, they are few in number, thin, and laterally discontinuous. Subsequently, this interval is considered a flow barrier with little significant reservoir potential.

The Upper Grandstand consists of a single upward-coarsening, river-dominated deltaic sand 35-80 ft thick (Figure 5). This sand also appears to be consistent in thickness and character across the field, with the greatest permeability in the upper part of the succession.

The upper Grandstand is overlain by the Killik (known as the Chandler in the subsurface; Figure 4). The Killik is a marginal marine to nonmarine delta plain deposit, and is a mud-rich interval with thin, discontinuous sandstones that cannot be correlated between wells. For this reason it is not considered a potential reservoir interval.

The Killik is overlain by the Ninuluk (Figure 4). In the Umiat area, Ninuluk consists of transgressive shoreface succession. However, the Ninuluk is eroded from the top of the Umiat anticline structure and is only found on the southern flank and in the footwall. For this reason, it is not considered a major reservoir interval in the Umiat field.

Effect of grain composition and diagenesis

The permeability distribution in the Grandstand sands is further complicated by diagenesis. Compositionally, the Umiat reservoir sandstones are lithic arenites rich in feldspar and metamorphic rock fragments. The percentage of metamorphic fragments is inversely proportional to permeability, suggesting that winnowing of ductile phylitic grains by high-energy shoreface deposits may be partially responsible for an increase in porosity at the top of Grandstand sandstones (Bartsch-Winkler, 1985; Huffman et al., 1985; Fox et al., 1979). Pore-filling authigenic minerals, such as kaolinite, also reduce porosity, while pore-lining authigenic minerals, such as illite and microcrystalline quartz, narrow pore throats and reduce permeability. However, these authigenic minerals are not uniformly developed throughout reservoir interval, probably due to variations in original detrital mineralogy.

Structural analysis

The Umiat structure is an east-southeast-trending, thrust-related anticline related to a detachment in the underlying Torok shale (Figures 2 & 6). The Nanushuk topset sands overlying the Torok are deformed into an open asymmetric anticline bounded to the north by two thrust faults. Closure exists in both the hangingwall and footwall portions of the fold.

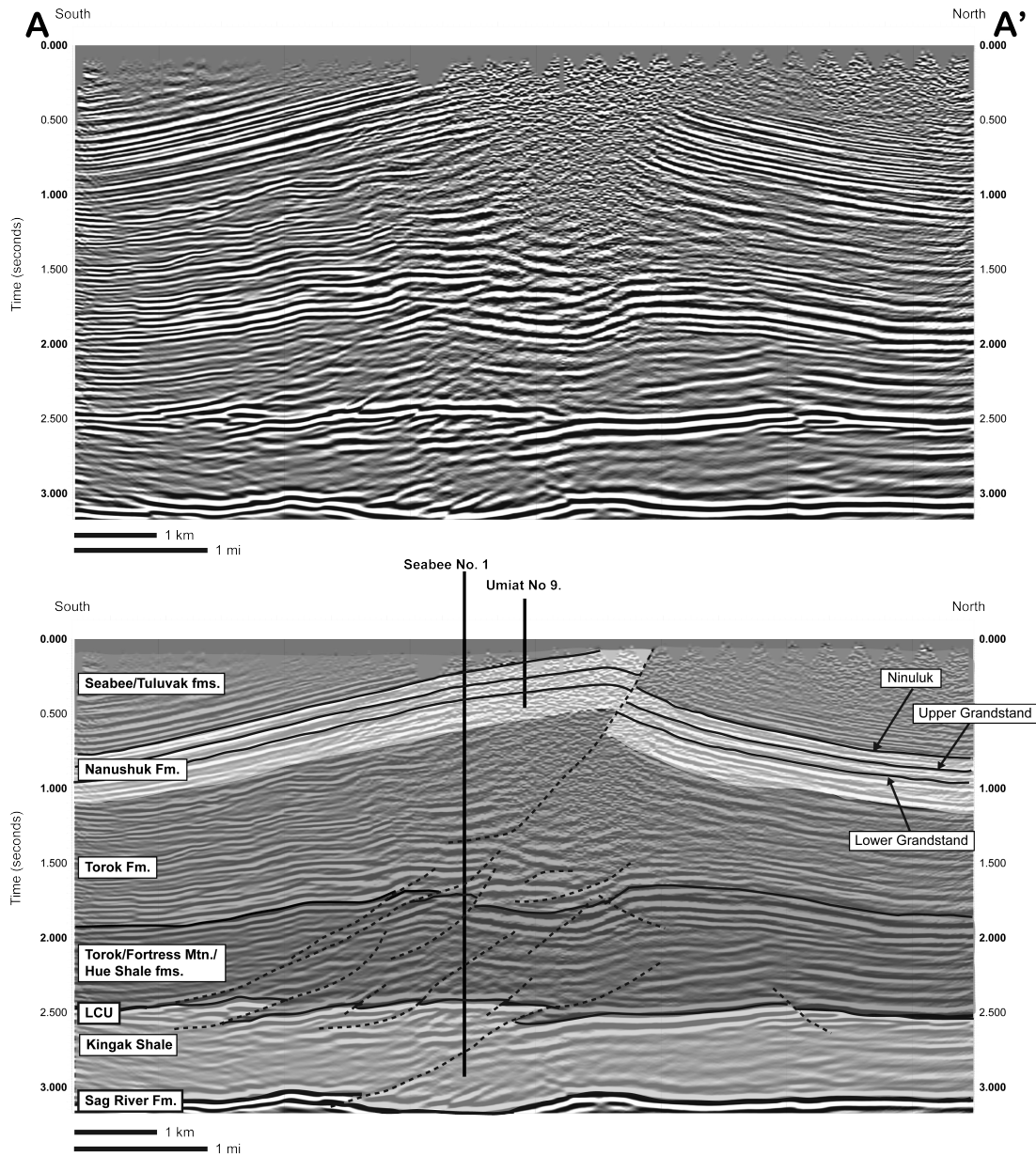


Figure 6. North-South seismic section through Umiat field. Top: uninterpreted; bottom: interpretation by G. Shimer. Location of seismic section shown on Figure 2. Seismic data courtesy of Renaissance Alaska Inc.

Natural fractures could enhance permeability if open or block permeability if they filled with ice or cement. Regional and local observations suggest that three sets of fractures may occur at Umiat: a conjugate set ENE-ESE striking fractures that are vertical with respect to bedding and are subparallel to the Umiat structure; a conjugate set of ~north-south striking fractures that are perpendicular to the Umiat structure; and fractures subparallel to and associated with the thrust

faults (Hanks et al., 2006; Duncan et al., 2012).

The existing vertical wells would not be expected to intersect many vertical fractures if the fractures are widely spaced, but several natural fractures have been identified in core from Umiat field (Figure 7A), indicating that these fractures do exist in the subsurface at Umiat.

Examination of nearby exposures of similar structures suggest that at least two sets of fractures exist in the area—an east-west striking set of conjugate (shear?) fractures and a ~north-south striking set of opening-mode fractures (Figure 7B). The east-west conjugate fractures are subparallel to the folds in the area, suggesting that these fractures may be related to these structures. The north-south fractures are approximately orthogonal to the structural grain, suggesting they may be part of a regional set of orogen-perpendicular extension fractures seen elsewhere in the Brooks Range. (Hanks et al., 2006). No fractures directly related to the faults were observed due to poor exposures.

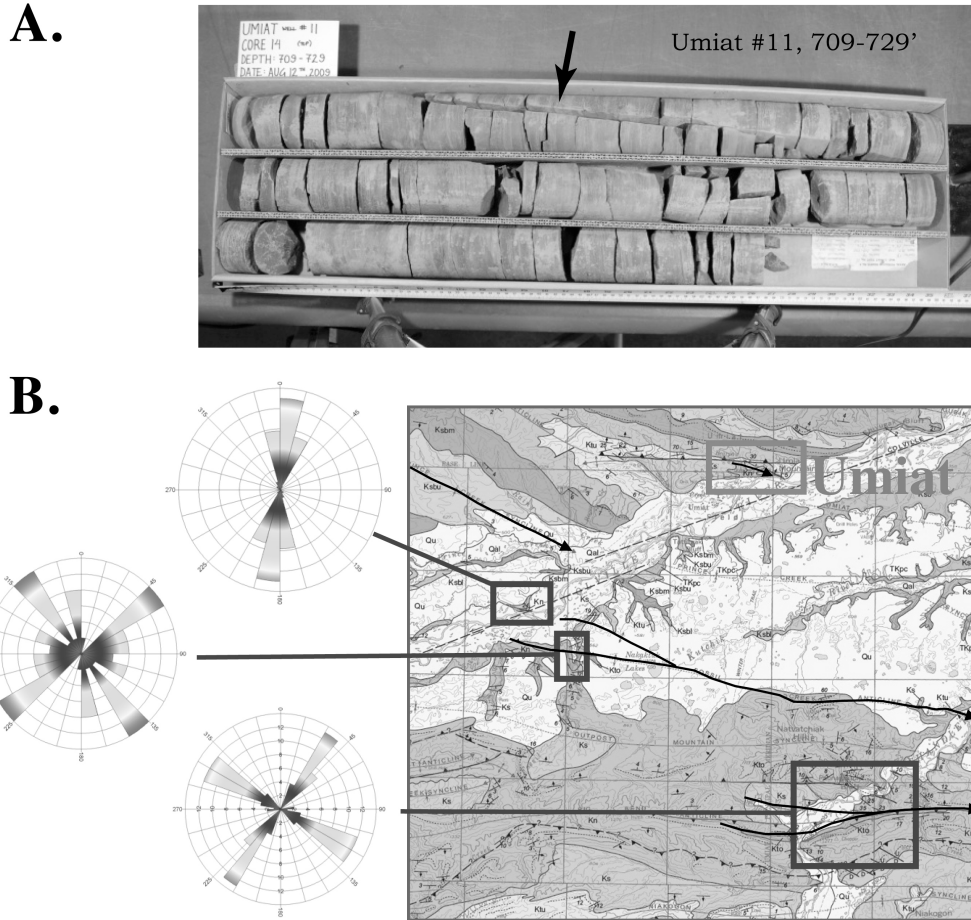


Figure 7. Natural fracture distribution at Umiat field. A. Natural fracture (arrow) observed in core from Umiat well# 11; B. Orientations of natural fractures in outcrops of correlative stratigraphy on similar structures near Umiat field. Map modified from Mull et al., 2004.

Reservoir model and oil-in-place estimates

A reservoir property model was constructed based on published data from Umiat field (Levi-Johnson, 2010) and subsequently modified to incorporate new information regarding sand continuity and permeability anisotropy (Figure 8). Geologic observations indicate that the Upper and Lower Grandstand have distinct petrophysical properties and flow structures and should be treated separately. In addition, the Lower Grandstand sand was subdivided into an upper and lower sand with an intervening shale that would act as a flow barrier. Observed variations in permeability and related variations in capillary pressure and water saturation height were

accommodated by subdividing sands into 3 different 'rock types' (Table 2 & Figure 9).

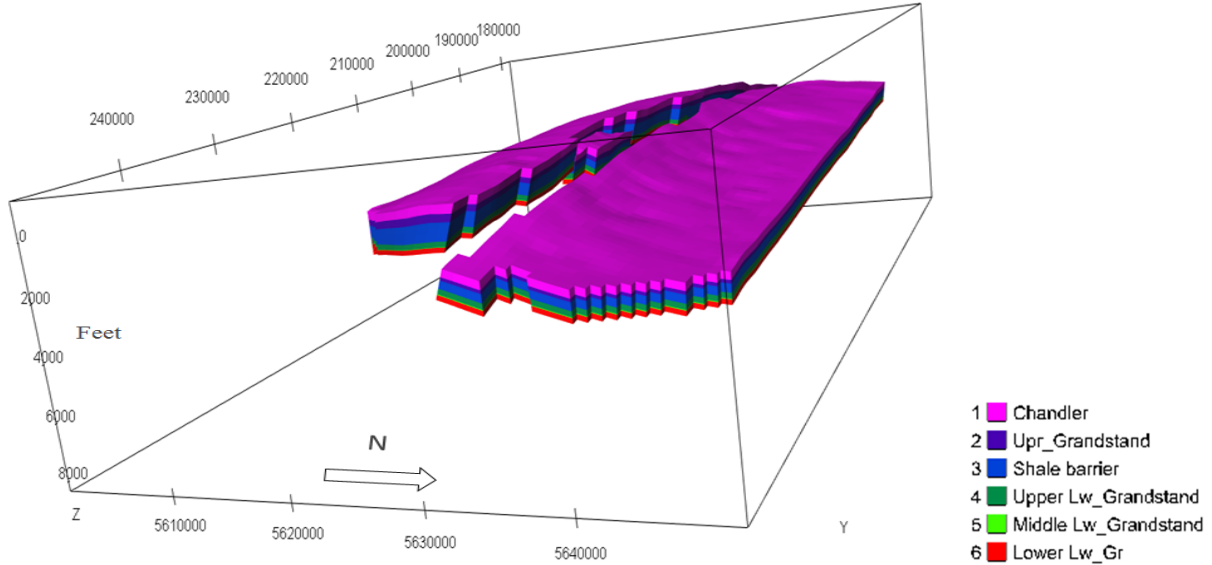


Figure 8. Reservoir model of the Umiat field. Faults not shown for clarity. Model is based on available seismic data, legacy well data, reexamination of legacy core and examination of nearby outcrops. Model was constructed using Roxar IRAP. Modified from Levi-Johnson, 2010.

Table 2. Sands of the Lower Grandstand have a wide range in permeability. Sands were subdivided into three 'rock types' based on permeability and assigned different capillary pressure curves in the simulation.

Rock Type	Permeability range (md)	Representative K for Pc class (md)
1	$K < 1$	0.408
2	$1 < K < 50$	22.5
3	$K > 50$	100

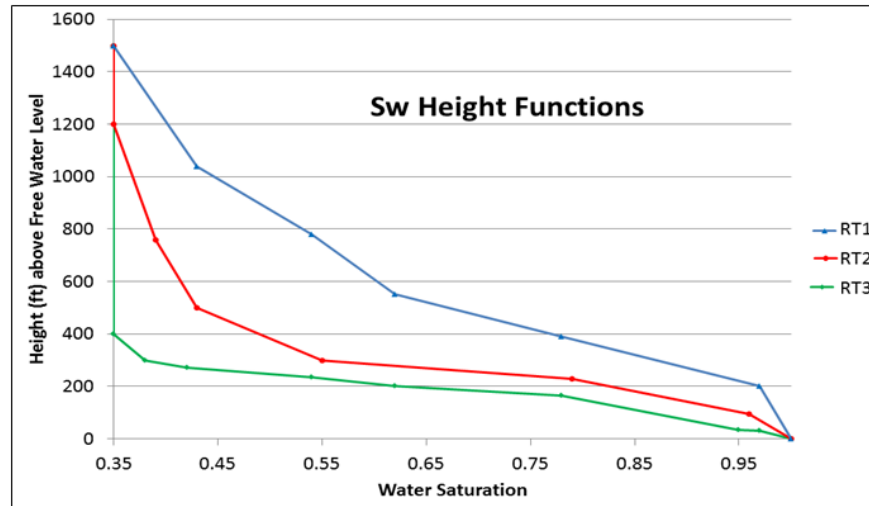


Figure 9. Water saturation height for different sand categories, as defined in Table 1.

A single realization of this geologic model using average observed porosity and Sw values yielded an estimated stock tank original-oil-in-place (STOOIP) of ~ 1.52 billion barrels with 99 bcf associated gas. A Monte Carlo simulation was conducted to evaluate the sensitivity of this OOIP value to a range of porosities, Swi, bulk volume (Vb), net-to-gross ratio (NTG) and oil formation volume factor (Bo) (Table 3). The results of this simulation yielded OOIP estimations ranging from P90 of 739 millions to a P10 of 2437 million barrels (Figure 10). The P50 value for OOIP was 1527 million bbls.

Table 3: Variable ranges used as input to Monte Carlo simulation of stock tank oil in place (STOOIP) calculations for Lower Grandstand.

Input	Range
Swi	0.35–0.45
NTG	0.1-0.7
Vb (*E +9 ft3)	36-56
ϕ (%)	5.00-22.00
Bo (rb/ SCF)	1.001-1.05

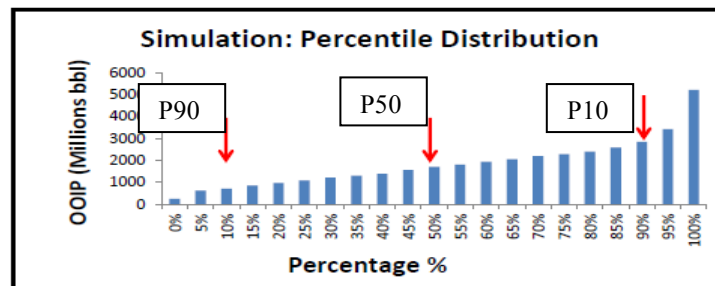


Figure 10: Result of Monte Carlo simulation for reserve volumetrics based on variable ranges in Table 2 and 10,000 runs.

Fluid properties

The phase behavior of the Umiat fluid needs to be well understood in order for a reservoir simulation to be accurate. However, only a small amount of Umiat oil was available; this oil was collected in the 1940’s and was severely weathered. The composition of this ‘dead’ Umiat fluid was characterized by gas chromatography. This analysis was then compared to theoretical Umiat composition derived using the Pedersen method (Pedersen et al., 1989) with original Umiat fluid properties published in the original reports (Table 4; Figure 11). This comparison allowed estimation of the ‘lost’ light hydrocarbon fractions. The Umiat dead oil sample was physically recreated by adding the lost light ends to the weatherized Umiat dead oil sample (Table 4). The procedure is discussed in more detail in Shukla (2011).

Table 4. Physical properties of Umiat dead oil samples as determined by this work and preceding studies..

Property	This work (GMC provided Umiat dead oil sample)	Schlumberger ADDGS report	Collins, 1958	This work (recreated Umiat dead oil sample)
Density at 288.7 K (60°F) and 101.3 kPa (14.7 psia)	877.8 kg/m ³ or 29.7°API	874.9 kg/m ³ or 30.2°API	842.0 kg/m ³ or 36.6°API	836.0 kg/m ³ or 37.6°API
Viscosity at 310.9 K (100°F) and 101.3 kPa (14.7 psia)	9.16 mPa.S	7.60 mPa.S	2.90 mPa.S	2.75 mPa.S (at 313.1 K)
Molecular weight (kg/kg-mole)	245.00	Not measured	184.17*	183.38**

- * Estimated from the TBP distillation data provided in Collins, 1958
- ** Not measured, but calculated from the molar composition of recreated Umiat dead oil sample.

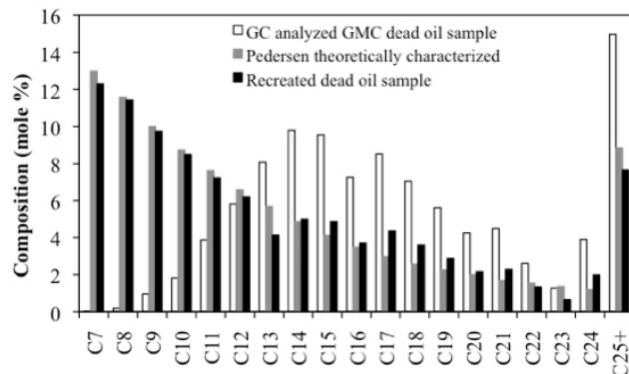


Figure 11. Molar compositions of legacy Umiat oil determined by gas chromatograph (GC) and theoretically determined using the Pedersen method were compared to determine the amount of light hydrocarbons lost during degradation of the legacy oil sample. This value was used to recreate a Umiat oil sample that was then used to determine Umiat fluid properties at reservoir conditions (e.g., Figure 12).

The physically recreated dead oil sample was then recombined with solution gas to produce a 'pseudo-live' oil sample, which was subsequently used for experimental PVT and phase behavior studies to determine fluid properties over the range of reservoir pressures and temperatures (e.g., Figure 12). The phase behavior of the 'live' oil was also simulated using the Peng-Robinson equation of state (EOS) (Robinson and Ping, 1978). The EOS model was tuned with measured experimental data to accurately simulate the differential liberation tests in order to obtain the necessary data for reservoir simulation studies, including bubble point pressure and oil viscosity (Table 5). The bubble point pressure of the reconstructed Umiat oil is 345 psi, suggesting that maintenance of reservoir pressures above that pressure will be important for the any proposed production technique.

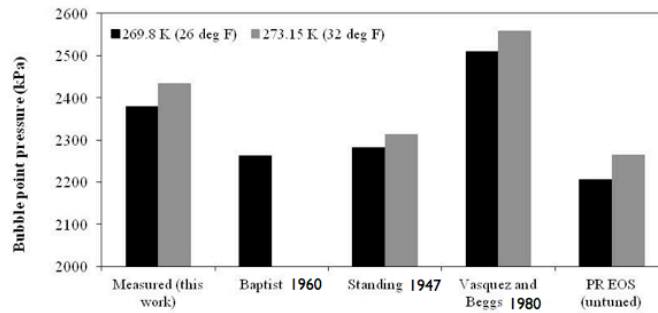


Figure 12. Comparison of Umiat oil bubble point pressures determined by this study with prior values.

Table 5
Fluid properties at initial reservoir conditions used to initialize simulation model.

Parameter	Value	Source
Oil density	52.1873 lb/ft ³	Shukla, 2011
Oil bubble point pressure	345 psi	Shukla, 2011
Gas density	0.04539 lb/ft ³	Shukla, 2011
Water phase density	62.4 lb/ft ³	http://www.simetric.co.uk
Water FVF	1.002	McCain, 1990
Water compressibility	3.06e ⁻⁶ 1/psi	https://www.fekete.com
Water viscosity	1.78 cp	Beal, 1964
Reservoir temperature	26	Baptist, 1960
Reservoir pressure	350 psia	Baptist, 1960
Reference depth	900 ft	Arbitrary

WOC depth	1500 ft	Third party (Linc Energy)
-----------	---------	---------------------------

Rock properties at low temperatures

A major part of predicting how the Umiat reservoir will perform is determining the relative permeability of oil in the presence of ice. Early in the project, UAF work on samples of the Umiat reservoir indicated that there is a significant reduction in the relative permeability of oil in the presence of ice (Figure 13; Godabrelidze, 2010). For samples of the Umiat reservoir saturated with deionized water and frozen, the average decline was 61%% (Figure 13). These samples were subsequently determined to be representative of the less permeable facies of the reservoir; more permeable facies may not experience such a dramatic decline in relative permeability. This was supported by experiments on Berea sandstone samples with permeabilities similar to that of the main reservoir facies (Venepalli, 2011). In these samples, continuous reduction in relative permeability was observed when temperatures were reduced from 23°C to -10°C, with an average reduction of 43.2% when saturated with deionized water and a reduction of 32.5% when saturated with water with salinities approximating those in the Umiat reservoir (Figure 14). This suggests that the reduction of the relative permeability is strongly dependent on both the reservoir temperature and salinity of connate water.

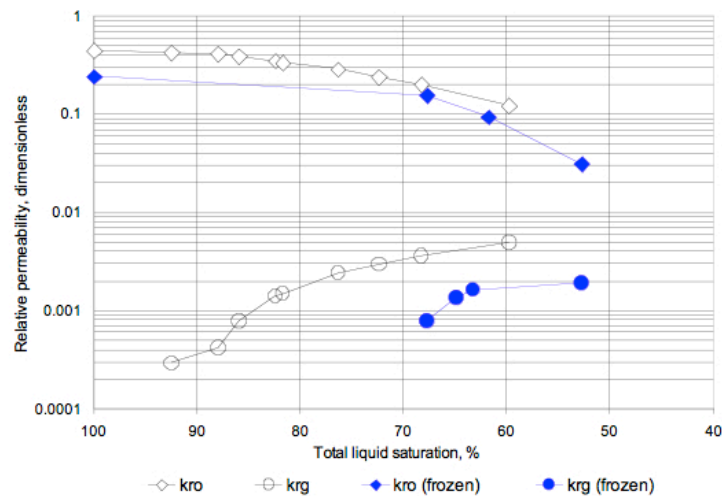


Figure 13: Gas and oil relative permeabilities of core plug 60 from Umiat well # 11 under frozen and unfrozen interstitial water conditions. From Godabrelidze, 2010.

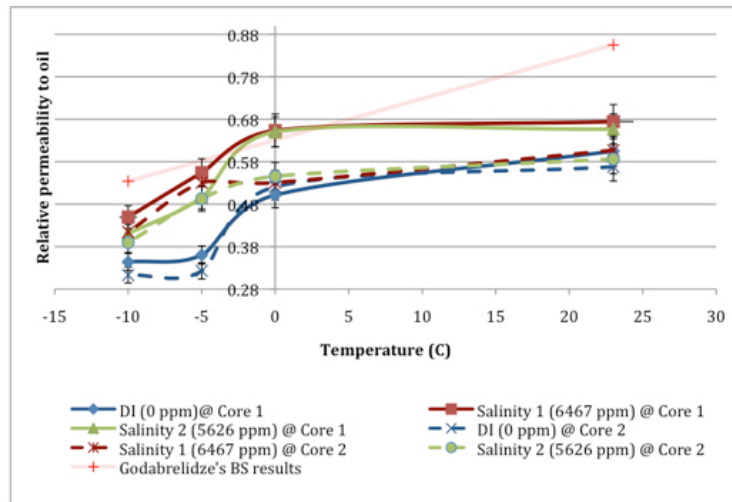


Figure 14: Relative permeability vs. temperature curves for two Berea sandstone cores for distilled (DI) and saline formation water. From Venepalli, 2011.

This reduction in relative permeability may be due to the formation of ice kernels in the center of pores (Venepalli, 2011). Theoretically, the radius of ice formed in the center of the pore can be determined using a modification of the traditional Kozeny–Carman equation assuming the pores and pore throat networks can be represented as a series of ‘N’ parallel pipes with the ice residing in the center of these pipes. Using the values of k_{ro} obtained from the experimental work as input to the Kozeny–Carman Equation at 23°C and -10°C, the radius of ice kernels required to account for the reduction in relative permeability to oil at the lower temperatures was 0.145 mm for deionized water and to 0.069 mm for a salinity of 6467 ppm.

Preliminary evaluation of drilling fluids indicate that the brine-based muds caused significantly less swelling in the Umiat reservoir sands when compared to fresh-water based muds and has lower apparent viscosity at high flow rates, which would reduce the pumping pressure required to circulate the fluid. However since freezing filtrate is another cause of formation damage, a simple water-based-mud may not a viable option. It is recommended that new fluids be tested, including different salts, brines, and polymers as well as an oil-based-mud. These fluids should be tested at low temperatures in order to determine the fluid properties under these conditions and to ensure that the freezing point is below that of the reservoir.

Reservoir simulations

Low reservoir pressures will require pressure support from the initial production of the field. There is no gas cap or indication of an active aquifer. In order to maintain thermal equilibrium with the permafrost for wellbore stability while providing the desired injectivity, pressure support will be provided by injection of lean natural gas. Gas will be sourced from undrilled underlying accumulations in the Torok or from nearby gas fields. The gas will be injected at reservoir temperature of 26° F.

To prepare the simulation model, the geologic model was gridded horizontally into 200 x 200 ft² grid blocks (Figure 8). To capture the vertical heterogeneity present in the field, the model was vertically subdivided into 32 grid layers with thicknesses ranging from 5 feet in the sands to 45 feet in the shales. Initial simulations focused on the Lower Grandstand, which was identified as having the best reservoir properties and, as the deepest reservoir interval, could have the most reservoir accessed by horizontal drilling while having the least amount of reservoir in the permafrost zone with the associated relative permeability reduction. This upscaled model was initialized with the rock and fluid properties determined by the experimental and theoretical work conducted earlier in the study (Table 5).

A wagon-wheel pattern was used in the simulation as the most efficient means of accessing the maximum amount of the reservoir interval while minimizing the surface footprint. In the proposed pattern, five well pads will be located on the hangwall of the Umiat structure, parallel to strike of the fold. Each pad will consist of one vertical well in the center along with two dual lateral injectors in the north and south at the top of the reservoir supporting pressure for a combination of four dual lateral producers at the bottom of the interval, each one angled at 36 degree in a square mile spike configuration. The horizontal wells have a total length of 3000 ft, with a 1500 ft horizontal leg, and a 4.5 inch open hole completion across the productive area. To reduce surface impact and the cost of infrastructure, only 5 pad locations were used in the simulation, with a total combination of 80 producers and 25 injectors.

Three scenarios were evaluated in the simulation: cold gas injection with bottom hole injection pressures of 400 and 600 psi and no gas injection. Higher injection pressures were not considered due to the low initial reservoir pressures (350 psi) and the desire to avoid overpressuring and fracturing the reservoir. Simulations were run for a projected 50 year lifespan. The impact of potential fractures was incorporated by testing the sensitivity of the reservoir performance to permeability anisotropy (K_v/K_h).

Simulation results indicate that recovery will be very sensitive to both injection pressure and permeability anisotropy (Figures 15 & 16). As expected, the higher the injection pressure, the higher the average reservoir pressure and the more oil production. Recovery over 50 years using 400 psi bhip is ~12%; 14% for 600 psi bhip; and 8% for no gas injection.

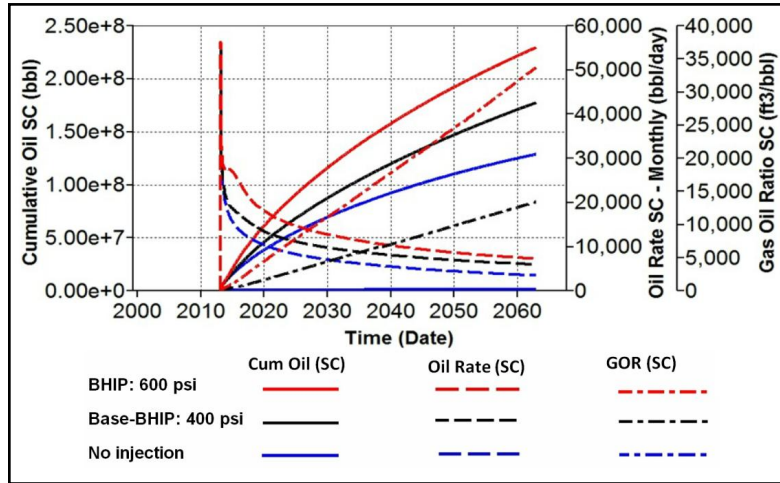


Figure 15. Simulation results showing Umiat cumulative oil production, oil rate, and producing gas-oil ratio (GOR) for different gas injection pressures over a 50 year projected life span.

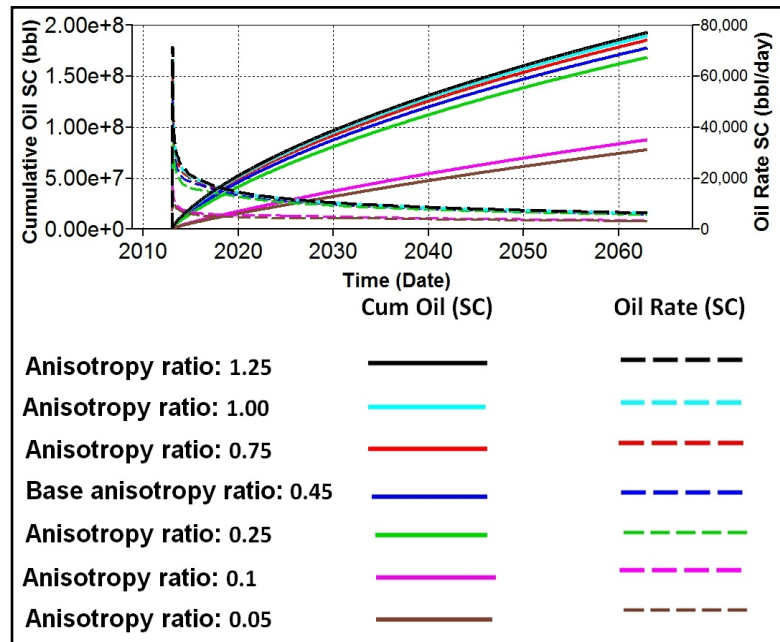


Figure 16. Simulation results showing Umiat cumulative oil production and oil rate for different permeability anisotropy ratios (Kv/Kh) over a 50 year projected life span.

The impact of potential fractures was incorporated into the simulation by testing the sensitivity of the reservoir performance to permeability anisotropy (K_v/K_h ; Figure 16). High K_v/K_h ratios ($>.5$) simulated enhanced vertical permeability due to open natural fractures. As expected, higher anisotropy ratios resulted in higher oil production and lower average reservoir pressures after 50 years of gas injection. The simulations also indicate that when the anisotropy ratio is very low

(<0.25), the average reservoir pressure increases by more than 6%. This suggests that the low vertical permeability is resulting in less fluid being displaced in the reservoir.

Discussion and Conclusions

Umiat oil field is a light oil in a shallow, frozen reservoir in the Brooks Range foothills of northern Alaska with estimated oil-in-place of over 1 billion barrels. Umiat field was discovered in the 1940's but was never considered viable because it is shallow, in the permafrost, and far from any transportation infrastructure. The increase in oil prices combined with the advent of modern drilling and production techniques has made Umiat an attractive exploration and production target, if the technical problems such as reduced permeability due to low temperatures and low reservoir pressure can be addressed. This DOE funded project targeted these issues by incorporating legacy geologic and engineering data with new data to develop new interpretations of the storage and flow capacity of the reservoir. This new geologic model was incorporated into a modern reservoir simulation to test the effectiveness of the proposed production technique--cold gas injection from spaced multilateral wells in a wagonwheel configuration.

The new geologic work identified three potential reservoir horizons within the Cretaceous Nanushuk Formation: the Upper and Lower Grandstand sands, and the overlying Ninuluk sand, with the Lower Grandstand considered the primary target. Seals are provided by thick interlayered shales. The Nanushuk in the Umiat area consists of mixed shoreface and deltaic sandstones and mudstones. A core-based study of the sedimentary facies of these sands combined with outcrop observations identified six distinct facies associations with distinctive permeability trends. The Lower Grandstand sand consists of two laterally continuous coarsening-upward shoreface sands sequences while the Upper Grandstand consists of a single laterally continuous coarsening-upward shoreface sand. The Ninuluk consists of a transgressive deltaic/shoreface succession.

Each of the shoreface sands in the Grandstand shows a distinctive permeability profile with high horizontal permeability at the top getting progressively poorer towards the base of the sand. In contrast, sandstones in the overlying Ninuluk are more permeable at the base of the sands, with decreasing permeability towards the sand top. These trends impart a strong permeability anisotropy to the reservoir and are incorporated into the reservoir model. These observations also suggest that horizontal wells should target the upper part of the major sands.

Natural fractures may superimpose another permeability pattern on the Umiat reservoir that need to be accounted for in both the simulation and in drilling. Examination of legacy core from Umiat field indicate that fractures are present in the subsurface, but don't provide information on their orientation and density. Nearby surface exposures of folds in similar stratigraphy indicate there are at least three possible fracture sets: an early, N/S striking set that may predate folding and two sets possibly related to folding: an EW striking set of extension fractures that are

parallel to the fold axes and a set of conjugate shear fractures oriented NE and NW. Analysis of fracture spacing suggests that these natural fractures are fairly widely spaced (25-59 cm depending upon the fracture set), but could provide improved reservoir permeability in horizontal legs drilled perpendicular to the open fracture set.

Based on the new observations and interpretations in this study, the Lower Grandstand sands were determined to be the primary reservoir target during initial phases of development. The Upper Grandstand is significantly thinner, and its shallower depth leads to pressure and temperature issues. The Ninuluk is eroded from most of the Umiat structure so is not considered a viable target at this time.

The phase behavior of the Umiat fluid needed to be well understood in order for the reservoir simulation to be accurate. However, only a small amount of Umiat oil was available; this oil was collected in the 1940's and was severely weathered. The composition of this 'dead' Umiat fluid was characterized by gas chromatography. This analysis was then compared to theoretical Umiat composition derived using the Pedersen method with original Umiat fluid properties published in the original reports. This comparison allowed estimation of the 'lost' light hydrocarbon fractions. An Umiat 'dead' oil sample then could be physically created by adding the lost light ends to the weatherized Umiat dead oil sample. This recreated sample was recombined with solution gas to create a 'pseudo-live' Umiat oil sample which was then used for experimental PVT and phase behavior studies to determine fluid properties over the range of reservoir pressures and temperatures. The phase behavior of the 'pseudo-live' oil was also simulated using the Peng-Robinson equations of state (EOS). The EOS model was tuned with measured experimental data to accurately simulate the differential liberation tests in order to obtain the necessary data for reservoir simulation studies, including bubble point pressure and oil viscosity. The bubble point pressure of the reconstructed Umiat oil is 345 psi, suggesting that maintenance of reservoir pressures above that pressure will be important for the any proposed production technique.

A major part of predicting how the Umiat reservoir will perform is determining the relative permeability of oil in the presence of ice. Early in the project, UAF work on samples of the Umiat reservoir indicated that there is a significant reduction in the relative permeability of oil in the presence of ice. However, it was not clear as to why this reduction occurred or where the ice resided. To explore this further, additional experimental and theoretical work was conducted. Core flood experiments were performed on two clean Berea sandstone cores under permafrost conditions to determine the relative permeability to oil (k_{r_o}) over a temperature range of 23°C to -10°C and for a range of connate water salinities. Both cores showed maximum reduction in relative permeability to oil when saturated with deionized water and less reduction when saturated with saline water.

This reduction in relative permeability can be explained by formation of ice crystals in the center of pores. Theoretically, the radius of ice formed in the center of the pore can be determined using the Kozeny–Carman Equation by assuming the pores and pore throats as a cube with 'N'

identical parallel pipes embedded in it. Using the values of k_{ro} obtained from the experimental work as input to the Kozeny–Carman Equation at -10°C , the radius of ice crystals dropped from $0.145\ \mu\text{m}$ to $0.069\ \mu\text{m}$ when flooding-water salinity is increased to 6467 ppm. This explains the reduction of relative permeability with decreasing salinity but does not take into consideration other effects such as variations in pore throat structure.

In addition, fluids like deionized water, saline water, and antifreeze (a mixture of 60% ethylene or propylene glycol with 40% water) were tested to find the best flooding agent for frozen reservoirs. At 0°C , 9% greater recovery was observed with antifreeze was used as a flooding agent as compared to using saline water. Antifreeze showed 48% recovery even at -10°C , at which temperature the rest of the fluids failed to increase production.

Preliminary evaluation of drilling fluids indicate that the brine-based muds caused significantly less swelling in the Umiat reservoir sands when compared to fresh-water based muds. However since freezing filtrate is another cause of formation damage, a simple water-based-mud may not a viable option. It is recommended that new fluids be tested, including different salts, brines, polymers and oil-based fluids. These fluids should be tested at low temperatures in order to determine the potential for formation damage, the fluid properties under these conditions and to ensure that the freezing point is below that of the reservoir.

The distribution and character of porosity, permeability and oil saturations predicted by the new geologic model were used in a Monte Carlo simulation to determine the range of oil-in-place for the Lower Grandstand reservoir. Reserve estimates range from a low of 739 million barrels to high of 2437 million barrels, with an average of 1527 million barrels. Further geologic information gained during development should help refine these estimates.

The geologic model was upscaled and used to simulate potential recovery using cold gas injection to maintain reservoir pressure. Cold gas injection was used in the simulations as there is no active aquifer support due to small peizometric head in the area and no existing gas cap. Consequently, cold gas injection is considered the most viable means of providing pressure maintenance while maintaining wellbore stability and reducing impact on the permafrost. Saline water injection may be a viable alternative, though this may have a detrimental effect on permafrost.

In order to reduce the surface footprint while accessing the maximum amount of the Lower Grandstand interval, simulations used development from 5 surface locations with a wagon-wheel pattern of multilateral injectors and producers. Horizontal well length and injection pressure were optimized to be 1500 ft and 400 psi respectively.

Simulations indicate oil recovery will be about 12% using a bottom-hole injection pressure of 400 psi. A higher bottom-hole gas injection pressure of 600 psi will yield a higher recovery of 15%. However, using a higher injection pressure may result in fracturing the reservoir that could

cause a reduction in oil recovery due to early breakthrough of gas.

Simulations of permeability anisotropy were used to simulate the impact of open fractures on potential recover. As expected, higher anisotropy ratios ($>.5$) resulted in higher oil production, suggesting that open fractures will lead to higher cumulative oil production. Very low vertical permeability (low K_v/K_h) reduced the effectiveness of the cold gas injection, reducing ultimate recovery. This is probably due to reduced ability of the injected gas to contact the reservoir away from the wellbore and subsequent reduction in the sweep efficiency.

Lessons learned

In the short term, the results of this work are being incorporated into Linc Energy's drilling and development plan. This project has also provided valuable information on the rock and fluid properties of low temperature reservoirs as well as the efficacy of potential production techniques for Umiat or similar shallow frozen reservoirs in the circum-Arctic.

A far more detailed and accurate geologic model of the Umiat reservoir was developed, including an evaluation of permeability anisotropy by facies and depositional environment. This is by far the best constrained and most accurate publicly available geologic model of this age of reservoir on the North Slope.

The revised geologic model and Monte Carlo simulation indicate the main reservoir interval at Umiat field, the Lower Grandstand, could contain well over >1 billion stock tank barrels of high quality crude. While the reservoir simulations suggests that recovery from the Umiat reservoir will be relatively low (12-15%) using cold gas injection, the volume of oil in place makes the accumulation still of interest to industry.

Natural fractures were recognized in both the core and subsurface. These were previously not thought to present. If these fractures are open and contributing to flow, recovery from the Lower Grandstand will be on the higher side of the simulation estimates.

An experimental technique was developed to determine the relative permeability of oil and gas in the presence of ice. This was used to determine the degree of relative permeability reduction that could be anticipated in those parts of the reservoir in the permafrost zone. This experimental approach can be used to evaluate relative permeability in other low temperature reservoirs or in oil spills in rocks at low temperatures and pressures.

An approach was developed that could be used to synthesize a reservoir fluid when only a degraded sample was available. This approach could be useful in any situation where fluid properties are needed but live oil samples are not available.

Future work

- Linc Energy is drilling initial wells during the upcoming drilling season (2012-2013) and will acquire new rock and fluid samples that they will share with UAF
- The simulations in this study focused on the primary reservoir interval, the Lower Grandstand sand. Significant reserves are projected for the overlying Upper Grandstand sand, but these sands are at lower temperatures and pressures than the Lower Grandstand, and will need a different approach to development and pressure maintenance. Future simulations studies will address this issue.
- Additional rock property analysis and NMR imaging on a wider range of samples and over a wider range of conditions are needed to determine where exactly in the pores the ice resides .
- A better understanding of the efficacy of drilling fluids of various compositions in horizontal legs at low temperatures is needed if reservoirs of this sort are to be economically developed.
- The fracture distribution in rocks buried to shallow depths does not appear to consistently follow regional and theoretical trends. Is a new model needed or just a revision of existing models?
- Production from Umiat is predicated on the availability of low-cost natural gas for cold gas injection. If gas is not found below the main Umiat structure as predicted, what is the next best pressure maintenance mechanism?
- The Umiat reservoir resides in a pressure/temperature zone close to the stability zone for gas hydrates. Should Linc be concerned about gas hydrate formation?

Technology transfer

In addition to 16 technical reports to DOE, this project supported, in full or in part, 8 master's theses and 1 Ph.D. dissertation, all of which are all publicly available. Seven peer-reviewed publications have been submitted for publication as part of this project. In addition, team members have presented 14 papers and/or posters summarizing various aspects of this work at AAPG and SPE conferences. All of these publications are listed in the Bibliography at the end of this report.

Acknowledgments

This work was funded by the Department of Energy under Award Number DE- FC26-08NT0005641.

This project benefited greatly from interactions with our industry partners--Renaissance Alaska (2008-2011) and Linc Energy (2011-2012). In particular, we would like to thank A. Huckabay and V. Bangia whose contributions in the early phases of the study were critical to its success.

Wes Wallace and Cheryl Sanders contributed significantly to the structural interpretations discussed in this report. The Alaska Division of Geological and Geophysical Surveys (ADGGS) provided access to legacy Umiat core and fluid samples and helicopter support for geologic field studies. Roxar (now Emerson) provided IRAP geologic modeling; simulation software was provided by CMG (Computer Modeling Group).

REFERENCES

- Ahlbrandt, T.S., Huffman Jr., A.C., Fox, J.E., and Pasternack, I., 1979, Depositional framework and reservoir-quality studies of selected Nanushuk group outcrops, North Slope, Alaska, *in*, T.S. Ahlbrandt, ed., Preliminary geologic, petrologic, and paleontologic results of the study of Nanushuk Group rocks, North Slope, Alaska: U.S. Geological Survey Circular 794, p. 14-31.
- Ahmed, T, 2001, Reservoir Engineering Handbook”, Gulf Professional Publishing, p. 218.
- Ayan, C., Colley, N., Cowan, G., Ezekve, E.; Wannell, M., Goode, P., Halford, F.; Joseph, J., Mongini, A., Obondoko, G., and Pop, J., 1994. Measuring Permeability Anisotropy, Oilfield Review, Schlumberger, p.p. 24-35.
- Alaska Geologic Materials Center Data Report No.353, 2008. Available online at <http://www.dggs.dnr.state.ak.us/webpubs/dggs/gmc/text/gmc353.PDF>
- Andersland, O.B. and Ladanyi, B., 2004, Frozen ground engineering: The American Society of Civil Engineers & John Wiley & Sons, Inc.
- Anderson, D.M., Tice, A.R., 1971, Low-temperature phases of interfacial water in clay–water systems: Proceedings - Soil Science Society of America, vol.35, 47 – 54.
- Bailey, A., 2009, Renaissance says field development will depend on sustained oil prices: Newspaper of Petroleum News, Vol. 14, No. 37.
- Bann, K.L., Fielding, C.R., MacEachern, J.A., and Tye, S.C., 2004, Differentiation of estuarine and offshore marine deposits using integrated ichnology and sedimentology: Permian Pebbly Beach Formation, Sydney Basin, Australia, *in*, D. McIlroy, ed., The Application of Ichnology to Palaeoenvironmental and Stratigraphic Analysis: Lyell Meeting 2003, The Geological Society of London, Special Publication 228, p. 179-211.
- Baptist, O.C., 1959, Oil production from frozen reservoir rocks, Umiat, Alaska: Journal of Petroleum Technology, SPE 1219-G, p.85-88.
- Baptist, O.C., 1960, Oil recovery and formation damage in permafrost, Umiat Field, Alaska, US Department of Interior, Federal Bureau of Mines, Report of Investigations.
- Bartsch-Winkler, S.B., 1985, Petrography of sandstones of the Nanushuk Group from four measured sections, central North Slope, Alaska, *in* A.C. Huffman, ed., Geology of the Nanushuk Group and Related Rocks, North Slope, Alaska: U.S. Geological Survey Bulletin 1614, p. 75-97.

- Beal, C., 1964. The Viscosity of Air, Water, Natural Gas, Crude Oil and Its Associated Gases at Oil Field Temperatures and Pressures, SPE 946094-G, Journal of Transactions of the AIME, Vol. 165, No. 1, pp. 94–115.
- Bergquist, H.R., 1958, Micropaleontologic study of the Umiat Field, Northern Alaska, *in* F.R. Collins, ed., Test Wells, Umiat Area Alaska: U.S. Geological Survey Professional Paper 305-B, p. 199-204.
- Bird, K.J., and Molenaar, C.M., 1992, The North Slope foreland basin, Alaska, *in* R.W. Macqueen and D.A. Leckie, eds., Foreland Fold and Thrust Belts: AAPG Memoir 55, p. 363-393.
- Bhattachaya, J. 2006, Deltas, *in* H.W. Posamentier, and R.G. Walker, eds., Facies Models Revisited: SEPM Special Publication No. 84, p. 237-292.
- Bhattacharya, J., and Giosan, L., 2003, Wave-influenced deltas: geomorphological implications for facies reconstruction: *Sedimentology*, v. 50, p. 187-210.
- Bhattacharya, J., and Walker, R.G., 1991, River- and wave-dominated depositional systems of the Upper Cretaceous Dunvegan Formation, northwestern Alberta: *Bulletin of Canadian Petroleum Geology*, v. 39, p. 165-191.
- Blythe, A.E., Bird, J.M., and Omar, G.I., 1996, Deformational history of the central Brooks Range, Alaska: Results from fission-track and $^{40}\text{Ar}/^{39}\text{Ar}$ analyses: *Tectonics*, v. 15, p. 440-455.
- Buatois, L.A., Santiago, N., Parra, K., and Steel, R., 2008, Animal-substrate interactions in an Early Miocene wave-dominated tropical delta: delineating environmental stresses and depositional dynamics (Tácata field, eastern Venezuela): *Journal of Sedimentary Research*, v. 78, p. 458-479.
- Chilingar, G.V., Herman H.R.; and Mannon, R.W., 1972. Oil and Gas Production from carbonate Rocks, American Elsevier Publishing Company, New York City, 99.
- Christ, M., and Kim, Y., 2009, Experimental Study on the Physical-Mechanical Properties of Frozen Silt: *KSCE Journal of Civil Engineering*, 13(5), 317-324.
- Clifton, H.E., 2006, A reexamination of facies models for clastic shorelines, *in* H.W. Posamentier, and R.G. Walker, eds., Facies Models Revisited: SEPM Special Publication No. 84, p. 293-337
- Coakley, B.J., and Watts, A.B., 1991, Tectonic controls on the development of unconformities: the North Slope, Alaska: *Tectonics*, v. 10, p. 101-130.

- Coleman, J.M., 1988, Dynamic changes and processes in the Mississippi River delta: Geological Society of America Bulletin, v. 100, p. 999-1015.
- Coleman, J.M., and Gagliano, S.M., 1965, Sedimentary structures, Mississippi River deltaic plain: Trans Gulf-Coast Ass. Geol. Socs., v. 14, p. 67-80.
- Collins, F.R., 1958, Test Wells, Umiat Area Alaska: U.S. Geological Survey Professional Paper 305-B, 206 p.
- Dafoe, L.T., Gingras, M.K., and Pemberton, S.G., 2010, Wave-influenced deltaic sandstone bodies and offshore deposits in the Viking Formation, Hamilton Lake area, south-central Alberta, Canada: Bulletin of Canadian Petroleum Geology, b. 58, p. 173-201.
- Danesh, A., 1998, PVT and Phase Behavior of Petroleum Reservoir Fluid, Elsevier, Amsterdam.
- Decker, P. L., 2007, Brookian sequence stratigraphic correlations, Umiat field to Milne Point field, west-central North Slope, Alaska: Alaska Division of Geological and Geophysical Surveys Preliminary Interpretive Report 2007-2, 21 p.
- Department of Energy, [2009]. Alaska North Slope Oil and Gas A Promising Future or an Area in Decline?, Addendum report, DOE/NETL-2009-1385, http://www.netl.doe.gov/technologies/oil-gas/publications/AEO/ANS_Potential.pdf
- Detterman, R.L., 1956, New and redefined nomenclature of the Nanushuk group, *in*, G. Gryc, and others, eds., Mesozoic Sequence in Colville River Region, Northern Alaska: American Association of Petroleum Geologists Bulletin v. 40, p. 233-244.
- Dott Jr., R.H. and Bourgeois, J., 1982, Hummocky stratification: significance of its variable bedding sequences: Geological Society of America Bulletin, v. 93, p. 663-680.
- Dumas, S., and Arnott, R.W.C., 2006, Origin of hummocky and swaley cross-stratification—the controlling influence of unidirectional current strength and aggradation rate: Geology, v. 34, p. 1073-1076.
- Duncan, A., 2007, Evolution of fractures and Tertiary fold-and-thrust deformation in the central Brooks Range foothills, Alaska [M.S. thesis]: Fairbanks, AK, University of Alaska Fairbanks.
- Elliot, T., 1974, Interdistributary bay sequences and their genesis: Sedimentology, v. 21, p. 611-622.

- Engelder, T., 1985, Loading paths to joint propagation during a tectonic cycle: an example from the Appalachian Plateau, U.S.A.: *Journal of Structural Geology*, v. 7, p. 459-476.
- Flint, A.G., 1988, Sharp-based shoreface sequences and “offshore bars” in the Cardium Formation of Alberta: Their relationship to relative changes in sea level, *in* Sea-Level Changes-An Integrated Approach: SEPM Special Publication No. 42, p. 357-370.
- Fox, J.E., Lambert, P.W., Pitman, J.K., and Wu, C.H., 1979, A study of reservoir characteristics of the Nanushuk and Colville Groups, Umiat Test Well 11, National Petroleum Reserve in Alaska: U.S. Geological Survey Circular 820, 47 p.
- Frey, R.W., 1990, Trace fossils and hummocky cross-stratification, Upper Cretaceous of Utah: *PALAIOS*, v.5, p. 203-218.
- Gaffney, Cline & Associates, 2006, Umiat field, Alaska: Technical and commercial review; prepared for Renaissance Alaska, LLC. Houston, Texas.
- Gani, M.R., Bhattacharya, J.P., and MacEachern, J.A., 2008, Using ichnology to determine relative influence of waves, storms, tides, and rivers in deltaic deposits: Examples from Cretaceous Western Interior Seaway, U.S.A., *in*, J.A. MacEachern, K.L. Bann, M.K. Gingras, and S.G. Pemberton, eds., *Applied Ichnology*, SEPM Short Course Notes No. 52, p. 209-225
- Gates, G. L. and Caraway, W.H., 1960 (A), Effect of completion fluids on well productivity in permafrost, Umiat field, Alaska: *Journal of Petroleum Technology*, SPE 201383-G, p.33-40,
- Gates, G. L. and Caraway, W.H., 1960 (B), Well productivity related to drilling muds: Umiat field, Naval Petroleum Reserve No.4, Alaska: [Washington] U.S. Dept. of the Interior, Bureau of Mines.
- Ghedan, S.G., B. M, Thiebot, and D.A, Boyd, 2006. Modeling Original Water Saturation in the Transition Zone of a Carbonate Oil Reservoir, *Journal of Reservoir Evaluation and Engineering*, SPE 88756, pp. 681–687
- Gingras, M.K., MacEachern, J.A., and Dashtgard, S.E., 2011, Process ichnology and the elucidation of physico-chemical stress: *Sedimentary Geology*, v. 237, p. 115-134.
- Godabrelidze, V., 2010, Characterization and fluid flow properties of frozen rock systems of Umiat oil field, Alaska, M.S. Thesis, University of Alaska Fairbanks.
- Gryc, G., ed., 1988, *Geology and Exploration of the National Petroleum Reserve in Alaska, 1974-1982*: U.S. Geological Survey Professional Paper 1399, 940 p.

- Hagdorn, A.R., Brown, K.E., 1964. Experimental Study of Pressure Gradients Occurring During Continuous Two Phase Flow in Small-Diameter Vertical Conduits, *Journal of Petroleum Technology*, pp. 475–484.
- Hampson, G.J. 2000, Discontinuity surfaces, clinoforms, and facies architecture in a wave-dominated, shoreface-shelf parasequence: *Journal of Sedimentary Research*, v. 70, p. 325-340.
- Hampson, G.J., and Howell, J.A., 2005, Sedimentologic and geomorphic characterization of ancient wave-dominated deltaic shorelines: Upper Cretaceous Blackhawk Formation, Book Cliffs, Utah, U.S.A., *in* L. Giosan and J.P. Bhattacharya, eds., *River Deltas—Concepts, Models, and Examples*: SEPM Special Publication No. 83, p. 133-154.
- Hampson, G.J., and Storms, J.E.A., 2003, Geomorphological and sequence stratigraphic variability in wave-dominated, shoreface-shelf parasequences: *Sedimentology*, v. 50, p. 667-701.
- Hanks, C.L., Parris, T., Wallace, W.K., 2006, Fracture paragenesis and microthermometry in Lisburne Group detachment folds: implication for the thermal and structural evolution of the northeastern Brooks Range, Alaska. *AAPG Bulletin* 90 vol.1, 1-20.
- Hanks, C, Shimer, G, Ahmadi, M, Oraki Kohshour, I, McCarthy, P, Dandekar, A, Mongrain, J, Wentz, R, and Davis, J., 2012, Can A Shallow Frozen Reservoir Be Successfully Exploited? A Predevelopment Case Study Of The Umiat Oil Field, Northern Alaska, SPE 159249-MS.
- Hanks, C., Shimer, G., Davis, J., Wentz, R., Godabrelidze, V., Shukla, C., Levi-Johnson, O., Huckabay, A., McCarthy, P., Mongrain, J., Dandekar, A., Bangia, V., 2011, Production of light oil from a shallow frozen reservoir: A predevelopment case study of the Umiat oil field, northern Alaska: *Offshore Technology Conference* paper 22064.
- Hayes, M., Hanks, C.L., 2008, Evolving mechanical stratigraphy during detachment folding: *Journal of Structural Geology*, vol. 30, pp. 548-564
- Holmes, S.P., and Miller, N., 2006, Aspects of the ecology and population genetics of the bivalve *Corbula gibba*: *Marine Ecology Progress Series*, v. 315, p. 129-140.
- Houseknecht, D.W., and Schenk, C.J., 2005, Sedimentology and sequence stratigraphy of the Cretaceous Nanushuk, Seabee, and Tuluvak formations exposed on Umiat Mountain, North-Central Alaska: *U.S. Geological Survey Professional Paper* 1709-B, 18 p.

- Houseknecht, D.W., Bird, K.J., and Schenk, C.J., 2009, Seismic analysis of clinoform depositional sequences and shelf-margin trajectories in Lower Cretaceous (Albian) strata, Alaska North Slope: *Basin Research*, v. 21, p. 644-654.
- Hubbard, R.J., Edrich, SP., and Rattey, .P., 1987, Geologic evolution and hydrocarbon habitat of the 'Arctic Alaska microplate': *Marine and Petroleum Geology*, v. 4, p. 2-34.
- Huffman Jr., A.C., ed., 1985, *Geology of the Nanushuk Group and Related Rocks, North Slope, Alaska*: U.S. Geological Survey Bulletin 1614, 129 p.
- Huffman Jr., A.C., Ahlbrandt, T.S., Pasternack, I., Stricker, G.D., and Fox, J.E., 1985, Depositional and sedimentologic factors affecting the reservoir potential of the Cretaceous Nanushuk Group, central North Slope, Alaska, *in* A.C. Huffman, ed., *Geology of the Nanushuk Group and Related Rocks, North Slope, Alaska*: U.S. Geological Survey Bulletin 1614, p. 61-74.
- Johnson, E.F., Bossler, D.P. and Naumann, V.O., 1959, Calculation of relative permeability from displacement experiments, *Trans. AIME*, 216, p. 370-372.
- Joshi Technologies International Inc, 2008, Umiat Field, Alaska: Development with Horizontal wells; prepared for Renaissance Alaska, LLC. Houston, Texas.
- Katz, D.L. and A. Firoozabadi, 1978, Predicting phase behavior of condensate/crude oil using methane interaction coefficient, *J. Pet. Tech.*, 30, 1649-1655.
- Ketzer, J.M., Morad, S., Evans, R., and Al-Aasm, I.S., 2002, Distribution of diagenetic alterations in fluvial, deltaic, and shallow marine sandstones within a sequence stratigraphic framework: evidence from the Mullaghmore Formation (Carboniferous), NW Ireland: *Journal of Sedimentary Research*, v. 72, p. 760-774.
- Kleinberg, R.L., Flaum, C., and Collett, T.S., 2004, Magnetic resonance log of Mallik 5L-38: hydrate saturation, growth habit, relative permeability and control of accumulation. In: Dallimore, S.R., Collett, T.S. (Eds.), *Scientific Results from the Mallik 2002 Gas Hydrate Production Research Well, Mackenzie Delta, Northwest Territories, Canada*: Geological Survey of Canada, Ottawa, Bulletin 585.
- Kleinberg, R. L., and Griffin, D. D., 2005, NMR measurements of permafrost: unfrozen water assay, pore-scale distribution of ice, and hydraulic permeability of sediments: *Cold Regions Science and Technology*, vol. 42, 63–77.
- Kljcec, N. M., Yurkowski, K. J., and Lipsett, L. R., 1974, Successful drilling of the permafrost with a bentonite-XC polymer-KCl mud systems, *JCPT*, January – March.

- Kumar, N., K.J. Bird, P.H. Nelson, J.A. Grow and K.R. Evans, 2002, A Digital Atlas of Hydrocarbon Accumulations within and adjacent to the National Petroleum Reserve—Alaska (NPRA): USGS Open-File Report 02-71.
- Lamb, M.P., Myrow, P.M., Lukens, C., Houck, K., and Strauss, J., 2008, Deposits from wave-influenced turbidity currents: Pennsylvanian Miniturn Formation, Colorado, U.S.A.: *Journal of Sedimentary Research*, v. 78, p. 480-498.
- Legg, G.W., and Brockway, R., 1983, Geological Report Seabee Test Well No. 1: U.S. Geological Survey Report, 79 p.
- LePain, D.L., and Kirkham, 2001, Potential reservoir facies in the Nanushuk Formation (Albian-Cenomanian), central North Slope, Alaska: Examples from outcrop and core, *in*, D.W. Houseknecht, ed., NPRA Core Workshop - Petroleum Plays and Systems in the National Petroleum Reserve – Alaska: SEPM Core Workshop No. 21, p. 19-36
- LePain, D.L., McCarthy, P.J., and Kirkham, R., 2009, Sedimentology, stacking patterns, and depositional systems in the middle Albian-Cenomanian Nanushuk Formation in outcrop, Central North Slope, Alaska: Alaska Division of Geological and Geophysical Surveys Report on Investigations 2009-1, 86 p.
- Levi-Johnson, I.O., 2010, Petrophysical Property Modeling of Umiat Field, a Frozen Oil Reservoir, Master's Thesis, University of Alaska Fairbanks, 144 p.
- Li, W., Bhattacharya, J.P., Zhu, Y., Garza, D., and Blankenship, E., 2011, Evaluating delta asymmetry using three-dimensional facies architecture and ichnological analysis, Ferron 'Notom Delta', Capital Reef, Utah, USA: *Sedimentology*, v. 58, p. 478-507.
- Linc Energy report, 2012, Linc Energy's Umiat Oil Field Update, <http://www.lincenergy.com/data>
- MacEachern, J.A., Bann, K.L., Bhattacharya, J.P., and Howell, C.D., 2005, Ichnology of Deltas: Organism response to the dynamic interplay of rivers, waves, storms and tides, *in* L. Giosan, and J.P. Bhattacharya, eds., *River Deltas—Concepts, Models, and Examples*, SEPM Special Publication No. 83, p. 49-85.
- Masoudi, R., Hafidz M., Karkooti, and H., Othman, M., 2012, On the Concept and Challenges of Water Saturation Determination and Modeling in Carbonate Reservoirs, SPE International Petroleum Technology Conference, ISBN 978-1-61399-148-0.
- Masterson IV, W. D. , 2001, Petroleum Filling History of Central Alaskan North Slope Fields, Ph.D. Thesis, The University of Texas at Dallas.

- May, F.E., and Shane, J.D., 1985, An analysis of the Umiat delta using palynologic and other data, North Slope, Alaska, *in* A.C. Huffman, ed., *Geology of the Nanushuk Group and Related Rocks, North Slope, Alaska*: U.S. Geological Survey Bulletin 1614, p. 97-120.
- McCain, W.D., 1990, *The Properties of Petroleum Fluids*, Second edition, PennWell Publishing Company, p 444.
- Molenaar, C.M., 1982, Umiat Field, an oil accumulation in a thrust-faulted anticline, North Slope of Alaska, *in*, R.B. Powers, ed., *Geologic Studies of the Cordilleran Thrust Belt: Rocky Mountain Association of Geologists*, v. 2, p. 537-548.
- Molenaar, C.M., 1985, Subsurface correlations and depositional history of the Nanushuk Group and related strata, North Slope, Alaska, *in* A.C. Huffman, ed., *Geology of the Nanushuk Group and Related Rocks, North Slope, Alaska*: U.S. Geological Survey Bulletin 1614, p. 37-60.
- Moore, T.E., Wallace, W.K., Bird, K.J., Karl, S.M., Mull, C.G., and Dillon, J.T., 1994, *Geology of Northern Alaska*, *in* *The Geology of North America*, v. G-1, *The Geology of Alaska*: Geological Society of America, p. 49-140.
- Morad, S., Al-Ramadan, K., Ketzer, J.M., and De Ros, L.F., 2010, The impact of diagenesis on the heterogeneity of sandstone reservoirs: A review of the role of depositional facies and sequence stratigraphy: *AAPG Bulletin*, v. 94, p. 1267-1309.
- Mull, C.G., 1985, Cretaceous tectonics, depositional cycles, and the Nanushuk group, Brooks Range and Arctic Slope, Alaska, *in* A.C. Huffman, ed., *Geology of the Nanushuk Group and Related Rocks North Slope, Alaska*: U.S. Geological Survey Bulletin 1614, p. 7-36.
- Mull, C.G., Houseknecht, D.W., and Bird, K.J., 2003, Revised Cretaceous and Tertiary stratigraphic nomenclature in the Colville Basin, northern Alaska: U.S. Geological Survey Professional Paper 173, 51 p.
- Mull, G.G., Houseknecht, D.W., Pessel, G.H., and Garrity, C.P., 2004, *Geologic map of the Umiat quadrangle, Alaska*: U.S. Geological Survey Scientific Investigations Map 2817-A, scale 1:250,000.
- Myrow, P.M., Fischer, W., and Goodge, J.W., 2002, Wave-modified turbidites: combined flow shoreline and shelf deposits, Cambrian, Antarctica: *Journal of Sedimentary Research*, v. 72, p. 641-656.
- Myrow, P.M., and Southard, J.B., 1996, Tempestite deposition: *Journal of Sedimentary Research*, v. 66, p. 875-887.

- Narr, W., and Suppe, J., 1991, Joint spacing in sedimentary rocks: *Journal of Structural Geology*, v. 13, p. 1037-1048.
- Nelson, C.H., 1982, Modern shallow-water graded sand layers from storm surges, Bering Shelf: a mimic of Bouma sequences and turbidite systems: *Journal of Sedimentary Petrology*, v., 52, p. 537-545.
- Nunn, J.A., Czerniak, M., and Pilger Jr., R.H., 1987, Constraints on the structure of Brooks Range and Colville Basin, northern Alaska, from flexure and gravity analysis: *Tectonics*, v. 6, p. 603-617.
- Olariu, C., and Bhattacharya, J.P., 2006, Terminal distributary channels and delta front architecture of river-dominated delta systems: *Journal of Sedimentary Research*, v. 76, p. 212-233.
- O'Sullivan, P.B., Murphy, J.M., and Blythe, A.E., 1997, Late Mesozoic and Cenozoic thermotectonic evolution of the central Brooks Range and adjacent North Slope foreland basin, Alaska: Including fission track results from the Trans-Alaska Crustal Transect (TACT): *Tectonics*, v. 102, p. 20,821-20,845.
- Pattinson, S.A.J., 2005, Storm-influenced prodelta turbidite complex in the Lower Kenilworth Member at Hatch Mesa, Book Cliffs, Utah, U.S.A.: Implications for shallow marine facies models: *Journal of Sedimentary Research*, v. 75, p. 420-439.
- Pattinson, S.A.J., 1995, Sequence stratigraphic significance of sharp-based lowstand shoreface deposits, Kenilworth Member, Book Cliffs, Utah: *AAPG Bulletin* v. 79, p. 444-462.
- Pedersen K.S. and A. Fredenslund, 1987, *Chem. Eng. Sci.*, Vol. 42, No. 1, pp.182–186.
- Pedersen, K.S., A. Fredenslund, and P. Thomassen, 1989, *Properties of Oils and Natural Gases*, Gulf Publishing Company, USA,
- Pemberton, S.G., and MacEachern, J.A., 1995, The sequence stratigraphic significance of trace fossils: examples from the Cretaceous foreland basin of Alberta, Canada, *in* J.C. Van Wagoner and G.T. Bertram, eds., *Sequence Stratigraphy of Foreland Basin Deposits: Outcrop and Subsurface Examples from the Cretaceous of North America*: American Association of Petroleum Geologists, Memoir 64, p. 429-475
- Peneloux, A., E. Rauzy, and R. Freze, 1982, *Fluid Phase Equilibria*, 8, 7-23,.
- Pratt, B.R., 1998, Syneresis cracks: subaqueous shrinkage in argillaceous sediments caused by earthquake-induced dewatering: *Sedimentary Geology*, v. 117, p. 1-10.
- Robinson, D.B. and D.Y. Peng, 1978, The characterization of the heptanes and heavier fractions for the GPA Peng-Robinson programs: GPA Research Report 28, Tulsa.

- Roebuck, I.F, 1987, Gas-Injection Pressure Maintenance in Oil Reservoirs, Petroleum Engineering Handbook., Society of Petroleum Engineers, pp. 43-1& 43-19.
- Roxar. RMS, Irap Instruction Manual, 1994-2008.
- Sahoo, B.C., Vajjha, R.S., Ganguli, R., Chukwu, G. A., and Das, D. K., 2009, Determination of Rheological Behavior of Aluminum Oxide Nanofluid and Development of New Viscosity Correlations: Petroleum Science and Technology, 27, 1757–1770.
- Samarskiy, A. G., et. al., 2008, High performance freshwater flocculating drilling fluid helps to increase efficiency of extended reach drilling operations and cut costs on Uvat oilfield, paper SPE presented at the Russian Oil and Gas Technical Conference and Exhibition, Moscow, Russia, 28-30 Oct.
- Schindler, J.F., 1988, History of exploration in the National Petroleum Reserve in Alaska, with emphasis on the period from 1975-1982, *in* G. Gryc, ed., Geology and Exploration of the National Petroleum Reserve in Alaska, 1974-1982: U.S. Geological Survey Professional Paper 1399, p. 13-76.
- Schneider, J.H., 2003. Empirical Capillary Pressure Relative Permeability Correlation, http://www.jhschneider.com/Empirical_Capillary_Relationship
- Shang, B, Hamman, J.G.; and Caldwell, D.H., 2008, Improved Water Saturation Estimation Using Equivalent Rock Element Model And Applications to Different Rock Types, Europec/EAGE Conference and Exhibition, ISBN 978-1-55563-178-9.
- Shukla, C., 2011, Fluid characterization and phase behavior studies for frozen reservoir of Umiat oil field, Alaska, M.S. Thesis, University of Alaska Fairbanks.
- Smith, D.W., Low, N., 1996, Cold regions utilities monograph: American Society of Civil Engineers.
- Standing, M.B., 1947, Drilling & Production Practices, API, 275-87.
- Taylor, K.G., Gawthorpe, R.L., and Van Wagoner, J.C., 1995, Stratigraphic control on laterally persistent cementation, Book Cliffs, Utah, Journal of the Geological Society, v. 152, p. 225-228.
- Thomas, S, and Faruq Ali, S.M., 1994. A Realistic Look at Enhanced Oil Recovery. <http://www.scientiairanica.com/pdf/articles/00000911/si010304.pdf>
- Van Golf-Racht, T.D., 1981. Fundamentals of Fractured Reservoir Engineering, Elsevier Publishing Company. pp. 212–214

- Van Wagoner, J.C., Mitchum, R.M., Campion, K.M., and Rahmanian, V.D., 1990, Siliciclastic sequence stratigraphy in well logs, cores, and outcrops: AAPG Methods in Exploration 7, 55 p.
- Vasquez, M.E. and Beggs, H.D., 1978, Journal of Petroleum Technology, 968-70, 1980. D.B. Robinson, D.Y. Peng, The characterization of the heptanes and heavier fractions for the GPA Peng-Robinson programs, GPA Research Report 28, Tulsa.
- Venepalli, K., 2011, Implications of pore-scale distribution of frozen water for the production of hydrocarbon reservoirs located in permafrost: M.S. thesis, University of Alaska Fairbanks. 101 pp.
- Walker, J.D., and Geissman, J.W., 2009, Geologic Time Scale: Geological Society of America, doi: 10.1130/2009.CTS004R2C.
- Watt, J., Huckabay, A., and Landt, M.R., 2010, Umiat: a North Slope giant primed for oil development: Oil and Gas Journal, v. 108, p. 30-38.

BIBLIOGRAPHY

Theses completed

- Godabrelidze, V., 2010. "Characterization and fluid flow properties of frozen rock systems at Umiat Oil Field, Alaska." M.S. thesis, University of Alaska Fairbanks.
- Levi-Johnson, O., 2010. "Petrophysical property modeling of Umiat field, a frozen reservoir." M.S. thesis, University of Alaska Fairbanks.
- Shukla, C., 2011, "Fluid characterization and phase behavior studies of oil from the frozen reservoir of Umiat Oil Field, Alaska." M.S. thesis, University of Alaska Fairbanks.
- Venepalli, K., 2011. "Implications of the Pore-Scale Distribution of Frozen Water for the Production of Hydrocarbon Reservoirs Located in the Permafrost." M.S. thesis, University of Alaska Fairbanks.

Theses/Dissertations in progress

- Davis, J., in progress, Petrography and Diagenesis of the Nanushuk Formation at Umiat field, central North Slope, Alaska: M.S. thesis, University of Alaska Fairbanks
- Oraki-Kohshour, in revision, Geological modeling and reservoir simulation of Umiat: M.S. thesis, University of Alaska Fairbanks
- Sanders, C., in revision, Structural geometry of the Big Bend anticline, Brooks Range foothills, Alaska: M.S. thesis, University of Alaska Fairbanks.
- Shimer, G., in progress, Sedimentology and stratigraphy of the Nanushuk Formation, North Slope, Alaska: Ph.D. dissertation, University of Alaska Fairbanks.
- Wentz, R., in revision, Fracture distribution and character in and around the Umiat anticline: M.S. thesis, University of Alaska Fairbanks.

Peer-reviewed publications

- Godabrelidze, V., Dandekar, A., Hanks, C., Mongrain J. and Patil S., in preparation, Measurement of gas-oil relative permeability for frozen rock systems: To be submitted to Transport in Porous Media
- Shimer, G., McCarthy, P., Hanks, C., and Davis, J., in review, Sedimentology, stratigraphy, and reservoir properties of an unconventional reservoir in the Cretaceous Nanushuk Formation at Umiat field, North Slope, Alaska: manuscript submitted to AAPG Bulletin.

- Shukla, C., Dandekar, A., Hanks, C., Mongrain, J. and Patil, S., in preparation, Fluid Characterization and Phase Behavior Studies of Oil from Frozen Reservoir of Umiat Oil Field, Alaska: To be submitted to Fluid Phase Equilibria
- Hanks, C., Shimer, G., Oraki-Kohshour, I., Ahmadi, M., McCarthy, P., and Dandekar, A., in review, Integrated reservoir characterization and simulation of a shallow, light oil, low temperature reservoir: Umiat Field, National Petroleum Reserve, Alaska: manuscript submitted to AAPG Bulletin.
- Hanks, C., P. McCarthy, G. Shimer, A. Dandekar, J. Mongrain, C. Shukla, V. Godabrelidze, K. Venepalli, R. Wentz, J. Davis, I. Oraki-Kohshour, O. Levi-Johnson, W. Wallace, C. Sanders, 2012, Can A Shallow Frozen Reservoir Be Successfully Exploited? A Predevelopment Case Study Of The Umiat Oil Field, Northern Alaska: 2012 SPE ATCE paper 159249
- Hanks, C., Shimer, G., Davis, J., Wentz, R., Godabrelidze, V., Shukla, C., Levi-Johnson, O., Huckabay, A., McCarthy, P., Mongrain, J., Dandekar, A., Bangia, V., 2011, Production of light oil from a shallow frozen reservoir: A predevelopment case study of the Umiat oil field, northern Alaska: Offshore Technology Conference paper 22064.
- Kohshour, I.O, Ahmadi, M. and Hanks, C., in review, Uncertainty Assessment in Geologic Modeling and Sensitivity Analysis of Static and Dynamic Models in Umiat: A Frozen Shallow Oil Accumulation in National Petroleum Reserve of Alaska: To be submitted to Petroleum Science and Engineering.

Abstracts

- Davis, J., McCarthy, P., Hanks, C., 2011, Petrologic and Geochemical Controls on Diagenesis for the Nanushuk Formation, North Slope, Alaska: in Program with Abstracts 2011 joint AAPG Pacific Section/SPE Western Regional meetings, Anchorage, Alaska.
- Demallie, J., 2012, "Drilling Fluid Characteristics and Formation Damage in Umiat Field, Alaska." 2012 American Association of Drilling Engineers Technical Conference and Exhibition
- Hanks, C., Huckabay, A., Mongrain, J., Dandekar, A., Bangia, V., McCarthy, P., 2011. "Production of Light Oil from a Shallow, Frozen Reservoir: A Predevelopment Case Study of the Umiat Oil Field, Northern Alaska." 2011 Arctic Technology Conference, Houston, Texas, February 2011
- Hanks, C., Mongrain, J., Dandekar, D., McCarthy, P., Godabrelidze, V., Shukla, C., Venepalli, K., Levi-Johnson, O., Shimer, G., and Wentz, R., 2010. "Integrated Geological and Engineering Studies in Support of Producing Light Oil from a

- Frozen Reservoir: A Case Study from Umiat Oil Field, Northern Alaska.” AAPG 2010 International Conference and Exhibition, Calgary, Alberta, Canada.
- Hanks, C.L., McCarthy, P.J., Huckabay, A., Mongrain, J., Dandekar, A., Patil, S., and Bangia, V., 2009. “Producing light oil from a frozen reservoir: reexamining Umiat Field, National Petroleum Reserve, Alaska.” 2009 AAPG Annual Meeting Abstracts
- Hanks, C.L., Shimer, G., McCarthy, P., Davis, J., Wentz, R., Mongrain, J., Dandekar, A., Shukla, C., Venepalli, K., Godabrelidze, V., Levi-Johnson, O., Huckabay, A., Bangia, V., Dunn, M., 2011, Reservoir Characterization and Modeling of a Frozen Light Oil Accumulation: Umiat Field, Northern Alaska: in Proceedings of the 2011 AAPG 3PArctic Conference, Halifax, Canada. (Accepted but withdrawn because travel not approved)
- Huckabay, A. and Hanks, C.L., 2009. “The Petroleum Geology of Umiat Oil Field, North Slope, Alaska.” Proceedings of the 2009 AAPG 3PArctic Conference, Moscow, Russia.
- Levi-Johnson, O., 2009. “Flow characteristics of the Nanushuk Group at Umiat Field.” 2009 Alaska Geological Society Technology Conference, Fairbanks, Alaska, May 2010.
- Mongrain, J., Hanks, C., Huckabay, A., Dandekar, A., Bangia, V., McCarthy, P., Patil, P., 2009. “Production methods for light oil in a frozen reservoir: Umiat Field, National Petroleum Reserve, Alaska.” Proceedings of the 2009 AAPG 3PArctic Conference, Moscow, Russia.
- Shimer, G., Davis, J., McCarthy, P., and Hanks, C.L., 2011, Foreland Basin Topset Deposits of the Cretaceous Nanushuk Formation, Umiat, Alaska: : in Proceedings of the 2011 AAPG 3PArctic Conference, Halifax, Canada (Accepted but withdrawn because travel not approved).
- Shimer, G., McCarthy, P., Hanks, C., 2011, Core-based Interpretation of Parasequence Stratigraphy within the Cretaceous Nanushuk Formation, Umiat, Alaska: in Program with Abstracts 2011 joint AAPG Pacific Section/SPE Western Regional meetings, Anchorage, Alaska.
- Shimer, G., Davis, J., McCarthy, P.J., and Hanks, C., 2010. “An Integrated Outcrop and Subsurface Facies Analysis of the Albian-Cenomanian Nanushuk Formation near Umiat, National Petroleum Reserve, Alaska.” AAPG 2010 International Conference and Exhibition, Calgary, Alberta, Canada

Shimer, G., McCarthy, P., Hanks, C., 2010. "Facies Analysis of Cretaceous Strata from the Umiat Wells, National Petroleum Reserve, Alaska." 2010 AAPG Annual Meeting Abstracts

Wentz, R., Hanks, C., Wallace, W., McCarthy, P., 2011, Fracture Distribution and Character in Exposed Cretaceous Rocks Near the Umiat Anticline, North Slope of Alaska: in Program with Abstracts 2011 joint AAPG Pacific Section/SPE Western Regional meetings, Anchorage, Alaska.